Understanding Microstructural Properties of Perovskite Ceramics through Their Wet-Chemical Synthesis

TOMASZ M. STAWSKI

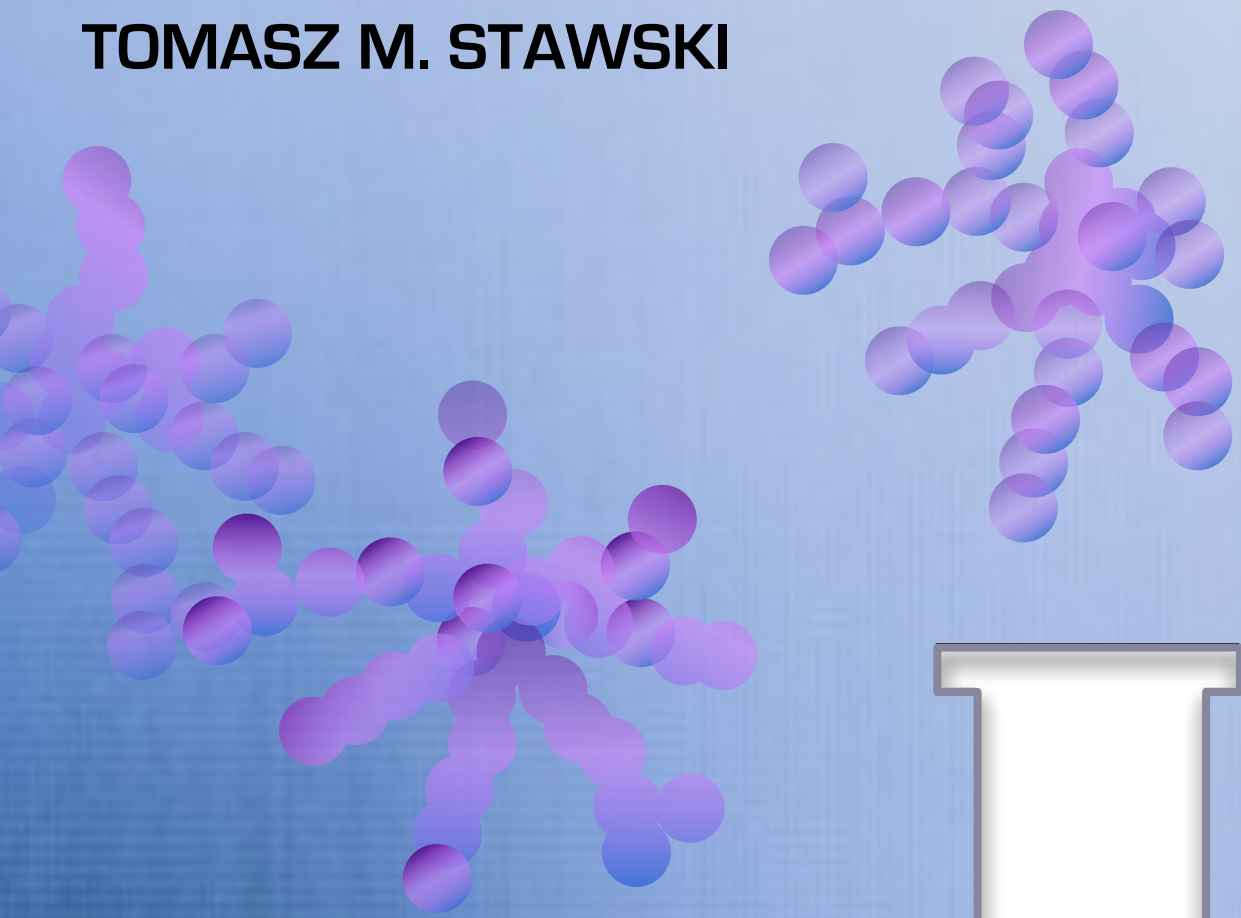

UNIVERSITEIT TWENTE.

MESA+
INSTITUTE FOR NANOTECHNOLOGY

Propositions

Accompanying the thesis

Understanding Microstructural Properties of Perovskite Ceramics through Their Wet-Chemical Synthesis

Tomasz M. Stawski

1. There is no reasonable analytical model describing small angle x-ray scattering of the initial stages of agglomeration involving only a few clusters.
2. Analytical models used for SAXS data analysis tend to give simple answers to problems concerning complicated systems and processes. Are the simple answers the right ones?
3. Barium titanate has lost its charm.
4. Each European nation perceives itself as exclusively truly European and the whole rest as slightly barbaric and in the best case adequate.
5. Scientists working in the field of natural sciences ought to develop interests in humanities and social sciences.
6. For the sake of us all, it should not work the other way round.

Understanding Microstructural Properties of Perovskite Ceramics through Their Wet-Chemical Synthesis

Ph. D. committee:

Chairman and secretary

Prof. dr. ir. W. Steenbergen (Universty of Twente)

Supervisors

Prof. dr. ir. J. E. ten Elshof (University of Twente)
Prof. dr. ing. D. H. A. Blank (University of Twente)

Members

Prof. dr. M. van Bael (University of Hasselt)
Dr. B. L. Mojet (University of Twente)
Dr. A. Petoukhov (University of Utrecht)
Prof. dr. J. G. E. Gardeniers (University of Twente)
Prof. dr. ing. A. J. H. M. Rijnders (University of Twente)

The research described in this thesis was performed within the Inorganic Materials Science group and the MESA+ Institute for Nanotechnology at the University of Twente, the Netherlands and within Dutch-Belgian beamline (DUBBLE BM-26B) of European Synchrotron Research Facility (ESRF), France.
This research was supported by the Dutch Technology Foundation STW, which is part of the Netherlands Organisation for Scientific Research (NWO) and partly funded by the Ministry of Economic Affairs, Agriculture and Innovation (project number 07711, "Sub-micron thin doped barium titanate films for MLCC technology").

Tomasz M. Stawski
Understanding Microstructural Properties of Perovskite Ceramics through Their Wet-Chemical Synthesis
Ph. D. thesis University of Twente, Enschede, the Netherlands.

ISBN: 978-90-365-3303-4
DOI: 10.3990/1.9789036533034
Printed by Wöhrmann Print Service, Zutphen, the Netherlands
Cover: designed by Tomasz M. Stawski

UNDERSTANDING MICROSTRUCTURAL PROPERTIES OF PEROVSKITE CERAMICS THROUGH THEIR WET-CHEMICAL SYNTHESIS

PROEFSCHRIFT

ter verkrijging van
de graad van doctor aan de Universiteit Twente,
op gezag van de rector magnificus,
prof. dr. H. Brinksma,
volgens besluit van het College voor Promoties
in het openbaar te verdedigen
op donderdag 15 december 2011 om 12.45 uur

door

Tomasz Maciej Stawski

geboren op 19 april 1983
te Gdynia, Pommeren, Polen

Dit proefschrift is goedgekeurd door de promotoren:
Prof. dr. ir. J. E. ten Elshof
Prof. dr. ing. D. H. A. Blank

Dla Kasi i Mai coby mogły być ze mnie dumne.

Table of Contents

1

Introduction

1.1. Wet-chemical synthesis of perovskite-type ceramics

A group of ceramics referred to as perovskites derives its name from the original *perovskite i.e.* calcium titanate, $CaTiO_3$. This mineral was discovered by Gustav Rose in the Ural Mountains, who named it in honor of Russian mineralogist Lev Aleksevich von Perowski [1,2]. Perovskite-structure materials exhibit a general ABX_3 stoichiometry where *A* and *B* are metal/half-metal cations, and *X* is an anion of typically oxygen or halogens (Br, Cl, F). Several equivalent descriptions of the structure are possible [2], among which a pseudo-cubic unit cell as found in Figure 1.1A constitutes a relevant example. Here, eight larger *A*-site cations reside in the corners of the cube, whereas the smaller *B*-site cation is located in the middle of a unit cell. The positive charge of the cations is compensated by six *X*-site anions located face-centered. In the crystal (Figure 1.1B) *X*-site anions form octahedral cages around the *B*-site cation (Figure 1.1C), whereas the *A*-site cation fills the dodecahedral holes (Figure 1.1D) [1,2].

More than 20 elements have been known to occupy the *A*-site position, and more than 50 elements have been found to occupy the *B*-site in perovskites [2]. Interestingly, magnesium silicate, $MgSiO_3$, has been recognized as the most common mineral in the Earth [2]. Considering a large number of elements that can be combined into ABX_3-type structure it is not astonishing that a wide variety of properties is exhibited by perovskites. They are utilized among others as dielectrics, piezoelectrics, ferroelectrics, semiconductors, metallic conductors, superconductors, ferromagnets, anti-ferromagnets, or multiferroic materials. The research projects described in this work focus on technologically important perovskite-structure oxides, namely barium titanate, ($BaTiO_3$ or BTO), and lead zirconate titanate ($PbZr_{1-x}Ti_xO_3$ or PZT). In contrast to $CaTiO_3$, which exists as a cubic phase, the structures of BTO and PZT are distorted to lower symmetries (hence a pseudo-cubic description). In the case of barium titanate the distortion originates from the displacement of the Ti^{4+} cation from the center of the octahedral oxygen anion cage [1-4]. It results in a temperature-dependent deviation from cubic symmetry to tetragonal, rhombohedral or orthrombic

phases. In terms of properties, lowering of unit cell symmetry leads to a spontaneous polarization, which is responsible for ferroelectricity in the material. Similarly, it was shown in literature that the ferroelectric behavior of lead zirconate titanates results from collective displacements of zirconium and titanium, as well as distortions in the positions of lead [5].

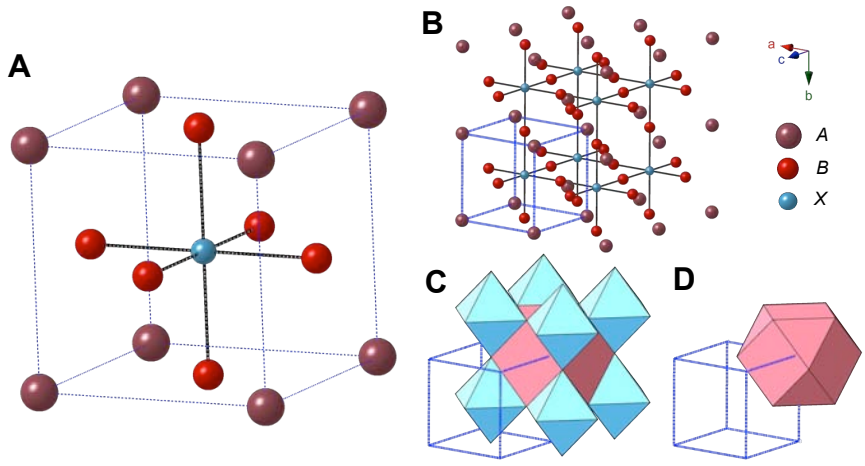

Figure 1.1. a) Pseudo-cubic unit cell of the perovskite-type ABX_3 structure; b) Part of the crystal based on the perovskite unit cell; c) X_6 octahedral cages and partially visible *A*-site-based dodecahedron; d) *A*-site-based dodecahedron.

Barium titanate is a widely used high-*k* ceramic dielectric material. It is utilized in a wide range of applications, many of which are based on the use of $BaTiO_3$ thin films. It is an important dielectric material, for instance in commercial multi-layer ceramic capacitors [4,6]. When integrated with silicon technology (primarily CMOS), barium titanate could be applied as dielectric material for dynamic random access memories (DRAMs) [7-9], and as ferroelectric in non-volatile ferroelectric memories (FeRAMs) [8,9].

Because of its wide range of applications a lot of interest has been also dedicated to the fabrication and characterization of lead zirconate titanate thin films [8-11]. PZT is technologically important due to its large remnant polarization, low coercive field, and high piezoelectric coefficients. In order to fabricate devices integrating thin films of BTO, PZT or other related perovskite oxides, new deposition techniques, as well as new powder production methods are desired. There are two major routes for the fabrication of metal oxide thin films, namely physical and wet-chemical techniques. The physical techniques include among others metal-organic chemical vapor deposition (MOCVD), sputtering, and pulsed laser deposition [12-17]. Classical tape casting and post-processing of perovskite metal oxide powder-containing slurries could also be regarded as a physical technique [6]. One of the feasible alternatives is

the deposition of amorphous precursors of oxides and their further reaction and crystallization into a perovskite phase [3,4,18-21]. Good control and understanding of the process in all stages is required to obtain a film or a powder with the desired electrical and morphological properties. This can be achieved by wet-chemical processing methods. The wet-chemical methods, among others, include the sol-gel route and metal-organic deposition (MOD) [18-26]. Among the latter, the sol-gel technique has attracted considerable attention because of its simplicity, low cost, good compositional control and its ability for large area film fabrication [3,18,19]. Moreover, as the wet-chemical methods are based on the use of liquid precursors, direct deposition of precursor thin films onto substrates by means of spin-casting, deep-casting or misted source deposition is possible, typically followed by pyrolysis, crystallization, and sintering [18,19,26].

In its primary assumptions the wet-chemical fabrication concept is fairly uncomplicated, as illustrated in Figure 1.2. At the beginning a liquid precursor system is established. It is composed of species "carrying" metal ions desired in the final ceramics and provides homogenous mixing of different elements at all process stages leading to the final product. In the next step, the liquid precursor is either cast onto a substrate when a thin film is desired, or held in a reaction vessel if a powder or gel is to be obtained. The as-dried product is referred to as a xero-gel. The xero-gel, being essentially a solid, still contains in its pores a substantial amount of residual solvents, as well as other organic species bound as ligands. Therefore it must be heat-treated at higher temperatures (typically above 300 °C) in order to evaporate residual solvents, and to decompose/pyrolyze other persisting organics. As a result an amorphous or semi-amorphous structure is obtained, composed of binary metal oxides, metal carbonates or other inorganic phases [18,20,21]. Further heat treatment at higher temperatures (typically above 500 °C, depending on the perovskite) leads to nucleation, growth and sintering of the nano-sized perovskite phase. The general heat processing protocol can be realized in a number of subsequent steps at different temperatures, using varying heating rates and dwell times, or simply as a single step process in which the xero-gel is directly processed at high temperature. The influence of the heat treatment process of sol-gel derived PZT and BTO on the microstructure and related physical properties of thin films and powders is relatively well understood and is covered by the scientific literature [3,18,20,21].

Alkoxide-based systems are commonly utilized in the sol-gel process, either pure mixed-metal alkoxides, or together with carboxylic acids or hydroxides carrying one or more of the metal components. I refer here to these systems as sol-gel precursors. However, it is noted that some authors discriminate between classical sol-gel synthesis, exclusively based on metal alkoxides dissolved in alcohols, and other processes such as chelate synthesis involving modification of alkoxides by chelating agents *e.g.* acetyl acetone or carboxylic acids [3,18]. Therefore, the use of metal

carboxylates dissolved in carboxylic acids constitutes, according to this specific terminology, either a chelate synthesis, or a hybrid route (since it involves two or more chemically different metal sources, among which a least one is an alkoxide and others are carboxylates). As becomes evident from this thesis, such a division is not necessary, because the evolution of hybrid precursors is anyway driven by a sol-gel transition of either modified or unmodified alkoxides. However, the kinetics of formation and morphology of reaction products are of course dependent on the presence of chemical modifiers [3,4,18-21,28-30].

The hydrolysis and condensation reactions of metal alkoxides, $M(OR)_x$ (where M is a metal and R is an alkyl group), are the key reactions in sol-gel chemistry. Upon reaction metal-oxygen-metal bonds are formed (M-O-M), according to the following reaction scheme:

⇒ Hydrolysis reaction

$M(OR)_x + H_2O \rightarrow M(OR)_{x-1}(OH) + ROH$: nucleophilic attack by a water molecule onto a metallic center

⇒ Condensation reactions

$2M(OR)_{x-1}(OH) \rightarrow M_2O(OR)_{2x-3}(OH) + ROH$: via alcohol elimination

$2M(OR)_{x-1}(OH) \rightarrow M_2O(OR)_{2x-2} + H_2O$: via water elimination

Depending on hydrolysis ratio, used catalysts, and modifying alcohols, different metal oxide morphologies can be obtained [28-31]. It must be noted, however, that the abovementioned reaction scheme is merely a conceptual sketch, as different metal alkoxides can form oligomeric species in their parent alcohols, the structure of which is dependent on the nature of the metallic centers and the alkoxy ligands [28,30-32]. Furthermore, the reactivity of alkoxides, the number of reactive sites of alkoxide species that can undergo hydrolysis, and the preferred coordination number of the metallic center, are also dependent on the chelating ligands and reaction conditions used [28,30-33]. A straightforward path of hydrolysis and condensation reactions as outlined above can therefore not be generalized in practice. Oligomeric clusters of metal oxides, metal hydroxides, metal oxo-alkoxides, metal oxo-alkoxy-carboxylates, *etc.*, are formed and referred to as sol. Their further physical and chemical agglomeration leads to the growth of a polymeric network, reaching at some point a macroscopic scale structure known as a gel. As an example of aqueous silica, $Si(OH)_4$ clearly shows [31], the reaction conditions strongly impact the ceramics morphology: (1) monomers react into particles; (2) in acidic solutions or in the presence of flocculating salts, sub-10 nm particles aggregate into networks which form a gel or (3) in basic solutions with salts absent, the growth of homogenous sol particles occurs, with particle sizes reaching 100 nm (Figure 1.3) [31].

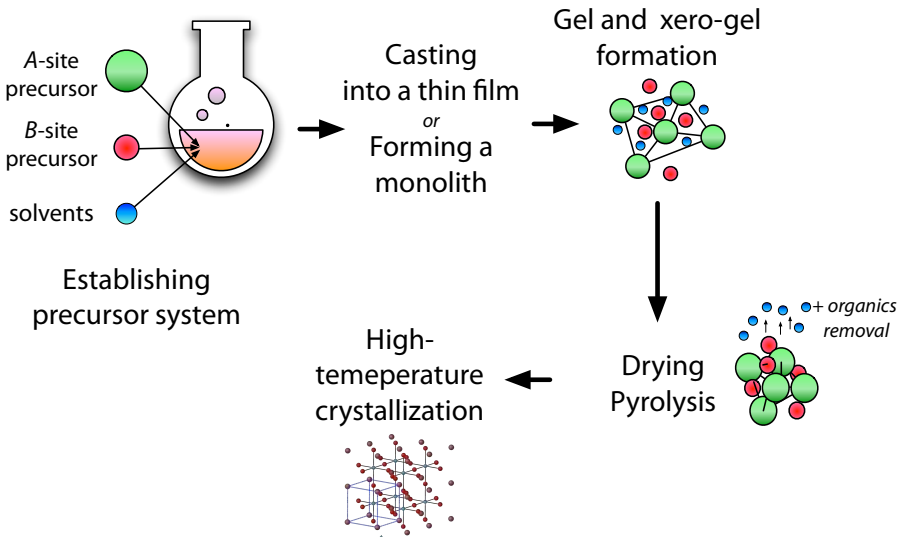

Figure 1.2. Concept of wet-chemical processing leading to perovskite-structure ceramics.

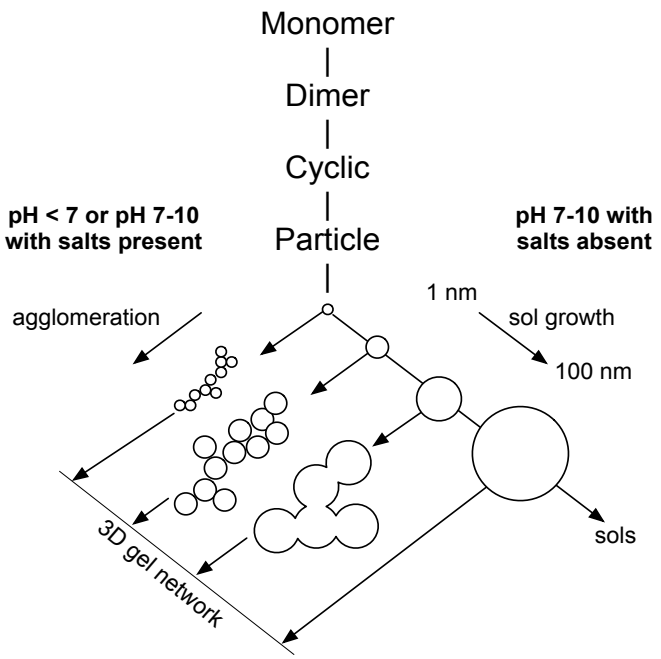

Figure 1.3. Scheme representing the evolution of aqueous silica system from monomers to developed sols and gels, in relation with reaction conditions. Based on ref. [31].

The evolution of aqueous silicates has been heavily investigated in the last three decades. This is mainly due to the technological significance of silica, but also due to the impeded reactivity of silicon carrying-precursors in comparison with transition metal analogs, providing with a good study model system for sol-gel science in general [31,32]. Furthermore, silica does not require heat processing to yield the desired phase. That makes it simpler to link the properties of sols with the properties of expected solid products.

The morphology of BTO and PZT precursors formed in upon reaction of titanium or zirconium alkoxides with carboxylic acids and metal carboxylate salts remains, to the best of my knowledge, a true *terra incognita* despite on-going knowledge build-up in the past. Hence, a large part of this work is devoted to the elucidation of the structure and morphology of selected amorphous precursors of BTO and PZT under various experimental conditions. Related questions concerning sol-gel homogeneity and stability are addressed.

1.2. Scope of this thesis

This thesis comprises of seven full research chapters on the morphology, properties and processing of sol-gel precursor systems of barium titanate (BTO) and lead zirconate titanate (PZT) thin films and powders. In all the considered problems, the synthesis leading to nano-sized perovskite ceramics constitutes the main research theme. In different morphological forms (powders, films, etc.), these materials have been under intensive investigation by the research community, ever since a number of size-dependent effects related to the nano-forms of PZT and BTO have been discovered.

An aspect that cannot be disregarded is the fact that early-stage wet-chemical synthesis might actually influence the properties of the resulting perovskite products. Wet-chemical methods, and particularly the sol-gel technique, are usually viewed as methods in which "near-atomic level of mixing" is reached, in contrast to solid-state synthesis [4,20]. However, the expression "near-atomic level of mixing" is not well-defined in terms of the actual minimum size scale above which mixing can be considered to be homogeneous. It is known that the functional properties of different perovskite ceramics or the same materials, synthesized by sol-gel type reactions, differ depending on the initial precursor chemistry and processing route [18-22,35]. Thus, one can hypothesize that the homogeneity* and stability of sol-gel precursors are dynamic properties that are established in far more complicated processes than mixing alone. It may therefore be assumed that the very fact of reaching the nano-scale with respect to grain size and film thickness in the ceramics is not the only factor

* Homogeneity is also inherently associated with certain length scales. On atomic level obviously no substance is homogeneous.

that determines its properties. The way of synthesis determines the actual size of the crystallites, their shape, nucleation in solution or at the interface, and finally the defect chemistry. Since these aspects are adjustable to a certain extent, they do not result only from the nature of PZT and BTO, but are related to the structure and kinetics of metal-carrying sols. It is the purpose of this thesis to explore the early stages of selected sol-gel methods in terms of their molecular structure and condensation kinetics, and attempt to relate these to known properties of the final nano-sized perovskite ceramics.

1.3. Thesis outline

In Chapter 2 the low-temperature alkoxide–hydroxide precipitation synthesis of nano-sized crystalline barium titanate in nonaqueous media is presented. The influence of the reaction medium on the nature of the product by investigating the reaction of titanium (IV) alkoxide with barium hydroxide hydrates in 2-methoxyethanol and benzyl alcohol, respectively, is investigated. It is demonstarted in this chapter that a change of the ligand surrounding the metallic center has a direct impact onto the sensitivity of the alkoxide towards hydrolysis, because BTO precipitates only in benzyl alcohol, On the other hand, an amorphous xero-gel is the only product of the same synthesis in 2-methoxyethanol. This experiment clearly indicates that reactivity of the Ti(IV) alkoxide precursor could be a key factor controlling a phase and morphology of the desired product, and is as such discussed in detail.

Chapter 3 is a continuation of the research presented in the preceding chapter. The morphology, phase, and defect structure of nano-sized $BaTiO_3$ powders synthesized by the alkoxide-hydroxide process in benzyl alcohol under reflux conditions are considered. The origin of the room-temperature cubic-phase stabilization is discussed in terms of the presence of lattice hydroxyl defect implemented upon synthesis, and residing in the oxygen sites, as well as the so-called "grain-size" effect [34]. Hydroxyl defects are often observed in wet-chemically prepared powders, especially via hydrothermal method. This method, however, yields barium titanate powders typically > 200 nm, since at this grain-size cubic-to-tetragonal distortion has been often observed. Therefore, it is difficult to distinguish between the hydroxyl-defect chemistry impact and the actual grain-size effect. In the case of alkoxide-hydroxide precipitated BTO these two effects are far more clearly separated, because upon heat-treatment in the range 250 – 700 °C only a minor grain growth up to sub-40 nm range is observed. On the other hand this temperature range is sufficient for curing of hydroxyl defects leading initially to a development of peculiar nano-porosity in BTO nano-crystals.

In Chapters 4 and 5 the morphological properties and evolution of alkoxide-carboxylate precursors of barium titanate are discussed. In Chapter 4 the evolution of hydrolyzed alkoxide-carboxylate sol-gel precursor solutions of barium titanate upon gelation at constant concentration of reactants (closed system) is investigated. The properties of sols are probably controlled by a sort of spatial separation between Ti-oxoacetate and Ba-carboxylate-rich domains [18]. The separation is determined by *e.g.* carboxylic acid chemistry, sol concentration and chelating/stabilization agents. No details of nanoscale evolution processes, or of the structure of TiO_x oligomers in contact with metal carboxylates, has been reported to my knowledge. Therefore, it is the aim of this work to confirm that the separation actually takes place and to obtain a better understanding of the evolution of nanostructures in hydrolyzed solutions of titanium alkoxide and barium acetate in acetic acid. The logical consequence of the work from the preceding chapter is presented in Chapter 5, as the structural evolution in wet sol-gel precursor films of barium titanate upon drying (open system) is considered. Relatively few details are known on the kinetics and morphology of barium titanate alkoxide-carboxylate precursors upon reaction and physical drying. Due to the fact that volatile components of the system evaporate, the actual precursor concentration increases rapidly, yielding fast sol-gel transitions in the final stages of physical drying. It is the aim of this work to monitor the structural evolution in wet thin films from solutions of titanium alkoxide and barium acetate in acetic acid during the drying process. It is clearly shown that the morphology of the dried xero-gel strongly depends on the initial sol composition.

Analogical studies of the alkoxide-carboxylate precursor of lead zirconate titanate precursor are considered in Chapters 6 and 7. In Chapter 7 the structural evolution of sol-gel derived PZT precursor films during and after physical drying is discussed. In this process volatile components are lost from the film, and precursor concentrations increase progressively. I consider a selected number of solutions and process conditions, to get insight into the structures that formed in the sol stage, and into the processes that occurres*in situ* on the nanoscale when a PZT sol-gel thin film is being dried. Analogically, Chapter 7 presents the evolution of nanostructure in sol-gel derived PZT and zirconia precursor sols at different hydrolysis ratios. It is known that the nature of the sol has a profound effect on the microstructure, orientation and electrical properties of the PZT films. As it has been pointed out by R. W. Schwartz and co-workers [19], it is especially these stages of the sol-gel processing of PZT on which no information has been available till now, especially where it concerns the quantitative microstructural parameters of sols and their relationship to measurable chemical properties. The aim of this study is to elucidate the structure of PZT precursor sols on a nanometer-length scale.

Chapter 8 addresses the issue of interface diffusion of Si and dielectric properties degradation related to the fabrication of high quality columnar barium titanate thin

films obtained by the alkoxide-carboxylate method in a multi-step processing approach. The influence of high temperature processing of sol-gel derived thin films on platinum and strontium ruthenate coated silicon wafers is investigated. In order to nucleate the perovskite phase heterogeneously at the electrode interface, it must be deposited in a sequence of very thin layers, with a heat-treatment at 700 – 800 °C after each deposition step [35]. The method of production exposes the film to extreme conditions, such as fast cooling and heating, and high temperature, which may be a problem when silicon-based substrates are used. It is therefore demonstrated, how the route as such leading to a specific morphology of BTO film, could affect properties of the fabricated device (a capacitor).

In Chapter 9 general conclusions are drown. Furthermore, several open questions are discussed, indicating possible directions for future research.

1.4. References

[1] De Graef, M.; McHenry M. E. Structure of Materials: An Introduction to Crystallography, and Symmetry, Cambridge University Press, New York, **2007**.

[2] Mitchel, R. H. Perovskites: a revised classification scheme for an important rare earth element host in alkaline rocks. In *Rare Earth Minerals: Chemistry, Origin and Ore Deposition*; ed. Jones, A. P.; Wall, F.; Williams, C. T. Chapman & Hall, London, 41-75, **1996**.

[3] Schwartz, R. W. *Chem. Mater.,* 9, 2325-2340, **1997**.

[4] Chandler, D. C.; Roger, C.; Hampden-Smith, M. J. *Chem. Rev.,* 93, 1205-1241, **1993**.

[5] Warren, W. L.; Robertson, J.; Dimos, D.; Tuttle, B. A.; Pike, G. E.; Payne, D. A. *Phys. Rev. B,* 53, 3080-3087, **1995**.

[6] Yoon, D. *J. Ceram. Proc., 7*, 343-354, **2006.**

[7] Schroeder, H.; Kingon, A. High-Permittivity Materials for DRAMs. In *Nanoelectronics and Information Technology: Advanced Electronic Materials and Novel Devices*, ed. Waser, R., Wiley VCH GmbH & Co, Weinheim, 540-563, **2003**.

[8] Scott, J. F.; Paz de Araujo, C. A. *Science,* 246, 1400-1405, **1989**.

[9] Scott, J. F. *Science*, 315, 954-959, **2007**.

[10] Muralt, P. *J .Micromech. Microeng.*, 10, 136-146, **2000**.

[11] Kondo, M.; Sato, K.; Ishii, M.; Wakiya, N.; Shinozaki, K.; Kurihara, K. *Jpn. J. Appl. Phys.*, 45, 7516-7519, **2006**.

[12] Kim, H. R.; Jeong, S.; Jeon, C. B.; Kwon, O. S.; Hwang, C. S. *J. Mater. Res.*, 16, 3583-3591, **2001**.

[13] Otani, Y.; Okamura, S.; Shiosaki, T. *J. Electroceram.*, 13, 15-22, **2004**.

[14] Lin, Y. C.; Chuang, H. A.; Shen, J. H. *Vacuum*, 83, 921-926, **2009**.

[15] Bouregba, R.; Poullain, G.; Vilquin, B.; Murray, H. *Mater. Res. Bull.,* 35, 1381-1390, **2000**.
[16] Zhu, T. J.; Lu, L.; Lai, M. O. *Appl. Phys. A.,* 81, 701-714, **2005**.
[17] Dekkers, M.; Nguyen, M. D.; Steenwelle, R.; te Riele, P. M.; Blank, D. H. A.; Rijnders, G. *Appl. Phys. Lett.,* 95, 0129021-0129023, **2009**.
[18] Schwartz, R. W.; Schneller, T. S.; Waser, R. *C. R. Chimie, 7*, 433-461, **2004**.
[19] Schwartz, R. W.; Narayanan, M. Chemical Solution Deposition - Basic Principles, In *Solution Processing of Inorganic Materials*, ed. Mitzi, D. B., John Wiley & Sons, Inc., New Jersey, 33-76, **2009**.
[20] Pithan, C.; Hennings, D. H.; Waser, R. *Int. J. Appl. Ceram. Technol.,* 2, 1-14, **2005**.
[21] Phule, P. P.; Risbud, S. H. *J. Mater. Sci.*, 25, 1169-1183, **1990**.
[22] Schwartz, R. W.; Boyle, T. J.; Lockwood, S. J.; Sinclair, M. B.; Dimos, D.; Buchheit, C. *Integr. Ferroelectrics, 7*, 259-277, **1995**.
[23] Yi, G.; Sayer, M. *Ceram. Bull.*, 70, 1173-1179, **1991**.
[24] Klee, M.; Eusemann, R.; Waser, R.; Brand, W.; van Hal, H. *J. Appl. Phys.*, 72, 1566-1576, **1992**.
[25] Cui, T.; Markus, D.; Zurn, S.; Polla, D. L. *Microsyst. Technol.,* 10, 137-141, **2004**.
[26] Phule, P. P.; Risbud, S. H. *Adv. Ceram. Mater.,* 3, 183-185, **1988**.
[27] Huffman, M. *Integr. Ferroelectrics,* 10, 39-53, **1995**.
[28] Rozes, L.; Sanchez, C. *Chem. Soc. Rev.,* 40, 1006-1030, **2011**.
[29] Doeuff, S.; Henry, M.; Sanchez, C. *Mat. Res. Bull.,* 25, 1519-1529, **1990**.
[30] Schubert, U. *J. Mater. Chem.,* 15, 3701-3715, **2005**.
[31] Brinker, C. J.; Scherer, G. W. Sol-gel science: The Physics and Chemistry of Sol-Gel Processing, Academic Press, London, **1990**.
[32] Wright, J .D.; Sommerdijk, N. A. J. M. Sol-gel Materials Chemistry and Applications, Advanced Chemistry Texts, CRC Press, Boca Raton, **2001**.
[33] Schubert, U.; Hüsing, N.; Lorenz, A. *Chem. Mater., 7*, 2010-2027, **1995**.
[34] Frey, M. H.; Payne, D. A. *Chem. Mater.*, *7*, 123-129, **1995**.
[35] Hoffmann, S.; Waser, R. *J. Eur. Ceram. Soc.*, 19, 1339-1343, **1999**.

2

Effects of Reaction Medium on the Phase Synthesis and Particle Size Evolution of Barium Titanate*

Abstract

The low-temperature alkoxide–hydroxide precipitation synthesis of nano-sized crystalline barium titanate ($BaTiO_3$) in non-aqueous media is presented. In this report, I show the influence of the reaction medium on the nature of the product by investigating the reaction of titanium (IV) *iso*-propoxide with barium hydroxide hydrates in 2-methoxyethanol and benzyl alcohol, respectively. A perovskite phase precipitated only in benzyl alcohol, but not in 2-methoxyethanol. One molar equivalent of water, present in barium hydroxide monohydrate, was sufficient to hydrolyze the alkoxide and form nanocrystalline $BaTiO_3$. Depending on the water concentration, the process led directly to crystalline powder of particle sizes ranging from 3 to 10 nm, and with a clear correlation between particle size and amount of water.

2.1. Introduction

Barium titanate ($BaTiO_3$) is a high-*k* dielectric material used in commercial multi-layer ceramic capacitors. The minimum $BaTiO_3$ layer thickness that can be achieved with state of the art tape casting methods is about 1 μm, which implies the use of starting powders with a particle size of *ca.* 200 nm [1]. Further reduction of the barium titanate layer thickness requires finer powders obtained by new synthesis techniques.

The barium titanate synthesis methods developed in the last decades can be divided into (1) solid precursor based methods, *e.g.* mixed oxide method and citrate route, and (2) wet-chemical methods, *e.g.* sol-gel, alkoxide-hydroxide sol precipitation, and hydrothermal route. In both groups substantial progress has been made, as can be seen by comparing the review of Pithan *et al.* from 2005 [2] with that of Phule *et al.* from 1990 [3].

* Published in:
Stawski, T. M.; Veldhuis, S. A.; Göbel, O. F.; ten Elshof, J. E.; Blank, D. H. A. *J. Am. Ceram. Soc.*, 93, 3443-3449, **2010**.

The wet-chemical methods provide nanometer-sized powders (5 – 100 nm) of high purity and homogeneity and of adjustable composition, as mixing of components on the molecular level is possible. Among these methods the sol-gel process, in particular the alkoxide-acetate synthesis, the double alkoxide synthesis, the micro-emulsion synthesis, and the precipitation methods (alkoxide-hydroxide sol precipitation) have received much attention [2]. The relatively high processing temperature that is required for the perovskite phase to crystallize [4] is a disadvantage of the sol-gel process for powder synthesis. The morphology of the powder has therefore been difficult to predict, due to uncontrollable grain growth and sintering effects at higher temperatures. Alternatively, the alkoxide-hydroxide sol precipitation route is known to yield crystalline $BaTiO_3$ below 100 °C [5-8]. Essentially, titanium(IV) alkoxide is added drop-wise to an aqueous basic solution of barium hydroxide with pH > 11, adjusted by KOH. It has been suggested that titanium(IV) alkoxides hydrolyze to form $[Ti(OH)_6]^{2-}$, releasing four alcohol molecules [9]. The hydroxotitanate ion is then neutralized by Ba^{2+} cations at high pH, and barium titanate forms. In this scheme, four molecules of water are initially consumed during hydrolysis, and three are released upon precipitation of the oxide.

An alternative absorption mechanism postulated on the basis of electron microscopy studies suggests that precipitation of the complex oxide is a two-step process [8,10]. In the first stage titanium(IV) alkoxide is hydrolyzed, and an amorphous TiO_2 gel forms upon condensation. Subsequently, Ba^{2+} cations diffuse into the gel and a complex oxide precipitates. In this alternative reaction scheme two molecules of water are consumed during hydrolysis, and one molecule is released upon precipitation of the oxide. Both schemes suggest that at least one mole of water per mole of alkoxide is required for precipitation to occur. Of course, other factors should also be considered, such as mixing of water with the solvent, water diffusion in the system, and polarity match between solvent phase and growing solid phase. It was noted that when aqueous media were used, the as-synthesized powders were agglomerated and irregular. This was at least to some extent caused by the uncontrollable hydrolysis of the alkoxide in the presence of an overwhelming amount of water compared to metal alkoxide.

Precipitation in non-aqueous media was also studied. Yoon *et al.* [11,12] showed that a mixture of Ti(IV) *iso*-propoxide and barium hydroxide octahydrate in *iso*-propanol precipitated directly into nano-crystalline barium titanate above 80 °C. The crystal water of the hydroxide appeared to be sufficient for hydrolysis. They observed an increase in particles size from 7.5 nm to several μm, as well as agglomeration of as-formed barium titanate when the water concentration was increased. These studies indicated that water concentration was an import factor that controled phase, particle size, morphology, and degree of agglomeration of the as-formed particles, and could also be related to the hydrolysis of the alkoxide.

Titanium(IV) *iso*-propoxide is fairly unstable in air and prone to hydrolysis even in the presence of moisture in air. A common practice in the sol-gel chemistry is to stabilize the compound by dissolving it in various solvents [13-17]. In the simplest case this can be the parent alcohol. The relative reactivity is impeded by the decrease of alkoxide concentration. By dissolving titanium(IV) *iso*-propoxide in another alcohol, the original alkoxide ligands can be partially or completely exchanged for other alcohol groups. For instance, titanium(IV) *iso*-propoxide reacts with 2-methoxyethanol forming a new Ti(IV) methoxyethoxide (either fully or partially substituted) [9,17], a compound of higher stability in the presence of water [14].

These factors have not been investigated in combination, despite the fact that reaction medium, nature of the metal alkoxide, water concentration and water release seem to be crucial to understand the hydrolysis of the alkoxide and the subsequent precipitation of a perovskite phase. Especially the situation in which the hydrolysis rate is reduced significantly is interesting, as it might enable the synthesis of sub-10 nm nano-crystalline $BaTiO_3$ of adjustable phase, particle size and morphology. In this chapter I show the influence of the reaction medium on the nature of the product by investigating the reaction of titanium (IV) *iso*-propoxide with barium hydroxide hydrates in 2-methoxyethanol and benzyl alcohol, respectively.

2.2. Experimental

2.2.1. Materials

Titanium(IV) *iso*-propoxide ($Ti[OCH(CH_3)_2]_4$, > 99.999%), 2-methoxyethanol (99.3%), *iso*-propanol (C_3H_7OH, > 99.9%) barium hydroxide octahydrate ($Ba(OH)_2{\cdot}8H_2O$, > 98%) and barium hydroxide monohydrate ($Ba(OH)_2{\cdot}H_2O$, > 98%) were acquired from Sigma-Aldrich. Benzyl alcohol (> 99%) was bought from Acros. The reactants were used as received from the suppliers without further purification and were stored in a water-free environment (< 0.1 ppm H_2O). All solvents 2-methoxyethanol, benzyl alcohol and *iso*-propanol were provided as water-free, and additionally dried by means of molecular sieves (molsieve 3Å, Sigma-Aldich).

2.2.2. Route A: titanium(IV) iso-propoxide and barium hydroxide octahydrate in 2-methoxyethanol

A solution of 0.2 mol/dm^3 titanium(IV) *iso*-propoxide in 2-methoxyethanol was prepared. Barium hydroxide octahydrate was added to this solution, so that the resulting molar ratio of Ba to Ti was 1.00. The mixture was stirred vigorously for 15 minutes to form a homogenous precursor and then refluxed for 2 h at 100 °C under continuous stirring. After cooling down to room temperature the precursor was

dried on a watch glass at 60 °C for 72 hours. The dried powder was then heat-treated at 200 °C, 400 °C, 550 °C, 650 °C, 850 °C, and 1000 °C for 4 h in air, using heating and cooling rates of 4 °C/min.

2.2.3. Route B: titanium(IV) iso-propoxide and barium hydroxide octahydrate in benzyl alcohol

A solution of 0.2 mol/dm^3 titanium(IV) *iso*-propoxide in benzyl alcohol was prepared. Barium hydroxide octahydrate was added to this solution, so that the resulting molar ratio of Ba to Ti was 1.00. The mixture was stirred vigorously for 15 minutes to forma homogenous precursor and then refluxed for 2 h at 100 °C, 135 °C, 150 °C, and 175 °C under continuous stirring. The solution was dried on a watch glass at 60 °C for 72 h, forming a powder. All powders were heat-treatedat 850 °C for 4 h in air (heating and cooling rates 4 °C/min).

2.2.4. Route C: titanium(IV) iso-propoxide and barium hydroxide octahydrate in benzyl alcohol with a crystal water removed

A solution of 0.2 mol/dm^3 barium hydroxide octahydrate in benzyl alcohol was prepared. In order to remove the crystal water from barium hydroxide, the solution was refluxed at 150 °C for 8 h and cooled down to room temperature (heating and cooling rates 4 °C/min). Then a 0.2 mol/dm^3 solution of titanium(IV) *iso*-propoxide in water-free benzyl alcohol was added, resulting in a molar ratio of Ba to Ti of 1.00. The mixture was refluxed for 2 h at 150 °C under continuous stirring. It was transferred to the watch glass and dried at 60 °C for 72 h.

2.2.5. Route D: titanium(IV) iso-propoxide and barium hydroxide monohydrate in benzyl alcohol

A solution of 0.2 mol/dm^3 titanium(IV) *iso*-propoxide in water-free benzyl alcohol was prepared. Barium hydroxide monohydrate was added to this solution, so that the resulting molar ratio of Ba to Ti was 1.00. The mixture was stirred vigorously for 15 minutes to homogenize the precursor, then refluxed for 2 h or 24 h at 150 °C under continuous stirring. The solution was transferred to an hour glass and dried at 60 °C for 72 hours, forming a whitish powder. Distilled water was added to some of these mixtures by injection under vigorous stirring, yielding a solution with a molar ratio of water to Ti of 1, 2, 3, or 7. Addition of 7 moles of water per mole of $Ba(OH)_2{\cdot}H_2O$ corresponds to the water amount in barium hydroxide octahydrate (route B). After reflux, the solutions were transferred to a watch glass and dried at 60 °C for 72 h to form a powder.

2.2.6. Characterization

The exact amount of crystal water present in $Ba(OH)_2 \cdot 8H_2O$ and $Ba(OH)_2 \cdot H_2O$ and the melting/decomposition temperatures of the compounds were determined by thermal gravimetric analysis and differential scanning callorimetry (TGA/DSC). The anlaysis was performed from 25 °C to 250 °C at a heating rate of 20 °C/min in (Netzsch STA 449 F3 Jupiter TGA/DSC system).

The reaction of titanium(IV) *iso*-propoxide with benzyl alcohol was investigated with ^1H nuclear magnetic resonance (NMR, Varian 300 MHz spectrometer, the data were analyzed by means of MestReNova 6 software suite). For the sake of comparison *iso*-propanol and benzyl alcohol spectra were measured individually, giving characteristic peaks of the compounds. These results were juxtaposed with the spectrum of as-synthesized titanium(IV) alkoxide and pure titanium(IV) *iso*-propoxide.

X-ray powder diffraction patterns of all samples obtained during the experiments were measured on a diffractometer with a Cu anode and a Ni filter for $Cu_{K\beta 1}$radiation, $I_{K\alpha 2} : I_{K\alpha 1} = 2 : 1$ (Philips PW1830). Selected samples were investigated by High-Resolution Scanning Electron Microscopy (HR-SEM, 0.5 keV – 2.0 keV, Zeiss 1550) and Transmission Electron Microscopy (TEM, 400 keV, FEI Instruments).

2.3. Results and Discussion

2.3.1. Route A: titanium(IV) iso-propoxide and barium hydroxide octahydrate in 2-methoxyethanol

The dried solution after refluxing was a yellowish xero-gel, as illustrated by the HR-SEM picture in Figure 2.1. The morphology was typical for amorphous sol-gel derived barium titanate precursor powders [18,19]. XRD analysis showed that the powder was amorphous after drying at 60 °C, as shown by the corresponding pattern in Figure 2.2. Heat treatment of the material between 200 °C and 550 °C did not yield crystalline barium titanate. Upon heating to 200 °C no crystalline material was present in the X-ray diffraction pattern, while some intermediate phases were present in samples heated to higher temperatures. The XRD pattern of the powder treated at 400 °C showed a predominant barium carbonate phase. In the powder calcined at 550 °C the oxycarbonate phase $Ba_2Ti_2O_5CO_3$ (BTC) [4] and barium carbonate was found. Heat treatment at 650 °C and higher resulted in the formation of crystalline $BaTiO_3$. Traces of impurity phases with peak positions at $2\theta = 23.9°$ and $2\theta = 34.0°$ were attributed to barium carbonate. The crystallite sizes of the barium titanate phase were estimated by the Scherrer equation based on the full width at half

maximum of the (111) peak. For powders prepared at 650 °C, 850 °C, and 1000 °C, average grains sizes were approximately 15 nm, 33 nm, and 49 nm, respectively.

In route A, titanium(IV) *iso*-propoxide reacted with 2-methoxyethanol exchanging part (or all) of its *iso*-propoxy groups by 2-methoxyethanol ligands [9,17]. The reaction between barium hydroxide and titanium(IV) alkoxide in 2-methoxyethanol led to an amorphous Ba-Ti precursor material and itscrystallization and decomposition into nano-crystalline $BaTiO_3$ via some intermediate phases. The oxycarbonate phase formed above 270 °C and existed up to 600 °C and is likely to occur in non-hydrolyzed barium titanate precursors [2-4,20]. The presence of barium carbonate at elevated temperatures was a result of the pyrolysis of the organic residues around 400 °C [21]. However, the amount of as-formed $BaCO_3$ was much lower in the alkoxide-hydroxide process than in other semi-alkoxide routes involving acetates [21]. BTC decomposed further into nano-crystalline barium titanate and carbon dioxide, whereas $BaCO_3$ remained present in the system up to much higher temperatures. Its thermal stability impeded the formation of the perovskite-type phase because it decomposed into BaO and CO_2 only above 850 °C.

The absence of precipitation and $BaTiO_3$ formation at temperatures < 100 °C may result from insufficient hydrolysis of titanium(IV) *iso*-propoxide stabilized by 2-methoxyethanol, when no additional water was added to the system. The crystal water present in barium hydroxide octahydrate should in principle be sufficient for complete hydrolysis of titanium(IV) *iso*-propoxide into $[Ti(OH)_6]^{2-}$. When carried out in *iso*-propanol the same reaction led directly to nano-crystalline $BaTiO_3$ as reported by Yoon *et al.* [11,12] However, 2-methoxyethanol decreased the reactivity of titanium(IV) *iso*-propoxide by substituting its parent alkoxy ligands and forming a coordination sphere around the titanium ion [14,22]. Consequently, hydrolysis and condensation proceeded too slowly for condensation of $BaTiO_3$ at low temperatures to occur.

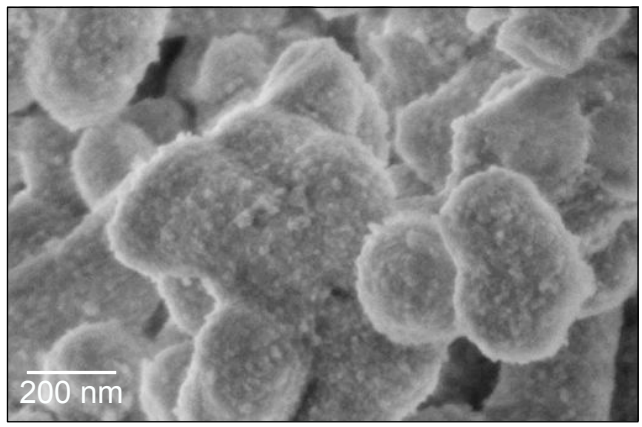

Figure 2.1. High-resolution SEM image of xero-gel dried at 60 °C. The material was formed in the reaction of $Ti[OCH(CH_3)_2]_4$ and $Ba(OH)_2{\cdot}8H_2O$ in 2-methoxyethanol at 100 °C.

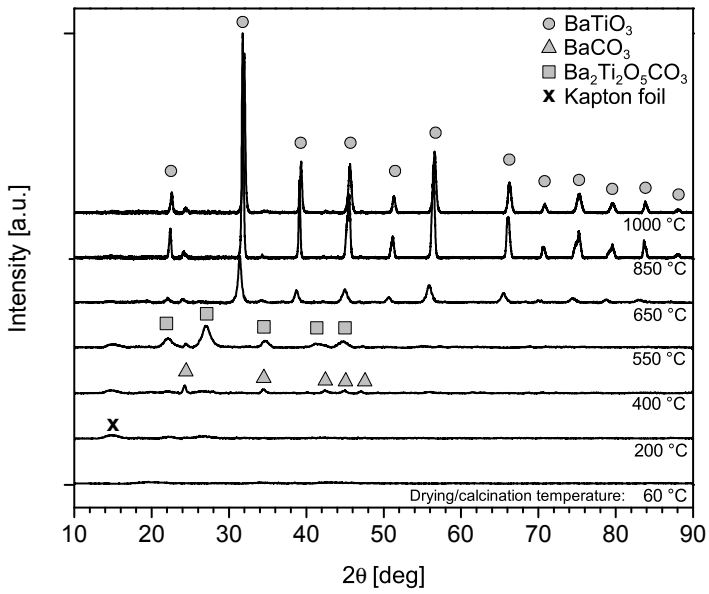

Figure 2.2. X-ray diffraction patterns of the powder formed in the reaction of $Ti[OCH(CH_3)_2]_4$ and $Ba(OH)_2{\cdot}8H_2$ in 2-methoxyethanol at 100 °C, after drying at 60 °C and subsequent heat treatment.

2.3.2. Routes B – D: titanium(IV) iso-propoxide and barium hydroxide octahydrate and monohydrate in benzyl alcohol. NMR characterization of titanium(IV) iso-propoxide in benzyl alcohol and thermal analysis of barium hydroxide octahydrate and monohydrate.

Route B yielded crystalline barium titanate. The size of the crystallites and the degree of crystallinity did not depend significantly on the reaction temperature, as can be concluded from the XRD patterns in Figure 2.3. The patterns contained some additional low-intensity peaks at 2θ = 23.9°, which were attributed to barium carbonate, and at 2θ = 15.0°, which originated from the Kapton foil used to support the powder. Peak broadening analysis of the (111) peak indicated that the crystallite size of the as-synthesized powder was *ca.* 9 nm.

The particle size estimated from transmission electron microscopy images (TEM) in Figure 2.4. was in good agreement with this value. The particle size distribution histogram derived from the TEM micrograph is shown in the inset of Figure 2.4A, and indicates an average particle size of 8 ± 2 nm. This powder was synthesized at 150 °C and the histogram was based on 200 particles. The high degree of crystallinity of particles as small as 5 nm can be clearly seen in the TEM micrograph in Figure 2.4B. Calcination at 850 °C for 4 h in air led to an apparent increase of the crystallite size and decomposition of the residual phase. The XRD patterns of the as-

synthesized and thermally treated powders are compared in Figure 2.5. The average crystallite size after heat-treatment was 50 nm, based on peak broadening analysis. Figure 2.6. shows a TEM micrograph of the calcined powder, indicating highly crystalline particles as small as 20 nm.

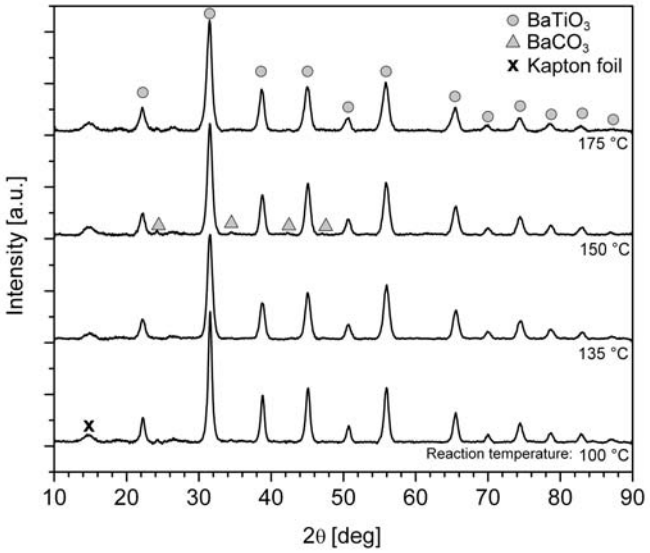

Figure 2.3. X-ray diffraction patterns of barium titanate powder formed in route B at 100 °C - 175 °C.

The ^{1}H NMR spectra of *izo*-propanol and benzyl alcohol are shown in Figures 2.7A and B, including the attributed chemical shifts. In the case of *izo*-propanol a characteristic septet is visible in the proximity of δ_H = 3.9 ppm. The NMR spectrum of pure titanium(IV) *izo*-propoxide in Figure 2.7C clearly exhibits the same septet, although it is shifted to δ_H = 4.5 ppm. However, the NMR spectrum of titanium(IV) *izo*-propoxide in benzyl alcohol contains the aforementioned septet back at δ_H = 3.9 ppm (Figure 2.7D). This suggests that *izo*-propanol was released from Ti(IV) *izo*-propoxide, most likely by being exchanged by phenylmethoxy ligands. Quantitative analysis of the spectrum indicated that at least 3.5 moles of *izo*-propanol per 1 mole of alkoxide were present, suggesting almost complete exchange of the original propoxy ligands by phenylmethoxy ligands.

TGA/DSC data of $Ba(OH)_2{\cdot}8H_2O$ and $Ba(OH)_2{\cdot}H_2O$ are presented in Figure 2.8. Thermal analysis of barium hydroxide octahydrate showed that it melted and decomposed below 100 °C releasing 6.823 moles of crystal water per mole of Ba (38.93% mass loss) and forming barium hydroxide monohydrate. Further increase in temperature resulted in a release of 1.004 mole of water between 120 °C and 150 °C (5.73% mass loss). The total water content in $Ba(OH)_2{\cdot}8H_2O$ was 7.827 moles of water per mole of Ba. The weight loss was in good agreement with the thermal

analysis data of barium hydroxide monohydrate, where 9.73% mass loss was found, corresponding to 1.024 moles of water per mole of Ba. Therefore, a suspension/solution of barium hydroxide octahydrate in benzyl alcohol refluxed at 150 °C for 8 h can be assumed to be water-free. The solution of barium hydroxide in benzyl alcohol showed a tendency to form agglomerates, which was prevented by vigorous stirring and sonication after dissolution. After synthesis following water-free route C, the resulting powder was completely amorphous.

Material synthesized via route D at 150 °C from barium hydroxide monohydrate was crystalline barium titanate, as shown in Figure 2.9. The signal-to-background ratio was lower than in route B, indicative of a lower degree of crystallinity. The width of the (111) peak indicated a crystallite size of *ca.* 3 nm, compared to 9 nm for barium titanate synthesized from barium hydroxide octahydrate. To verify that this was related to the water concentration, the reaction time and concentration of water were varied.

The X-ray diffraction pattern of a sample synthesized by refluxing barium hydroxide monohydrate for 24 h was in good agreement with the patterns shown in Figure 2.9, which were obtained by 2 h refluxing. The crystallite size calculated from the Scherrer equation was again ca. 3 nm for the 24 h refluxed sample. However, a change in the concentration of water in the system affected the properties of as-synthesized powders significantly. Crystalline barium titanate was formed in all cases. The crystallite size increased with water concentration. For solutions with 1, 2, 3, and 7 moles of water added per mole of Ti alkoxide, the average crystallite sizes were 6.0 nm, 8.2 nm, 9.0 nm, and 9.4 nm, respectively. A trace amount of residual $BaCO_3$ was observed in all diffraction patterns.

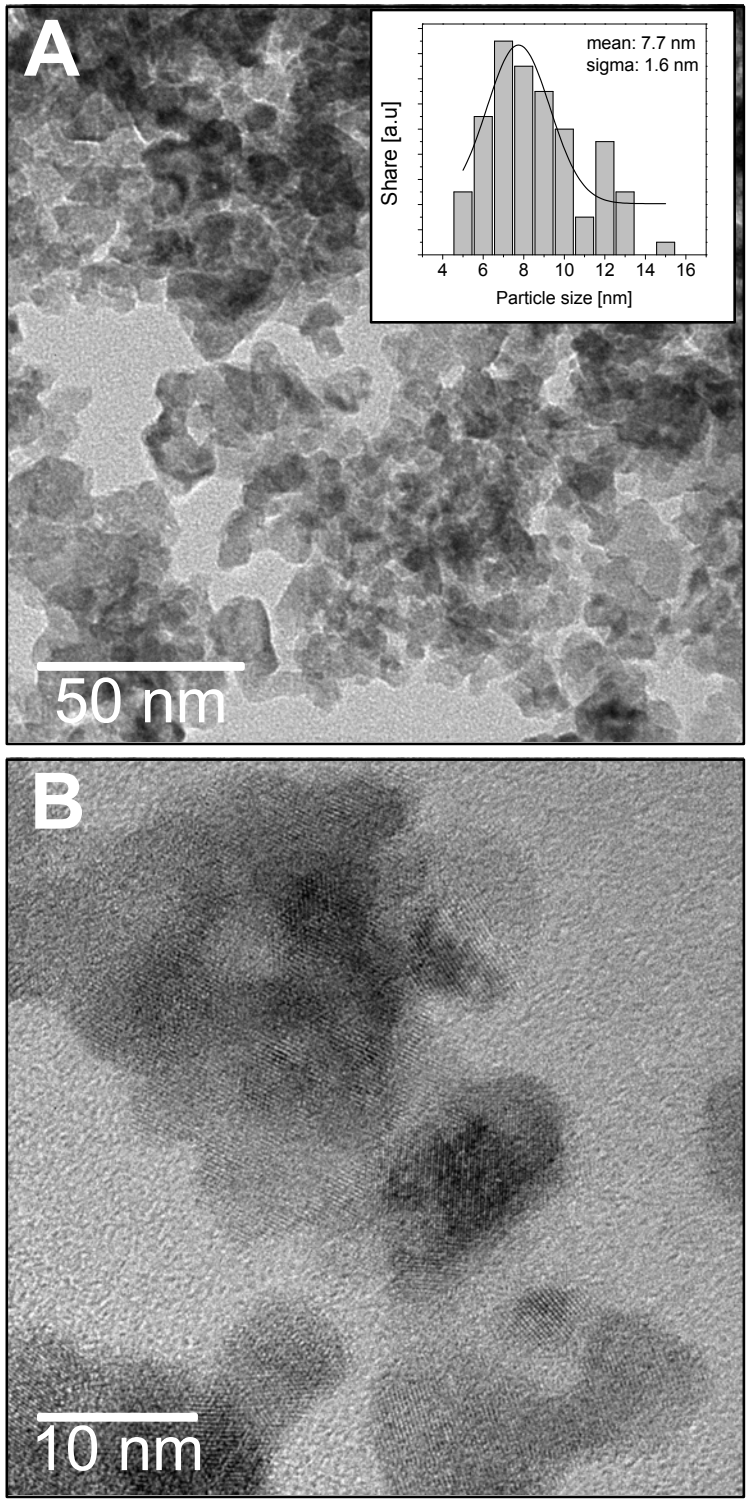

Figure 2.4. TEM image and particle size distribution of barium titanate powder formed in route B at 150 °C. a) Bright field, sample area: 175 nm x 175 nm. b) Bright field, sample area: 44 nm x 44 nm.

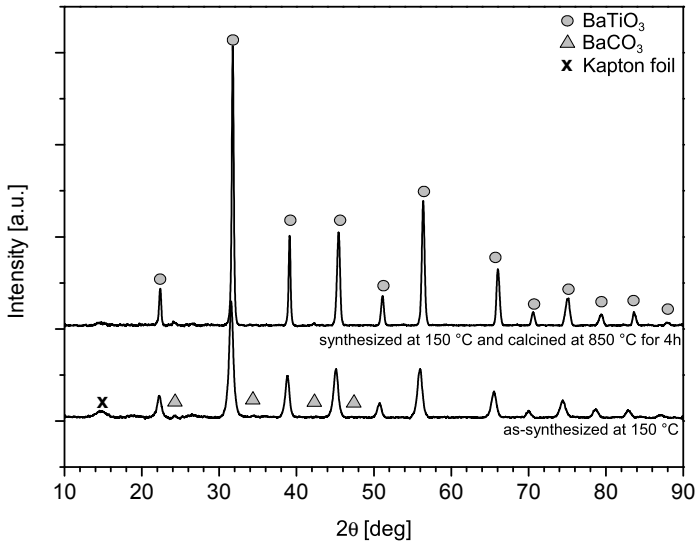

Figure 2.5. Comparison of X-ray diffraction patterns of barium titanate powder formed in route B at 150 °C, before and after calcination at 850 °C for 4 h in air.

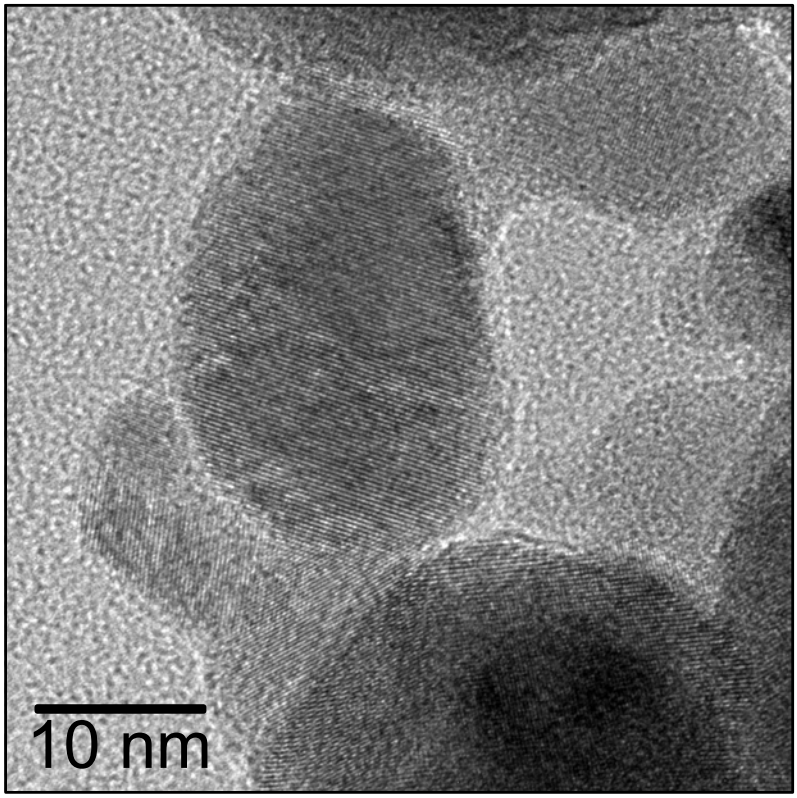

Figure 2.6. TEM image of barium titanate powder formed in route B at 150 °C, and calcined at 850 °C for 4 h in air. Bright field, sample area: 44 nm x 44 nm.

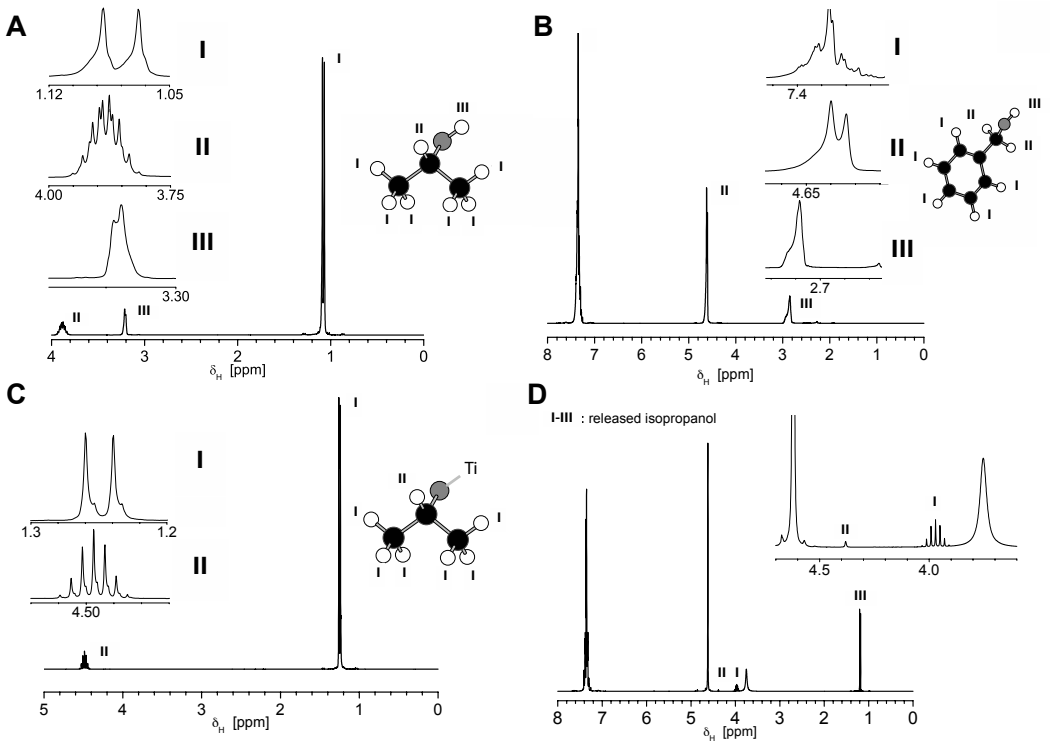

Figure 2.7. ^{1}H NMR spectra of a) *ώω*-propanol; b) benzyl alcohol; c) titanium(IV) *ώω*-propoxide; and d) titanium(IV) *ώω*-propoxide in benzyl alcohol.

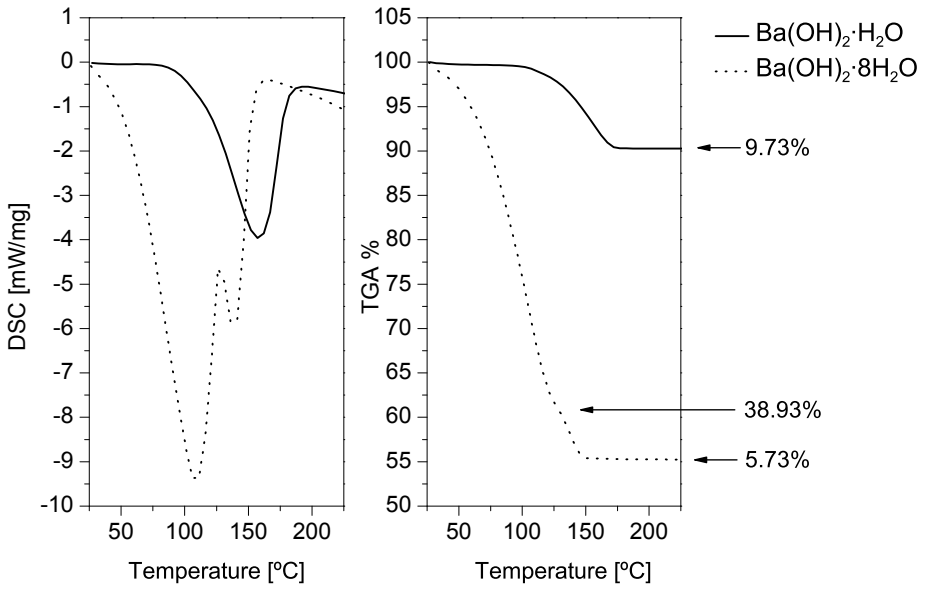

Figure 2.8. TGA/DSC thermal analysis of barium hydroxide octahydrate and barium hydroxide monohydrate.

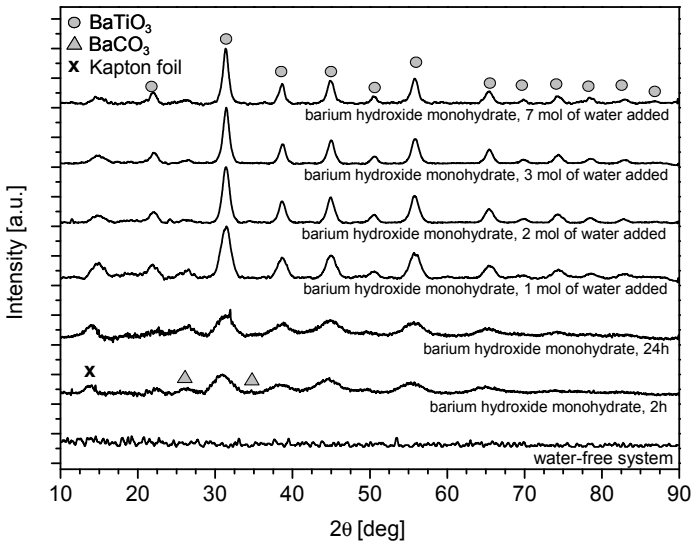

Figure 2.9. X-ray diffraction patterns of barium titanate powder formed in route D. Unless stated differently, the reaction time is 2 h.

The synthesis from titanium(IV) alkoxide and barium hydroxide in benzyl alcohol was different from that in 2-methoxyethanol, since it led directly to nano-crystalline barium titanate. Similar to the reported synthesis in *iso*-propanol, water present in barium hydroxide octahydrate (and monohydrate) was sufficient to hydrolyze the alkoxide and eventually lead to the perovskite phase [11,12].

The ^{1}H NMR measurements showed that at least 88 mol% of the *iso*-propoxy ligands were directly exchanged by benzyl alcohol ligands during preparation of the precursor solution. The *in situ* formed titanium precursor was less stable than its 2-methoxyethanol counterpart. This can be explained as follows:

(1) 2-methoxyethanol is a bidentate ligand and in general multidentate ligands are known to be more strongly bonded than the monodentate ligands. This is due to the chelate effect and the resulting higher stability constant [22].

(2) The decreased stability of the formed alkoxide can also result from less efficient packing of the phenyl-methoxy groups around the central metal ion and/or the presence of an aromatic ring, reducing the electron density between ligand and Ti atom, and hence decreasing the strength of the bond.

The crystal water from barium hydroxide octahydrate was therefore more than sufficient to hydrolyze the titanium complex, and a nano-crystalline perovskite phase was directly formed. The crystal water from barium hydroxide octahydrate that was released between 100 °C and 150 °C was consumed by the hydrolysis of the metal alkoxide. This may explain why there were no variations observed between the

products formed between 100 °C and 175 °C. When all or most of the crystal water was removed from barium hydroxide octahydrate during an 8 hour reflux process, no barium titanate was formed. The resulting amorphous xero-gel had a structure similar to that of the 2-methoxyethanol derived material. It proved that the presence of a sufficient concentration of water and a sufficiently reactive precursor were essential for the hydrolysis of titanium(IV) alkoxide in order to be able to form nano-crystalline powder. Longer reaction times did not lead to changes in the particle sizes and crystallinity of the powders. This suggested that water was consumed relatively quickly during the reaction, within the first 2 hours. The concentration of water added to the system determined the final size of particles.

2.4. Conclusions

Sufficient hydrolysis of titanium(IV) alkoxide was essential for precipitation and barium titanate formation to occur. When the metal alkoxide was dissolved and stabilized in 2-methoxyethanol, a barium titanate phase did not form without further thermal processing, despite the fact that theoretically enough water was present in the system. This was attributed to the overall high stability of titanium(IV) methylethoxide (either fully or partially substituted) in comparison with titanium(IV) *iso*-propoxide or titanium(IV) phenylmethoxide. The titanium alkoxide precursor was stabilized less in benzyl alcohol than in 2-methoxyethanol, but when an insufficient amount of water was present, no $BaTiO_3$ phase was formed in either case. Precipitation of barium titanate only occurred when the water concentration was high enough, and the degree of stabilization of the alkoxide by the solvating medium was sufficient, but not so strong that it impeded the formation of the oxide phase. In order to synthesize sub-10 nm nano-crystalline barium titanate powders with a narrow size distribution a low-temperature reaction in an appropriate solvent were essential. Only then thermal post-processing could be avoided.

2.5. References

[1] Yoon, G. *J. Ceram. Proc. Res.*, *7*, 343-354, **2006**.

[2] Pithan, C.; Hennings, D. H.; Waser, R. *Int. J. Appl. Ceram. Technol.,* 2, 1-14, **2005**.

[3] Phule, P. P.; Risbud, S. H. *J. Mater. Sci.*, 25, 1169-1183, **1990**.

[4] Frey, M. H.; Payne, D. A. *Chem. Mater.,* 7, 123-129, **1995**.

[5] Flaschen, S. S. *J. Am. Chem. Soc.*, *77*, 6194, **1955**.

[6] Chaput, F.; Boilot, J. P. *J. Mat. Sci. Lett.,* 6, 1110-1112, **1987**.

[7] Chaput, F.; Boilot, J. P.; Beauger, A. *J. Am Ceram. Soc., 73*, **1990**.

[8] Golubko, N. V.; Yanovskaya, M. I.; Romm, I. P. *J. Sol-Gel Sci.Technol.,* 20, 135-143, **2001**.

[9] Kiss, K.; Meander, J.; Vukasovich, M. S.; Lockhart, R. J. *J. Am. Ceram. Soc.,* 49, 291-295, **1966**.

[10] Diaz-Guemes, M. I.; González Carreño, T.;Serna, C. J.; Palacios, J. M. *J. Mater. Sci.,* 24, 1011-1014, **1989**.

[11] Yoon, S.; Baik, S.; Kim, M. G.; Shin, N. *J. Am Ceram. Soc.,* 89, 1816-1821, **2006**.

[12] Yoon, S.; Baik, S.; Kim, M. G.; Shin, N.; Kim, I. *J. Am Ceram. Soc.,* 90, 311-314, **2007**.

[13] Campion, J. F.; Payne, D. A.; Chae, H. K.; Maurin, J. K.; Wilson, S. R. *Inorg. Chem.,* 30, 3244-3245, **1991**.

[14] Sedlar, M.; Sayer, M. *J. Sol-Gel Sci.Technol.,* 5, 27-40, **1995**.

[15] Mosset, A.; Gautier-Luneau, I.; Galy, J.; Strehlow, P.; Schmidt, H. *J. Non-Cryst. Solids,* 100, 339-344, **1988**.

[16] Phule, P. P.; Risbud, S. H. *Adv. Ceram. Mat.,* 3, 183-185, **1988**.

[17] Toyoda, M,; Hamaji, Y.; Tomono, K.; Payne, D. A. *Jpn. J. Appl. Phys.,* 32, 4158-4162, **1993**.

[18] Moon, J.; Suvacib, E.; Li, T.; Costantinoc, S. A.; Adair, J. H. *J. Eur. Ceram. Soc.,* 22, 809-815, **2002**.

[19] MacLaren, I. ; Ponton, C. B. *J. Eur. Ceram. Soc.,* 20, 1267-1275, **2000**.

[20] Chandler, C. D.; Roger, C.; Hampden-Smith, M. J. *Chem. Rev.,* 93, 1205-1241, **1993**.

[21] Veith, M.; Mathur, S.; Lecerf, N.; Huch, V.; Decker, T.; Beck, H. P.; Eiser, W.; Haberkorn, R. *J. Sol-Gel Sci.Technol.,* 17, 145-158, **2000**.

[22] Schubert, U. *J. Mater. Chem.,* 15, 3701-3715, **2005**.

3

Phase Evolution of Barium Titanate Nano-powders from Alkoxide-Hydroxide Precipitation Process under Restricted Hydrolysis Conditions in Benzyl Alcohol*

Abstract

The evolution of morphology, phase, and defect structure of nano-sized $BaTiO_3$ powders synthesized by an alkoxide-hydroxide process in benzyl alcohol under reflux conditions were investigated. Powders were heat-processed at temperatures ranging from 250 to 850 °C. X-ray powder diffraction (XRD) revealed that $BaTiO_3$ remained in a room temperature cubic phase with a crystallite size below 30 nm when heat-processed up to 700 °C. Limited particle growth and sintering effects were observed with transmission electron microscopy (TEM), but internal pores of 1 – 2 nm diameter inside the crystallites were well visible. Their presence is attributed to curing of lattice hydroxyl defects, as was confirmed by infrared spectroscopy (FT-IR) and thermogravimetric analysis and differential scanning calorimetry (TGA/DSC). Raman spectroscopy (FT-RS) revealed the development of local tetragonal/orthorhombic distortions in nanocrystalline grains after heat treatment at 350 °C or higher, but the volumetric cubic-to-tetragonal transition was observed only after heat treatment at 850 °C. Its occurrence was accompanied by substantial grain growth to ~100 nm size, and that transformation enabled the complete removal of hydroxyl defects and reordering/crystallization due to volume diffusion.

3.1. Introduction

Barium titanate ($BaTiO_3$) is a high-*k* dielectric material used in commercial multi-layer ceramic capacitors. The minimum $BaTiO_3$ layer thickness that can be achieved with state of the art tape casting methods is about 1 µm, which implies the use of starting powders with a particle size of *ca.* 200 nm [1]. Further reduction of the barium titanate layer thickness requires finer powders obtained by new synthesis techniques.

* In preparation:
Stawski, T. M.; Veldhuis, S. A.; Göbel, O. F.; Podstawka-Proniewicz, E. ; Blank, D. H. A; ten Elshof, J. E.

Barium titanate powders can be synthesized by wet-chemical methods, yielding nanometer-sized particles (5 – 100 nm) of high purity and homogeneity, and adjustable composition, as mixing of components on the near-molecular level is possible [2]. Among these methods the alkoxide-hydroxide sol precipitation route has received much attention [2-6]. It is a viable alternative to alkoxide-carboxylate process where relatively high processing temperatures are required for the perovskite phase to crystallize [7]. The latter is disadvantageous for powder synthesis. Alternatively, the alkoxide-hydroxide sol precipitation route is known to yield crystalline $BaTiO_3$ below 100 °C [3-6].

In the classical approach, titanium(IV) alkoxide is added dropwise to a basic aqueous solution of barium hydroxide with pH >11, adjusted by KOH. Highly agglomerated $BaTiO_3$ with crystal sizes >100 nm precipitates instantaneously. Precipitation in non-aqueous media has also been studied. Yoon *et al.* [8,9] showed that a mixture of Ti(IV) *iso*-propoxide and barium hydroxide octahydrate in *iso*-propanol precipitated directly into nano-crystalline (7.5 nm) barium titanate powder above 80 °C. In a previous chapter I studied an analogous reaction, and demonstrated that the reaction medium had a profound influence on the crystallinity and phase of the resulting product [10]. When benzyl alcohol was used as a reaction medium, sub-10 nm crystalline partially articles of barium titanate were formed in the reaction between titanium phenylmethoxide and barium hydroxide octahydrate or monohydrate at 100 – 175 °C. In contrast, the use of 2-methoxyethanol, yielded no crystalline phases at the reaction temperature of 100 °C. An amorphous xero-gel was obtained instead. $Ba_2Ti_2O_5CO_3$ (oxocarbonate) was formed at 550 °C, which transformed into crystalline barium titanate above 650 °C. The difference was attributed to the high stability of titanium(IV) methylethoxide (fully or partially substituted) in comparison with titanium(IV) phenylmethoxide under similar hydrolysis conditions.

$BaTiO_3$ powders obtained from wet-chemical methods are known to exist predominantly in a non-ferroelectric cubic form instead of a tetragonal phase. This phenomenon has been attributed to the grain size and was thoroughly investigated and theoretically analyzed [1,11]. The ultimate dielectric response of $BaTiO_3$ was obtained at a grain-size of 0.7 – 1 μm [1,11]. As the grain size decreases further, the dielectric properties are no longer enhanced, but degrade severely as a cubic phase develops when the grain size is less than 200 nm. Such systems lack an observable tetragonal-to-cubic transition at T_C = 132 °C (Curie temperature) [12]. This phenomenon has been explained in terms of (1) twinning of polycrystalline materials with decreasing grain size, (2) lack of driving force for the ferroelectric transition and depolarization fields, and (3) the defect structure of $BaTiO_3$ as resulting from the processing method [11]. Especially the last aspect is worth considering when it comes to wet-chemical processing at low temperatures. It is well known that hydroxyl defects exist in the barium titanate lattice structure at the positions of oxygen lattice

sites. These cause charged defects that are probably compensated by vacancies in the cation sub-lattice [11,13,14]. It has been proposed that a high concentration of point defects interferes with the long-range polar ordering, which is a driving force of the cubic-to-tetragonal transition below the Curie temperature [11]. Hydroxyl defects were observed in $BaTiO_3$ prepared by hydrothermal and alkoxide-caboxylate routes [11,15] by infrared spectroscopy (FT-IR), due to the presence of OH^- absorption bands between 3450 cm^{-1} and 3550 cm^{-1} [13-15]. Internal OH^- defects in $BaTiO_3$ were also reported to yield a peak in Raman scattering spectra (FT-RS) at 810 cm^{-1} [14]. Hennings *et al.* showed that in the case of hydrothermally prepared cubic powders with crystallite sizes above 200 nm, the onset of tetragonal phase formation below T_C began after a heat treatment already at 500 °C. Grain growth was negligible at this temperature, but the temperature was sufficiently high to remove the majority of hydroxyl defects from the lattice [15]. Full restoration of tetragonality marked by reaching a unit cell parameter ratio $(c\text{-}a)/a$ = 1% [16] was observed after processing at 600 °C. More recently it was shown that untreated hydrothermal powders of sub-100 nm crystallite size consisted of 18 mass% tetragonal and 82 mass% cubic phase [16]. The $(c\text{-}a)/a$ ratio equalled 0.74%. It was also reported that a chemical solvothermal treatment of hydroxyl defects in hydrothermal $BaTiO_3$ by either N-methyl-2-pyrrolidinone [17] or dimethylformamide [18] led to a cubic-to-tetragonal transition without heat treatment. Interestingly, Begg *et al.*, who also investigated hydrothermal barium titanate, did not correlate water release with the occurrence of a tetragonal distortion at room temperature [19]. Frey and Payne suggested similarly that hydroxyl defect-containing barium titanate obtained by the alkoxide-carboxylate process did not undergo a cubic-to-tetragonal transition at room temperature due to defect curing, but due to grain growth from 35 nm to 100 nm [11]. The conclusion was based on the observation that complete curing of hydroxyl defects took place only after heat treatment above 800 °C, while the cubic phase remained present unless the powder was calcined at 1000 °C or higher. Nonetheless, hydroxyl defect-free nano-crystalline $BaTiO_3$ displayed Raman activity typical for orthorhombic and tetragonal phases when processed below 800 °C [11]. And Raman activity typical for the tetragonal phase was observed in particles as small as 17 nm without hydroxyl defects [20].

It seems that the "grain size" effect in $BaTiO_3$ is influenced by a number of factors like crystallite size, synthesis method, ceramics form (powder or sintered material) and reactivity upon heat processing [1]. It was the purpose of this work to analyze the resulting room-temperature phases of barium titanate, formed from titanium(IV) phenylmethoxide and barium hydroxide octahydrate in benzyl alcohol, in the context of some of these factors. The as-synthesized material has a high purity and crystallinity and very small crystallite size [10]. Heat treatment of the powder at 850 °C led to moderate grain growth; the crystallite size did not exceed 60 nm on average. The development of a tetragonal phase in sub-100 nm $BaTiO_3$ powders

obtained by this uncomplicated synthetic method would be of potential technological relevance.

3.2. Experimental

3.2.1. Materials

Titanium(IV) *iso*-propoxide ($Ti[OCH(CH_3)_2]_4$, > 99.999%), and barium hydroxide octahydrate ($Ba(OH)_2{\cdot}8H_2O$, > 98%) were acquired from Sigma-Aldrich. Benzyl alcohol (> 99%) was bought from Acros. The reactants were used as received from the suppliers without further purification and were stored in a water-free environment (< 0.1 ppm H_2O). Benzyl alcohol was provided as water-free, and additionally dried by means of molecular sieves (molsieve 3Å, Sigma-Aldrich).

3.2.2. Synthesis of $BaTiO_3$

A solution of 0.2 mol/dm^3 titanium(IV) *iso*-propoxide in benzyl alcohol was prepared. Barium hydroxide octahydrate was added to this solution, so that the resulting molar ratio of Ba to Ti was 1.00. The mixture was stirred vigorously for 15 minutes to form a homogenous precursor and then refluxed for 2 h at 175 °C under continuous stirring. The solution was dried on a watch glass at 60 °C for 72 h, forming a powder of nano-crystalline $BaTiO_3$ [10]. The powder was divided into several batches and heat-treated at temperatures between 250 and 700 °C for 24 h and at 850 °C for 8 h in air (heating and cooling rate 4 °C/min).

3.2.3. Characterization

X-ray powder diffraction patterns were measured on a diffractometer with a Cu anode and a Ni filter for Cu K_β radiation, $I_{K\alpha 2} : I_{K\alpha 1} = 2 : 1$ (Philips PW1830). Patterns were collected in a step-mode with a resolution of 0.01° and a counting time of 2.5 s/step. Angle-dependent instrumental broadening effects and diffraction pattern displacement were corrected for by means of a Si standard (the British Drug House) mixed with the powders. The diffraction data were further processed using the X'Pert HighScore Plus 2.1 software package. Peaks were fitted with *pseudo*-Voigt function profiles. The cell parameters were refined from the as-fitted profiles using the McMaille algorithm [21]. Crystallite sizes were obtained by the Scherrer algorithm using full-width at half maximum (FWHM) data of several selected fitted profiles.

Powders heat-treated at various temperatures were dispersed in *iso*-propanol, sonicated for 10 minutes and deposited onto holey carbon copper grids (CF200-Cu, Electron Microscopy Sciences). Then the samples were dried at 60 °C for 1 h on a hot-stage and used for transmission electron microscopy (TEM) characterization (Philips CM300ST-FEG at 300 kV). Samples were investigated at

low magnification to locate typical areas and features of interest were examined at high magnification. Crystallographic information was obtained by local Fourier transforms (FT) of areas of the images with high levels of crystallinity. The microscope software packages GATAN Microscopy Suite 1.8 was used for this purpose.

Raman spectra (FT-RS) were recorded on a THERMO spectrometer (Nicolet 5700 NXR 9650) combined with a liquid nitrogen-cooled germanium detector. Typically between 300 and 4000 scans were collected with a resolution of 4 cm^{-1}. Excitation at 1064 nm from a continuum-wave Nd^{3+}:YAG laser was used. The output power was set to 100 mW. No thermal degradation of the sample was observed during the measurements.

Infrared spectra (FT-IR) were recorded in an attenuated-total-reflection mode (ATR) (Bruker Tensor 27 equipped with DLaTGS detector, and Pike GladiATR). Typically between 128 and 256 scans were collected with a resolution of 4 cm^{-1}.

The defect and impurity chemistry of the compounds was determined by thermal gravimetric analysis and differential scanning calorimetry (TGA/DSC). The analysis was performed from 25 to 900 °C with a heating rate of 5 °C/min in air (Netzsch STA 449 F3 Jupiter TGA/DSC system, air flow 60 ml/min).

3.3. Results

3.3.1. Powder diffraction

X-ray diffraction patterns of as-synthesized powders and powders heat-treated between 250 and 850 °C are presented in Figure 3.1A. In all cases the diffraction patterns were attributed to $BaTiO_3$. Traces of impurity phases were attributed to barium carbonate. The intensity was normalized against the area of the (111) peak of either tetragonal or cubic $BaTiO_3$ [16] at 2θ ~ 39.0°. As can be easily noticed the FWHM of the diffraction peaks decreased with increasing calcination temperature, indicating crystallite growth. Moreover, a temperature-dependent shift of diffraction peaks to higher 2θ was noticeable, indicating shrinkage of the unit cell and/or phase transition (peak 2θ ~ 39.0°, see the inset in Figure 3.1A). A characteristic splitting of certain diffractions peaks occurred in the powder calcined at 850 °C (peak 2θ ~ 45.0°, see the inset in Figure 3.1A), which is indicative of a tetragonal distortion, as the *a* and *c* lattice parameters became different and the (100) and (001) peak no longer coincided.

All diffraction patterns were fitted with *pseudo*-Voigt peak profiles. An exemplary fit to the pattern of the powder heat-treated at 850 °C is given in Figure 3.1B. This provided information on peak positions and FWHMs, corrected for

instrumental broadening effects. The crystallite size as a function of calcination temperature based on Scherrer analysis is shown in Figure 3.1C. The unit-cell parameters were obtained and refined using the McMaille algorithm assuming space group *Pm-3m* for samples up to 700 °C, and *P4mm* for the powder processed at 850 °C (Figure 3.1D). The as-synthesized powder and a powder that was heat-treated at 250 °C for 24 h had an average crystallite size of 10 ± 2 nm. Minor growth of particles up to *ca.* 12 nm was observed at temperatures below 450 °C. At temperatures between 450 and 700 °C, the size increased to ~25 nm. Heat-treatment at 850 °C led to a substantial grain growth up to 50 ± 15 nm, in spite of the fact that the calcination time was shortened from 24 to 8 h. Prolonged treatment at various temperatures influenced the lattice constant and phase of the investigated powders as well. No clear indications for the presence of a tetragonal phase was found by XRD at any temperature < 850 °C. Nevertheless, the unit-cell volume V (the inset in Figure 3.1D) decreased with increasing temperature, as was reflected in shorter lattice constants a (Figure 3.1D). For the as-synthesized powder these parameters equalled a = 4.0345(2) Å and V = 65.6715(4) Å^3. Heat treatment at 700 °C yielded a = 4.0066(7) Å and V = 64.3205(6) Å^3. After processing at 850 °C, a tetragonal phase was observed, with V = 64.1919(8) Å^3 and $(c-a)/a$ = 0.78%.

3.3.2. TEM imaging

The microstructure of as-synthesized and heat-treated powders was investigated by high-resolution TEM. Figures 3.2A&B present the typical morphology of as-synthesized powder and of material calcined at 250 °C for 24 h. Highly crystalline nanoparticles with sizes below 10 nm were predominant in both cases. The inset in Figure 3.2B illustrates the typical agglomerate structure at lower magnification. The shape of the crystals was generally roundish, but locally the overall morphology was not well defined ("cloud-like"), and resembled the morphology of a crystallized gel. As marked in the figure by broken circles, spherical defects with lower electron density were recognizable within the grains. A detailed analysis of the powders revealed that the concentration of such defects in powders treated at higher temperature was considerably higher than the number of defects in the as-synthesized material. By taking the morphology of the defects into account, their presence can be explained in terms of internal nano-porosity that developed upon prolonged heating. Thermal processing at 350, 400 and 450 °C yielded barium titanate with comparable microstructures. Figure 3.2C shows the morphology of the powder at 350 °C. The internal defects are marked by broken circles. The presence of spherical internal defects became even more pronounced at 400 °C (Figure 3.2D), while the grains grew to sub-15 nm size, as illustrated by the lower magnification image (the inset in Figure 3.2C). The shape of crystals was similar to the ones shown in Figures 3.2A&B. No sintering effects were visible at this temperature. Processing at 500 °C changed the microstructure of $BaTiO_3$ powders significantly, as shown in Figure 3.3A.

Sub-30 nm particles of spherical shape evolved (Inset I in Figure 3.3A). Sintering effects between large grains could be observed as a neck formation between grains. This is indicative of the onset of large-scale surface diffusion and/or coalescence of gel-like structures or nanocrystals into lower energy morphologies. Intragranular porosity was still present, and neither the shape nor the size of the pores changed considerably. Inset II in Figure 3.3A shows a typical grain with internal pores. Further temperature increase to 600 °C did not affect the morphology of the particles (Figure 3.3B), and internal porosity was still present. Similarly, the crystallite sizes did not change considerably (the inset in Figure 3.3B). Powders processed at 650 and 700 °C had a similar grain size and morphology as the ones processed at 600 °C, but their crystallite size was slightly larger, see insets I and II in Figure 3.3C. However, at these two temperatures no evidence was found for the existence of internal pores. Thus, they were either fully removed or their concentration was significantly decreased. Finally, heat-treatment at 850 °C led to substantial grain growth to ~100 nm size (Figure 3.4A). Particles heated to this temperature were most likely formed via Ostwald ripening and/or sintering by both surface and volume diffusion processes, resulting in large well-defined grains (the inset in Figure 3.4A). Figure 3.4B presents an HR-TEM image of the area corresponding to the one marked with a broken square in Figure 3.4A. Clear lattice fringes are present. The FT of this particular region is presented in Figure 3.4C. Splitting of some of the diffraction spots can be recognized. This indicated that the investigated area was composed of either several crystallites, or several domains within one single crystal. Based on the $1/\partial$ values the reflections were attributed to the {001}/{100}, {101}/{110}, and {002}/{200} reflections of tetragonal $BaTiO_3$, as marked in the figure. The tetragonality ratio, $(c\text{-}a)/a$ based on FTs equalled 0.23%.

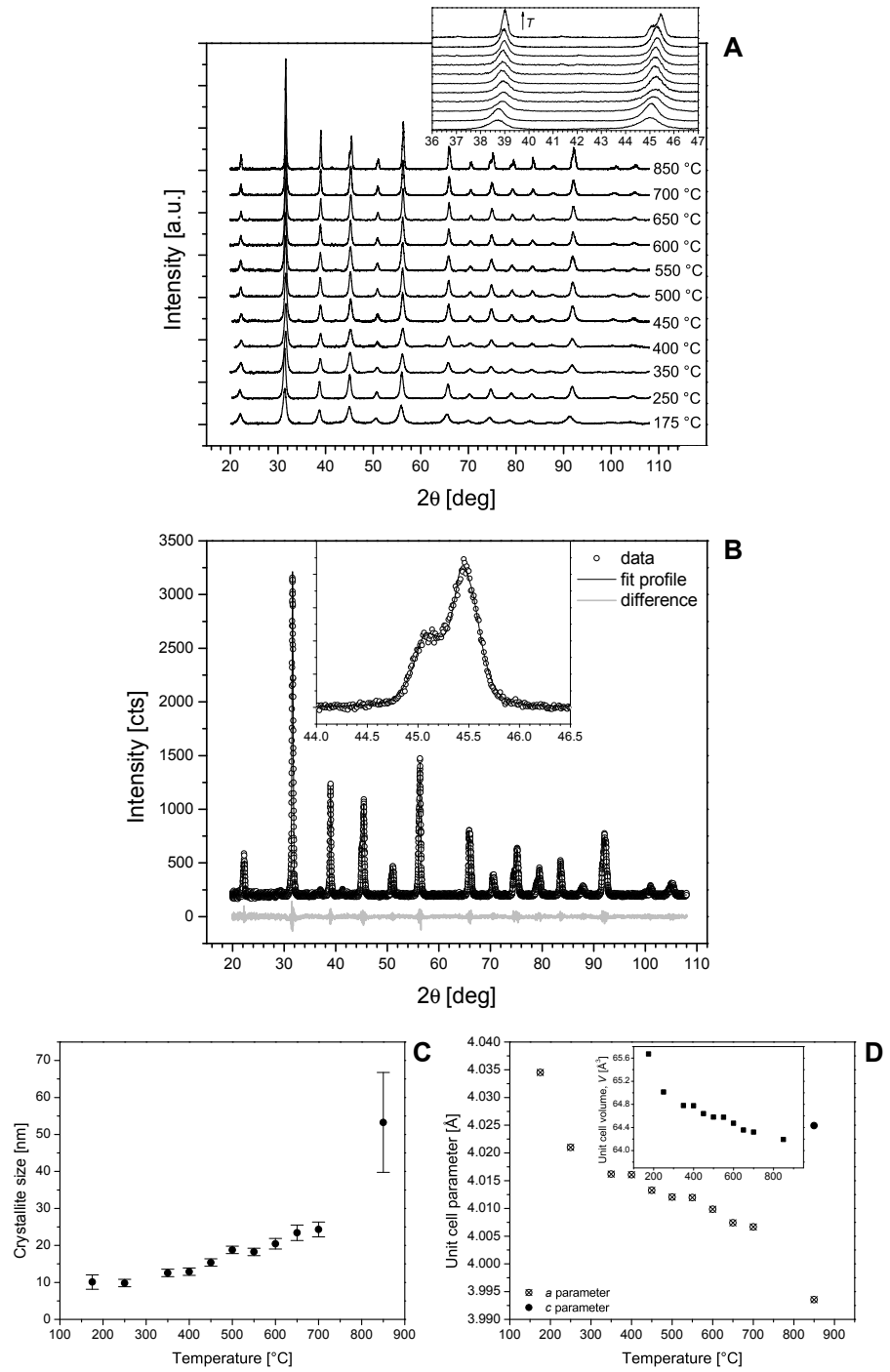

Figure 3.1. a) XRD patterns of as-synthesized and heat-treated $BaTiO_3$ powders. Inset demonstrates the shift and splitting of selected diffraction peaks to higher angles with increasing calcination temperature; b) Example fit of pseudo-Voigt function profile to XRD pattern of powder heat-treated at 850 °C. Inset shows the split (002)/(200) peaks of tetragonal barium titanate; c) Evolution of average crystallite size as a function of processing temperature. d) Evolution of unit cell parameter(s) as a function of processing temperature. Inset shows the evolution of unit cell volume with temperature.

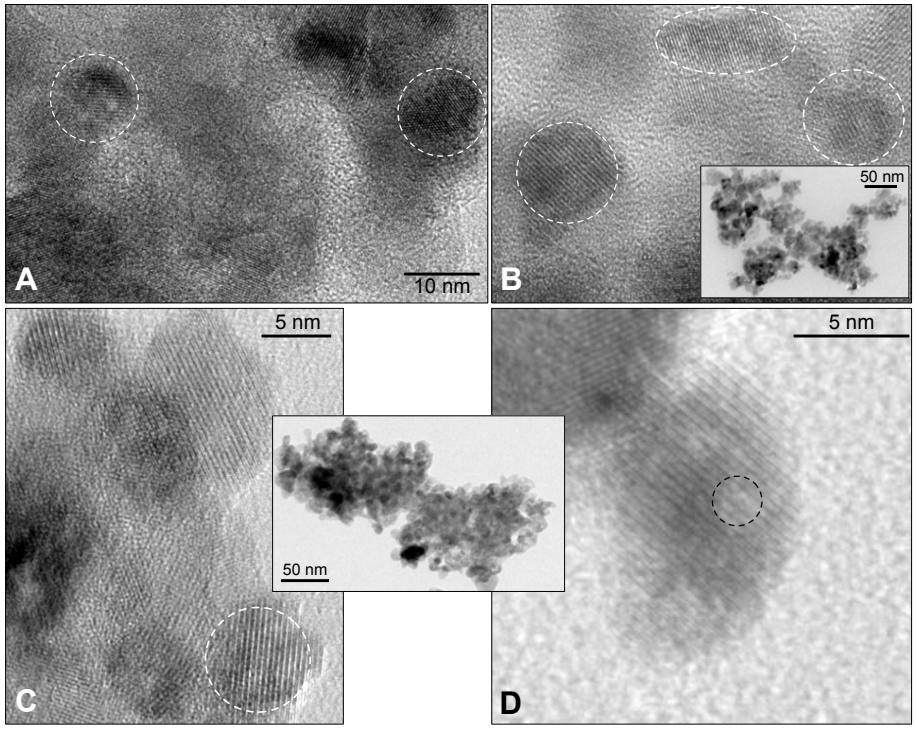

Figure 3.2. Bright-field HR-TEM images of $BaTiO_3$ powders: a) as-synthesized; b) heat-treated at 250 °C for 24 h. Inset shows the typical morphology of the powders at 175 and 250 °C; c) heat-treated at 350 °C for 24 h. Inset presents the morphology of powders heated to 350 - 450 °C; d) a crystallite with a focal plane selected to emphasize the internal porosity, heat-treated at 400 °C. Examples of crystals with internal pore-like defects are marked with broken circles.

3.3.3. Vibrational FT-RS and ATR-IR characterization

Figure 3.5A presents Raman scattering spectra of the powders. The data demonstrate the presence of an asymmetric local structure in $BaTiO_3$ that results in Raman activity [14,22-24]. The cubic phase of barium titanate is not expected to exhibit Raman activity on the basis of symmetry. However, broad bands at 520 and 250 cm^{-1} have often been observed and are due to local disorder of Ti ions [23,24]. All 12 possible Raman optical modes in barium titanate are explained in the work of Venkateswaran *et al.* [24]. In tetragonal $BaTiO_3$ with *P4mm* symmetry one would expect a broad peak with a centroid around 260 cm^{-1} - A_1(TO) optical mode; a sharp peak at 315 cm^{-1} – B_1, E(TO+LO) optical mode; an asymmetric broad peak at 520 cm^{-1} – A_1, E(TO) optical mode; and a broad peak at around 720 cm^{-1} – A_1, E(LO).

A dip around 180 cm^{-1} in bulk $BaTiO_3$ ceramics has been attributed to anharmonic coupling between three A_1(TO) phonons [23,24]. It is known for nanoceramics that this feature takes the form of a peak resulting from phonon damping caused by internal stress, defects, or the presence of an orthorhombic phase [11,23,24]. In the investigated powders such a peak was observed for powders calcined at T < 850 °C, whereas a dip appeared when T = 850 °C. Tetragonality was confirmed by the

presence of a peak at 308 cm^{-1}, which was attributed to the B_1, E(TO+LO) phonon mode. This peak is clearly evolving above T = 350 °C, and appears to be present in the as-synthesized powder and at 250 °C, albeit it is strongly dampened. Peaks at 717 cm^{-1} and 519 cm^{-1} behaved similarly. No peaks were found in the proximity of 810 cm^{-1}. These would have indicated the presence of internal hydroxyl lattice defects [23]. If present, internal hydroxyl defects were below the detection limit of FT-RS. However,a peak was observed at around 690 cm^{-1}, which can be attributed to a barium carbonate impurity [23]. On the other hand, the presence of hydroxyl defects in the lattice and OH groups at the surface was confirmed by ATR-IR spectra in the range between 4000 cm^{-1} and 2500 cm^{-1} (Figure 3.5B). A predominant broad band originating from either surface adsorbed water or alcohol (*e.g.* benzyl alcohol) was present. This band was present in all samples, independent of the calcination temperature, and was probably related to the re-adsorption of water at the surface in ambient atmosphere. On the other hand, a weak peak/shoulder at 3550 cm^{-1} was noticeable in powders calcined up to 600 °C, and it can be attributed to lattice hydroxyl defects. The lattice hydroxyls disappeared above 600 °C.

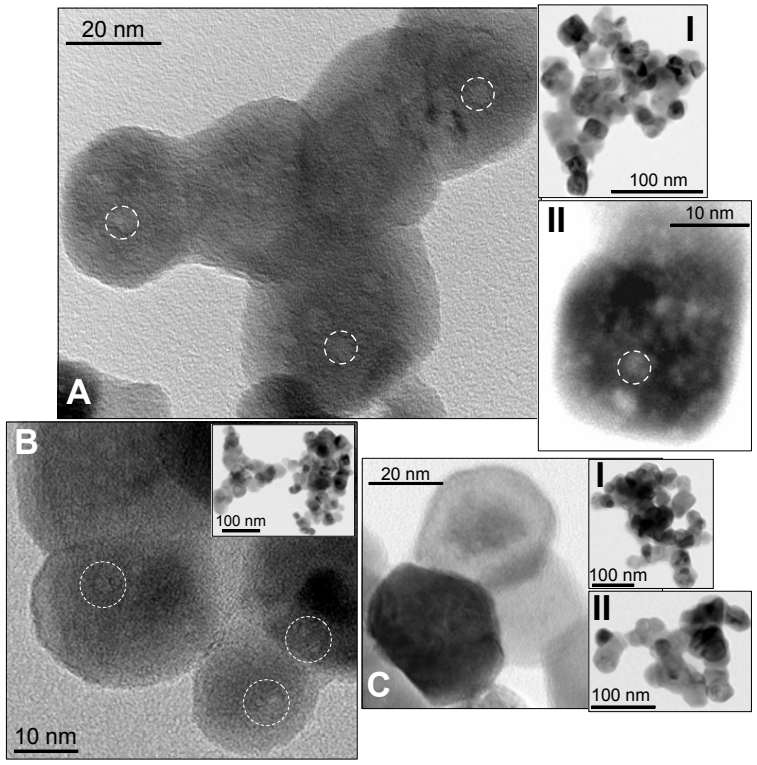

Figure 3.3. Bright-field HR-TEM image of heat-treated $BaTiO_3$ powder: a) T = 500 °C for 24 h. Inset I shows the typical morphology of the powder at lower magnification. Inset II shows a crystallite with a focal plane selected to emphasize the internal porosity; b) T = 600 °C for 24 h. Inset shows a typical morphology of the powder at lower magnification; c) T = 650 °C for 24 h. Inset I shows a typical morphology of the powder heat-treated at 650 °C at lower magnification. Inset II shows a typical morphology of the powder heat-treated at 700 °C at lower magnification.

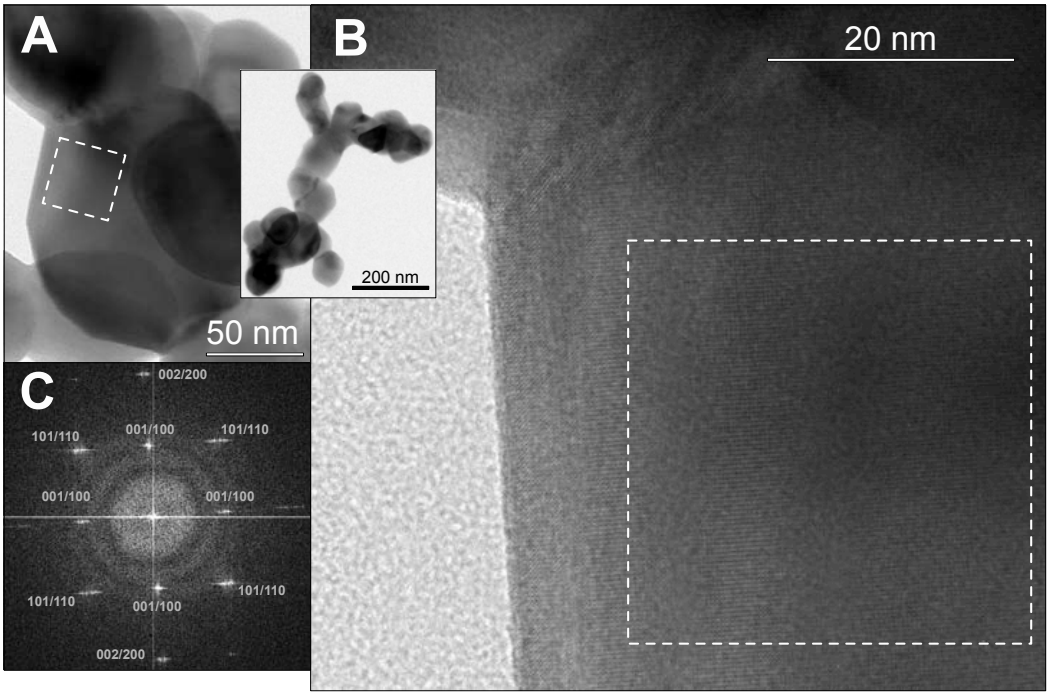

Figure 3.4. a) Bright-field HR-TEM image of BaTiO3 powders heat-treated at 850 °C for 8 h. Inset shows a typical morphology of the powder at lower magnification; b) Bright-field HR-TEM image of selected crystallite; c) FT of part of image (b), marked with a broken square. The {001}/{100}, {101}/{110}, and {002}/{200} reflections of tetragonal $BaTiO_3$ are marked.

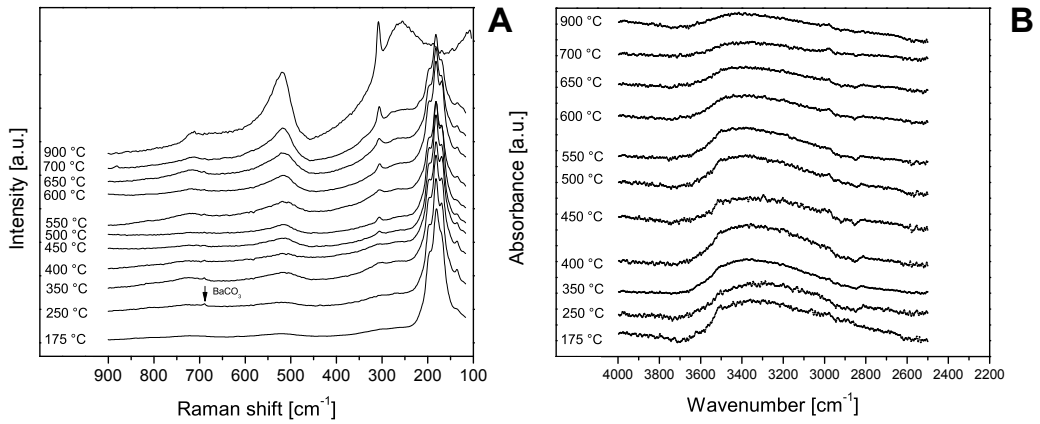

Figure 3.5. a) FT-RS spectra of as-synthesized and heat-treated $BaTiO_3$ powders. $BaCO_3$ phase is marked. b) ATR-IR spectra of as-synthesized and heat-treated $BaTiO_3$ powders in the wavelength region typical for hydroxyl defects.

3.3.4. TGA/DSC characterization

Figure 3.6A shows information from TGA and DSC analysis of as-synthesized powder, powders heat-treated at 250 °C for 24 and 96 h, respectively, and material calcined at 350 °C for 24 h. A clear distinction between different processing conditions can be made, but the details in the curves are quite complicated. Therefore, I focus mainly on the major trends that are relevant for data interpretation. The as-synthesized powder exhibited a gradual multi-step weight decrease by *ca.* 11% until approximately 600 °C, followed by a further 1.6% weight loss above 600 °C. The largest mass decrease of around 9% took place below 450 °C, and was accompanied by a large exothermic DSC peak with an onset at 370 °C. The small mass loss above 600 °C corresponds to a slow endothermic process with an onset at the same temperature. Heat-treatment at 250 °C for 24 h led to a material with slightly different thermal characteristics. The total mass change decreased to *ca.* 8%.

The largest mass decrease of around 5% occurred below 450 °C, and was accompanied by the exothermic peak with an onset around 300 °C, which was much weaker and considerably shifted to a lower temperature in comparison with the as-synthesized powder. The DSC signal remained relatively constant until 450 °C, when a broad endothermic peak developed marking probably an onset of a very slow endothermic process. Finally in the case of the material calcined at 350 °C for 24 h, the mass change resembled the one observed for the powder treated at 250 °C for 96 h, having a total mass decrease of *ca.* 7%. The DSC signal contained a broad endothermic peak with an onset at 450 °C.

Figure 3.6B depicts TGA/DSC data of selected powders calcined at $T > 400$ °C. The overall mass loss depended on treatment temperature. None of the investigated powders exhibited an exothermic DSC peak around 300 – 370 °C. A slowly developing broad endothermic peak was observed in all cases. A minor endothermic peak at 800 °C in a few powders can be attributed to the decomposition of $BaCO_3$. The DSC signal from $BaTiO_3$ samples processed at 700 and 850 °C in the temperature range 20 – 150 °C is compared in Figure 3.6C. The cubic-to-tetragonal transition is normally observed in this temperature region. The DSC curve of the powder calcined at 850 °C exhibited an endothermic peak around 120 °C, indicating the transition, whereas the powder processed at 700 °C clearly lacks such a feature.

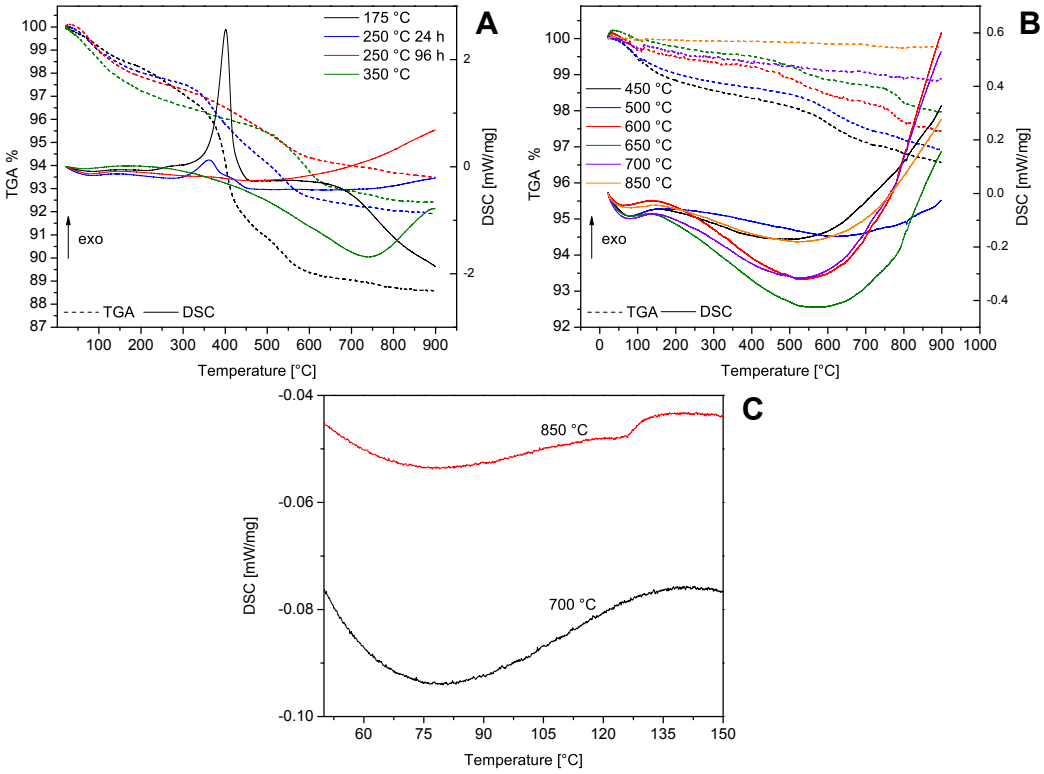

Figure 3.6. TGA/DSC scans of $BaTiO_3$ powders in air. Heating/cooling rate 5 °C /min; a) powders heat-treated to 175-350 °C; b) powders heat-treated between 400 °C and 850 °C; c) comparison of DSC signals of powders calcined at 700 °C and 850 °C in the temperature range where the cubic-to-tetragonal transition occurs.

3.4. Discussion

A consistent image of the phase evolution of alkoxide-hydroxide-precipitated nanosized $BaTiO_3$ emerged from the experimental data. As-synthesized barium titanate was crystalline in XRD and TEM, with average crystallite sizes < 10 nm. XRD unit cell refinement showed that the unit cell volume was large at this stage. Such effects have been reported for $BaTiO_3$ prepared from wet-chemical methods, and have been attributed to the presence of either OH^- or/and CO_3^{2-} defects in the perovskite lattice [11,15]. Prolonged heat treatment at a relatively low temperature of 250 °C led to a decrease of the unit cell volume by *ca.* 1%, indicating substantial removal of hydroxyl defects. TEM analysis revealed the presence of internal porosity within the nanocrystals. Such pores were also present in the as-synthesized powder, but at much lower concentration. Processing up to 450 °C led to minor crystallite growth, further formation of pore defects, and unit cell volume decrease. The onset of particle sintering was at 500 °C, but particle growth was limited to particle sizes

below 20 nm. This suggests that surface diffusion was probably the predominant driving force for sintering at these low temperatures. However, coalescence of smaller crystallites with a large surface energy cannot be excluded completely.

A well-developed pore structure persisted up to 600 °C. The decrease of unit cell size with temperature can be rationalized in terms of hydroxyl defect curing, which is known to occur at temperatures from 100 to 800 °C [11,15,25]. Hennings *et al.* reported internal porosity in hydrothermal powders that had been heat-treated above 500 °C. The loss of porosity was associated with hydroxyl defect removal and point defect migration and annihilation [14,25]. However, in that study the intragranular porosity had dimensions from a few to 200 nm. Hydrothermal barium titanate processed below 500 °C did not exhibit internal porosity in TEM, but its density measured by pycnometry was lower than the expected value of 6.05 g/cm^3. The authors attributed the difference to the existence of discrete point defects, which merged and formed pores upon curing at higher temperatures.

In the presented case I observed pores with a size of several nanometres already far below a processing temperature of 500 °C. The difference may be explained by considering that the reactivity of sub-10 nm powders is much higher than that of hydrothermal crystallites of 200 nm size, due to their high surface energy.

The thermal characteristics of $BaTiO_3$ processed at lower temperatures can be explained by several factors. Barium titanate was precipitated in benzyl alcohol, a solvent with a high boiling point (205 °C). Post-processing of the powder involved drying at significantly lower temperature. Probably benzyl alcohol remained adsorbed at the surface of $BaTiO_3$ nanoparticles and was only removed by oxidation at higher temperatures. This hypothesis was confirmed by TGA/DSC. A large exothermic peak that can be attributed to the pyrolysis of organics was found for the as-synthesized powder, whereas prolonged heat treatment at 250 °C led to partial and ultimately to complete removal of that peak. It illustrates that the benzyl alcohol removal process was very slow at the considered temperature. The solvent seems to be strongly bound to $BaTiO_3$, since it was pyrolyzed rather than evaporated. Trapping of benzyl alcohol is most likely caused by the gel-like high-surface area structure of the as-synthesized $BaTiO_3$ nanopowder. It implies the possible formation of a semi-crystalline oxocarbonate phase, $Ba_2Ti_2O_5CO_3$ [2]. I observed its presence in an analogous synthesis in 2-methoxyethanol in Chapter 2 and in ref. [10]. In the present study, $BaTiO_3$ is formed predominantly, but considering the large organic residue, it may be assumed that $Ba_2Ti_2O_5CO_3$ and/or $BaCO_3$ are also formed upon drying or heat treatment. It is in agreement with the small mass loss above 600 °C in all powders, which can be attributed to CO_2 release from the oxocarbonate phase [2]. $BaCO_3$ decomposes above 800 °C. The Raman data confirmed the presence of CO_3^{2-}. The mass change below 600 °C observed in samples processed between 350 and 700 °C is therefore the result of internal hydroxyl defect curing and surface water

release. The broad endothermic DSC peak can also be attributed to these slow processes. The DSC signal also incorporates the decomposition of semi-crystalline oxocarbonate phase, $Ba_2Ti_2O_5CO_3$ with a release of CO_2 and its re-crystallization into $BaTiO_3$.

TEM and XRD of powders heat-treated at 650 and 700 °C showed minor grain growth, and significant shrinkage of the unit cell to a volume that was only 0.26 – 0.20% larger than that of sample calcined at 850 °C. No more internal porosity was observed at these processing temperatures and ATR-IR indicated the absence of internal hydroxyls. On the other hand, TGA of the material calcined at 700 °C showed a 0.5% mass loss until 600 °C, suggesting that some hydroxyl defects were still present in that powder. I hypothesize that full defect curing and hydroxyl removal in these nanopowders occurs only in combination with grain growth. The considered powders remained essentially cubic. Only treatment at 850 °C showed the complete removal of hydroxyl defects and a clear room temperature cubic-to-tetragonal transition in XRD and DSC. On the other hand, the Raman data suggested that tetragonality was partially retained by processing above 350 °C. The difference can be explained in terms of local structure disorder, which is visible by spectroscopic methods and is caused by internal defects and lattice strain by internal pores. The presence of a positive peak in the Raman spectra around 190 cm^{-1} can be attributed to a local orthorhombic phase. It was also observed by Frey and Payne in sol-gel derived powders [11]. Full tetragonality was retained upon crystallite growth to ~100 nm (in TEM) grain size. Stabilization of the cubic phase at room temperature is often attributed to the excessive surface energy or high hydrostatic pressure in $BaTiO_3$ nano-powders, which is lowered upon grain growth upon annealing at sufficiently high temperature [11,19,26,27]. This theory explains well the cubic-to-tetragonal transition after annealing at 850 °C as observed by me, but it does not explain the Raman activity of powders that were heat-treated at considerably lower temperatures. I hypothesize that removal of hydroxyl defects from as-synthesized powders upon heating leads to pore formation, which results in local strains inside particles and to local non-correlated distortions around Ti^{4+} ions. This results in Raman activity that can be attributed to tetragonal or orthorhombic symmetry. Considering that these pores constitute a relatively large fraction of the total volume of a nanocrystals, the internal strains may be extensive. Therefore it is the dip at 180 cm^{-1} related to anharmonic coupling between three A_1(TO) phonons that proves that barium titanate is tetragonal at room temperature, because its appearance coincides with the observation of crystallographic tetragonality in XRD.

3.5. Conclusions

The phase evolution of the $BaTiO_3$ nanocrystalline powder can be explained in terms of two effects:

(1) Due to the high surface energy of the sub-10 nm $BaTiO_3$ nanocrystals, the material exhibits an enhanced reactivity that demonstrates itself by grain growth and sintering effects at temperatures as low as 500 °C. Heat treatment at 600 °C or higher led to complete removal of internal hydroxyl groups and the development of intragranular porosity. Local disorder in the crystal is observed by Raman activity and can be attributed to a local tetragonal or orthorhombic phase.

(2) High-temperature treatment is necessary to fully cure the hydroxyl defect structure of nanocrystalline barium titanate, It is accompanied by substantial grain growth. Grain growth to ~100 nm particle sizes from sub-25 nm crystallites implies that volume diffusion occurs, which finally resulted in the formation of a fully tetragonal $BaTiO_3$ phase.

3.6. References

[1] Yoon, G. *J. Ceram. Proc. Res.*, *7*, 343-354, **2006**.

[2] Pithan, C.; Hennings, D. H.; Waser, R. *Int. J. Appl. Ceram. Technol.,* 2, 1-14, **2005**.

[3] Flaschen, S. S. *J. Am. Chem. Soc.*, *77*, 6194, **1955**.

[4] Chaput, F.; Boilot, J. P. *J. Mat. Sci. Lett.,* 6, 1110-1112, **1987**.

[5] Chaput, F.; Boilot, J. P.; Beauger, A. *J. Am Ceram. Soc., 73*, **1990**.

[6] Golubko, N. V.; Yanovskaya, M. I.; Romm, I. P. *J. Sol-Gel Sci.Technol.,* 20, 135-143, **2001**.

[7] Frey, M. H.; Payne, D. A. *Chem. Mater., 7*, 123-129, **1995**.

[8] Yoon, S.; Baik, S.; Kim, M. G.; Shin, N. *J. Am Ceram. Soc.,* 89, 1816-1821, **2006**.

[9] Yoon, S.; Baik, S.; Kim, M. G.; Shin, N.; Kim, I. *J. Am Ceram. Soc.,* 90, 311-314, **2007**.

[10] Chapter 2; Stawski, T. M.; Veldhuis, S. A.; Göbel, O. F.; ten Elshof, J. E.; Blank, D. H. A. *J. Am. Ceram. Soc.*, 93, 3443-3448, **2010**.

[11] Frey, M. H.; Payne, D. A. *Phys. Rev. B*, 54, 3158-3168, **1996**.

[12] Yashima, M.; Hoshina, T.; Ishimura, D.; Kobayashi, S.; Nakamura, W.; Tsurumi, T.; Wada, S. *J. Appl. Phys.*, 98**,** 014313-1-8, **2005**.

[13] Laulicht, I.; Benguigui, L. *Solid State Comm.*, 32, 771-775, **1979**.

[14] Noma, T.; Wada, S.; Yano, M.; Suzuki, T. *J. Appl. Phys.*, 80, 5223-5233, **1996**.

[15] Hennings, D.; Schreinemacher, S. *J. Eur. Ceram. Soc.*, 9, 41-46, **1992**.

[16] Kim, Y. -I.; Jung, J. K.; Ryu, K. -S. *Mater. Res. Bull.*, 39. 1045-1053. **2004**.

[17] Kota, R.; Lee, B. I. *J. Mater. Sci.: Mater. Electron.*, 18, 1221-1227, **2007**.

[18] Badheka, P.; Qi, L.; Lee, B. I. *J. Eur. Ceram. Soc.*, 26, 1393-1400, **2005**.
[19] Begg, B. D.; Vance, E. R. ; Nowotny, J. *J. Am. Ceram. Soc., 77*, 3186-3192, **1994**.
[20] Wada, S.; Yasuno, H.; Hoshina, T.; Nam, S. -M.; Kakemoto, H.; Tsurumi, T. *Jpn. J. Appl. Phys.*, 42, 6188-6193, **2003**.
[21] Le Bail, A. *Powder Diffr.,* 19, 249-254, **2004**.
[22] Begg, B. D.; Finnie, K. S.; Vance, E. R. *J. Am. Ceram. Soc.,* 79, 2666-2672, **1996**.
[23] Shiratori, Y.; Pithan, C.; Dornseiffer, J.; Waser, R. *J. Raman Spectrosc.*, 38**,** 1288-1299, **2007**.
[24] Venkateswaran, U. D.; Naik, V. M.; Vaik, R. *Phys. Rev. B*, 58, 14256-14260, **1998**.
[25] Hennings, D. F. K.; Metzmacher, C.; Schreinemacher, B. S *J. Am. Ceram. Soc.,* 81, 179-182, **2001**.
[26] Uchino, K.; Sadanaga, E.; Hirose, E. *J. Am. Ceram. Soc., 72*, 1555-1558, **1989**.
[27] Yen, F.; Chang, C. T.; Chang, Y. *J. Am. Ceram. Soc., 73*, 3422-3427, **1970**.

[1]

4

Nanoscale Structure Evolution in Alkoxide-Carboxylate Sol-Gel Precursor Solutions of Barium Titanate*

Abstract

The evolution of hydrolyzed alkoxide-carboxylate sol-gel precursor solutions of barium titanate was investigated by time-resolved small angle x-ray scattering (SAXS) and viscosity measurements. Sols were prepared from titanium(IV) *iso*-propoxide in 2-methoxyethanol and barium acetate in acetic acid. Analysis of the experimental data showed that the evolution of the sol went through three stages. In stage (i) mainly isolated primary scatterers of *ca.* 0.45 nm radius formed. Stage (ii) showed the growth of branched oligomeric mass fractal-like structures with 3 – 15 nm gyration radius and fractal dimension 1.9 – 1.5, as well as the presence of internally ordered structures with a correlation length of *ca.* 1.8 nm. In stage (iii) higher-level hierarchy developed in the sol, probably due to cluster-cluster aggregation of the fractal-like branched oligomers into a gel. The data suggest that the agglomerates of scatterers are Ti-based, and are constructed of small spherical primary particles of very similar size. The inorganic core of these particles has a radius of *ca,* 0.45 nm, and they have a outer organic ligand shell of *ca,* 0.45 nm thickness. Ba-related species remained dissolved in the acetic acid matrix, and were present as ions. No Ba-related species could be seen with SAXS. Ba seemed to exert an indirect influence on the growth and precipitation or stabilization of the titanium-based structures from solution.

4.1. Introduction

Barium titanate ($BaTiO_3$) is a high-*k* dielectric material used in commercial multi-layer ceramic capacitors. The minimum $BaTiO_3$ layer thickness that can be achieved with state of the art tape casting methods is about 1 μm, which implies the use of starting powders with a particle size of *ca.* 200 nm [1]. Further reduction of the

* Published in:
Stawski, T. M.; Veldhuis, S. A.; Besselink, R.; Castricum, H. L.; Portale, G.; Blank, D. H. A.; ten Elshof, J. E. *J. Phys. Chem. C*, 115, 20449-20459, **2011**.

barium titanate layer thickness requires finer powders obtained by new synthesis and deposition techniques.

The barium titanate synthesis methods developed in the last decades can be divided into (1) solid precursor based methods, *e.g.* mixed oxide method and citrate route, and (2) wet-chemical methods, *e.g.* sol-gel, alkoxide-hydroxide sol precipitation, and hydrothermal route. In both groups substantial progress has been made, as can be seen by comparing the review of Pithan *et al.* from 2005 [2] with that of Phule and Risbud from 1990 [3].

Wet-chemical methods provide nanometer-sized powders (5 – 100 nm) of high purity and homogeneity, and of adjustable composition, as near-atomic level mixing of components is possible. Among these methods the sol-gel process, in particular the alkoxide-carboxylate synthesis, the double alkoxide synthesis, the micro-emulsion synthesis, and the precipitation methods (alkoxide-hydroxide sol precipitation) have received much attention [2]. Furthermore, as the sol-gel process is based on liquid precursors, direct deposition of amorphous precursor thin films onto substrates by means of spin-casting, deep-casting or misted source deposition, followed by pyrolysis and crystallization is possible [4-6].

The alkoxide-carboxylate route has been employed widely for $BaTiO_3$ synthesis since the first reports by Phule and Risbud in 1988 [7]. Barium titanate xerogels were synthesized from titanium(IV) *iso*-propoxide in *iso*-propanol and barium acetate in acetic acid. Acetic acid was used as a solvent enabling the complete dissolution of barium acetate. Acetic acid is also known to chelate metal centers in alkoxides, leading to the formation of oligomeric metal oxoacetates [5,8-11]. This approach was further extended to other oxide precursor systems, such as barium strontium titanate, lead zirconate titanate, lead lanthanum zirconate titanate [4,5]. The influence of precursor chemistry and processing conditions on the morphology of crystalline thin films processed from sol-gel were also investigated [12,13]. Use of acetic acid or propionic acid favored the growth or larger grains and yielded higher density barium titanate films in comparison with films synthesized from 2-ethylhexanoate based precursors. The difference was attributed to the higher pyrolysis temperature of the system containing the shorter carboxylic acid, leading to formation of transition oxocarbonate phase, $Ba_2Ti_2O_5CO_3$ [14]. As a result crystallization occurred at higher temperatures, which led to increased density of thin films and to larger grains. The morphology of crystalline barium strontium titanate and barium titanate films derived from alkoxide-carboxylate route could be also modified [13]. When the sol concentration was sufficiently low for a given composition of precursors, provided that films were deposited in a number of steps and crystallized after each deposition, columnar grains were formed. Above a certain threshold concentration only a granular morphology was observed.

The stabilization of titanium alkoxide precursors is believed to play an important role, as it can modify the hydrolysis and condensation pathways. Hasenkox *et al.* noted that application of titanium alkoxide stabilized with acetylacetone resulted in denser films with larger grain sizes and better dielectric properties, which was attributed to the monomeric character of the titanium precursor and the homogenous mixing of Ti and Ba precursors on the nanometer scale [8]. The authors hypothesized that in the case of non-stabilized solutions, an oligomeric TiO_x phase might form, and the extent of phase formation would depend on the extent of oligomerization of Ti alkoxide derived structure and chemical gel formation. The structure of such an alkoxide-carboxylate gel was proposed by Hennings *et al.* [4,15] based on transmission electron microscopy (TEM), energy disperse spectroscopy (EDS), and infrared spectroscopy (FT-IR) analysis. Metal carboxylate species were assumed to adsorb at the surface of titanium oxoacetate polymer. The separation between Ti-rich and Ba-rich regions exceeded 100 nm.

The properties of alkoxide-carboxylate derived thin films are therefore probably controlled by separation between immiscible or partly immiscible Ti-oxoacetate and Ba-carboxylate-rich domains. The separation is determined by *e.g.* carboxylic acid chemistry, sol concentration and chelating/stabilization agents. No details of nanoscale spatial separation processes, or of the structure of TiO_x oligomers in contact with metal carboxylates, has been reported to my knowledge. It was the aim of this work to obtain a better understanding of the evolution of nanostructure in hydrolyzed solutions of titanium alkoxide and barium acetate in acetic acid. I employed time-resolved small-angle x-ray scattering (SAXS) to study the structural evolution in this system on a nanometer scale. In the next section a model is derived to which the experimental SAXS data could be fitted. The model is based on the assumption that hydrolysis yields two types of distinguishable x-ray scattering structures in solution, namely (i) mass fractal-like structures, and (ii) structures with internal correlations. Both structure types are thought to be assembled from similar spherical primary scatterers, and they seem not to interact in solution. In terms of sol-gel chemistry, the fractal-like structures can be associated with branched oligomeric species dissolved in a solvent matrix, and the structures with internal correlations resemble dense agglomerates of primary particles (precipitates).

In addition to SAXS, I also used viscosity measurements as a function of time and temperature to monitor the global changes in the solution and locate the main transitions of the process. Gelation of the system was promoted by hydrolysis of the barium titanate precursor sol with varying concentrations of water, which enabled me to follow the extent of oligomer growth by time-resolved SAXS.

4.2. Experimental

4.2.1. Synthesis of barium titanate precursor sols

Barium acetate (> 99%, Riedel-deHaën) and titanium(IV) *iso*-propoxide (99.999%, Sigma-Aldrich) were used as precursors. Glacial acetic acid (99.8%, Acros) and 2-methoxyethanol (> 99.3%, Sigma-Aldrich) were used as solvents, stabilizers, and chelating agents. Two stock solutions were made. A Ba-acetate solution was prepared by dissolving barium acetate in acetic acid and refluxing at 105 °C for 8 h to remove all remaining water. The final concentration was adjusted to 1.0 mol/dm^3 by dilution with acetic acid. The second stock solution was based on 1.0 mol/dm^3 titanium *iso*-propoxide in 2-methoxyethanol, and was prepared in a glove box under nitrogen atmosphere. All stock solutions were stirred at room temperature for 24 h. They were then stored at room temperature. Prior to the experiments, the stock solutions were mixed in 1 : 1 molar ratios and stirred for 5 min, yielding a concentration of 0.50 mol/dm^3 in the final BTO precursor solution. Solutions of this concentration were used in all experiments. Hydrolysis was initiated by addition of water immediately after two stock solutions had been mixed and stirred. Sols with hydrolysis ratios [H_2O]/[Ti] of 2.8, 5.5, 16.7, 25, and 33 were investigated.

4.2.2. Viscosity measurements

The viscosity of BTO precursor sols as a function of time was measured at 40 – 60 °C, using an Anton Paar AMVn-HT rolling-ball viscometer. For all the measurements a glass capillary (Ø = 3.00 mm) was used, together with a steel ball (Ø = 2.5 mm) with a density of 7.71 g/cm^3. The setup was calibrated using Anton Paar SH C120 calibration standard.

4.2.3. Small angle x-ray scattering

SAXS experiments were performed on the Dutch-Belgian beamline (DUBBLE) BM-26B at the ESRF in Grenoble, France [16]. The beam was focused at the corner of a 2D gas-filled multi-wire proportional detector in order to maximize the range of accessible q values (scattering vector values). The beam energy was 16 keV (λ = 0.0776 nm). The samples were placed at a distance of 1.5 m from the detector and the intensity was measured in the range $0.13 < q < 9.00$ nm^{-1}. The raw data were corrected for the pixel-dependent detector sensitivity and integrated for channels with the same q values. To investigate the evolution of BTO precursor sols *in situ* at elevated temperatures, SAXS data were collected on sols in glass sealed capillaries (Ø = 1.0 mm, glass no. 14, Hilgenberg, Malsfeld, Germany) that were mounted into a Linkam oven for capillaries, which was operated at 60 °C. Measurements were performed with 5 min intervals over a period of typically 1 – 3 h.

4.3. Small angle x-ray scattering data interpretation

In SAXS experiments elastic scattering of x-rays by a sample that has local electronic density fluctuations is recorded at very small angles. Structural information about entities with dimensions of < 50 nm can be derived from the measured angular range [17-20]. In a typical SAXS experiment, the scattering intensity $I(\boldsymbol{q})$ is plotted versus the modulus of the scattering vector $\boldsymbol{q}$ (nm^{-1}), which is related to the scattering angle 2θ and the wavelength λ (nm) of the incident beam via:

$$q = 4\pi / \lambda \sin\theta \tag{4.1}$$

In general the scattering amplitude A in a given direction from an object of electron density $\rho(\boldsymbol{r})$ is expressed by [17-19]:

$$A(\boldsymbol{q}) = \int \rho(\boldsymbol{r}) \exp(-i\boldsymbol{q} \cdot \boldsymbol{r}) \mathrm{d}\boldsymbol{r} \tag{4.2}$$

Hence, the scattered intensity in the direction defined by a scattering vector is $I(\boldsymbol{q})=AA^*$, where A^* is the complex conjugate of A.

4.3.1. Sphere form factor

The amplitude of the form factor of a homogenous sphere, $F(q)$, of radius r_0 is given by Equation (4.3) [17-19]:

$$F(q, r_0) = 3\frac{\sin(qr_0) - \cos(qr_0)}{(qr_0)^3} \tag{4.3}$$

The scattered intensity $I(q)$ from the dilute system of non-interacting, monodisperse, homogenous spherical particles of number density N, with electron density difference between the particles and the surrounding medium (scattering contrast) $\Delta\rho$ and particle volume V can be expressed by Equation (4.4), where $P(q)$ is the form factor. V can be incorporated into the form factor.

$$I(q) = N(\Delta\rho)^2 V^2 F^2(q, r_0) = N(\Delta\rho)^2 P(q, r_0) \tag{4.4}$$

4.3.2. Structure factor

For systems with a higher concentration of particles, Equation (4.4) is insufficient to describe $I(q)$ as it neglects interference of scattering from different species due to interactions between particles, such as Coulomb repulsion-attraction phenomena, agglomeration and clustering effects, or spatial correlations within the system [21]. These can be included by introducing the structure factor, $S(q)$, where the function describing the scattered intensity takes the general form of Equation (4.5):

$$I(q) = N(\Delta\rho)^2 P(q) S(q) \tag{4.5}$$

Assuming isotropic interactions and a monodisperse shape of particles [17,21-26], the structure factor is defined by Equation (4.6):

$$S(q) = 1 + 4\pi \int_0^\infty [g(r) - 1] r^2 \frac{\sin qr}{qr} \mathrm{d}r \tag{4.6}$$

where $g(r)$ is the pair correlation function.

4.3.3. Mass-fractal-like particles

Let us assume that primary particles can cluster together and form branched oligomers. Such a system may be described in terms of the well-established mass-fractal models [24-25]. Essentially, a fractal-like particle is defined here as an object whose radius of gyration, R_g, is related to the number of primary particles n of which the particle is constructed, via Equation (4.7) [24-26]:

$$n = k_0 \left(\frac{R_g}{r_0} \right)^D \tag{4.7}$$

Here D is the so-called fractal dimension, r_0 is the radius of a primary particle of the fractal-like agglomerate, and k_0 is a constant. For true fractals, the parameter D expresses the dimensionality of the system, and its value can take a value between 1 and 3. For real systems with a fractal-like structure, such as branched inorganic polymers, complex clusters and other growing sol components, D is merely a fit factor that is associated with the internal shape and structure of the system under investigation. Its value is generally also between 1 and 3.

In the case of finite structures described by fractal concepts a cut-off distance, ξ, is introduced. This parameter is often interpreted as a characteristic length, above which the mass distribution in the structure no longer follows Equation (4.7). This occurs, for instance, at the perimeter of the structure where the local density of the agglomerate drops substantially. In such systems the pair correlation function from Equation (4.6) can often be approximated by Equation (4.8) [23-26].

$$g(r) - 1 = 4\pi D r_0^{-D} r^{D-3} \exp\left(-\frac{r}{\xi} \right)^a \tag{4.8}$$

where a is an arbitrary constant For a = 1, the integral can be solved analytically by substituting Equation (4.8) into Equation (4.6), yielding the well-known function for $S_F(q)$ [24-26]:

$$S_F(q) = 1 + \frac{D\Gamma(D-1)\sin\left[(D-1)\arctan(q\xi)\right]}{(qr_0)^D\left(1+q^{-2}\xi^{-2}\right)^{(D-1)/2}} \tag{4.9}$$

The radius of gyration R_g of a fractal-like structure is related to cut-off distance ξ by Equation (4.10) [23-26]:

$$R_g^2 = D(D+1)\xi^2/2 \tag{4.10}$$

The mass-fractal structure factor is valid when $r_0 << \xi$. It implies that very small entities composed of only a few primary particles cannot be described in terms of the model, because they do not exhibit self-similar behaviour over a range of length scales. In this study, such clusters are typically present at the beginning of sol-gel reactions. In the case of very small particles that are not fractal-like, the Guinier approximation can be used [17] to determine R_g. For $qR_g < 1$, the following approximation is valid independent of particle shape:

$$I(q) = N(\Delta\rho)^2 V^2 \exp(-q^2 R_g^2/3) \tag{4.11}$$

4.3.4. Structures with internal correlations

Systems composed of spherical primary particles of similar size can also form non-fractalic partially ordered correlated structures [27]. Such systems can also be approximated by hard-sphere potentials and be described by structure factor models based on the Percus-Yevick approximation [28-30]. Structure factor, $S_F(q)$, describes a system in terms of a volume fraction ν of interacting particles with hard-sphere radius R_{HS}, as defined by Equation (4.12). The degree of ordering of particles, located at a distance $2R_{HS}$ from another particle depends on the volume fraction.

$$S_C(q) = \frac{1}{1 + 24\nu G(2qR_{HS})/(2qR_{HS})} \tag{4.12}$$

$$G(2qR_{HS}) = \alpha\frac{\sin(2qR_{HS}) - (2qR_{HS})\cos(2qR_{HS})}{(2qR_{HS})^2} + \beta\frac{2(2qR_{HS})\sin(2qR_{HS}) + (2-(2qR_{HS})^2)\cos(2qR_{HS}) - 2}{(2qR_{HS})^3} + \gamma\frac{-(2qR_{HS})^4\cos(2qR_{HS}) + 4\left[3(2qR_{HS})^2 - 6\right]\cos(2qR_{HS}) + 4\left[(2qR_{HS})^3 - 6(2qR_{HS})\right]\sin(2qR_{HS}) + 24}{(2qR_{HS})^5}$$

$$\alpha = (1+2\nu)^2/(1-\nu)^4$$

$$\beta = -6\nu(1+\nu/2)^2/(1-\nu)^4$$

$$\gamma = \nu\alpha/2$$

4.3.5. Double Structure Factor model

It is assumed that systems under investigation are initially composed of non-agglomerated, identical spherical particles that formed upon hydrolysis. The scattered intensity is described by Equation (4.4). As the system evolves, mass-fractal-like agglomerates characterized by a fractal dimension D and cut-off distance ξ, as defined by Equation (4.9), start to form. It is noted that such fractal models do not describe small clusters that are formed in the earliest stages of a sol-gel process well.

On the other hand, it is assumed that ordered structures with internal correlations that can be described in terms of Equation (4.12). Hence, both $S_F(q)$ and $S_C(q)$ are present in $I(q)$, and they originate from physically and spatially different species. Provided that these two types of structures have no or very little interaction, a weight factor $0 < \varepsilon < 1$ can be defined to express the relative contribution to scattering intensity by fractal-like agglomerates. The scattered intensity of such a system, as a function of time, t, is given by Equation (4.13).

$$I(q,t) = N(\Delta\rho)^2 P(q,t)\left\{\varepsilon(t)S_F(q,t) + \left[1-\varepsilon(t)\right]S_C(q,t)\right\} \tag{4.13}$$

Here, the intensity prefactor $N(\Delta\rho)^2$ refers to primary particles with a form factor $P(q)$ that are part of mass fractal-like agglomerates that can be described in terms of the structure factor $S_F(q)$. The factor $[1-\varepsilon(t)]N(\Delta\rho)^2$ refers to the scattering contribution of structures that can be described by the structure factor $S_C(q)$. A few examples of scattering curves that can be simulated by Equation (4.13) are presented in Figure 4.1. Equation (4.13) was used to fit all experimental SAXS data using the Levenberg–Marquardt algorithm [31,32]. I used $S_F(q)$ and $S_C(q)$ as defined by Equations (4.9) and (4.12), respectively. I also attempted to fit the experimental data under the more general assumption that these two types of structures may be interacting, but this did not result in good fits to the data.

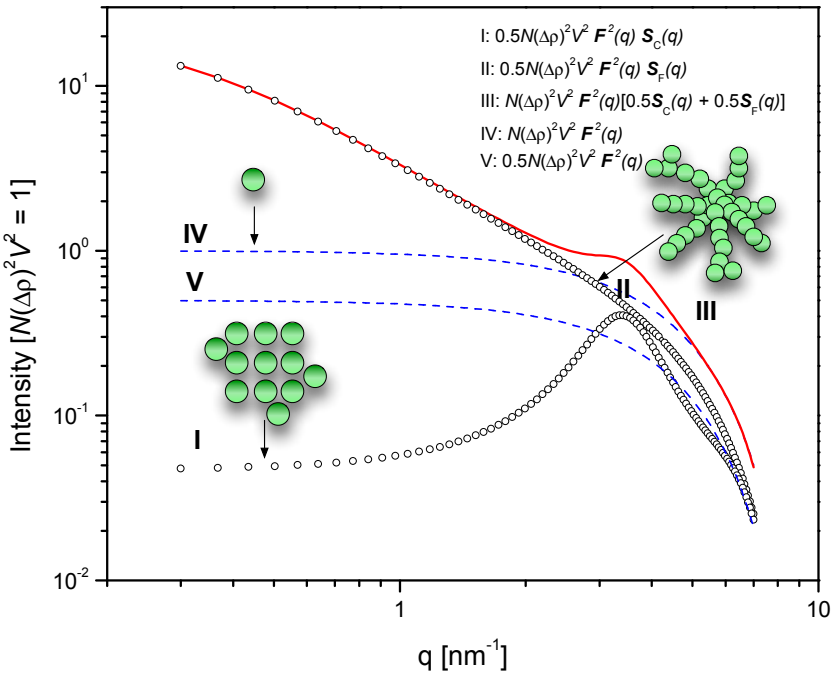

Figure 4.1. Simulated SAXS curves using Equations (4.4) and (4.13), with $N(\Delta\rho)^2V^2$ set to 1. i) $I(q)$ of internally correlated structure with r_0 = 0.5 nm, ν = 0.3, $2R_{HS}$ = 1.8 nm, and ε = 0.5. ii) $I(q)$ of fractal-like structure with r_0 = 0.5 nm, D = 1.8, ξ = 3 nm (R_g = 4.76 nm), and ε = 0.5. iii) $I(q)$ of linear combination of structures i and ii. iv) $I(q)$ of sphere form factor of r_0 = 0.5 nm. v) $I(q)$ of sphere form factor of r_0 = 0.5 nm and ε = 0.5.

4.4. Results and Discussion

4.4.1. Viscosity measurements

Figure 4.2A shows the change in viscosity η as a function of time at different temperatures for a precursor sol with $[H_2O]/[Ti]$ = 16.7. The behaviour of this system is typical for sols within the whole range of investigated hydrolysis ratios. The gelation time t_g was determined as a function of temperature. Assuming Arrhenius-type behaviour for the temperature dependency, the experimental data points can be fitted by linear regression to Equation (4.14).

$$\ln t_g = E_a / RT + \text{const} \tag{4.14}$$

where E_a is the activation energy. Figure 4.2B depicts this dependence as $\ln t_g$ vs. T^{-1}. The obtained activation energy was *ca.* 120 kJ/mol. The data were also

fitted to the Mass Fractal Growth (MFG) model [33,34]. In this model, the viscosity changes in a gel with a mass-fractal type growth regime follow Equation (4.15).

$$\ln\left(\eta / \eta_0 - 1\right) = \text{const} + q_r(3 - D)t \tag{4.15}$$

where η_0 is the viscosity of the solvent medium, q_r a rate constant, and D the fractal dimension. Figure 4.3A presents plots of the relative viscosity change $\ln(\eta/\eta_0 - 1)$ as a function of t/t_g for selected temperatures. In view of Equation (4.15) a linear relationship between viscosity and time is expected in the period at which mass-fractal branched agglomerates develop ($D > 1$). As Figure 4.3A shows, a linear relationship was found in the range $0.2 < t/t_g < 0.8$. Data collected at other temperatures exhibited similar trends. The rate of reaction was highest at 60 °C, and due to the limited time resolution of the viscometer, only data for $t/t_g > 0.2$ could be monitored at that particular temperature.

The regime $t/t_g < 0.2$ did not follow Equation (4.15), showing that other growth modes were present. The trends may be explained in terms of presence of small agglomerates in which branching is not yet profound.

Equation (4.15) no longer holds at $t/t_g > 0.8$, suggesting that the mechanism of growth changes, and one or more processes other than mass-fractal growth become dominant. Probably, $t/t_g = 0.8$ marks the onset of hierarchical aggregation of fractal-like particles, leading to the formation of physical gel network [33-35].

In the Near-Linear Growth model (NLG) it is assumed that the viscosity of a near-linear polymer is related to its molecular weight M by Flory's Equation (4.16) [36]. The evolution of $M(t)$ with time t can be parametrized by f, which is defined as the number of functional groups of the monomer [37,38]. The relevant equations read:

$$\ln \eta = \text{const} + m \ln M(t) \tag{4.16}$$

$$\frac{M(t)}{M(0)} = \frac{(f-2) + 2t / t_g}{(f-2)\left[1 - t / t_g\right]} \tag{4.17}$$

Here, m is a constant and $M(0)$ is the molecular weight of the monomer. It can be shown that when f is slightly larger than 2 in the NLG regime, Equation (4.18) is valid [36-38]:

$$\ln \eta = \text{const} + m \ln \frac{2M(0)}{f-2} + m \ln\left(\frac{t / t_g}{1 - t / t_g}\right) \tag{4.18}$$

Linear growth can be visualized by a straight line in the plot of lnη vs. ln[$t/t_g/(1-t/t_g)$]. The linear dependence does not hold for $t/t_g < 0.2$, as can be seen in inset I of Figure 4.3B. However, the linear trend in inset II in Figure 4.3B shows that the NLG model does fit the trend for $0.8 < t/t_g < 0.97$. This is the region in Figure 4.3A that according to me is dominated by hierarchical aggregation of fractal-like structures. Description within NLG does not necessary imply that the actual aggregates are linear, but that they are of relatively low density. The fractal-like particles from which the aggregate is constructed have only two or slightly more than two neighbours. Such a gel structure agrees well with model proposed by Pope and Mackenzie [33], and completely analogous behaviour has also been observed upon gelation of a barium hydroxide – titanium *izo*-propoxide in 2-methoxyethanol BTO precursor system [33].

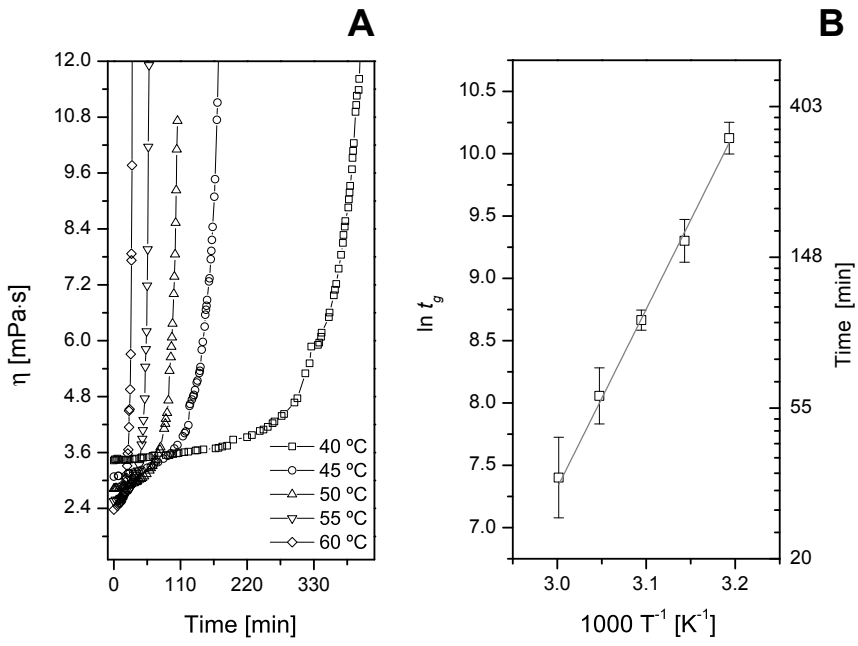

Figure 4.2. a) Viscosity of a 0.5 mol/dm^3 barium titanate precursor sol with [H_2O]/[Ti] = 16.7 as a function of time and temperature; b) Arrhenius-type representation based on gelation times at different temperatures. Gelation times were used as kinetic parameters to describe the rate of the sol-gel process (in sec).

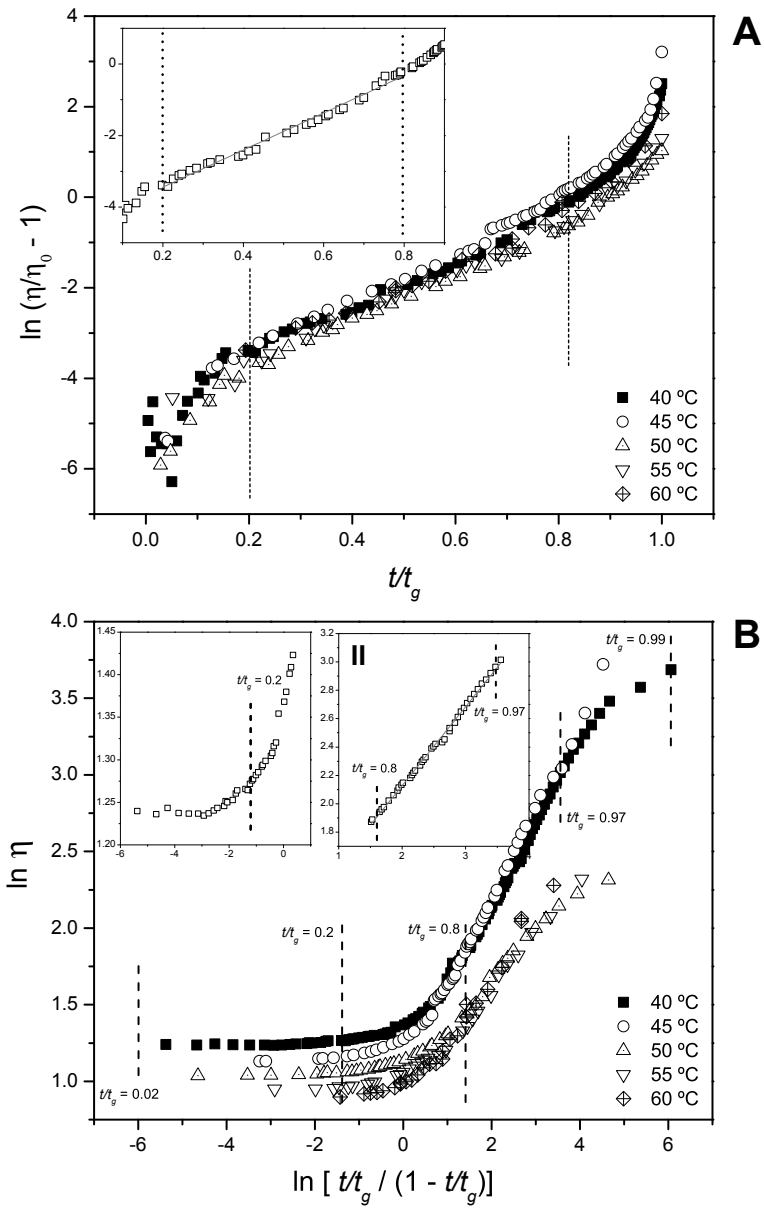

Figure 4.3. a) MFG model representation of viscosity of sol with $[H_2O]/[Ti] = 16.7$: $\ln(\eta/\eta_0 - 1)$ as a function of t/t_g at different temperatures. Inset presents measurement at 40 °C with a linear fit for $0.2 < t/t_g < 0.8$ (correlation coefficients $R^2 > 0.99$); b) NLG model representation: $\ln \eta$ as a function of $\ln[t/t_g/(1 - t/t_g)]$ at different temperatures. Inset I presents measurement at 40 °C for $t/t_g < 0.2$. Inset II represents the measurement at 40 °C with a linear fit in the range $0.8 < t/t_g < 0.97$ (correlation coefficient $R^2 > 0.99$).

4.4.2. Time-resolved SAXS of hydrolyzed barium titanate precursor sols

The structural evolution in 0.5 mol/dm^3 barium titanate precursor sols with varying hydrolysis ratios was monitored by SAXS at 60 °C for periods of 60 – 180 min. Time-resolved scattering curves of sols with hydrolysis ratios between 5.6 and 33 are shown in Figure 4.4A – D.

An example of fits of Equation (4.13) to experimental SAXS curves is presented in Figure 4.4E, where a sol with [H_2O]/[Ti] = 16.7 after 5 to 60 min of reaction is shown. Best fits of parameters characterizing all sols as a function of time are presented in Figures 4.5 – 4.7.

Figure 4.5A shows the evolution of r_0 as a function of time for several hydrolysis ratios. In all investigated sols this parameter increased slightly as the sol-gel reaction progressed and reached a plateau around the same value, independent of hydrolysis ratio. For the sol with [H_2O]/[Ti] = 5.6, growth of r_0 from 0.43 nm to 0.46 nm occurred during the first 20 min of the process. The general trends suggest that the primary particles that were formed were fairly identical in all systems.

Figure 4.5B depicts the evolution of D. For the sol with [H_2O]/[Ti] = 5.6, D could be accurately established from fitting routines after the 25th minute of the process. During the first 20 minutes, small agglomerates were formed, with D = 3 ± 1 (not shown here) within experimental error. After this first period the value of D decreased from 2.7 until it reached a constant value of 1.9 – 2.0. The first determinable values of D were smaller at higher hydrolysis ratios, with final values of 1.4 – 1.7 for [H_2O]/[Ti] = 16 – 33, after 30 min of reaction.

The evolution of the gyration radii of the fractal-like structures, calculated from ξ using Equation (4.6), are shown in Figure 4.5C. Since fractal-like structures were not formed yet, the first four data points in the plot of the sol with the lowest hydrolysis ratio were calculated using the Guinier approximation Equation (4.11). The scattering data of that sol are plotted as ln $I(q)$ vs. q^2 for $q < R_g^{-1}$, see the inset in Figure 4.5C. The radii of gyration increased from 0.6 nm up to a constant value of *ca.* 3.1 nm. In general, R_g increased with hydrolysis ratio. For [H_2O]/[Ti] = 25, R_g grew from *ca.* 1.8 nm to a constant value of 7.5 nm. In the sol with [H_2O]/[Ti] = 33 they grew from 3.3 nm to ~ 20 nm after 30 min. In the latter two sols a maximum in R_g, accompanied by an inflection point in the value of D, could be observed after approximately 30 min.

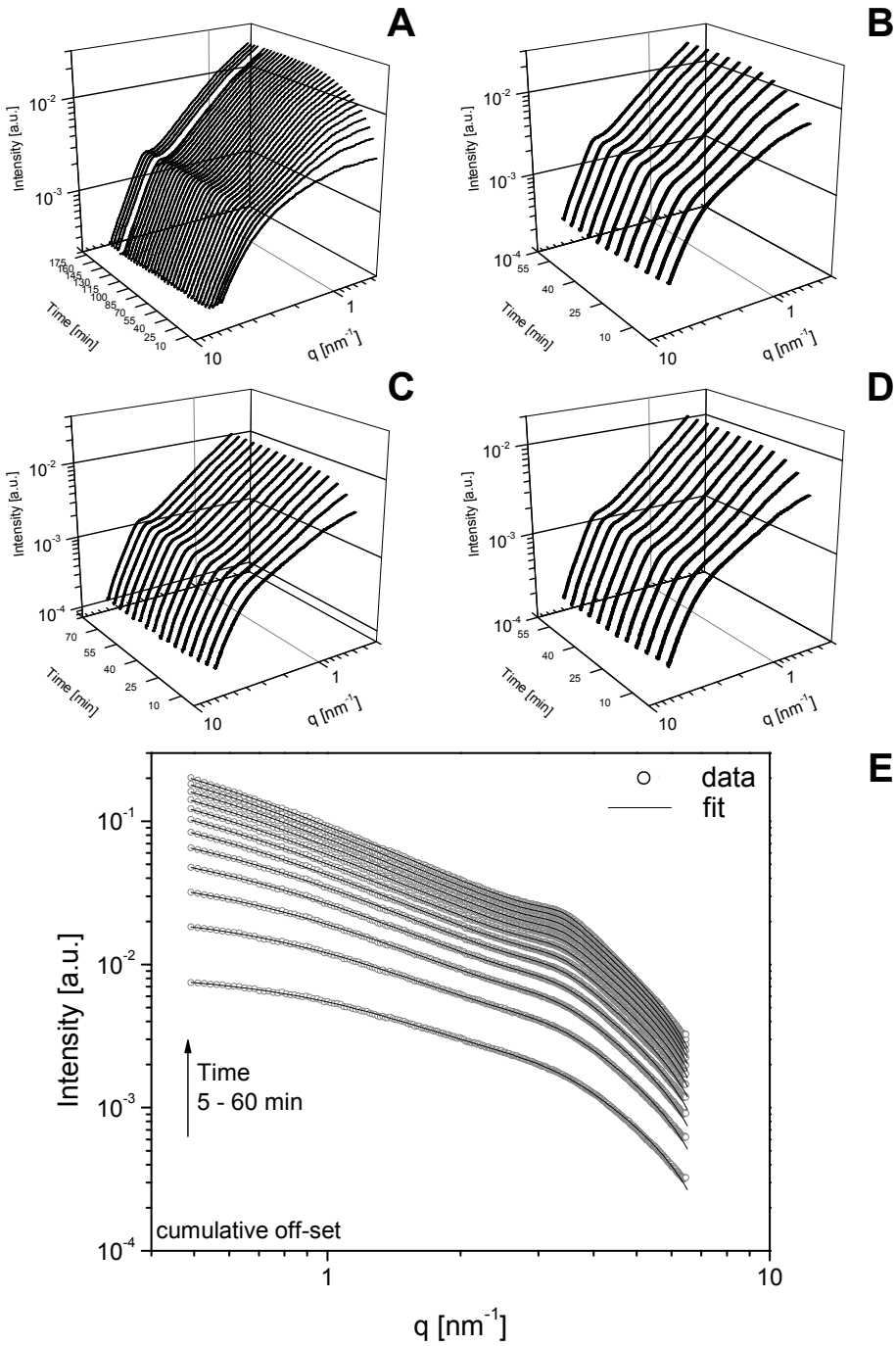

Figure 4.4. Time-resolved SAXS patterns at 60 °C, showing evolution of barium titanate precursor sols of initial 0.5 mol/dm^3 concentration with varying hydrolysis ratio. a) $[H_2O]/[Ti]$ = 5.6, b) $[H_2O]/[Ti]$ = 16.7, c) $[H_2O]/[Ti]$ = 25.0, d) $[H_2O]/[Ti]$ = 33.0. e) Scattering curves of sol with $[H_2O]/[Ti]$ = 16.7 with best fits based on Equation (4.13).

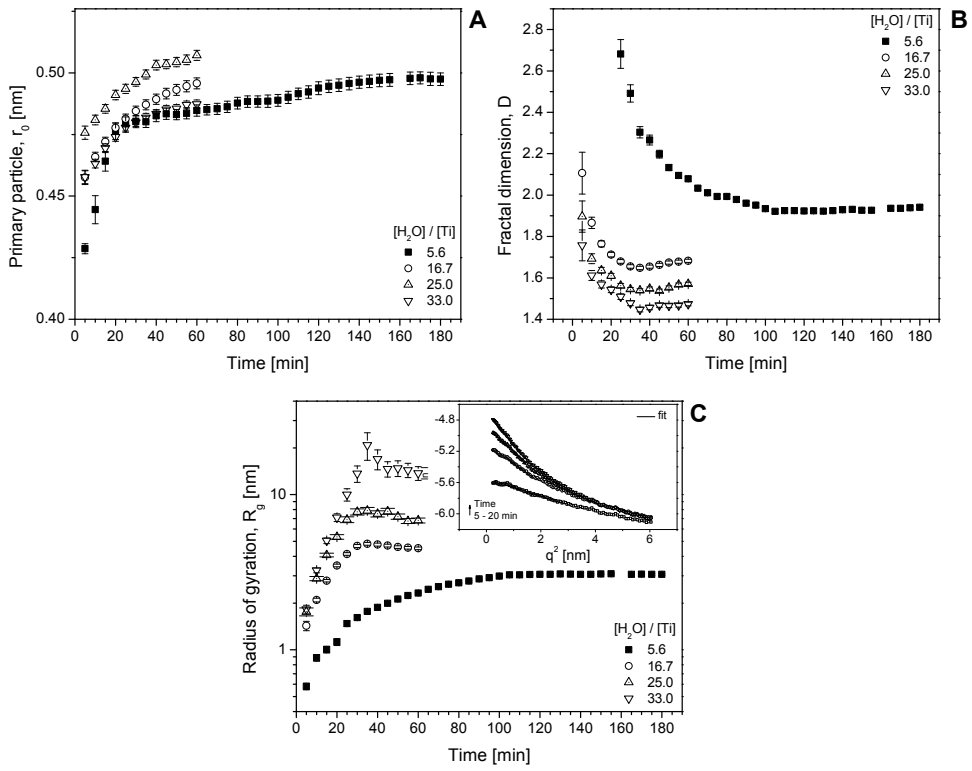

Figure 4.5. Fitted parameters from mass-fractal structure factor $S_F(q)$ and spherical form factor $P(q)$: a) primary particle radius, r_0; b) fractal dimension, D; c) radius of gyration, R_g; Inset shows scattering data for the first 20 minutes plotted as ln $I(q)$ vs. q^2 for $q < R_g^{-1}$.

Figure 4.6 shows the evolution of the parameters for correlation length and packing density in the structures with internal correlations. The development of this correlation is illustrated in detail in inset I of Figure 4.6A, where data of a BTO sol with $[H_2O]/[Ti]=16.7$ are shown. The structure factor manifested itself as a wide maximum around q_{max} = 3.3 nm^{-1}. This corresponds to a dimension of $2\pi/q_{max}$ = 1.9 nm in real space. The scattering maximum shifted to lower q-values as the system developed, indicating minimal growth. But the intensity of the correlation peak increased, which is indicative of an increasing degree of order in the structural feature from which the correlation originated. The hard-sphere diameter $2R_{HS}$ was 1.8 – 1.9 nm and increased only slightly (Figure 4.6A), while the average volume fraction of hard spheres ν at a distance $2R_{HS}$ around an arbitrary sphere (a measure for packing density) increased from 10% to 40% (Figure 4.6B).

Figure 4.7 depicts the evolution of parameters $N(\Delta\rho)^2$ and ε. The intensity factor related to the fractal-like structures is $\varepsilon N(\Delta\rho)^2$, and the intensity factor of the internally correlated structures is $(1-\varepsilon)N(\Delta\rho)^2$. Due to the fact that samples were measured in capillaries with slightly varying dimensions the intensity is shown in

arbitrary units. Absolute values of $N(\Delta\rho)^2$ can only be compared within a single time-resolved series of measurements, but general trends can be interpreted. For sols with $[H_2O]/[Ti] > 16$, the overall decrease of $N(\Delta\rho)^2$ was mainly due to the decrease of the contribution from internally correlated structures. The factor $\varepsilon N(\Delta\rho)^2$ remained fairly constant. Initially, $\varepsilon \sim 0.5$. Then, as the reaction progressed more than 70% of the total intensity pre-factor $N(\Delta\rho)^2$ was associated with fractal-like particles. For a sol with lower hydrolysis ratio, *i.e.* $[H_2O]/[Ti] = 5.6$, the same trend was observed, but slower, with an onset at $t = 25$ min. The scattering curve in the first 20 min can be fitted fairly well by the sphere form factor Equation (4.4), suggesting that the system consisted of isolated spherical primary particles in the earliest stage of development.

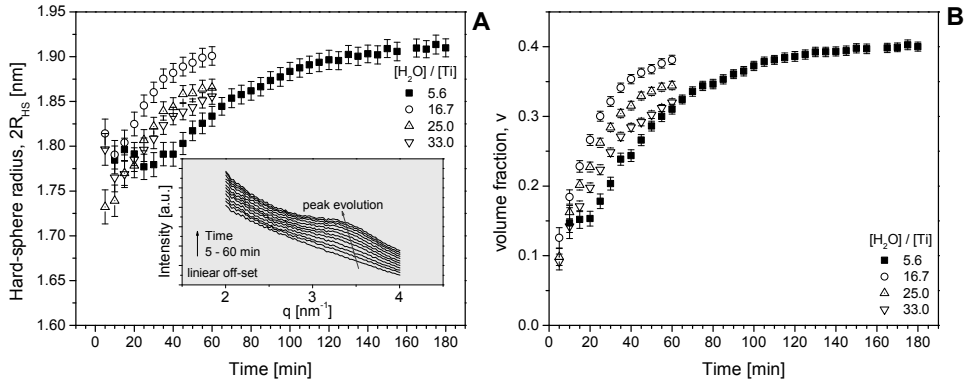

Figure 4.6. Fitted parameters from correlation structure factor $S_C(q)$: a) double hard-sphere radius $2R_{HS}$; inset: evolution of correlation peak in corresponding SAXS pattern; b) evolution of volume fraction, v.

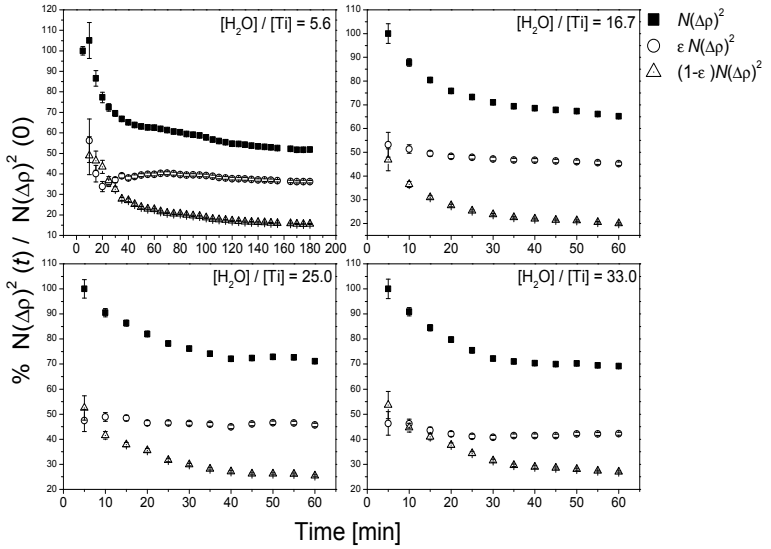

Figure 4.7. Evolution of $N(\Delta\rho)^2(t)$, contribution of mass fractal-like structures $\varepsilon N(\Delta\rho)^2(t)$, and contribution from internally correlated structures $(1-\varepsilon)N(\Delta\rho)^2(t)$. All values of $N(\Delta\rho)^2$ were normalized against $N(\Delta\rho)^2$ at $t = 5$ min of each of the investigated series.

4.4.3. Interpretation of data

The viscosity measurements indicated that oligomerization and gelation in the hydrolysed alkoxide-carboxylate precursor of barium titanate was strongly temperature-dependent, with apparent activation energy of 120 kJ/mol. The question arises with which process or structural feature one can associate this value. The rheological sol-gel transition of barium titanate sols prepared from titanium(IV) *iso*-propoxide in 2-methoxyethanol and barium hydroxide monohydrate in water and methanol also had an activation energy of 120 kJ/mol [34]. However, in that case neither acetic acid, nor barium acetate were used, and gelation occurred at high pH rather than in an acidic medium as in this study. An activation energy of 120 kJ/mol was also measured during the gelation of a TiO_2 system derived from titanium(IV) *n*-butoxide stabilized with acetylacetone in *n*-butanol [35], and was found to be independent of hydrolysis ratio. Such values of E_a are relatively high. For instance, the activation energy of the sol-to-gel transition of hydrolytic silicate systems is in the range between 40 and 80 kJ/mol [39], whereas in non-hydrolytic alumina gels it is 80 – 105 kJ/mol [39]. The value that was found in the present study seems to be associated with the condensation of the Ti precursor, as is similar to the activation energy of pure titanium(IV) *n*-butoxide.

The analysis showed that the structural evolution of the BTO sol could be divided into three periods: (i) $t/t_g < 0.2$, where neither MFG, nor NLG could be applied. SAXS measurements showed the presence of only small isolated primary particles in this period; (ii) $0.2 < t/t_g < 0.8$, where mass fractal-like structures, composed of primary particles, were formed. The SAXS data showed that besides fractal-like structures also other structures with internal correlations were present, in particular from the early stages of sol development in stage (ii); (iii) $0.8 < t/t_g < 0.97$, where higher order clustering effects, probably cluster-cluster aggregation of the mass fractal-like structures into a larger scale 3D gel network occurred.

The primary particles formed in stage (i) were spherical in shape and had a radius of 0.45 – 0.50 nm. Similar structural motifs have been observed in a number of titania-related gelling systems [41-44]. Titanium(IV) alkoxide-derived clusters, synthesized in reactions with carboxylic acids, are known to yield various geometrical shapes depending on the molar ratio [O]/[Ti] per cluster [44]. For [O]/[Ti] = 1.0, two cluster geometries are known: hexaprismane and octacyclane [44-47]. The latter is a ring structure, built of eight coordination octahedra. Hexaprismane is usually formed in the presence of highly acidic ligands, and has an inorganic core $Ti_6(\mu_3\text{-}O)_6$. The diameter of the inorganic core is 0.46 nm, roughly two times smaller than the diameter of the primary scatterers. Larger spherical titanium oxoalkoxide clusters with inorganic cores $Ti_{12}O_{16}$, $Ti_{17}O_{24}$, and $Ti_{18}O_{27}$ are known to form in acetic acid at elevated temperatures [48]. The minor size changes of r_0 observed in my experiments could be attributed to evolution of the ligand

environment around the core, and/or variations in [O]/[Ti]. It is noted that the outer organic ligand shell surrounding an inorganic core is not directly visible by SAXS, because its local electron density is too similar to the electron density of the surrounding solvent phase. The diameter of the cluster including outer shell is therefore larger than r_0.

Acetic acid acts as a key chelating agent and its presence suggests the formation of titanium acetates and/or titanium (oxo)alkoxyacetates due to (partial) exchange of alkoxy ligands by acetate. Ti alkoxides in an excess of acetic acid formed a water-soluble precipitate with stoichiometry $TiO(CH_3COO)_2$ at $[CH_3COOH]/[Ti] > 5$, as invetsigated by NMR, FTIR and EXAFS [49]. The coordination number of Ti in the precipitate was 6, all alkoxy groups were removed, and acetate ligands were found in the bridging positions. The clusters were oligomeric in nature, and Ti-Ti correlations of 3.12 Å were shown by EXAFS. The chemical composition of the precipitated product was independent of alkoxy group. On the other hand, it is known that complexation of Ti-alkoxides by carboxylates is disadvantageous at elevated temperatures because practically all acid involved in the reaction is transformed into esters and water [48]. This shows that no straight-forward conclusions can be drawn on the structure of Ti-oxoclusters based only on reaction conditions.

Simple mixing experiments showed that titanium *iso*-propoxide in 2-methoxyethanol indeed formed a precipitate in an excess of acetic acid when no external water was added. However, in the presence of barium acetate, precipitation occured after an approximately ten times longer period than when barium was absent. When water was also added to the system no precipitation occured, but gelation was observed instead, as SAXS and viscosity measurements showed. Apparently, the as-formed titanium (oxo)alkoxyacetate clusters [49] were hydrolyzed by water and condensed into a gel. These observations show that the presence of barium ions somehow influences the reaction scheme between alkoxide and acetate ligands in Ti-based clusters and oligomers, suppressing the rapid formation of Ti-based precipitates. The SAXS data provide no indication that Ba ions are structurally associated with as-formed Ti-clusters, and it is indeed known that barium ions do not easily participate in coordination complexes. But the interaction could also be indirect. For instance, the presence of divalent barium ions affects the ionic strength of the solution significantly, and this influences the screening of charges in solution, thereby chaning the ionic interactions and reactivity of charged species present in solutions. However, it is stressed that several alternative explanations between which one cannot discriminate based on the current experimental evidence are also possible.

The evolution of D and R_g in the fractal-like structures in stage (ii) was clearly dependent on hydrolysis ratio. Lower ratios yielded smaller agglomerates with higher D. The obtained values of D and R_g are typical for various TiO_2 gelling precursor systems [43,50,51]. Most likely, branched oligomers are the actual structures in

solution that yield scattering patterns that can be described best in terms of a fractal structure. They are composed of the type of primary scatterers discussed above. As can be seen in Figure 4.4B and 4.4C, R_g reached a maximum and D a minimum value after ~ 30 min. After that D increased slightly, and R_g decreased. Although it cannot be ruled out completely that the trend is influenced to a small degree by the increasing error in the determination of ξ, it is plausible that it presents an actual physical process. Possibly, it is an effect of syneresis, a process in which a polymeric particle or network contracts spontaneously under the influence of ongoing condensation, thereby expelling liquid from the spaces between the polymer segments [52]. Syneresis is expected to result in smaller particles with a higher D value, in agreement with the experimental data for the highest hydrolysis ratios. An alternative explanation is that the fractal-like Ti-based oligomers, which form relatively low-density structures at high hydrolysis ratios, merge with each other at this point, leading to reconfiguration and compaction of these structures. Since the factor $\varepsilon N(\Delta\rho)^2$ remained more or less constant in time for all investigated samples, the change of N and $\Delta\rho$ over the course of reaction was probably negligible.

For the structures with internal correlations, it was found that the hard-core radius R_{HS} hardly increased, but the volume fraction ν increased by a factor of ~4. This means that the primary hard sphere scatterers remained constant in size, but they reorganized in the course of the process, increasing their internal degree of packing considerably. The hard sphere radius R_{HS} was ~0.9 nm, and is based on the mutual spacing between scattering entities. Since, I think that these hard sphere scatterers have the same physical origin as the primary scatterers in the fractal-like structures, where r_0 = 0.45 nm, this means that the outer organic ligand shell has an estimated thickness $R_{HS} - r_0$ ~ 0.45 nm. So the internally correlated structures are probably ordered agglomerates of Ti-based clusters. Given the fact that the experimental correlation peak in the SAXS patterns had a distinct maximum, it seems that these Ti-based clusters must be very similar in size. The overall size of these ordered agglomerates cannot be determined from the experimental data. They must be smaller than the wavelength of visible light, because the solutions were completely transparent in the visible range. The contribution of these structures to the total x-ray scattering intensity of the system decreased in the course of reaction, as expressed by the factor $(1-\varepsilon)N(\Delta\rho)^2$ in Figure 4.7. The effect is most likely related to a decrease of scattering contrast $\Delta\rho$, possibly due to the increased packing density observed in these species.

The evolution of $\varepsilon N(\Delta\rho)^2(t)$ and $(1-\varepsilon)N(\Delta\rho)^2(t)$ showed that both fractal-like structures and structures with internal correlations had already formed at the beginning of stage (ii). In my model, I assume that these structures are constructed from the same primary particles. Hence, a common form factor $P(q)$ was used. I found that the radii r_0 of these primary scatterers increased by about 10% in the

course of the experiment. The model does not include scattering interactions between fractal-like structures and internally correlated structures, *i.e.* interactions between branched titania oligomers and packed agglomerates. Attempts to fit the experimental data with a model that included such effects were not successful. Hence, it is concluded that these two types of structures do not interact physically on the agglomerate level. Probably they are located in spatially different regions of the sol.

4.5. Conclusions

The BTO precursor sols investigated here consisted of titanium-based oligomeric structures and Ti-based agglomerates of nanoparticles of similar size. Barium remained dissolved in acetic acid, and was seen to suppress rapid formation of a titanium-rich precipitate from solution. The structural evolution of the titania nanostructures could monitored by SAXS and viscosity measurements, and involved three phases: (i) formation of isolated primary scatterers and very small agglomerates of such scatterers (induction), (ii) growth of branched oligomeric mass fractal-like structures, in parallel to agglomerates of primary scatterers of very similar constant size that increase their packing density, and (iii) gelation. The contribution to the total scattering intensity of the non-fractal-like agglomerates decreased in the course of stage (ii) to less than 20%, so the gelation process occured mainly due to the aggregation of fractal-like oligomers. The microstructure of these fractal-like titania oligomers depended on hydrolysis conditions. The overall scheme of the sol-gel process based on the SAXS and viscosity data presented in this chapter is shown in Figure 4.8.

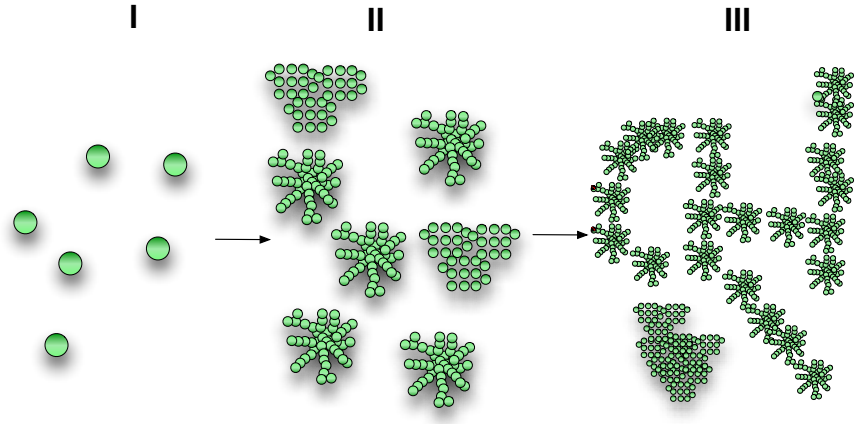

Figure 4.8. Schematic representation of the sol-gel process of BTO precursor sols. i) induction stage: formation monodisperse spherical primary particles with an inorganic core diameter $2r_0$ = 0.9 nm, and an outer organic ligand shell of ~0.45 nm thickness ($R_{HS} - r_0$); ii) Growth of branched oligomeric structures, and increasing packing density in agglomerates of titania nanoparticles of very similar size; iii) Cluster-cluster aggregation of fractal-like titania oligomers into 3D macroscopic gel of low density, in which each constituent titania oligomer has a limited number of direct neighbours, *i.e.* just above 2 on average.

4.6. References

[1] Yoon, D. *J. Ceram. Proc. Res., 7*, 343-354, **2006**.

[2] Pithan, C.; Hennings, D. H.; Waser, R. *Int. J. Appl. Ceram. Technol., 2*, 1-14, **2005**.

[3] Phule, P. P.; Risbud, S. H. *J. Mater. Sci.*, 25, 1169-1183, **1990**.

[4] Schwartz, R. W.; Schneller, T. S.; Waser, R. *C. R. Chimie, 7*, 433-461, **2004**.

[5] Schwartz, R. W.; Narayanan, M. Chemical Solution Deposition - Basic Principles, In *Solution Processing of Inorganic Materials*, ed. Mitzi, D. B., John Wiley & Sons, Inc., New Jersey, 33-76, **2009**.

[6] Huffman, M. *Integr. Ferroelectrics,* 10, 39-53, **1995**.

[7] Phule, P. P.; Risbud, S. H. *Adv. Ceram. Mater.,* 3, 183-185, **1988**.

[8] Schwartz, R. W. *Chem. Mater.*, 9, 2325-2340, **1997**.

[9] Schwartz, R. W.; Boyle, T. J.; Lockwood, S. J.; Sinclair, M. B.; Dimos, D.; Buchheit, C. *Integr. Ferroelectrics*, *7*, 259-277, **1995**.

[10] Yi, G.; Sayer, M. *Ceram. Bull.*, 70, 1173-1179, **1991**.

[11] Assink, R. A.; Schwartz, R. W. *Chem. Mater.*, 5, 511-517, **1993**.

[12] Hasenkox, U.; Hoffmann, S.; Waser, R. *J. Sol-Gel Sci. Technol.*, 12, 67-79, **1995.**

[13] Hoffmann, S.; Waser, R. *J. Eur. Ceram. Soc.,*19, 1339-1343, **1999**.

[14] Frey, M. H.; Payne, D. A. *Chem. Mater., 7*, 123-129, **1995**.

[15] Hennings, D.; Rosenstein, G.; Schreinemacher, H. *J. Eur. Ceram. Soc.,* 8, 107-115, **1991**.

[16] Bras, W.; Dolbnya, I.P.; Detollenaere, D.; van Tol, R.; Malfois, M.; Greaves, G. N.; Ryan, A. J.; Heeley, E. *J. Appl. Crystallogr.,* 36, 791-794, **2003**.

[17] Guinier, A.; Fournet, G. Small Angle Scattering of X-rays, John Wiley & Sons Inc, New York, **1955**.

[18] Kratky, O. A Survey In *Small Angle X-ray Scattering*, ed. Glatter, O.; Kratky, O. Academic Press, London, 3-13, **1982**.

[19] Porod, G. General theory In *Small Angle X-ray Scattering*, ed. Glatter, O.; Kratky, O. Academic Press, London, 17-52, **1982**.

[20] Craievich, A.F. *Mater. Res.,* 5, 1-11, **2002**.

[21] Pedersen, J. S. *Adv. Colloid Interface Sci.,* 70, 171-210, **1997**.

[22] Squires, G. L. Introduction to the Theory of Thermal Neutron Scattering, Cambridge University Press, **1978.**

[23] Sorensen, C. M. *Aerosol Sci. Technol.,* 35, 648-687, **2001**.

[24] Teixeira, J. *J. Appl. Cryst.,* 21, 781-785, **1998**.

[25] Freltoft, T.; Kjems, J. K.; Sinha, S. K. *Phys. Rev. B*, 33, 269-275, **1986**.

[26] Berry, M. V.; Percival, I. C. *Opt. Acta,* 33, 577-591, **1986**.

[27] Pontoni, D.; Narayanan, T.; Petit, J. -M.; Grübel, G.; Beysens, D. *Phys. Rev. Lett,* 90, 188301, **2003**.

[28] Percus, J. K.; Yevick, G. J. *Phys. Rev.* 110, 1-13, **1958.**
[29] Vrij, A. *J. Chem. Phys.*, 71, 3267-3270, **1979**.
[30] Baxter, R. J. *J. Chem. Phys.*, 49, 2770-2774, **1968**.
[31] Levenberg, K. *Q. Appl. Math.,* 2, 164–168, **1944**.
[32] Marquardt, D. *SIAM J. Appl. Math.,* 11, 431–444, **1963**.
[33] Pope, E. J. A.; Mackenzie, J. D. *J. Non-Cryst. Solids*,101, 198-212, **1998**.
[34] Brasseur, A.; Michaux, B.; Pirard, R.; Cantfort van, O.; Pirard, J. P.; Lecloux, A. J. *J. Sol-Gel Sci. Technol.*, 9, 5-15, **1997**.
[35] Ponton A.; Barboux-Doeuff, S.; Sanchez, C. *Colloids Surf. A*, 162, 177-192, **2000**.
[36] Flory, P. J. *J. Am. Chem. Soc.*, 65, 372-382, **1943**.
[37] Bechtold, M. F.; Vest, R. D.; Plambeck, Jr., L. *J. Am. Chem. Soc.*, 90, 4590-4598, **1968**.
[38] Bechtold, M. F.; Mahler, W.; Schunn, R. A. *J. Polym. Sci. Poly. Chem.*, 18, 2823-2855, **1980**.
[39] Scherer, G. W. *J. Ceram. Soc. Jpn.,* 95, 21-44, **1987**.
[40] Grader, G. S.; Hazan, de, Y.; Cohen, Y.; Bravo-Zhivotovskii, D. *J. Sol-Gel Sci. Technol.*, 10, 5-12, **1997**.
[41] Jalava, J. -H.; Hiltunen, E.; Kähkönen, H.; Erkkilä, H.; Härmä, H.; Taavitsainen, V. -M. *Ind. Eng. Chem. Res.*, 39, 349-361, **2000**.
[42] Torma, V.; Peterlik, H.; Bauer, U.; Rupp, W.; Husing, N.; Bernstorff, S.; Steinhart, M.; Goerigk, G.; Schubert, U. *Chem. Mater.*, 17, 3146-3153, **2005**.
[43] Pattier, B.; Henderson, M.; Brotons, G.; Gibaud, A. *J. Phys. Chem. B,* 114, 5227-5232, **2010**.
[44] Rammal, A.; Brisach, F.; Henry, M. *C. R. Chimie*, 5, 59-66. **2002**.
[45] Papiernik, R.; Hubert-Pfalzgraf, L. G.; Vaissermann, J.; Heriques Baptista Goncalves, M. C. *J. Chem. Soc., Dalton Trans.*, 14, 2285-2287, **1998**.
[46] Sui, R.; Charpentier, A. S.; Rizkalla, A. S.; Jennings, M. C. *Acta Cryst.*, E62, m373-m375, **2006**.
[47] Boyle, T. J.; Alam, T. M.; Tafoya, C. J.; Scott, B. L. *Inorg. Chem.*, 37, 5588-5594, **1998**.
[48] Rozes, L.; Sanchez, C. *Chem. Soc. Rev.*, 40, 1006-1030, **2011**.
[49] Doeuff, S.; Henry, M.; Sanchez, C. *Mat. Res. Bull.*, 25, 1519-1529, **1990**.
[50] Kamiyama, T.; Mikami, M.; Suzuki, K. *J. Non-Cryst. Solids,* 150, 157-162, **1992**.
[51] Blanchard, J.; Ribot F.; Sanchez, C.; Bellot, P. –V.; Trokiner, A. *J. Non-Cryst. Solids,* 265, 83-97, **2000**.
[52] Brinker, C. J.; Scherer, G. W. Sol-gel science: The Physics and Chemistry of Sol-Gel Processing, Academic Press, **1990**.

5

Nanostructure Development in Alkoxide-Carboxylate-Derived Precursor Films of Barium Titanate*

Abstract

The structural evolution in wet alkoxide-carboxylate sol-gel precursor films of barium titanate upon drying was investigated by time-resolved small angle x-ray scattering (SAXS). The morphology of as-dried amorphous precursor thin films was investigated by transmission electron microscopy (TEM) and electron energy loss spectroscopy (EELS). Sols were prepared from titanium(IV) *iso*-propoxide in 2-methoxyethanol and barium acetate in acetic acid. The structures that were visible with SAXS could be divided into oligomeric structures with fractal-like scattering characteristics, and randomly packed agglomerates of nanoparticles of similar size. The fractal-like morphologies disappeared during film drying, probably because they were not stable in the absence of a solvent matrix. Only the ordered agglomerate-like structures remained in the as-dried films. EELS on as-dried films showed that spatial separation between barium and titanium-rich domains occurred during the drying of the thin films on a length scale of nanometers, depending on hydrolysis ratio. This demonstrates that as-dried films are not necessarily uniform on the mesoscopic level.

5.1. Introduction

Barium titanate ($BaTiO_3$) is a high-*k* dielectric material used in commercial multi-layer ceramic capacitors. The minimum $BaTiO_3$ layer thickness that can be achieved with state of the art tape casting methods is about 1 μm. Barium titanate is used in crystalline form, which implies the use of starting powders with a particle size of *ca.* 200 nm [1]. Further reduction of the barium titanate layer thickness requires finer powders obtained by new synthesis and deposition techniques. One of the feasible alternatives is the deposition of amorphous precursors of barium titanate and their

* In preparation:
Stawski, T. M.; Veldhuis, S. A.; Besselink, R.; Castricum, H. L.; Portale, G.; Blank, D. H. A.; ten Elshof, J. E.

further reaction and crystallization to a perovskite phase [2]. Good control and understanding of the process in all stages is required to obtain a film with the desired electrical and morphological properties. This can be achieved by wet-chemical processing methods.

Wet-chemical methods provide nanometer-sized powders (5 – 100 nm) of high purity and homogeneity, and of adjustable composition, as near-atomic level mixing of components is possible [3]. Among these methods the sol-gel process, in particular the alkoxide-carboxylate synthesis, the double alkoxide synthesis, the micro-emulsion synthesis, and the precipitation methods (alkoxide-hydroxide sol precipitation) have received much attention [3]. As the sol-gel process is based on liquid precursors, direct deposition of precursor thin films onto substrates by means of spin-casting, deep-casting or misted source deposition, followed by pyrolysis and crystallization is possible [2,4,5]. The alkoxide-carboxylate route has been employed widely for $BaTiO_3$ synthesis since the first reports [6]. Barium titanate xerogels were synthesized from titanium(IV) *iso*-propoxide in *iso*-propanol and barium acetate dissolved in acetic acid. Acetic acid was used as a solvent enabling the complete dissolution of barium acetate. Acetic acid is also known to chelate metal centers in alkoxides, leading to the formation of oligomeric metal oxoacetates [3,4,7]. Therefore the alkoxide-carboxylate process is often referred to as a hybrid process, because it combines a classical sol-gel precursor (metal alkoxide) with a non-sol-gel precursor (metal carboxylate) [2,4].

The influence of precursor chemistry and processing conditions on the morphology of crystalline thin films processed from the hybrid process was investigated [8,9]. Use of acetic acid or propionic acid favored the growth or larger grains and yielded higher density films in comparison with films synthesized from longer carboxylic acid based precursors. The difference was attributed to the higher pyrolysis temperature of the system containing the shorter carboxylic acid, which led to the formation of the transition oxocarbonate phase $Ba_2Ti_2O_5CO_2$ [3,10]. Crystallization occurred at higher temperatures, which led to increased film density and larger grains. The morphology of crystalline $(Ba,Sr)TiO_3$ and $BaTiO_3$ films derived from the alkoxide-carboxylate route could be also modified [9]. When the sol concentration was sufficiently low, columnar grains formed, provided that the films were deposited in a number of steps and crystallized after each deposition step. Above a certain threshold concentration a granular morphology was observed. The stabilization of titanium alkoxide precursors is believed to play an important role here, as it can modify the hydrolysis and condensation pathways. For instance, stabilization of titanium alkoxide with acetylacetone resulted in denser films with larger grain sizes and better dielectric properties [2,8]. This was attributed to the monomeric character of the titanium precursor and the homogenous mixing of Ti and Ba precursors on the nanometer scale. It was hypothesized that in the case of non-stabilized solutions, an oligomeric

TiO_x phase might form, and the extent of phase formation would depend on the extent of Ti alkoxide oligomerization. The structure of such an alkoxide-carboxylate gel was proposed by Hennings *et al.* [11], based on transmission electron microscopy (TEM), energy dispersive spectroscopy (EDS), and infrared spectroscopy (FT-IR) analysis. Metal carboxylate species were assumed to adsorb on the surface of the titanium oxoacetate polymer. The separation between Ti-rich and Ba-rich regions exceeded 100 nm.

Relatively few details are known on the kinetics and morphology of barium titanate alkoxide-carboxylate precursors upon reaction and physical drying. In Chapter 4 and in ref [12], I reported the structural evolution of hydrolyzed sols by small angle x-ray scattering (SAXS) and viscosity measurements. The results suggested that both fractal-like and agglomerate-like structures were present in solution. The primary scatterers from which these structures were formed were Ti-based, and consisted of small spherical primary particles of very similar size. The majority species after reaction in constant volume were fractal-like structures.

However, for sol-gel processing of thin films the drying stage of the sol is also very interesting. Due to the fact that volatile components of the system evaporate, the actual precursor concentration increases rapidly, yielding fast sol-gel transitions in the final stages of physical drying. It was the aim of this work to monitor the structural evolution in wet thin films from model solutions of titanium alkoxide and barium acetate in acetic acid during the drying process. I employed time-resolved small-angle x-ray scattering (SAXS) to study the structural characteristics of drying films. I used transmission electron microscopy (TEM), and electron energy loss spectroscopy (EELS) for the characterization of as-deposited precursor films.

5.2. Experimental

5.2.1. Synthesis of barium titanate (BTO) precursor sols

Barium acetate (> 99%, Riedel-deHaën) and titanium(IV) *iso*-propoxide (99.999%, Sigma-Aldrich) were used as precursor materials. Glacial acetic acid (99.8%, Acros) and 2-methoxyethanol (> 99.3%, Sigma-Aldrich) were used as solvents, stabilizers, and chelating agents. Two stock solutions were made. A Ba-acetate solution was prepared by dissolving barium acetate in acetic acid and subsequent refluxing at 105 °C for 8 h to remove all remaining water. The final concentration was adjusted to 1.0 mol/dm^3. The second stock solution was based on titanium *iso*-propoxide with 2-methoxyethanol as solvent yielding a precursor of 1.0 mol/dm^3. It was stirred in a glove box under nitrogen atmosphere. Both stock solutions were stirred at room temperature for 24 h. They were then stored at room temperature. Prior to the experiments, the stock solutions were mixed in 1 : 1 molar

ratios and stirred for 5 minutes, yielding a concentration of 0.50 mol/dm^3 in the final BTO precursor solution. Solutions of this concentration were used in all experiments. Hydrolysis was initiated by addition of water immediately after the two stock solutions had been mixed and stirred. The hydrolysis ratio h was defined as:

$$h = [H_2O]/[Ti] \quad (5.1)$$

5.2.2. Transmission Electron Microscopy (TEM) and Electron Energy Loss Spectroscopy (EELS)

BTO precursor sols with h = 0.0, 2.8, 5.6, and 33, respectively, were spin-casted (Laurell WS-400B-6NPP-Lite spincoater) onto holey carbon TEM copper grids (CF200-Cu, Electron Microscopy Sciences) at 4000 rpm for 40 s. The as-prepared films were dried at 60 °C for 1 h on a hot-stage and used for transmission electron microscopy (TEM) characterisation (Philips CM300ST-FEG at 300 kV).

Features of interest were examined at high magnification (GATAN 2k x 2k Ultrascan1000 CCD camera). Energy filtered images (GATAN model Tridiem with 2k x 2k CCD camera) were recorded at the highest possible magnification that still provided stable images, with negligible or compensable drift using the 3-windows method for Ba-$M_{4,5}$ (pre-edge 716 eV, post-edge 801 eV, slit width 40 eV, 10 s exposure) and Ti-$L_{2,3}$ (pre-edge 406 eV, post-edge 481 eV, slit width 30 eV, 10 s exposure). Colour mix maps juxtapositioning selected combinations of elements were manually corrected for drift depending on the element, using the microscope GMS software package.

5.2.3. Time-resolved Small Angle X-ray Scattering (SAXS) of drying BTO films

In SAXS experiments elastic scattering of x-rays by a sample that has local electronic density fluctuations is recorded at very small angles [13-16]. The scattering intensity $I(\boldsymbol{q})$ is recorded versus the modulus of the scattering vector $\boldsymbol{q}$ (nm^{-1}), which is related to the scattering angle 2θ and the wavelength λ (nm) of the incident beam via

$$q = 4\pi / \lambda \sin\theta \quad (5.2)$$

SAXS experiments were performed on the Dutch-Belgian beamline (DUBBLE) BM-26B of the ESRF in Grenoble, France [17]. The beam was focused at the corner of a 2D gas-filled multi-wire detector in order to maximize the range of accessible q values (scattering vector values). The beam energy was 16 keV (λ = 0.0776 nm). The samples were placed at a distance of 1.5 m away from the detector. Structural information on particles with dimensions up to 50 nm can be derived from the investigated angular range, $0.13 < q < 9.00$ nm^{-1} [13-16]. The raw data were corrected for the pixel-dependent detector sensitivity and integrated for channels with the same q values using a matlab/fit2d routine available at BM-26B.

The setup that was used to follow the evolution of drying thin films is schematically illustrated in Figure 5.1. BTO sols were contained in a Kapton foil that was mounted on an aluminium rotor head with a diameter of *ca.* 11 cm. The rotation speed was 100 rpm, ensuring a homogenous distribution of liquid film over the surface of the Kapton foil. The rotation axis was not completely perpendicular to the incoming x-ray beam, as illustrated in Figure 5.1. This allowed detection of the scattered x-ray beam. Time-resolved SAXS patterns of drying BTO thin films with hydrolysis ratio h = 0.0, 5.6, and 33.0 were recorded at 60 °C over a period up to 60 min. The scattering intensity of the empty chamber background, *i.e.* Kapton foil under the same conditions, was subtracted in order to achieve the background correction.

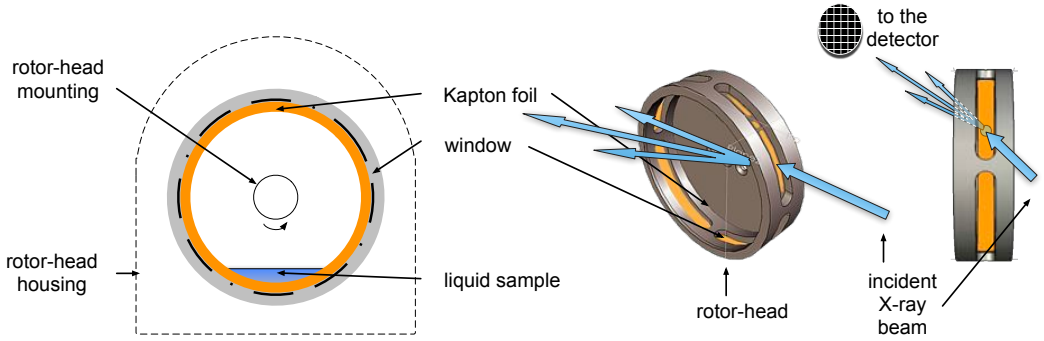

Figure 5.1. Schematic of the setup used for *in situ* x-ray scattering measurements of drying of precursor thin films from liquid precursors.

5.3. Small angle x-ray scattering data interpretation

The scattered intensity $I(q)$ from the dilute system of non-interacting, monodisperse, homogenous spherical particles of number density N, with electron density difference between the particles and the surrounding medium (scattering contrast) $\Delta\rho$ and particle volume V can be expressed by Equation (5.3), where $P(q)$ is the form factor. V can be incorporated into the form factor.

$$I(q) = N(\Delta\rho)^2 V^2 F^2(q, r_0) = N(\Delta\rho)^2 \left(V 3 \frac{\sin(qr_0) - qr_0 \cos(qr_0)}{(qr_0)^3} \right)^2 = N(\Delta\rho)^2 P(q, r_0) \qquad (5.3)$$

Equation (5.3) is insufficient to describe sysems with higher concentrations of particles, as it neglects the interference between species [19]. These can be included by introducing a structure factor, $S(q)$. Assuming an isotropic interactions and particle shapes in a monodisperse system [13,18-22], the scattered intensity takes the general form:

$$I(q) = N(\Delta\rho)^2 P(q) S(q) \qquad (5.4)$$

Let us assume that the primary particles cluster together and form larger polymer-like structures with a substantial degree of branching. Such a system can be described in terms of the well-established mass-fractal models [19-22]. Here, a fractal-like agglomerate is defined as an object whose radius of gyration R_g is related to the number of primary particles n building the agglomerate via Equation (5.5) [19-22]:

$$n = k_0 \left(\frac{R_g}{r_0} \right)^D \tag{5.5}$$

Here D is the fractal dimension of the agglomerate, r_0 is the radius of primary particles forming agglomerates, and k_0 is a constant. The value of k_0 can be estimated by assuming an isolated particle, where n = 1, as explained in ref [19]. For spheres the relationship $R_g = (3/5)^{1/2} r_0$ holds thus, $k_0 = (5/3)^{D/2}$. Equation (5.5) presents a mathematical definition that does not the require self-similarity over a range of length scales as is required for mathematical fractal structures [23]. The parameter D can therefore not be interpreted as a true dimensionality, but rather as a fit parameter that relates the mass of an agglomerate, *i.e.,* number of particles, to its radius of gyration via Equation (5.5). The parameter D is a measure of the density of the fractal-like structure, although the structures that can be described in terms of this formalism do not have to resemble true fractals.

In the case of finite structures described by fractal concepts a cut-off distance, ξ, is introduced. This parameter is often interpreted as a characteristic length above which the mass distribution in the structure no longer follows Equation (5.5), for instance at distances outside the perimeter of the fractal-like structure. The structure factor of such mass-fractal agglomerates is expressed by Equation (5.6) [20-22]:

$$S_F(q) = 1 + \frac{D\Gamma(D-1)\sin\left[(D-1)\arctan(q\xi)\right]}{(qr_0)^D \left(1 + q^{-2}\xi^{-2}\right)^{(D-1)/2}} \tag{5.6}$$

The radius of gyration R_g of a fractal-like structure is related to cut-off distance ξ by Equation (5.7) [20-22]:

$$R_g^2 = D(D+1)\xi^2 / 2 \tag{5.7}$$

The mass-fractal structure factor is valid when $r_0 << \xi$. Very small structures, typically formed at the start of a sol-gel reaction [12], cannot be described well with this model due to their limited size.

Systems composed of spherical primary particles may not only form fractal-like structures, but also more ordered non-fractal-like correlated structures. Interaction of spherical randomly packed particles can be expressed in terms of a hard-sphere

radius R_{HS} and a volume fraction ν. The degree of ordering of particles, located at a distance $2R_{HS}$ from another particle depends on the volume fraction. Based on the Percus-Yevick approximation, the structure factor describing such an interaction is given by Equation (5.8) [24-26].

$$S_C(q) = \frac{1}{1 + 24\nu G(2qR_{HS})/(2qR_{HS})} \tag{5.8}$$

$$G(2qR_{HS}) = \alpha \frac{\sin(2qR_{HS}) - (2qR_{HS})\cos(2qR_{HS})}{(2qR_{HS})^2} + \beta \frac{2(2qR_{HS})\sin(2qR_{HS}) + (2 - (2qR_{HS})^2)\cos(2qR_{HS}) - 2}{(2qR_{HS})^3} + \gamma \frac{-(2qR_{HS})^4 \cos(2qR_{HS}) + 4\left[3(2qR_{HS})^2 - 6\right]\cos(2qR_{HS}) + 4\left[(2qR_{HS})^3 - 6(2qR_{HS})\right]\sin(2qR_{HS}) + 24}{(2qR_{HS})^5}$$

$$\alpha = (1 + 2\nu)^2/(1-\nu)^4$$

$$\beta = -6\nu(1 + \nu/2)^2/(1-\nu)^4$$

$$\gamma = \nu\alpha/2$$

The investigated system is initially composed of non-agglomerated, monodisperse, spherical particles, which are formed upon hydrolysis. As the system evolves, mass-fractal-like structures, characterized by a fractal dimension D and cut-off distance ξ, start to form. But structures with internal correlations are also formed in parallel, and they are derived from the same spherical primary particles [12]. The two types of structures evolving in solution are associated with branched oligomeric or polymeric structures, which are described by the structure factors $S_F(q)$, and agglomerates of similarly sized scatterers, described by $S_C(q)$. A weighting factor $0 < \varepsilon < 1$ is introduced that describes the contribution of fractal-like structures to the total scattering intensity. The scattered intensity of such a system, as a function of time, t, can be defined by Equation (5.9):

$$I(q,t) = N(\Delta\rho)^2 P(q,t)\left\{\varepsilon(t) S_F(q,t) + \left[1 - \varepsilon(t)\right] S_C(q,t)\right\} \tag{5.9}$$

The intensity pre-factor $\varepsilon N(\Delta\rho)^2$ is associated with the scattering contribution from primary particles of form-factor $P(q)$ that have formed fractal-like structures, whereas $(1\text{-}\varepsilon)N(\Delta\rho)^2$ refers to the remaining particles with internal correlations that can be described in terms of the structure factor $S_C(q)$.

5.4. Results and discussion

5.4.1. Time-resolved SAXS measurement of thin film drying process

Figures 5.2 – 5.4 present measured scattering curves together with appropriate fits of Equation (5.9). Due to the fact that all three samples were measured with different calibrations of the experimental setup, the intensity is shown in arbitrary units. Fits of $N(\Delta\rho)^2$ can only be compared within a single measurement series, but differences in trends between different series can be interpreted. All $N(\Delta\rho)^2$ values were normalised against a value from the same series at the beginning of the process.

5.4.2. Drying of non-hydrolysed precursor sol

Figure 5.2 displays data of a drying film of a non-hydrolysed precursor sol of barium titanate The data set was fitted with Equation (5.9). The evolving system could be described in terms of the spherical form factor and the hard sphere interaction structure factor only, *i.e.*, $\varepsilon = 0$. The factor $N(\Delta\rho)^2$ decreased quickly to *ca.* 7% of its initial value after 28 min (Figure 5.5A, $h = 0$). This is an effect of solvent evaporation. The concentration of scattering entities in the film increases as a result of solvent loss during drying. This leads to increasingly homogeneous film morphology, with accompanying loss of scattering contrast $\Delta\rho$ between scatterers and their surroundings.

The evolution of radii of the primary particles, r_0 from 0.32 to 0.45 nm is shown in Figure 5.5B. The evolution of corresponding hard-sphere radii and volume fraction as a function of time is presented in Figures 5.6A and 5.6B. R_{HS} remained practically constant between 0.6 and 0.7 nm. The hard-sphere volume fraction increased from 1.7% to reach 24%, indicating an increasing order in the system in the course of drying.

5.4.3. Drying of precursor sol with h = 5.6

The structural evolution in the film with $h = 5.6$ upon drying was different, as can be seen in Figure 5.3A. The factor $N(\Delta\rho)^2$ decreased to *ca.* 20 – 23% of its initial value after 28 min (Figure 5.5A, $h = 5.6$). A slow on-going evolution in the dried material after that period can be recognized in the SAXS patterns in Figure 5.3. Especially the shift of the broad maximum around $q = 3.5$ nm^{-1} to higher q, and the ongoing decrease of scattering intensity in the q-range 1 – 2 nm^{-1} is well visible in Figure 5.3A. The size of the primary particles varied between 0.41 and 0.45 nm (Figure 5.5B), very close to values found in the sols [12].

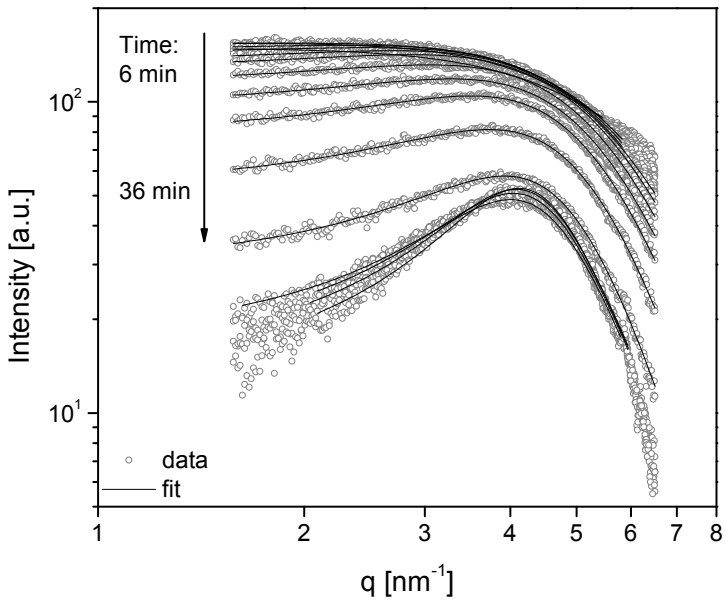

Figure 5.2. Time-resolved SAXS pattern of drying barium titanate precursor film with h = 0.0 at 60 °C. Data were fitted with the model described by Equation (5.9) assuming a constant value ε = 0.

The first scattering curve in the series could be fitted using only the sphere form factor from Equation (5.4). From the 4th minute onwards, Equation (5.9) was used. Fitted values of $\varepsilon(t)$ are presented in Figure 5.5A. The fraction $1-\varepsilon(t)$ from agglomerates factor increased from 65% at t = 4 min to > 98% at t = 28 min. This indicates that the dried film was composed almost exclusively of internally correlated structures. The hard sphere radius and volume faction are presented in Figure 5.6A and 5.6B, respectively. R_{HS} decreased slightly from ~0.9 nm to 0.72 nm. This change is visible in Figure 5.3 as a shift of the maximum around q_{max} = 3.5 nm^{-1} to slightly higher q-values. In this case the dimension in real space $\partial = 2R_{HS} = 2\pi/q_{max}$, which agrees well with the fitted values of all scattering curves. The volume fraction parameter ν increased from *ca.* 5% to 30%.

The obtained values of $\varepsilon(t)$ enabled me to estimate the fractions of primary particles that participated in fractal-like agglomerates, and to seperate the scattering curves into $P(q)S_F(q)$ and $P(q)S_C(q)$ contributions. Figure 5.3B presents the experimental scattering curve and contributions $P(q)S_C(q)$ and $P(q)S_F(q)$ at t = 16 min. The simulated scattering curve from a system of individual, non-interacting particles of similar radius r_0 is also shown. The increase in the experimental $I(q)$ curve at q < 4 nm^{-1} upon decreasing q is caused by the presence of fractal-like structures with gyration radius R_g that are composed of spherical primary particles of radius r_0. Fitting of $P(q)S_F(q)$ yielded the parameters D = 2.2 ± 0.2 and R_g = 1.13 ± 0.01 nm.

Since r_0 = 0.43 nm, the number of particles in the fractal-like agglomerate can be estimated from Equation (5.5), and is equal to approx. 15.

I also fitted the same data with Beaucage's unified exponential/power-law approach [27-29] to compare the values from both fits. In Beaucage's description the Guinier approximation [13] is used to obtain information on different length scales. In this case, two levels are present, namely primary particles of radius of gyration $R_s = (3/5)^{1/2} r_0$, and larger structures of gyration radius R_g. The transition regions between two Guinier regimes are taken into account by error functions that simulate power-law regions. In the present case a two-level fit function, as expressed by Equation (5.10), is required.

$$I(q) = G\exp\left(-\frac{q^2 R_g^2}{3}\right) + B\exp\left(-\frac{q^2 R_s^2}{3}\right)\left(\frac{[\mathrm{erf}(qR_g 6^{-1/2})]^3}{q}\right)^p + \\ + G_s\exp\left(-\frac{q^2 R_s^2}{3}\right) + B_s\left(\frac{[\mathrm{erf}(qR_s 6^{-1/2})]^3}{q}\right)^4 \tag{5.10}$$

Here G, G_s, and B are constants; p is a scaling exponent of the power law related to R_g, and B_s is constant specific for the description of the limiting q^{-4} Porod region scaling [13]. The following structural parameters were found from the best fit of experimental data to Equation (5.10): R_g = 1.15 ± 0.04 nm, p = 2.06 ± 0.65, and R_s = 0.38 ± 0.03 nm. The latter value corresponds to r_0 = 0.48 ± 0.04 nm. As can be seen these numbers are very similar to the ones obtained from fitting to Equation (5.6). The parameter p in the latter approach is equivalent to D in Equation (5.6), although the error in the fit of p is considerable, because of the short q-range between $q = 2\pi/R_g$ and $2\pi/R_s$. It can be concluded that Beaucage's structural model supports my findings based on Equation (5.6). I therefore used Equation (5.10) to fit all experimental data and obtained the same values of R_g as with Equation (5.6) within 3% error margin.

The best fits of D and R_g are presented in Figure 5.7. In the first 24 min of the drying process, when the film was still wet, small fractal-like structures were present along with a majority of internally correlated structures (Figure 5.6). The fractal-like structures remained relatively small (R_g ~1 nm) until t = 20 min. The D parameter was relatively high (> 2), indicating that the small clusters were relatively compact. Just before the film became dry at t = 22 min, a relatively rapid growth of R_g started, which was accompanied by a decrease of D, probably indicating a rapid agglomeration process.

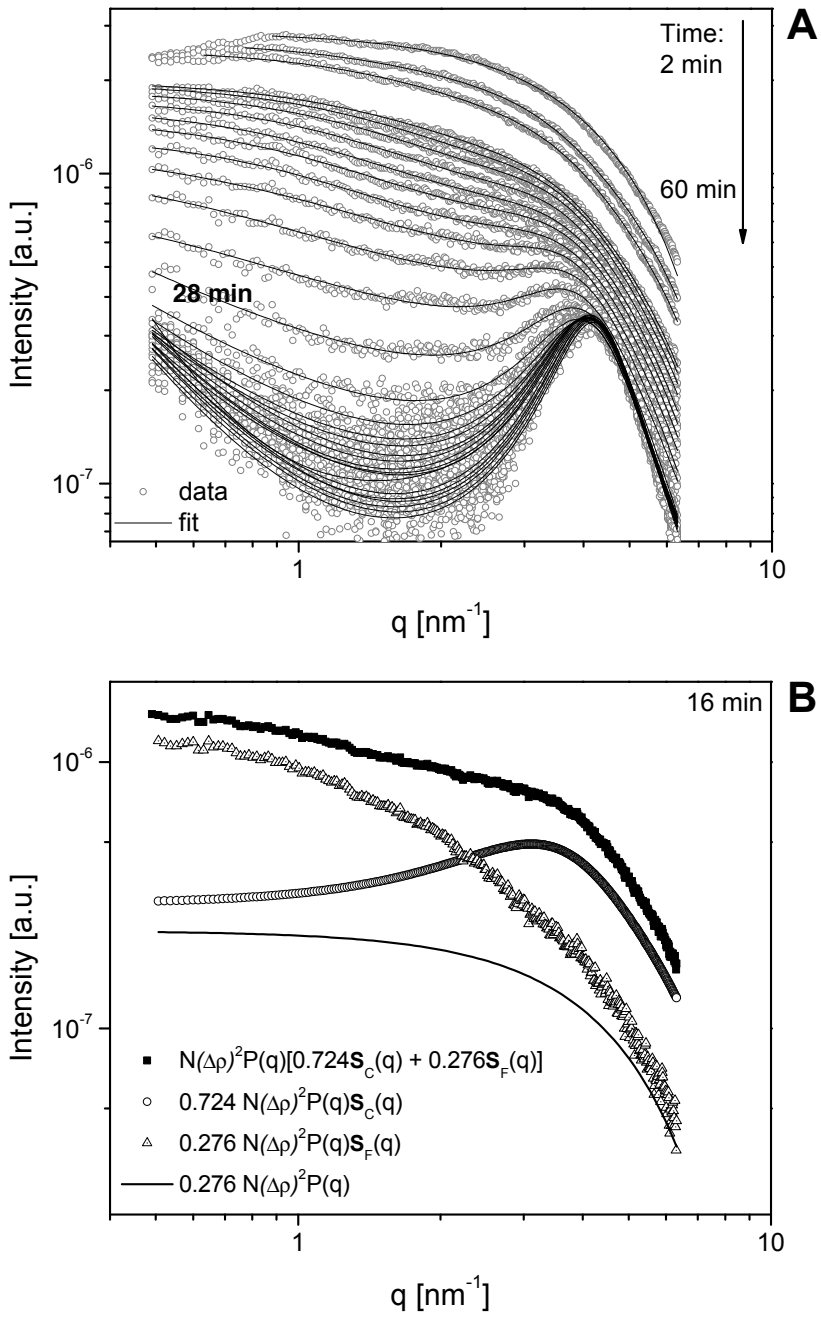

Figure 5.3. a) Time-resolved SAXS pattern of drying barium titanate precursor film with b = 5.6 at 60 °C. Data were fitted with the model described by Equation (5.9); b) Experimental scattering curve (squares) at t = 16 min and weighted contributions ($\varepsilon(t)$ = 0.276) of fractal-like particles $P(q)\underline{S}_F(q)$ (triangles) and $P(q)S_C(q)$ (circles). The simulated scattering curve of a system of non-interaction particles of similar radius r_0 (a curve) is shown for the sake of comparison.

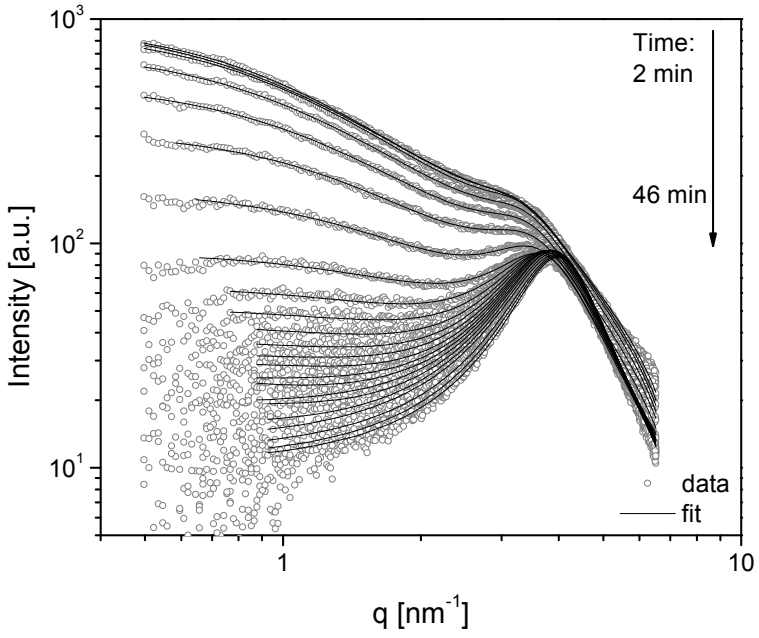

Figure 5.4. Time-resolved SAXS pattern of drying barium titanate precursor film with h = 33 at 60 °C. Data were fitted with the model described by Equation (5.9).

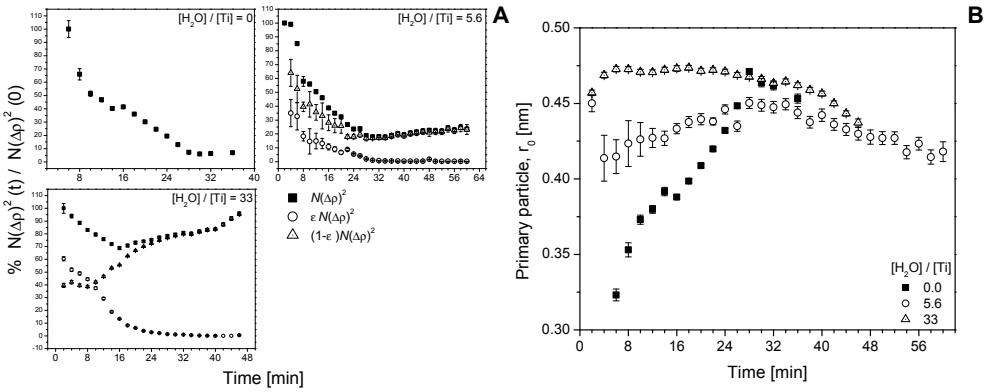

Figure 5.5. a) Evolution of $N(\Delta\rho)^2$, contribution from fractal-like structures $\varepsilon N(\Delta\rho)^2$, and contribution from internally correlated structures $(1\text{-}\varepsilon)N(\Delta\rho)^2$; b) Fitted parameter from spherical form factor $P(q)$: primary particle radius, r_0.

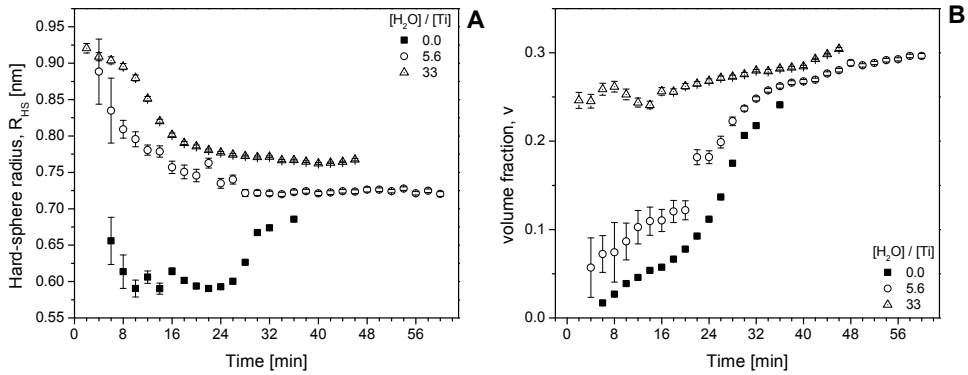

Figure 5.6. Fitted parameters from correlation structure factor $S_C(q)$: a) hard-sphere radius $2R_{HS}$; b) evolution of volume fraction, v.

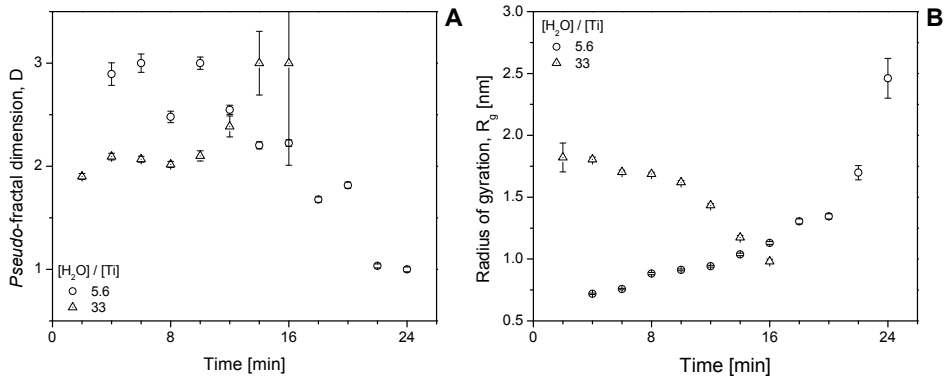

Figure 5.7. Fitted parameters from mass-fractal structure factor $S_F(q)$: a) pseudo-fractal dimension D; b) radius of gyration, R_g.

5.4.4. Drying of precursor sol with h = 33

The time-resolved scattering curves of a drying BTO precursor film with h = 33 is shown in Figure 5.4. The normalized factor $N(\Delta\rho)^2$ decreased slowly in the first 16 minutes to 70% of its original value, and then increased to > 90% (Figure 5.5A). The factor $1-\varepsilon(t)$, associated with the contribution of internally correlated structures to the total scattering intensity, increased from *ca.* 40% at t = 2 min to > 99% after t = 22 min. The contribution of fractal-like structures was considerable in the first 10 min, and then decreased quickly to almost zero. Drying increases the concentration of precursors, thereby shortening the gelation time. Highly hydrolysed sols are known to undergo sol-gel transition relatively quickly at 60 °C [12]. Therefore, a physical gel was formed in a shorter period of time than in the hydrolyzed film with h = 5.6. The size of the primary particles r_0 remained constant at 0.42 – 0.47 nm through-out the process (Figure 5.5B). R_{HS} in Figure 5.6A decreased

from initial 0.92 nm radius to a constant value of 0.77 nm after t = 24 min. The volume fraction parameter, ν was higher than in the other two sols.

The initial R_g values (Figure 5.7A) were higher than in the film with h = 5.6, but they decreased to similar values at t = 12 min. The parameter D increased from 1.9 to 2.4 in the same time interval (Figure 5.7B). The actual change of gyration radius was therefore small, whereas the morphology of the fractal-like structures became more densely packed, in view of the considerable change of D. Values of R_g and D after t = 12 min were 1.0 nm and 3, respectively, indicating the formation of small and fully dense agglomerates. It is noted that since the contribution of fractal-like structures to $N(\Delta\rho)^2$ was only ~10% of total, the absolute values determined here should be taken with care, because of the relatively low low signal-to-noise ratios.

5.4.5. EELS and TEM characterization

EELS analysis yielded two-dimensional qualitative maps of the distribution of Ba and Ti elements in as-dried, uncalcined films. Figures 5.8 shows TEM and corresponding EELS elemental mappings of Ba and Ti in films from sols with h = 0.0, 2.8, 5.6 and 33. The film thicknesses were practically constant in the characterized areas.

The film prepared from a sol with h = 0 showed very a homogenous morphology (Figure 5.8A). EELS mappings showed that Ba- and Ti-rich areas were small (1 – 2 nm) and homogenously distributed in the film, indicating good mixing of Ba and Ti species on molecular level.

In contrast, the bright-field TEM image of a film with h = 2.8 in Figure 5.8B indicated formation of quasi-spherical interconnected domains of 1 nm diameter, which had agglomerated into larger objects of 5 – 10 nm size (Figure 5.8B). These features appeared brighter, indicating that its electron density was lower than in the surrounding darker regions. The darker areas did not exhibit a particulate shape and were 5 – 10 nm in diameter. The morphology resembles the morphology found in the film with h = 5.6 (Figure 5.8C). The corresponding EELS mappings showed that the dark regions in the TEM images correspond to Ba-rich regions, and the bright regions to a Ti-rich phase. The Ba- and Ti-rich domains were separated over an average distance of 5-10 nm. The Ti-rich phase appears slightly smaller, with a correlation length of *ca.* 3 nm, in the film with lower h.

When h was increased to 33, the film showed a bright particle-like structure with diameters of 5 to 10 nm in a bright-field TEM image (Figure 5.8D). The EELS mapping showed that the Ba- and Ti-rich regions were separated on a length-scale of 15 – 20 nm. The Ti-rich areas seem to be isolated from other Ti-rich regions (in a 2D image), and they were of higher Ti density than in films with lower h. These results clearly demonstrate that the spatial separation of Ba and Ti in the film is dependent on the extent of hydrolysis of the precursor sols. It is noted that the bright-field TEM

images of the three hydrolysed sols did not show significant differences in morphology. The EELS mapping revealed more details of the structure of the film.

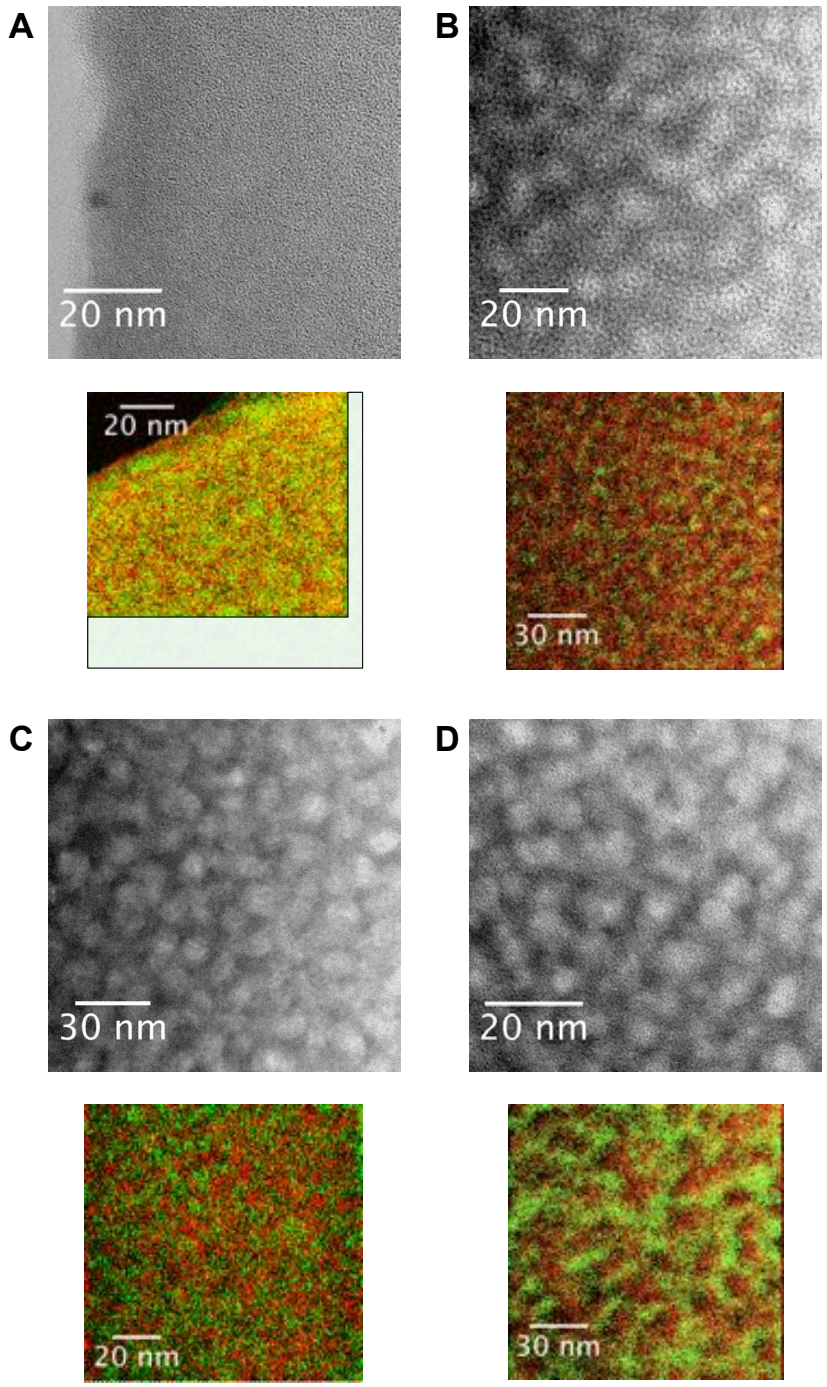

Figure 5.8. Bright-field TEM images (upper figure) and EELS mappings of Ba (red) and Ti (green) (lower figure) of as-dried BTO films with varying *b*; a) *b* = 0.0; b) *b* = 2.8; c) *b* = 5.6; d) *b* = 33.

5.4.6. Interpretation of data

In Chapter 4 concerning the structural evolution of BTO precursors sols in a constant volume of solvent, I found that the sol-gel process consisted of three phases: (i) formation of primary scatterers with r_0 = 0.45 nm and very small agglomerates thereof, (ii) growth of fractal-like structures and structures with internal correlations, which were attributed to branched polymer-like Ti-based oligomers and agglomerates of similarly sized particles (R_{HS} = 0.90 – 0.95 nm), respectively, and (iii) gelation as a result of cluster-cluster aggregation of the fractal-like structures.

In the current study on physically drying films with similar composition I found several analogies with my previous findings. The primary scatterers were spherical and had a radius r_0 of 0.32 – 0.47 nm, depending on the value of *h*, and the stage of the drying process. Typical values were ~0.45 nm, which is the same as found in the previous study. Similar structural motifs have been observed by SAXS in a number of titania-related gelling systems [30-34], suggesting that the scatterers in the present study were similarly composed of titania. It is noted that the value of r_0 hardly varied in the hydrolyzed films in the course of the drying process, while it increased in the first 24 min of drying of a non-hydrolyzed film. Apparently, the primary scatterers require the presence of water to grow to a size of 0.42 – 0.47 nm. The non-hydrolyzed film probably either absorbed moisture from air or was hydrolyzed due to the esterification reaction between solvent alcohol and acetic acid. By the end of the drying process the primary scatterers in all three investigated films appear to have the same size within experimental error, independent of the initial value of *h*.

The hard sphere radius R_{HS} in the structures with internal correlations (Figure 5.6) is larger than r_0. This suggests that the Ti-based core of size r_0 was probably surrounded by a stable ligand shell containing oxo, hydroxy, alkoxy and/or acetate groups. Since the electron density in the ligand shell is virtually identical to the density of the surrounding solvent matrix, it cannot be detected directly by SAXS. However, the average distance between primary scatterers in agglomerates with internal correlations is directly dependent on the thickness of the ligand shell, so they are included in R_{HS} [12]. The values of R_{HS} in different films were relatively similar, from 0.7 – 0.9 nm. Lower values were measured in the non-hydrolyzed film. In the hydrolyzed sols, the initial value was 0.9 nm and it decreased gradually to ~ 0.75 nm. In the non-hydrolyzed films the trend was opposite, and it followed the same increasing trend as r_0. But the final value of R_{HS} was fairly similar as in the other two sols. This suggests that in all cases, very similar species form at the primary structural level, with an inorganic core of ~0.45 nm radius and a ligand shell of ~0.3 nm thickness in the as-dried film. Since the hard sphere radius R_{HS} was ~0.9 nm, with an inorganic core of radius r_0 ~ 0.45 nm in hydrolyzed BTO sols [12], it seems that drying does not affect the radius of the inorganic core, but the thickness of the outer organic ligand shell shrinks by ~0.15 nm.

The increase of volume fraction ν upon drying shows the increasing packing density in as-dried films. Its initial value was close to zero for the non-hydrolyzed film, and $\nu = 0.25$ for the film with $h = 33$, but it evolved to very similar values of $\nu \sim 0.3$ in all investigated systems. In hydrolyzed BTO sols at a constant solvent volume [12], the final packing density was slightly higher ($\nu = 0.4$) than found in the present work. The same study showed that gelation occurs via aggregation of fractal-like branched oligomers, while the contribution of internally correlated structures to the total scattering intensity decreased during the course of the reaction. In contrast, in physically drying thin films, the contribution from fractal-like structures to scattering diminished in the course of drying. Moreover, their gyration radius remained much smaller than in sols with constant solvent volume. Apparently, the disappearance of fractal-like structures is associated with the loss of solvent from the sol. The fractal-like structures are probably not stable in the absence of a stabilizing solvent phase.

Very strong correlation peaks developed in nearly dry films, indicating that the as-dried film consisted entirely of agglomerates with correlated hard-sphere interactions, *e.g.*, random close-packed agglomerates composed of similarly sized nanoparticles.

The overall trends in $\varepsilon(t)$ and $N(\Delta\rho)^2$ in Figure 5.5A can be explained in terms of the occurrence of condensation (up to gelation) and physical evaporation of solvents from the film. Since the evolved nanostructures visible with SAXS are most likely entirely Ti-based [12], they influence the value of $\varepsilon(t)$ and $\Delta\rho$. On the other hand, the Ba ions remain dissolved in the acetic acid matrix and mainly influence the scattering contrast between nanostructure and solvent $\Delta\rho$. The latter ions precipitate when their concentration exceeds the actual solubility limit of the system, for instance as a result of loss of acetic acid from the film. The gradual decrease of $N(\Delta\rho)^2$ in Figure 5.5A in the first period of drying can be interpreted in terms of the mutual approach of Ti-based nanostructures upon solvent loss, which results in an effective decrease of $\Delta\rho$ between these nanostructures and their surroundings. However, the reversal in the trend of $N(\Delta\rho)^2$ in the hydrolyzed films after 16 – 24 min of drying suggests that the $\Delta\rho$ increases in the last stages of drying, and/or that N increases. The most plausible explanation for that phenomenon is that a Ba-rich phase precipitates from solution. The effect is particularly pronounced for the film with $h = 33$, which also shows the most pronounced degree of separation between Ti-rich and Ba-rich domains in the as-dried film (Figure 5.8D). My data showed that the Ti-based structures in solution are larger at higher water concentrations. It is well possible that the size of these structures is one of the main factors that determine the length scale on which phase separation of Ba- and Ti-rich domains occurs. Adjusting the value of h would thus enable composition modulation to reach larger length scales, in agreement with my findings.

5.5. Conclusions

The structures in solution that are visible with SAXS are Ti-rich, and can be divided into fractal-like branched oligomers, and dense agglomerates of similarly sized nanoparticles. A model was developed to describe the scattering behavior of these solutions in terms of these nanostructures, and this model was able to fit the experimental data well over a wide range of conditions. Both types of structures consisted of the same type of primary scatterers, namely particles with an inorganic core of ~0.45 nm radius, and an outer organic shell of ~0.3 nm thickness in the as-dried films. The shell was ~0.15 nm thicker in the initial sols, and probably shrunk in the course of drying. The fractal-like morphologies disappeared during film drying, most likely because they were not stable in the absence of a solvent matrix. Only the agglomerate-like structures remained in the as-dried films. In general, the trends visible in Figure 5.5 – 5.7 are similar for films with different values of *h*, especially after longer periods of time.

EELS showed that phase separation between barium and titanium-rich domains had occurred after the drying of these films. Their morphology looked similar in TEM analyses, but EELS showed considerable differences between films, because the distribution of Ba and Ti varied strongly depending on the hydrolysis conditions. Non-hydrolyzed sols yielded a homogenous distribution of elements, whereas high hydrolysis ratios promoted separation of Ba- and Ti-rich domains with a correlation length of *ca.* 15 nm. This demonstrates that such as-dried films are not necessarily uniform on the mesoscopic level.

5.6. References

[1] Yoon, D. *J. Ceram. Proc. Res.*, *7*, 343-354, **2006**.

[2] Schwartz, R. W.; Schneller, T. S.; Waser, R. *C. R. Chimie*, *7*, 433-461, **2004**.

[3] Pithan, C.; Hennings, D. H.; Waser, R. *Int. J. Appl. Ceram. Technol.*, 2, 1-14, **2005**.

[4] Schwartz, R. W.; Narayanan, M. Chemical Solution Deposition - Basic Principles, In *Solution Processing of Inorganic Materials*, ed. Mitzi, D. B., John Wiley & Sons, Inc., New Jersey, 33-76, **2009**.

[5] Huffman, M. *Integr. Ferroelectrics* 10, 39-53, **1995.**

[6] Phule, P. P.; Risbud, S. H. *Adv. Ceram. Mater.*,3, 183-185, **1988**.

[7] Assink, R.A.; Schwartz, R.W. *Chem. Mater.*, 5, 511-517, **1993**

[8] Hasenkox, U.; Hoffmann, S.; Waser, R. *J. Sol-Gel Sci. Technol.*, 12, 67-79, **1995.**

[9] Hoffmann, S.; Waser, R. *J. Eur. Ceram. Soc,*. 19, 1339-1343, **1999**.

[10] Frey, M. H.; Payne, D. A. *Chem. Mater.*, *7*(1), 123-129, **1995**.

[11] Hennings, D.; Rosenstein, G.; Schreinemacher, H. *J. Eur. Ceram. Soc.* 8, 107-115, **1991.**

[12] Chapter 4; Stawski, T. M.; Veldhuis, S. A.; Besselink, R.; Castricum, H. L.; Portale, G.; Blank, D. H. A.; ten Elshof, J. E. *J. Phys. Chem. C* 115, 20449-20459, **2011**..
[13] Guinier, A.; Fournet, G. Small Angle Scattering of X-rays, John Wiley & Sons Inc, New York, **1955**.
[14] Kratky, O. A Survey In *Small Angle X-ray Scattering*, ed. Glatter, O.; Kratky, O. Academic Press, London, 3-13, **1982**.
[15] Porod, G. General theory In *Small Angle X-ray Scattering*, ed. Glatter, O.; Kratky, O. Academic Press, London, 17-52, **1982**.
[16] Craievich, A.F. *Mater. Res.,* 5, 1-11, **2002**.
[17] Bras, W.; Dolbnya, I. P.; Detollenaere, D.; van Tol, R.; Malfois, M.; Greaves, G. N.; Ryan, A. J.; Heeley, E. *J. Appl. Crystallogr.* 36, 791-794, **2003**.
[18] Pedersen, J. S. *Adv. Colloid Interface Sci.*, 70. 171-210, **1997**.
[19] Sorensen, C. M. *Aerosol Sci. Technol.,* 35, 648-687, **2001.**
[20] Teixeira, J. *J. Appl. Cryst.,* 21, 781-785, **1988**.
[21] Freltoft, T.; Kjems, J. K.; Sinha, S. K. *Phys. Rev. B*, 33, 269-275, **1986**.
[22] Berry, M. V.; Percival, I. C. *Opt. Acta,,* 33, 577-591, **1986.**
[23] Vicsek, T. Fractal Growth Phenomena (2nd Edition), World Scientific Publishing Co. Pte. Ltd., Singapore, **1992**,
[24] Percus, J. K.; Yevick, G. J. *Phys. Rev.,* 110, 1-13, **1958.**
[25] Vrij, A. *J. Chem. Phys.,* 71, 3267-3270, **1979**.
[26] Baxter, R. J. *J. Chem. Phys.*, 49, 2770-2774, **1968**.
[27] Beaucage, G. *J. Appl. Cryst.,* 28, 717-728, **1995**.
[28] Beaucage, G. *J. Appl. Cryst.,* 29, 134-146, **1996**.
[29] Beaucage G.; Ulibarri, T. A.; Black, E. P.; Schaefer, D. W. Multiple Size Scale Structures in Silica-Siloxane Composities Studied by Small-Angle Scattering, In *Hybrid Organic-Inorganic Composites - ACS Symposium Series*, ed. Mark, J. E.; Lee, C. Y-C.; Bianconi, P. A. American Chemical Society, Washington DC, **1995**.
[30] Doeuff, S.; Henry, M.; Sanchez, C. *Mat. Res. Bull.,* 25, 1519-1529, **1990**.
[31] Jalava, J. -H.; Hiltunen, E.; Kähkönen, H.; Erkkilä, H.; Härmä, H.; Taavitsainen, V. -M. *Ind. Eng. Chem. Res.,* 39, 349-361, **2000**.
[32] Torma, V.; Peterlik, H.; Bauer, U.; Rupp, W.; Husing, N.; Bernstorff, S.; Steinhart, M.; Goerigk, G.; Schubert, U. *Chem. Mater.*,17, 3146-3153, **2005**.
[33] Pattier, B.; Henderson, M.; Brotons, G.; Gibaud, A. *J. Phys. Chem. B*, 114, 5227-5232, **2010**.
[34] Kessler, V.G. *J. Sol-Gel Sci. Technol.*, 51, 264-271, **2009**.

6

Development of Nanoscale Inhomogeneities during Drying of Sol-Gel Derived Amorphous Lead Zirconate Titanate Precursor Thin Films*

Abstract

The structural evolution of sol-gel derived lead zirconate titanate (PZT) precursor films during and after physical drying was investigated by transmission electron microscopy (TEM), electron energy loss spectroscopy (EELS), selected area electron diffraction (SAED) and time-resolved x-ray diffraction (XRD). Films were deposited from initial 0.3 mol/dm^3 precursor sols with varying hydrolysis ratios. Zr-rich grains of 1 – 10 nm size, embedded in a Pb-, Zr-, Ti- containing amorphous matrix were found in as-dried films. The Zr-rich regions were crystalline at hydrolysis ratios $[H_2O]/[Zr,Ti] < 27.6$, and amorphous at ratios > 100. X-ray diffraction analysis of PZT and zirconia sols revealed that the crystalline nanoparticles in both sols were identical, and were probably composed of nanosized zirconium oxoacetate-like clusters. This study demonstrates that time-resolved x-ray diffraction combined with electron energy loss spectroscopy mapping is a powerful tool to monitor the nanoscale structural evolution of sol-gel derived thin films.

6.1. Introduction

Because of its wide range of applications a lot of interest has been dedicated to the fabrication and characterization of lead zirconate titanate ($PbZr_{1-x}Ti_xO_3$; PZT) thin films [1-4]. PZT is technologically important because of its large remnant polarization, low coercive field, and high piezoelectric coefficients. There are two major routes for the fabrication of thin films, namely via physical and wet-chemical techniques. The physical techniques include metal-organic chemical vapor deposition (MOCVD) [5,6], sputtering [7,8], and pulsed laser deposition [9,10]. The chemical solution deposition techniques (CSD) [11] include the sol-gel route [12,13], and metal-organic deposition (MOD) [14,15]. The sol-gel technique has attracted

* Published in:
Stawski, T. M.; Veldhuis, S. A.; Castricum, H. L.; Keim, E.G.; Eeckhaut, G.; Bras, W.; Blank, D. H. A.; ten Elshof, J. E. *Langmuir,* 27, 11081-11089**, 2011**.

considerable attention because of its simplicity, low cost, good compositional control and its ability for large area film fabrication [16].

Typical sol-gel solutions consist of metal alkoxides and/or metal carboxylate precursors, solvents, water and catalyst. They can be deposited as thin films by dip coating or spin coating, after which they get a thermal treatment at high temperature for consolidation and PZT phase formation. It is known that the nature of the sol has a profound effect on the microstructure, orientation and electrical properties of the final films [12,16]. The structural chemistry of PZT sols has been studied by various analytical techniques, such as nuclear magnetic resonance (NMR) [17-21], Fourier transform infrared (FTIR) [19,20], gas chromatography-mass spectroscopy (GC-MS) [18], photon correlation spectroscopy (PCS) [21-23] and small angle x-ray scattering (SAXS) [21-23]. It has been noted, *e.g.* in the reviews of Schwartz *et al.* [11,24,25], that hardly any information is available about the structural evolution of PZT sols in later stages of the sol-gel process, such as during and after the drying of as-deposited thin films.

The properties of sols are controlled by the nature of the metal-carrying reagent, solvent, reagent concentration, water concentration, method of water addition, catalyst, solution preparation/reaction conditions and other factors [11,12,24,25]. For multicomponent (mixed metal) systems such as PZT, pre-hydrolysis of less reactive metal alkoxides is sometimes employed to improve compositional uniformity. Earlier studies showed that as soluble oligomers instead of precipitates can only be formed under water-lean conditions [25]. A key point is therefore to restrict the amount of water and to control the way in which it is added. Assink *et al.* reported that acetic acid acts as a key chelating agent, affecting the reactivity and promoting esterification reactions that result in many alkyl acetate esters as byproducts. This suggests the formation of metal acetates and/or metal alkoxy acetates due to (partial) exchange of alkoxy ligands by acetate [17], but detailed knowledge of the nature of precursor species in PZT solutions after water addition (hydrolysis) is scarce. An extended X-ray absorption fine structure (EXAFS) study of commonly used non-hydrolyzed PZT sols showed that the constituent solvent/modifiers such as acetic acid and acetylacetone have an effect on the degree of homogeneity in the distribution of Pb and Zr, but Pb-O-Zr bonds could not be determined in any of the samples [26]. It is believed that most metal alkoxides and metal carboxylates can form oligomeric structures in appropriate solvents.

Well-known examples are $Ti_6(O^iPr)_{10}(OOCCH_3)_4O_4$, $Ti_6(O^iPr)_8(OOCCH_3)_8O_4$ and $Zr_4O(OPr)_{10}(CH_3COCH_2COCH_3)$ [11,12]. Complexes of Pb and Ti or Zr precursors in similar solvents have also been reported, *e.g.*, $PbTi_2[(\mu_4\text{-}O)(OOCCH_3)(OCH_2CH_3)_7]_2$, $Pb_4Zr_4(\mu\text{-}O_2CR')_8(O^iPr)_{16}(OH^iPr)_2$, $Pb_2Ti_4(\mu\text{-}O_2CR')_4(OR)_{16}$, $Pb_2Ti_3(\mu_4\text{-}O)(\mu_3\text{-}O)(\mu\text{-}O_2CC_7H_{15})_2(\mu\text{-}O^iPr)_6(O^iPr)_4$, $PbZr_3(\mu_4\text{-}O)(OAc)_2(O^iPr)_{10}$ and several others [27-31]. All these complexes formed

in the absence of water, *i.e.*, without the hydrolysis step (water addition) that is typical for initiating sol-gel processes.

In the drying stage of sol-gel films the situation becomes even more complex, as complexation reactions and evaporation occur simultaneously, and there is a mutual influence [24,25,32]. For instance, loss of solvent due to physical drying increases the solution viscosity and reaction rate of species that are present in that solution. If more than one solvent is used, differences in the relative solvent evaporation rates at a given temperature lead to a gradually changing matrix for the sol particles, which may affect their solubility and reactivity, and induce spatial separation. Moreover, in comparison with many polar organic solvents, water is a relatively volatile reagent that may be evaporated before it is consumed in a thin film drying process. Obviously, this may have an effect on the final structure of the as-dried thin film. Neutron scattering studies indicated that alkoxide-based PZT sol-gel processing results in compositionally inhomogeneous samples [33]. This is due to compositional segregation that appears to occur early on during sol-gel processing, and is not fully eliminated by the final high temperature heat treatment.

It is the aim of this study to elucidate structural aspects of sol-gel PZT precursor thin films in the course of and directly after the drying process, in which volatile components are lost from the film, and precursor concentrations increase progressively. I used transmission electron microscopy (TEM), selected area electron diffraction (SAED), and electron energy loss spectroscopy (EELS) for the characterization of as-deposited dried precursor films. Time-resolved small angle x-ray scattering (SAXS) and diffraction experiments at small angles were used to monitor the structure and structural evolution of PZT sols and drying thin films on nm-length scale. In particular, I focused on a commonly used PZT solution composition that has been used to imprint PZT nanopatterns with a lateral resolution below 200 nm by soft lithography [34], and is based on the combination of acetic acid and 2-methoxyethanol as solvents [11-13,21-26]. A selected number of solutions and process conditions was investigated, to get insight into the structures that formed in the sol stage, and into the processes that occured *in situ* on the nanoscale when a PZT sol-gel thin film was being dried.

6.2. Experimental

6.2.1. Synthesis of lead zirconate titanate precursor sols

Lead(II) acetate trihydrate (99%, Sigma-Aldrich), zirconium(IV) *n*-propoxide (70% w/w in *n*-propanol, Alfa Aesar) and titanium(IV) *iso*-propoxide (99.999%, Sigma-Aldrich) were used as precursor materials. Glacial acetic acid (99.8%, Acros) and 2-methoxyethanol (> 99.3%, Sigma-Aldrich) were used as solvents, stabilizers, and chelating agents. Initially, three stock solutions were made. A Pb-acetate solution

was prepared by dissolving lead acetate trihydrate in acetic acid and subsequent refluxing at 105 °C for 8 h to remove all remaining water [13]. The other two solutions, based on titanium *iso*-propoxide and zirconium *n*-propoxide, respectively, were dissolved in 2-methoxyethanol and stirred in a glove box under nitrogen atmosphere. All stock solutions were stirred at room temperature for 24 h. They were then stored at room temperature. The concentration of individual stock solutions was 0.60 mol/dm^3. Prior to experiments, the stock solutions were mixed in the appropriate molar ratios and stirred for 5 – 10 min. Normally, Ti and Zr stock solution had been mixed first and added to lead acetate solution in acetic acid. The molar ratio of Pb to Zr to Ti was always kept at 100 : 52 : 48, yielding a concentration of 0.30 mol/dm^3 in the final PZT solution. Solutions of this concentration constituted the basis for all experiments. In the case of hydrolyzed solutions, water was immediately added after the three stock solutions had been mixed. The hydrolysis ratio h of the PZT sols is defined as:

$$h = [H_2O]/[Zr,Ti] \text{ (or } [Zr]) \quad (6.1)$$

where $[H_2O]$ and [Zr,Ti] (or [Zr]) are the concentrations of H_2O and PZT (or zirconia) precursors in solution, respectively. PZT sols with hydrolysis rations h of 0.0, 2.3, 4.6, 9.3, 27.6, 55.5, and 111 were investigated. It is noted that the value of h is a nominal value that does not include traces of water that may result from a natural esterification reaction of the solvents, *i.e.*

$$H_3CCOOH + HO\text{-}C_2H_4\text{-}OCH_3 \rightarrow H_3CCOO\text{-}C_2H_4\text{-}OCH_3 + H_2O.$$

6.2.2. Synthesis of zirconia precursor sol

Zirconium(IV) *n*-propoxide (70 % w/w in *n*-propanol, Alfa Aesar) was used as a precursor material. Glacial acetic acid (99.8 %, Merck), 2-methoxyethanol (99.3 %, Sigma-Aldrich) were used as chelating agents, solvents and stabilizers. A zirconium(IV) *n*-propoxide solution was dissolved in 2-methoxyethanol and stirred in a glove box under nitrogen atmosphere yielding a 1.00 mol/dm^3 stock solution. In the next step, the zirconium(IV) alkoxide stock solution was mixed with acetic acid yielding a 0.50 mol/dm^3 solution. Finally, the solution was hydrolyzed at h = 4.8.

6.2.3. TEM, SAED and EELS characterisation

PZT precursor sols with h = 0, 9.3, 27.6, and 111, respectively, were spin-casted (Laurell WS-400B-6NPP-Lite spincoater) onto holey carbon TEM copper grids (CF200-Cu, Electron Microscopy Sciences) at 4000 rpm for 40 seconds. Then the as-prepared films were dried at 60 °C for 1 h on a hot-stage and used for transmission electron microscopy (TEM) characterisation (Philips CM300ST-FEG at 300 kV). Samples were investigated at low magnification to find typical areas and features of interest were examined at high magnification (GATAN 2k x 2k

Ultrascan1000 CCD camera). Crystallographic information was obtained by local Fourier transforms (FT) of areas of the images exhibiting high levels of crystallinity. The microscope software packages GATAN Microscopy Suite 1.8 and ImageJ 1.38e [35] were used for this purpose. Energy filtered images (GATAN model Tridiem with 2k x 2k CCD camera) were recorded at the highest possible magnification that still provided stable images, with negligible or compensable drift using 3-windows method for Zr-$M_{4,5}$ (pre-edge 145 eV, post-edge 200 eV, slit width 20 eV, 8 s exposure), Ti-$L_{2,3}$ (pre-edge 406 eV, post-edge 481 eV, slit width 30 eV, 10 s exposure) and Pb-$M_{4,5}$ (pre-edge 2324 eV, post-edge 2534 eV, slit width 100 eV, 40 s exposure). The mapping of Pb-$M_{4,5}$ using EELS is particularly tedious. It was established that the Pb distributions that had been measured presented significant mappings, as discussed in more detail in the appendix at the end of this chapter. Due to the relatively long counting times necessary for Pb, some image drift occurred in some cases. Colour-mix maps juxtapositioning selected combinations of elements were manually corrected for drift depending on the element, using the microscope GMS software package. Electron diffraction images were taken at effective camera lengths of 587 and 774 mm (collected with Ultrascan1000 CCD camera).

6.2.4. Time-resolved X-ray Diffraction during drying of PZT films and precipitation of PZT sols

Time-resolved X-ray diffraction and small-angle x-ray scattering experiments were performed on the Dutch-Belgian beamline (DUBBLE) BM-26B of the ESRF in Grenoble, France [36]. I used a dedicated small-angle X-ray scattering beam line, due to the large lattice constants of the species found in the experiments. The beamline was suitable for measuring diffraction patterns at small angles. For some of the investigated sols I also measured typical small-angle scattering (SAXS) curves. In SAXS experiments elastic scattering of x-rays by a sample that has local electronic density fluctuations is recorded at very small angles. The scattering intensity $I(\boldsymbol{q})$ is recorded versus the modulus of the scattering vector $\boldsymbol{q}$ (nm^{-1}), which is related to the scattering angle 2θ and the wavelength λ (nm) of the incident beam via

$$q = 4\pi / \lambda \sin\theta \qquad (6.2)$$

The beam energy was 16 keV (λ = 0.0776 nm). The beam was focused at the corner of a 2D gas-filled multi-wire proportional detector in order to maximize the range of accessible q (scattering vector) values. The samples were placed at a distance of 1.5 m from the detector and the intensity was measured in the scattering vector range $0.13 < q < 8.2$ nm^{-1}. Structural information with dimensions of < 50 nm can be derived from this angular range [37,38]. The raw data were corrected for the pixel-dependent detector sensitivity. By applying Equation (6.2) and Bragg's law for diffraction

$$\lambda = 2\partial \sin\theta \qquad (6.3)$$

where ∂ is the lattice plane spacing in real space, the above-mentioned scattering vector range is equivalent to the plane spacing range 48.3 < ∂ < 0.76 nm for crystalline materials,.

To study the structure of PZT precursor sols, small quantities of solutions were contained in a sealed glass capillary (Ø = 1.5 mm, glass no. 14, Hilgenberg, Malsfeld, Germany) and measured at room temperature. PZT sols with h = 0.0, 2.3, 4.6, 9.3, 27.6, 55.5, and 111 after aging for 40 h at 60 °C in sealed containers were used in these studies. The scattering intensity from a capillary containing only the corresponding solvent(s) was subtracted from the overall intensity signal, whereby a correction was made for the fact that the concentration of solvent in a sol is lower than in the pure solvent. The scattering and diffraction data were collected for periods of typically 2 – 5 min at room temperature. To investigate the growth or precipitation of zirconia sols at elevated temperatures, scattering curves $I(q)$ were collected on sols in glass sealed capillaries (Ø = 1.0 mm, glass no. 14, Hilgenberg, Malsfeld, Germany) that were mounted into a programmable thermostat (Linkam) that was heated to 60 °C. Measurements were done with 2 – 5 min intervals for time periods of typically 1 h. Time-resolved scattering patterns of a developing zirconia precursor sol (h = 4.8) were recorded for 60 min at 60 °C in a capillary using a Linkam heating stage.

The setup that was used to follow the evolution of drying thin films is schematically illustrated in Figure 5.1 in Chapter 5. PZT sols were contained in a Kapton foil that was mounted on an aluminum rotor head with a diameter of *ca.* 11 cm. The rotation speed was 100 rpm, ensuring a homogenous distribution of liquid film over the surface of the Kapton foil. The rotation axis was not completely perpendicular to the incoming x-ray beam, as illustrated in the figure. This allowed detection of the scattered or diffracted x-ray beam. The scattering intensity was recorded at 60 °C at regular time intervals for 40 min. The scattering intensity of the empty chamber, *i.e.* Kapton foil under the same conditions, was subtracted as correction for the background contribution. Time resolved SAXS patterns of drying PZT thin films with h = 9.3 were recorded at 60 °C for 40 min using this setup.

6.3. Results and Discussion

6.3.1. TEM and EELS analysis of as-dried PZT thin films

The dried films prepared from fresh solutions of PZT sols with h = 0.00, 9.3 and 27.6 exhibited practically the same microstructure. See Figures 6.1A-B and 6.2A. In all three samples the film consisted of an amorphous matrix with numerous embedded highly crystalline particles with a diameter of 1 – 10 nm. The amorphous structure of the matrix was confirmed by the representative SAED pattern of Figure 6.1C.

Figure 6.1A shows an area from the film from a PZT sol with h = 27.6. The area contains highly crystalline particles. The corresponding Fourier transforms of three selected particles are shown in Figure 6.2B. The quality of the FTs depends on the quality and size of crystalline region of interest. Minimal drift or a different focus plane can lead to an asymmetric shape of the peak in reciprocal space and make analysis difficult. The accuracy also decreases with increasing length of $1/\partial$. The data revealed spots at characteristic values of $1/\partial$ at approximately 3.60, 4.06, 5.88, 6.80, 7.16, and 10.1 nm^{-1}. The same characteristic lengths were found in films from sols with h = 0 and 9.3 (not shown here). Only small differences were found between different FTs.

The local composition of the films was investigated by a derivative mode of energy-filtered TEM (EF-TEM) termed electron energy loss spectroscopy (EELS). EELS analysis yielded two-dimensional qualitative maps of the distribution of specific elements in a film. The highest possible magnifications that still provided negligible or compensable image drift were applied.

Figure 6.3A shows an unfiltered TEM image of an as-dried film, made from a PZT sol with h = 27.6. Some crystalline areas are indicated by circles. The near-corresponding combined EELS maps with the distributions of Zr and Ti is shown in Figure 6.3B. The indicated crystalline particles from Figure 6.3A correspond with areas of high Zr and low Ti concentration. The spatial position between regions of interest in Figure 6.3A and B is not exactly the same (the same refers to other elemental maps), as the position of the nano-particles embedded in the matrix can be slightly influenced by the electron beam.

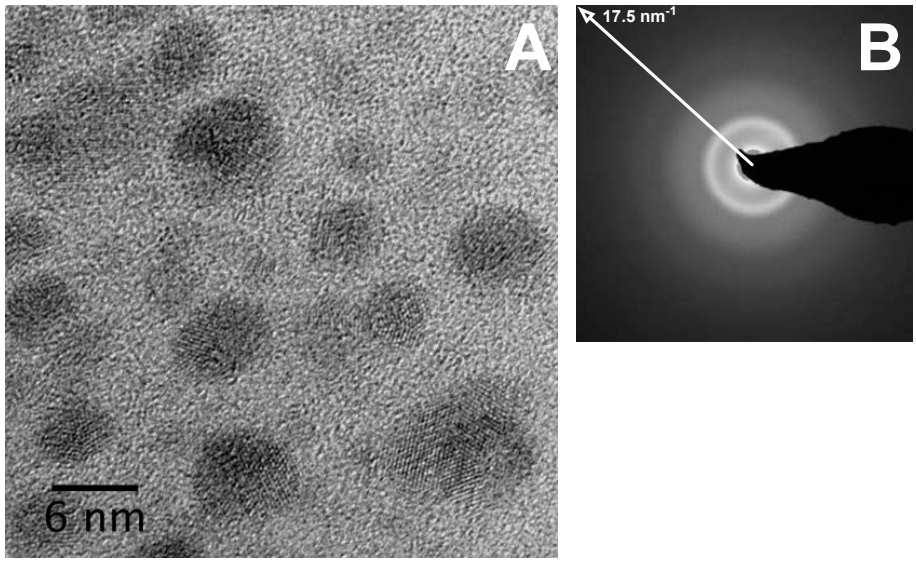

Figure 6.1. a) TEM bright-field images of dried films from fresh PZT precursor sols h = 0; b) Representative electron diffraction pattern of film from fresh sol without added water at L = 587 mm.

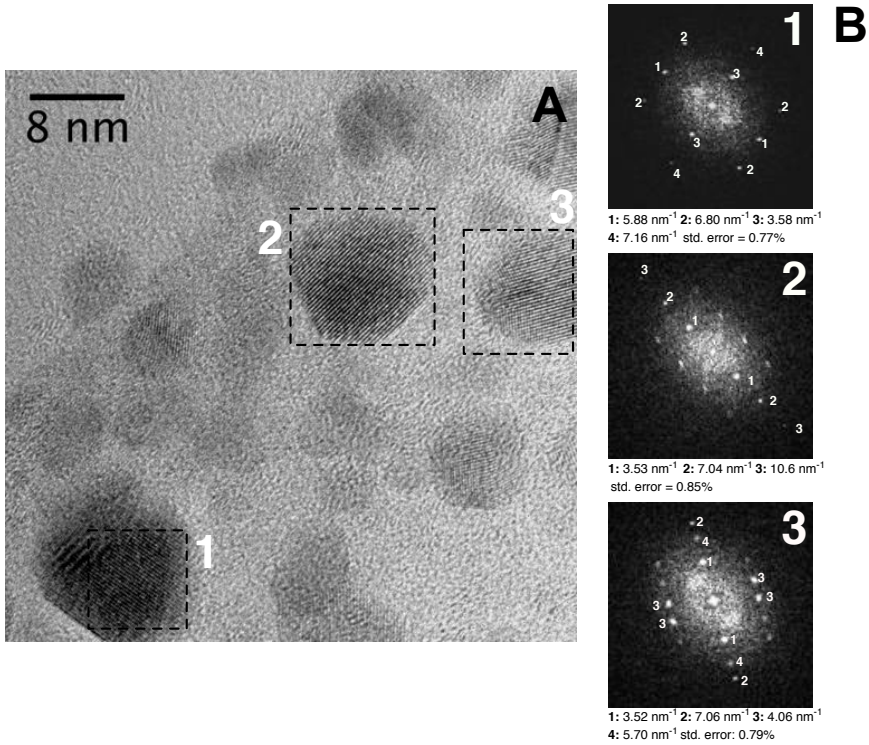

Figure 6.2. a) TEM bright-field image of an area from the film made from fresh PZT precursor sol with h = 27.6. b) FT images of the selected areas 1, 2, and 3 including corresponding crystallographic data.

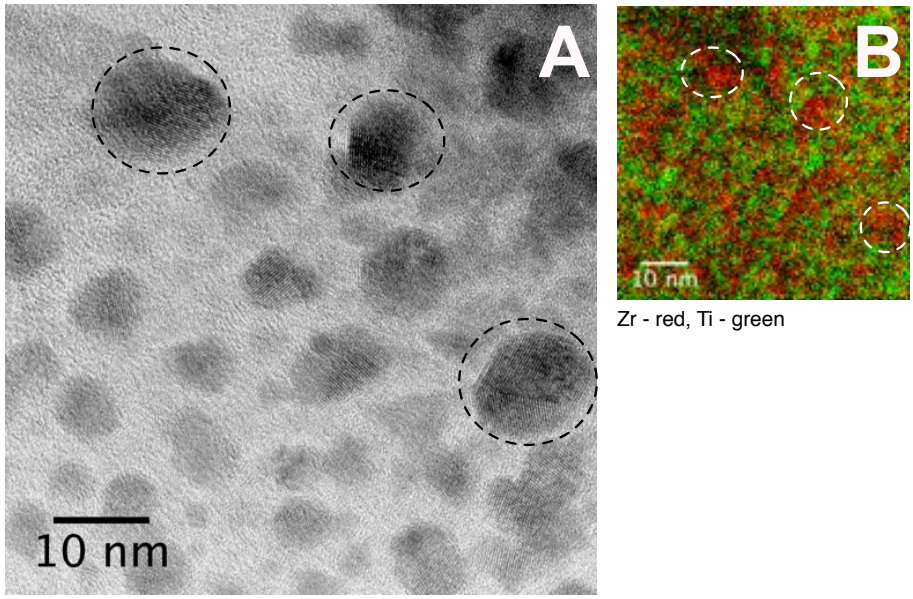

Figure 6.3. a) TEM bright-field image of the film made from fresh PZT precursor sol with h = 27.6; b) Corresponding elemental EELS mappings of Zr and Ti, combined into colour image.

Similar element distribution maps of Ti, Zr and Pb were also made of a film deposited from a water-free PZT sol (h = 0). Figure 6.4A shows the unfiltered TEM image, again containing dark crystalline nanoparticles. When the Ti and Zr distribution maps are superimposed in Figure 6.4B, the same Zr enrichment in crystalline areas can be seen. Figure 6.4C shows the distributions of Pb and Ti.

Ti is detected primarily in the amorphous areas of the film, while Pb seems to be distributed homogeneously over the entire area. But the crystalline areas are more strongly enriched in Zr than that they contain Pb (Figure 6.4D). However, Zr is also present in the amorphous matrix. It may be concluded that the crystalline nanoparticles in all investigated films contain primarily Zr. The amorphous matrix, in which the particles are embedded, contains Ti, Zr, and Pb. The high Zr concentration in the crystalline nanograins of Figures 6.1 – 6.4 suggests that it is a zirconium oxide-related phase.

The $1/\partial$-values of the FTs and their relative intensities agree with diffraction data from various phases ZrO_x, especially some of the recently characterized phases of zirconia nano-powders derived from wet-chemical synthesis routes [39,40]. More accurate identification is not possible due to the limited number of diffraction peaks, the polymorphism of zirconium oxide, and the limited size of the nanograins. However, in view of the environment in which these nanograins developed, it is very unlikely that a substoichiometric zirconia phase would have developed, so based on all available experimental data it is plausible that the nanograins consist of ZrO_2.

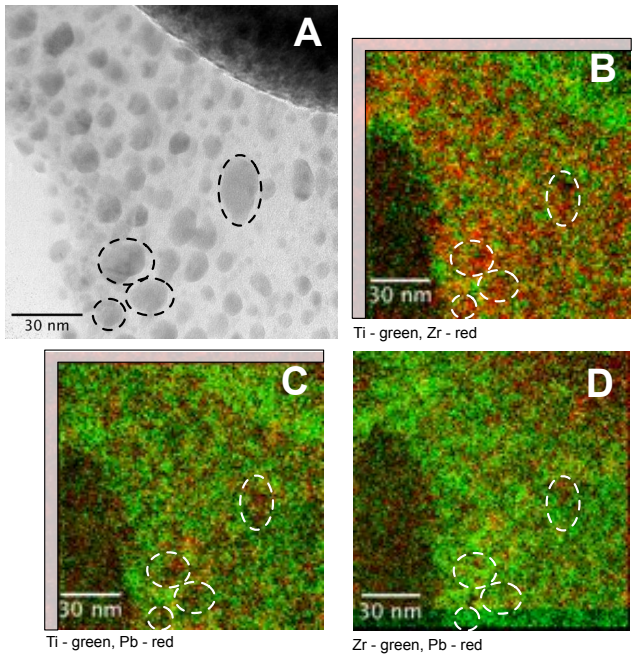

Figure 6.4. a) TEM bright-field image of the film made from the fresh PZT precursor sol without water, *i.e.*, h = 0.00; b-d) Corresponding elemental EELS mappings of Zr, Ti, and Pb, combined into colour images.

An experiment with a large excess of water, h = 111, was carried out to determine its influence on the morphology of as-deposited films. In this experiment water rather than organic solvents was the main component of the solvent mixture. A bright-field TEM image of the corresponding as-deposited film is shown in 6.5A. Darker grain-like regions, similar in size and shape to the ones shown in Figures 6.1 – 6.4 can be seen, but in this case the grains were virtually amorphous instead of crystalline. Figures 6.5B and 6.5C show the bright-field TEM and corresponding EELS mappings of Zr and Ti, respectively, in more representative regions. Figure 6.5C shows that the dark regions in Figure 6.5B correspond to areas with increased Zr concentration. Areas with majority concentrations of Zr and Ti are separated from each other on a length scale less than 10 nm. These results demonstrate that the crystalline character of the Zr-rich nanoparticles shown in Figures 6.1 – 6.4 is somehow related to the lower hydrolysis ratios in those sols. So while Zr-rich areas are still being formed at high water concentrations, their morphology is different, giving less or no evidence for crystallinity.

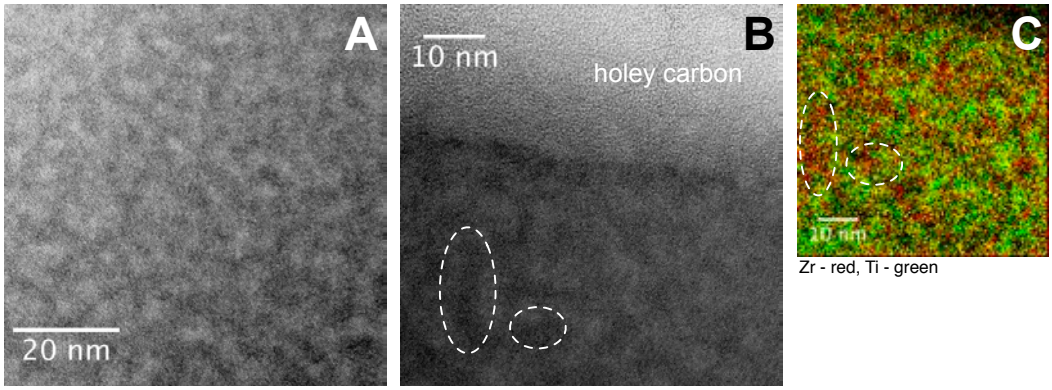

Figure 6.5. a) TEM bright-filed image of film made from fresh PZT precursor sol with h = 111; b) Bright-field TEM image of the same film recorded in a different area of the TEM specimen; c) Corresponding elemental EELS mappings of Zr and Ti, combined into colour image.

Ageing of PZT sols has a significant effect on the microstructure of the as-dried films. Films prepared from sols (h = 0) that had been aged for 40 h exhibited another microstructure than the films made from fresh sols. Figure 6.6A also shows evidence of agglomerate-like structures of ~ 40 nm diameter in the film. The corresponding EELS mappings in Figure 6.6B – D show a particle-like structure near the bottom of the figure, indicated by a dotted circle, that is strongly enriched in Zr, and is surrounded by an area that is strongly enriched in both Pb and Ti. A global SAED pattern of a film from an aged sol is shown in Figure 6.6E. Peak positions in the $1/\partial$ representation were found at approximately 3.65, 4.10, 4.97, 5.88, 6.70, 8.23, 8.95 and 10.1 nm^{-1}. Comparison of these values with the FTs in Figure 6.2B leads to the conclusion that the crystal structure in the polycrystalline film of Figure 6.6 closely

resembles the structure of the ZrO_2 nanoparticles in Figures 6.1 – 6.4. Small differences between the reciprocal distances, of the order of 2% or less, can be explained by differences in the calibrations of the camera length in SAED and HR-magnification in TEM.

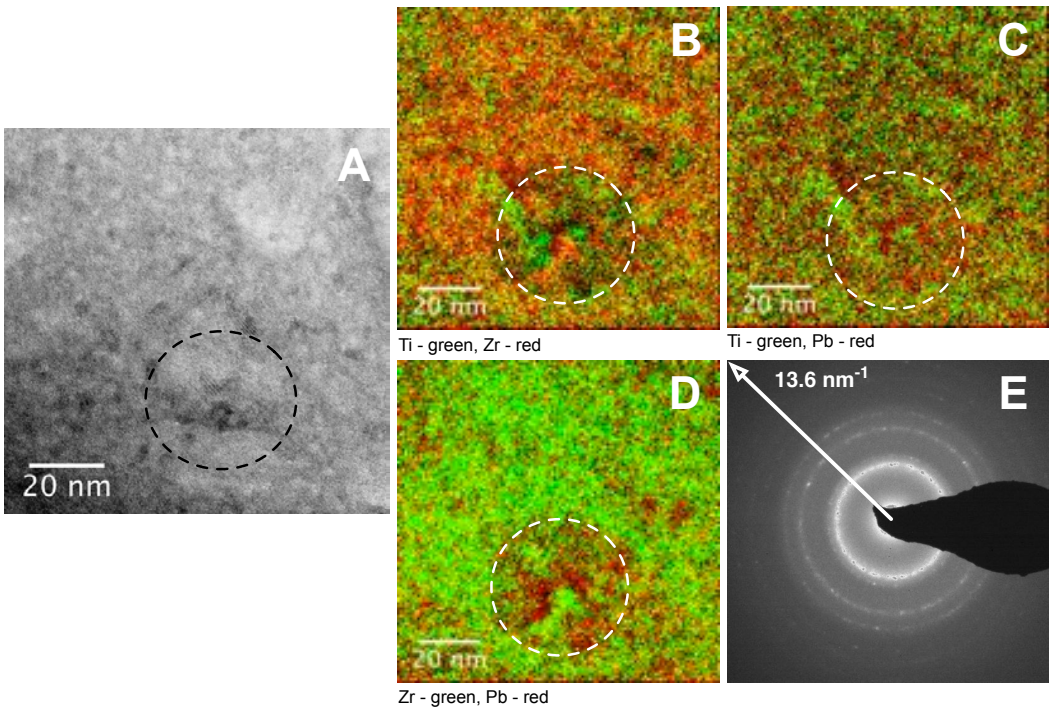

Figure 6.6. a) TEM image of film made from aged PZT precursor sol (h = 0.0); EELS mappings of: b) Zr and Ti; c) Pb and Ti; d) Pb and Zr; e) SAED pattern of film from aged PZT sol (h = 0).

6.3.2. Time-resolved XRD on drying thin films

In order to determine the structure of PZT sols in stages prior to the dried film stage, x-ray scattering/diffraction experiments were carried on 40 h aged PZT sols and *in situ* on drying thin films. This allowed to investigate and explain the emergence of the structural and compositional phenomena observed in as-dried films, as was discussed in the preceding section. Scattering/diffraction patterns of aged PZT precursor sols with varying h are shown in Figure 6.7A. In aged sols with h between 0.00 and 4.6, characteristic Bragg peaks developed. The narrow FWHM of these peaks indicates a high degree of order, which resulted from a crystallization process that occurred in the solution during ageing. Sols with $h > 9$ did not exhibit any sign of precipitation even after 40 h of ageing at 60 °C. In contrast, a precipitate could already be collected from the PZT sol without added water after a few minutes of ageing.

The diffraction pattern of the precipitate is shown in Figure 6.7B and 6.7C. The Bragg peaks are located at scattering vector positions q = 3.69, 3.97, 4.62, 5.20,

5.56, 5.87, and 6.09 nm^{-1}, which corresponds to $1/d$-values of 0.587, 0.632, 0.735, 0.828, 0.885, 0.934, and 0.969 nm^{-1}, respectively. The single spots in the 2D diffraction pattern in Figure 6.7C are indicative of a system with a small number of relatively large grains. Precipitates contained in sols with h up to 4.6 exhibited similar albeit less pronounced patterns.

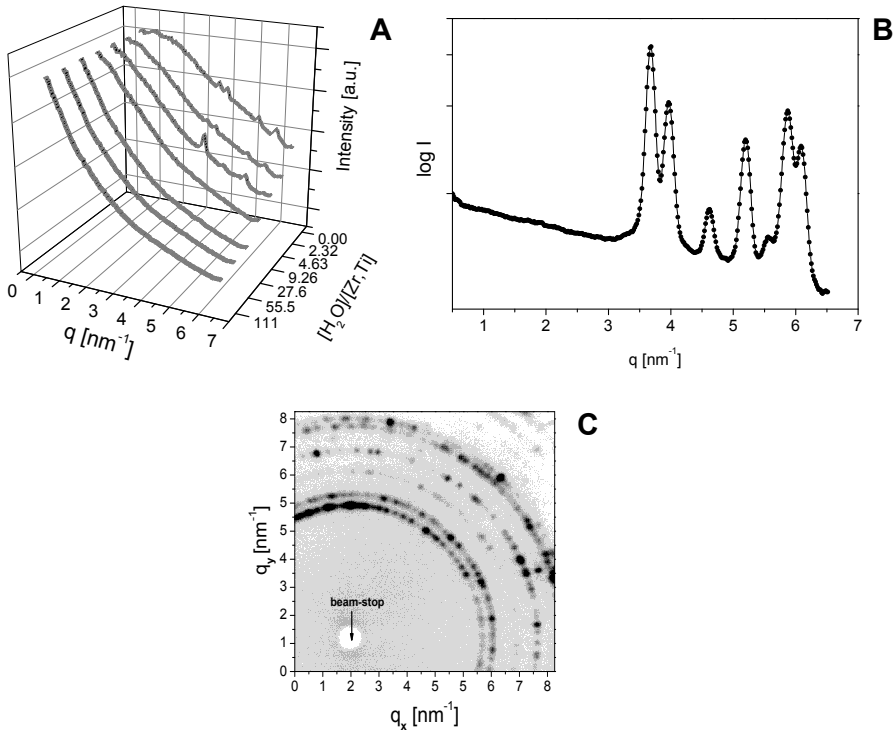

Figure 6.7. a) SAXS patterns of 0.3 mol/dm^3 PZT precursor sols with h between 0 and 111. b) SAXS/diffraction pattern of the phase precipitated from the PZT sol with h = 0.00. c) 2D SAXS/diffraction pattern of the same sol.

As was shown in the TEM analysis, the crystalline nanograins present in the as-dried PZT films and the precipitate from aged solutions contained mostly or exclusively Zr. By performing a series of simple mixing reactions of pairs of the three stock solutions and the two solvents (acetic acid and 2-methoxyethanol), it was found that precipitation was probably caused by the reaction between Zr alkoxide and acetic acid. It is most likely that an oligomeric zirconium alkoxyacetate or oxoacetate phase formed when h was small. Figure 6.8A illustrates the stability of a 0.50 mol/dm^3 solution of zirconium(IV) alkoxide in acetic acid at 60 °C. Bragg peaks of a precipitating crystalline phase were detected after 28 min of reaction. The corresponding 2D scattering pattern after 60 min is shown in Figure 6.8B. It demonstrates that the evolving Bragg peaks in Figure 6.8A result from a small number of crystalline grains. The peaks of the isotropic one-dimensional scattering

pattern are at scattering vector positions q = 3.69, 3.99, 4.63, 5.21, 5.62, 5.90, and 6.11 nm^{-1}. These q-values are in excellent agreement with those of the precipitates in the PZT precursor sols as shown in Figure 6.7. This suggests strongly that the precipitating phase in the PZT precursor sol is predominantly or exclusively related to the Zr component. Differences in relative intensities of corresponding peaks can be explained in terms of preferred orientation of crystals, as illustrated by the single reflections that are visible as isolated spots in Figure 6.8B.

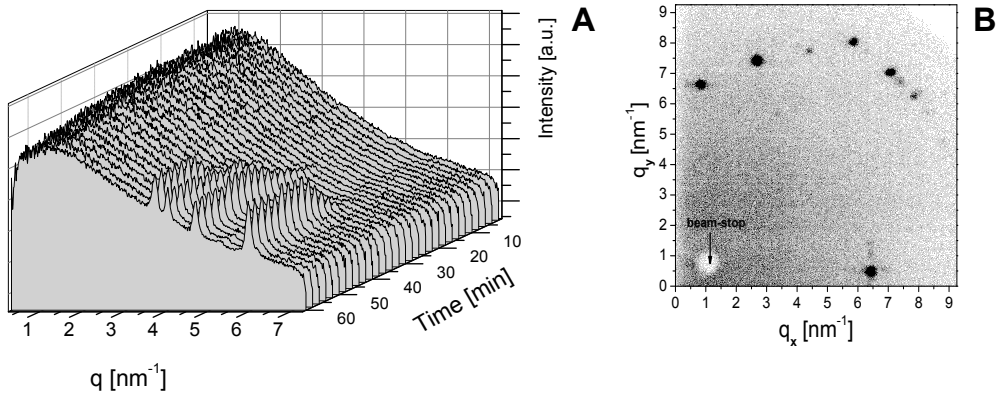

Figure 6.8. a) Time-resolved x-ray scattering patterns of developing 0.50 mol/dm^3 zirconia precursor sol at 60 °C; b) 2D SAXS pattern of zirconia precursor sol after 60 min of reaction.

It is apparent that the precipitating phase from PZT precursor sols contain the same or very closely related crystalline phase as the precipitate from a pure zirconia precursor sol when h < 5. In contrast, PZT sols with h > 9 did not show any evolving crystalline phase for at least 40 h at 60 °C. From the peak positions I attempted to identify the phase from Figures 6.7 and 6.9. The high values of ∂ indicated the presence of an oganometallic Zr compound in the group of zirconium alkoxy-carboxylates. Such crystals usually contain clusters composed of a hexanuclear octahedral zirconium oxo-hydroxo core and surrounding alkoxy and carboxy ligands, *e.g.*, $[Zr_6(\mu_3\text{-}O)_4(\mu_3\text{-}OH)_4(OOCR)_{12}]$ where R = *t*-butanoate, 2-methylpropanoate, propanoate, or acetate [41-43]. The actual crystal structure depends on the ligand environment. Furthermore, depending on the nature of the carboxylic acid group, dimerized hexanuclear clusters of general formula $[Zr_6O_4(OH)_4(OOCR)_{12}]_2$ have been synthesized, in which two hexanuclear subunits are bridged by four carboxylate ligands [43]. These clusters have the same stoichiometry but cannot be easily converted from one into the other despite their structural similarity. These systems obviously yield different diffraction patterns. In the experiments I used zirconium(IV) *n*-propoxide in 2-methoxyethanol (hence partially or completely substituted) and an excess of acetic acid. *n*-Propanol and water molecules were also

available in the sol. To the best of my knowledge, the crystal structure of a compound prepared under exactly the same conditions has never been solved and published. Nevertheless, based on x-ray diffraction pattern simulations from structural data of $[Zr_6O_4(OH)_4(OOCR)_{12}]_2$ complexes, I found close similarity between these hexanuclear octahedral zirconium oxo dimers and the compound in my experiments. Therefore, I refer to this crystalline nanophase as Zr oxoacetate clusters.

Thin film drying experiments using these sols were carried out with the designed setup (Figure 5.1, Chapter 5). A small volume of liquid was dropped into the rotating cylinder, just sufficient to form a thin wet PZT film that covered the entire spinning Kapton film, and dried in air. Figure 6.9 shows the time-resolved SAXS patterns of a drying film from a stable PZT precursor sol with h = 9.3 at 60 °C. A crystalline phase developed soon after drying started. The first indications appeared after about 4 min. The PZT film was most likely a dry after 10 – 12 min, when the scattering intensity reached a plateau. By this time the scattering intensity had decreased by ~90% or more over the entire q-range. This is an effect of solvent evaporation, which leads to loss of scattering contrast. The solid precursor entities in the film approach each other and agglomerate into larger structures in the course of drying. This leads to increasingly homogeneous film morphology, with accompanying loss of scattering contrast between scatterers and their surroundings. Furthermore, heavier elements such as Ti and especially Zr and Pb absorb light, which leads to decrease in scattering intensity. A detailed view into the process between 14 – 20 min is presented in Figure 6.9B. A very strong peak with a maximum at q = 5.63 nm^{-1}, accompanied by a weaker peak at q = 5.82 nm^{-1}, can be recognized. Peaks are also present at q = 3.00, 3.69 and 6.10 nm^{-1}. The peaks at q = 5.6 – 6.1 and 3.69 nm^{-1} can be attributed to the Zr oxoacetate nanoparticles. The origin of peak at q = 3.00 nm^{-1} is not exactly known, but it is probably related to another process taking place in the solution, possibly the aggregation of similarly sized nanoparticles.

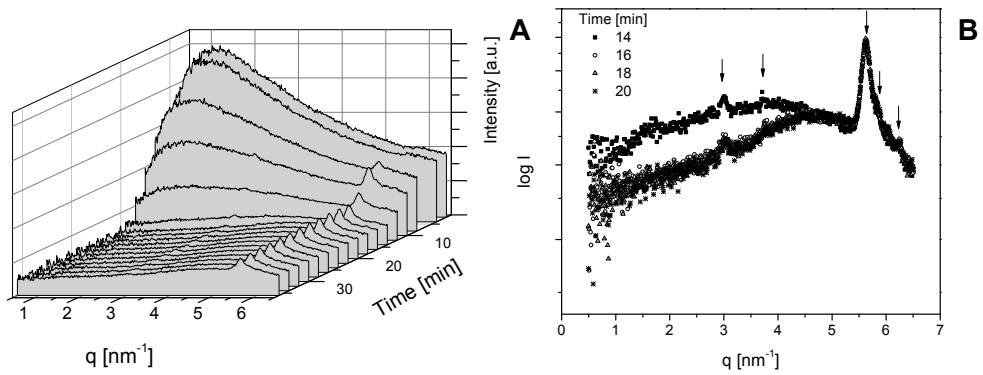

Figure 6.9. a) Time-resolved x-ray scattering measurement of developing PZT precursor with h = 9.3 upon drying at 80 °C. b) Detailed view of the process between 14th and 20th minute.

6.3.3. Influence of water and acetic acid on structure of films

The data presented above are the result of nucleation from nanoscale inhomogeneities in the sol-gel solution [33,44]. Chemical heterogeneity has also been observed in neutron scattering studies on PZT powders [33]. It was found that the Zr/Ti ratio varied widely at different locations in the samples. EXAFS studies of partially heat-treated PZT made from a 2-methoxyethanol based recipe also indicated chemical heterogeneity on an atomic level [45]. EXAFS on similar powders derived from metal *n*-butoxides indicated predominant Zr-O-Zr linkages, although Pb-O-Zr linkages were also observed [44]. My observations are in agreement with these studies. Water is responsible for hydrolysis of the metal alkoxides and hence, indirectly for the formation of sol particles. Secondly, due to its high polarity it facilitates dissociation in the solution. It should be noted that other polar solvents can play a similar role, *e.g.* methanol is often used in the Inverted Mixing Order method for the PZT precursor sol-gel system [11,12,17,24]. The presence of ions prevents oligomeric species from agglomeration and precipitation. But even in a stable sol, nucleation of precipitates can still be induced once a film is being formed, and water and other solvents evaporate from it. No clear differences were found between the microstructures of dried PZT films that had been prepared with hydrolysis ratios h anywhere between 0 and 27.6. This may be related to the presence of traces of water in the sample with nominal value $h = 0$. The crystalline particles are mainly Zr-based and most likely composed of zirconia. The amorphous matrix surrounding the Zr-rich grains contains both Zr and Ti, while Pb seems to be evenly distributed over the entire volume of the matrix. Even at the very high value $h = 111$, Zr-rich regions were present, but they were amorphous instead of crystalline. This supports the hypothesis that due to the high concentration of water in the drying film, it was longer present, thereby hindering crystallization of Zr-rich nanoparticles, or aiding in the transformation to an amorphous phase, *e.g.* a zirconium hydroxide related phase.

Acetic acid has been commonly used as stabilizing and chelating agent for many Ti and Zr alkoxides [11-13,16-18,46]. The overall $[CH_3COOH]/[Zr,Ti]$ and $[CH_3COOH]/[Zr]$ ratios exceeded 15 in this study. Doeuff *et al.* studied several Ti alkoxides and found that the product at $[CH_3COOH]/[Ti] > 5$ was a water-soluble precipitate with stoichiometry $TiO(CH_3COO)_2$ [47]. The chemical composition of the product was the same in all cases, irrespective of the nature of the alkoxy group.

In an equimolar mixture of Zr *n*-propoxide and Ti *iso*-propoxide with acetic acid at $[CH_3COOH]/[Zr,Ti] = 5$, the resulting cluster was $Zr_6Ti_3(OPr)_{16}(OAc)_8O_8$, with Pr = *iso*-$C_3H_7$ or *n*-C_3H_7 and Ac = acetate [46]. Precipitation was observed when $[CH_3COOH]/[Zr,Ti] > 5$.

Acetic acid modification of pure Zr *n*-propoxide and *n*-butoxide showed that up to three acetate ligands can react with Zr alkoxides [48]. Acetic acid is able to substitute terminal alkoxy groups without breaking the stable dimeric Zr-Zr unit present in

these alkoxides [49]. Hence, the chemical structure of the oxoacetate clusters does not depend on the alkoxy group, but on the metallic center and alkoxide to acetic acid ratio. The actual structure of mixed Zr/Ti oxoacetates should therefore depend on the [Zr]/[Ti] and [CH_3COOH]/[Zr,Ti] ratios. My experiments show that Zr oxoacetates are predominantly formed in solution, despite the high concentration of Ti precursor that was also present in solution. Since Zr alkoxides are more susceptible to substitution or hydrolysis than Ti alkoxides [50], this could explain why predominantly Zr-rich oxoacetates were formed in an excess of acetic acid. Ti oxoacetates may also have formed, but due to their oligomeric character and the presence of other species in the system such as lead(II) acetate and zirconium-based oligomers they remained amorphous. The Zr oxoacetates formed in excess of acetic acid precipitated either in the sol ($h < 5$) or in the drying thin film ($h > 9$). Zr oxoacetate probably formed molecular crystals rather than disordered oligomers [45]. This would explain why the PZT precursor sols exhibited both crystalline Zr-rich regions and Ti-rich amorphous regions. Since Zr oxoacetates are water soluble, no or limited crystallization could take place at $h > 100$, when water was present in the film for a long time during the evaporation process. In the film drying process the Zr oxoacetates could evolve into a crystalline ZrO_2 phase. Such transitions typically require a relatively high temperature [24]. In the present case, however, one is dealing with a limited number of sub-10 nm particles. Possibly, the extensive drying in the electron microscope vacuum and the energy of the electron beam were sufficient to re-crystallize Zr oxoacete into ZrO_2 In that case one cannot discriminate between the influence of the electron microscope measurement and spontaneous phase transformations induced by drying. Nevertheless, both the precursor sol and the as-dried thin films contain either Zr-oxoacetate or a crystalline ZrO_2 nanophase.

6.4. Conclusions

Zr-rich nanoparticles of 1 – 10 nm size are present in as-dried PZT films. At hydrolysis ratios h up to at least 27.6, these nanoparticles are crystalline, and the surrounding Ti and Zr-rich matrix is amorphous. The crystalline nanoparticle phase originates from crystalline material that precipitates from a pure zirconia sol in an excess of acetic acid, and is most likely a nanocrystalline zirconium oxoacetate phase. At $h < 5$, the zirconium oxoxacetate nanophase formed directly in fresh sols. Stable sols without a trace of crystallinity formed when h was between ~ 5 and 27.6. But the same crystalline nanophase formed *in situ* when these sols were dried as thin films. At $h > 100$, no crystallization of Zr-rich nanoparticles occurred in either the sol or in the as-dried film.

Films prepared from aged sols had a higher degree of crystallinity than films from fresh sols. EELS maps of Ti and Zr indicate that their spatial distribution in an aged film fluctuated on a length scale of 80 – 100 nm. It seems that such compositional heterogeneity occurs on a longer length scale in films from aged sols than from fresh sols.

6.5. References

[1] Scott, J. F.; Paz De Araujo, C. A. *Science*, 246, 1400-1405, **1989**.

[2] Scott, J. F. *Science*, 315, 954-959, **2007**.

[3] Muralt, P. *J. Micromech. Microeng.*, 10, 136-146, **2000**.

[4] Kondo, M.; Sato, K.; Ishii, M.; Wakiya, N.; Shinozaki, K.; Kurihara, K. *Jpn. J. Appl. Phys.*, 45, 7516-7519, **2006**.

[5] Kim, H. R.; Jeong, S.; Jeon, C. B.; Kwon, O. S.; Hwang, C. S. *J. Mater. Res.*, 16, 3583-3591, **2001**.

[6] Otani, Y.; Okamura, S.; Shiosaki, T. *J. Electroceram.*, 13, 15-22, **2004**.

[7] Lin, Y. C.; Chuang, H. A.; Shen, J. H. *Vacuum,* 83, 921-926, **2009**.

[8] Bouregba, R.; Poullain, G.; Vilquin, B.; Murray, H. *Mater. Res. Bull.,* 35, 1381-1390, **2000**.

[9] Zhu, T. J.; Lu, L.; Lai, M. O. *Appl. Phys. A,* 81, 701-714, **2005**.

[10] Dekkers, M.; Nguyen, M.D.; Steenwelle, R.; te Riele, P.M.; Blank, D.H.A.; Rijnders, G. *Appl. Phys. Lett.,* 95, 0129021-0129023, **2009**.

[11] Schwartz, R. W. *Chem. Mater.,* 9, 2325-2340, **1997**.

[12] Schwartz, R. W.; Boyle, T. J.; Lockwood, S. J.; Sinclair, M. B.; Dimos, D.; Buchheit, C. *Integr. Ferroelectrics, 7*, 259-277, **1995**.

[13] Yi, G.; Sayer, M. *Ceram. Bull.*, 70, 1173-1179, **1991**.

[14] Klee, M.; Eusemann, R.; Waser, R.; Brand, W.; van Hal, H. *J. Appl. Phys.*, 72, 1566-1576, **1992**.

[15] Cui, T.; Markus, D.; Zurn, S.; Polla, D. L. *Microsyst. Technol.,* 10, 137-141, **2004**.

[16] Schwartz, R. W.; Voigt, J. A.; Tuttle, B. A.; Payne, D. A.; Reichert, T. L.; DaSalla, R. S. *J. Mater. Res.*, 12, 444-456, **1997**.

[17] Assink, R. A.; Schwartz, R. W. *Chem. Mater.*, 5, 511-517, **1993**.

[18] Zhang, M.; Salvado, I. M. M.; Vilarinho, P. M.; Silvestre, A. J. D.; Silva, A. M. S. *J. Am. Ceram. Soc.,* 90, 358-363, **2007**.

[19] Caruso, R.; de Sanctis, O.; Frattini, A.; Gil, C. S. R., *Surface and Coating Techn.*, 122, 44-50, **1999**.

[20] Boyle, T. J.; Dimos, D.; Schwartz, R. W.; Alam, T. M.; Sinclair, M. B.; Buchheit, C. D. *J. Mater. Res.,* 12, 1022-1030, **1997**.

[21] Zhang, Q.; Huang, Z.; Vickers, M. E.; Whatmore, R. W. *J. Eur. Ceram. Soc.,* 19, 1417-1421, **1999**.

[22] Zhang, Q.; Vickers, M. E.; Patel, A.; Whatmore, R. W. *J. Sol-Gel Sci. Technol.*, 11, 141-152, **1998**.
[23] Zhang, Q.; Whatmore, R. W.; Vickers, M. E. *J. Sol-Gel Sci. Technol.*, 15, 13-22, **1999**.
[24] Schwartz, R. W.; Schneller, T. S.; Waser, R. *C. R. Chimie*, *7*, 433-461, **2004**.
[25] Schwartz, R. W.; Narayanan, M. Chemical Solution Deposition - Basic Principles, In *Solution Processing of Inorganic Materials*, ed. Mitzi, D. B., John Wiley & Sons, Inc., New Jersey, 33-76, **2009**.
[26] Malic, B.; Kosec, M.; Arcon, I.; Kodre, A. *J. Europ. Ceram. Soc.,* 25, 2241-2246, **2005**.
[27] Chae, H. K.; Payne, D. A.; Xu, Z.; Ma, L. *Chem. Mater.*, 6, 875-877, **1994**.
[28] Brethon, A.; Hubert-Pfalzgraf, L. G. *J. Sol-Gel Sci. Technol.*, 39, 159-167, **2006**.
[29] Brethon, A.; Hubert-Pfalzgraf, L. G., Daran, J. -C. *Dalton Trans.*, 1, 250-257, **2006**.
[30] Hubert-Pfalzgraf, L. G.; Daniele, S.; Papiernik, R.; Massiani, M. C.; Septe, B.; Vaissermann, J.; Daran, J. -C. *J. Mater. Chem., 7*, 753-762, **1997**.
[31] Daniele, S.; Papiernik, R.; Hubert-Pflazgraf, L. G.; Jagner, S.; Hikansson, M. *Inorg. Chem.,* 34, 628-632, **1995**.
[32] Brinker, C. J.; Hurd, A. J.; Schunk, P. R.; Frye, G. C.; Ashley, C. S. *J. Non-Cryst. Solids,* 147-148, 424-436, **1992**.
[33] Schneller, T.; Waser, R. *J. Sol-Gel Sci. Technol.,* 42, 337-352, **2007**.
[34] Khan, S. U.; Göbel, O. F.; Blank, D. H. A. ten Elshof, J. E. *Appl. Mater. Interfaces*, 10, 2250-2255, **2009**.
[35] Rasband, W.S., ImageJ, U.S. National Institute of Health, Bethesda, Maryland,, http://imagej.nih.gov/ij/, **1997-2011**.
[36] Bras, W.; Dolbnya, I. P.; Detollenaere, D.; van Tol, R.; Malfois, M.; Greaves, G. N.; Ryan, A. J.; Heeley, E. *J. Appl. Crystallogr.,* 36, 791-794, **2003**.
[37] Craievich, A. F. *Mater. Res.,* 5, 1-11, **2002**.
[38] Porod, G. General theory *In Small Angle X-ray Scattering*, ed. Glatter, O.; Kratky, O. Academic Press, London, 17-52, **1982**.
[39] Lamas, D. G.; Rosso, A. M.; Suarez-Anzorena, M.; Fernandez, A.; Bellino, M. G.; Cabezas, M. D.; Walsöe de Reaca, N. E.; Craievich, A. F. *Scripta Mater.*, 55, 553-556, **2006**.
[40] Bhagwat, M.; Ramaswamy, V. *Mater. Res. Bull.*, 39, 1627-1640, **2004**.
[41] Piszczek, A.; Radtke, A.; Grodzicki A.; Wojtczak, A.; Chojnacki, J. *Polyhedron*, 26, 679-685, **2007**.
[42] Kogler, F. R.; Jupa, M.; Puchberger, M.; Schubert, U. *J. Mater. Chem.*, 14, 3133-3138, 2004.
[43] Puchberger, M.; Kogler, F. R.; Jupa, M.; Gross, S.; Fric, H.; Kickelbick, G.; Schubert, U. *Eur. J. Inorg. Chem*,. 16, 3283-3293, **2006**.

[44] Malic, B.; Arcon, I.; Kodre, A.; Kosec, M. *J. Sol-Gel Sci. Technol.*, 16, 135-141, **1999**.

[45] Sengupta, S. S.; Ma, L.; Adler, D. L.; Payne, D. A. *J. Mater. Res.,* 10, 1345-1348, **1999**.

[46] Laaziz, I.; Larbot, A.; Julbe, A.; Guizard, C.; Cot, L. *J. Solid State Chem.,* 98, 393-403, **1992**.

[47] Doeuff, S.; Henry, M.; Sanchez, C. *Mat. Res. Bull.,* 25, 1519-1529, **1990**.

[48] Peter, D.; Erstel, T. S.; Bertagnolli, H. *J. Sol-Gel Sci. Technol.*, 5, 5-14, **1995**.

[49] Peter, D.; Erstel, T. S.; Bertagnolli, H. *J. Sol-Gel Sci. Technol.*, 3, 91-99, **1994**.

[50] Wright, J .D.; Sommerdijk, N. A. J. M. Sol-gel Materials Chemistry and Applications, Advanced Chemistry Texts, CRC Press, Boca Raton, **2001**.

6.5. Appendix: EELS mapping Pb-$M_{4,5}$

Electron energy loss spectra of as-dried PZT thin film with h = 9.3 are shown in Figure 6.10. The measurement demonstrates that the lead $M_{4,5}$ transition can be resolved with the used spectrometer at an exposure time of 25 s. In the experiments I used an exposure time of 40 s to determine the distribution of Pb. Some problems might result from the effect of drift. Therefore, the sample thickness was optimized in order to accomplish optimal conditions. The sample should be neither too thick, nor too thin. For lead mapping (and also for titanium and zirconium) I followed a "no-tolerance" policy for impeded data quality: pre-edge and post-edge spectra were collected with eight times binning. Hence, 2048x2048 images were averaged into 256x256 maps. Furthermore, I used the manual mode of the software to combine pre-edge and post-edge data. If I lost more than 1% of the map resolution in this procedure, I discarded the data set. Eventually all the mappings resulted in 256x256 elemental maps.

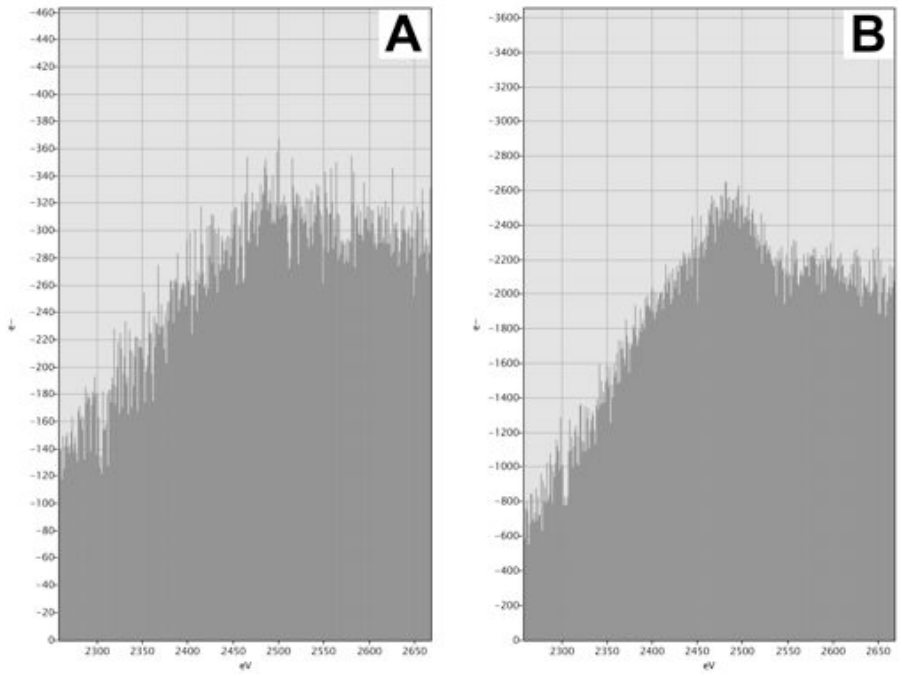

Figure 6.10. EELS mapping of Pb-$M_{4,5}$ edge (pre-edge 2324 eV, post-edge 2534 eV, slit width 100 eV). a) Exposure time 10 s; a) Exposure time 25 s.

7

Time-Resolved Small Angle X-ray Scattering Study of Sol-Gel Precursor Solutions of Lead Zirconate Titanate and Zirconia*

Abstract

The evolution of nanostructure in sol-gel derived lead zirconate titanate (PZT) and zirconia precursor sols at different hydrolysis ratios was investigated by small angle x-ray scattering (SAXS). The shape of the clusters in the zirconia sol could be described by the length-polydisperse cylindrical form factor. The zirconia-based clusters were characterized by a cross-sectional radius, r_0, of 0.28 nm, and a practically monodisperse length of *ca*. 1.85 nm. These clusters were probably constructed of zirconia-related tetrameric building blocks. Similar cylindrical structural motifs were observed in PZT precursor sols with $[H_2O]/[Zr,Ti]$ = 9.26 and 27.6, but the polydispersity in length was much higher. Clear scattering contributions from Ti and Pb centers were not detected, which was interpreted in terms of a homogeneous distribution of unbound lead ions in solution, and the relatively low scattering intensity from any Ti-based clusters or oligomers that may have been present in the sols.

7.1. Introduction

Lead zirconate titanate ($PbZr_{1-x}Ti_xO_3$; PZT) is a technologically important ceramic material mainly due to its large remnant polarization, low coercive field, and high piezoelectric coefficients. It is applicable in a wide range of applications, many of which are based on the use of PZT thin films. Therefore, various thin film fabrication methods have been extensively studied [1-4]. Most common are metal-organic chemical vapor deposition (MOCVD) [5,6], sputtering [7,8], and pulsed laser deposition for the deposition of thin films of PZT [9,10]. On the other hand, chemical solution deposition techniques (CSD) [11] including the sol-gel routes [12,13], and metal-organic deposition (MOD)[14,15] have been successfully employed to fabricate PZT thin films. The sol-gel technique has attracted considerable attention

* In preparation:
Stawski, T. M.; Besselink, R.; Veldhuis, S. A.; Castricum, H. L.; Blank, D. H. A.; ten Elshof, J. E.

because of its simplicity, low cost, good compositional control and its potential for large area film fabrication [16].

The properties of sols are controlled by the nature of the metal-carrying reagent, solvent, reagent concentration, water concentration, method of water addition, catalyst, solution preparation/reaction conditions and other factors [11,12]. Typically, PZT sol-gel solutions consist of Ti(IV) and Zr(IV) alkoxides and either Pb(II) or Pb(IV) carboxylate precursors, solvents, water and a catalyst. Acetic acid acts as a key chelating agent, affecting the reactivity and promoting esterification reactions that result in many alkyl acetate esters as byproducts. Metal oxoacetates and/or metal alkoxy acetates are formed due to (partial) exchange of alkoxy ligands by acetate [17]. Most metal alkoxides or metal carboxylates and oxocarboxylates can form oligomeric structures in appropriate solvents. Well-known examples are $Ti_6(O^iPr)_{10}(OOCCH_3)_4O_4$, $Ti_6(O^iPr)_8(OOCCH_3)_8O_4$ and $Zr_4O(OPr)_{10}(CH_3COCH_2COCH_3)$ [11,12]. Several complexes of Pb and Ti or Zr precursors in similar solvents have also been reported [18-22]. All of these complexes formed in the absence of water, *i.e.*, without the hydrolysis step that is typical for initiating sol-gel processes.

In the "classical" sol-gel process an alcohol, *e.g.* 2-methoxyethanol, is used as primary solvent for the dissolution and stabilization of the three elemental metal components. In the case of PZT a combined Pb-Ti-Zr alkoxide is known to form [11,12,16,17, 23-26]. Alternatively, in the chelating method, Pb(II) or Pb(IV) acetate is dissolved in acetic acid prior to mixing with alkoxides that have been modified by, for instance, 2-methoxyethanol. In this case, acetic acid is also known to chelate metal centers in alkoxides, leading to the formation of metal oxoacetates [11-13,17,23,24,27-29]. A derivative of the latter sol preparation method was utilized in the experiments described in this paper. In particular, I focused on a PZT model solution that has been used successfully to imprint PZT nanopatterns with a lateral resolution below 200 nm by soft lithography [30]. I showed in Chapter 6 and in ref [31] that nanocrystalline ZrO_2 domains of 2 – 10 nm develop in drying thin films of similar PZT model sols.

It is known that the nature of the sol has a profound effect on the microstructure, orientation and electrical properties of the films [12,16,26]. But despite various studies involving nuclear magnetic resonance [17,27,32-34], Fourier transform infrared spectroscopy [33,34], gas chromatography-mass spectroscopy [32], photon correlation spectroscopy [27-29] and small angle x-ray scattering [27-29], relatively few details are known about the structural evolution of PZT sols, especially where it concerns the quantitative microstructural parameters of sols and their relationship to measurable chemical properties.

Pioneering SAXS studies of alkoxide-carboxylate PZT precursor sols with a Pb : Ti : Zr ratio of 100 : 70 : 30 suggested that rod-like structures constituted an

important structural motif of lead zirconate titanate and lead zirconate precursor sols [27-29]. The radii of gyration were determined from fits of the experimental data to the Guinier approximation, and were found to be 4 – 5 nm [28]. Rod lengths were calculated by fitting to a Guinier approximation for rod-like particles, and were in the range of 6 – 8 nm [29]. However, the validity of this analysis depends on the absence of polydispersity in the rod lengths [28], which cannot be assumed *a priori* in such relatively complex solutions. The absence of clearly linear regions in a number of Guinier plots [28,29] suggests that the actual structure in solution may be more complicated than was initially concluded. The authors speculated on the formation of core-shell structures [29], but no features of a core-shell morphology were identified in the scattering curves.

It was the aim of this study is investigate the structure of relatively similar sol-gel PZT model solutions on a nanometer-length scale in more detail. The hydrolysis step was introduced in order to initiate the structural evolution of sols. *In situ* small angle x-ray scattering measurements were performed to investigate the evolution of PZT after hydrolysis in solutions containing stoichiometric ratios of Pb, Zr and Ti, and compared the results with scattering curves from zirconia precursor sols. I used a Length Polydisperse Cylinder model to fit the experimental data, and compared them with a Guinier approximation for rod-like particles.

7.2. Experimental

7.2.1. Synthesis of lead zirconate titanate (PZT) precursor sols

Lead(II) acetate trihydrate (99%, Sigma-Aldrich), zirconium(IV) *n*-propoxide (70% w/w in *n*-propanol, Alfa Aesar) and titanium(IV) *iso*-propoxide (99.999%, Sigma-Aldrich) were used as precursor materials. Glacial acetic acid (99.8%, Acros) and 2-methoxyethanol (> 99.3%, Sigma-Aldrich) were used as solvents, stabilizers, and chelating agents. Three stock solutions were made, each with a concentration of 0.60 mol/dm^3. A Pb-acetate solution was prepared by dissolving lead(II) acetate trihydrate in acetic acid and subsequent refluxing at 105 °C for 8 h to remove all remaining water. The other two solutions were based on titanium *iso*-propoxide and zirconium *n*-propoxide, respectively, with 2-methoxyethanol as solvent. They were stirred in a glove box under nitrogen atmosphere at room temperature for 24 h, and then stored at room temperature until further use. Prior to the experiments, the stock solutions were mixed in the appropriate molar ratios and stirred for 5 – 10 min. The Ti and Zr stock solutions were first mixed and added to the lead acetate solution. The molar ratio Pb : Zr : Ti was always kept at 100 : 52 : 48, yielding a concentration of 0.30 mol/dm^3 in the final PZT solution. Solutions of this concentration were used in all experiments. Hydrolysis was initiated by addition of water immediately after the

three stock solutions had been mixed. Two hydrolysis ratios were investigated, namely $[H_2O]/[Zr,Ti]$ = 9.26 and 27.6

7.2.2. Synthesis of zirconia precursor sol

Zirconium(IV) *n*-propoxide (70% w/w in *n*-propanol, Alfa Aesar) was used as precursor. Glacial acetic acid (99.8%, Merck) and 2-methoxyethanol (99.3%, Sigma-Aldrich) were used as chelating agents, solvents and stabilizers. Zirconium(IV) *n*-propoxide was dissolved in 2-methoxyethanol and stirred in a glove box under nitrogen atmosphere, yielding a 1.00 mol/dm^3 stock solution. Then the zirconium(IV) alkoxide stock solution was mixed with acetic acid, yielding a 0.67 mol/dm^3 solution. Finally, the solution was hydrolyzed at $[H_2O]/[Zr]$ = 5.

7.2.3. Time-resolved Small Angle X-ray Scattering of PZT and zirconia sols

SAXS experiments were performed on the Dutch-Belgian beamline (DUBBLE) BM-26B of the ESRF in Grenoble, France [35]. The beam was focused at the corner of a 2D gas-filled multiwire proportional detector in order to maximize the range of accessible q values (scattering vector values). The beam energy was 16 keV (λ = 0.0776 nm). The samples were placed at a distance of 1.5 m from the detector and the intensity was measured in the range $0.13 < q < 8.42$ nm^{-1}. The raw data were corrected for the pixel-dependent detector sensitivity and integrated for channels with the same q values. To investigate *in situ* the evolution of PZT and zirconia precursor sols at elevated temperatures, SAXS data were collected on sols in lithium borate beryllium oxide glass sealed capillaries (Ø = 1.0 mm, glass no. 14, Hilgenberg, Malsfeld, Germany) that were mounted into a thermostat (Linkam), which was operated at 60 °C. Measurements were done with 2 – 5 min intervals for time periods of typically1 h.

7.3. Small angle x-ray scattering data interpretation

In SAXS experiments the elastic scattering of x-rays by a sample that has local fluctuations in its electronic density is recorded at very small angles. Structural information about entities with dimensions of 0.3 - 50 nm such as colloids and powders can be derived from the used angular range [36-39]. In a typical SAXS experiment, the scattering intensity $I(\boldsymbol{q})$ is plotted versus the modulus of the scattering vector $\boldsymbol{q}$ (nm^{-1}), which is related to the scattering angle 2θ and the wavelength λ (nm) of the incident beam via

$$q = 4\pi / \lambda \sin\theta \qquad (7.1)$$

In general the scattering amplitude A in a given direction from an object of electron density $\rho(\boldsymbol{r})$ is expressed by Equation (7.2) [36,38].

$$A(\boldsymbol{q}) = \int \rho(\boldsymbol{r}) \exp(-i\boldsymbol{q}\cdot\boldsymbol{r}) \mathrm{d}\boldsymbol{r} \qquad (7.2)$$

Hence, the scattered intensity in the direction defined by a scattering vector is $I(\boldsymbol{q}) = AA^*$, where A^* is the complex conjugate of A.

7.3.1. Guinier approximation for rod-like particles

In the case of rod-like particles of length L and cross-sectional radius r_0, where $L >> r_0$, the scattering amplitude $A(q)$ can be split into length-related and cross-section-related components [38]. The scattering curve $I(q)$ of a rod-like object is given by Equations (7.3) and (7.4), where the cross-sectional radius of gyration R_C is related to r_0 via $r_0 = 2^{1/2}R_C$.

$$I(q) = I(0) \cdot L \cdot \frac{\pi}{q} \cdot I_C(q) \qquad (7.3)$$

$$I_C(q) \propto \exp\left(\frac{-q^2 R_C^2}{2}\right) \qquad (7.4)$$

Equation (7.4) is valid when $2\pi/L < q < 1/R_C$. The scattering intensity at zero angle is given by $I(0) = N(\Delta\rho)^2 V^2$, where V is the scattering volume of a particle, N is the number density of particles, and $\Delta\rho$ is the difference between the electron density of the scattering particle and its surrounding matrix. Equation (7.4) is independent of the actual shape of the cross-section in the applicable q range, provided that the particle sizes and shapes are sufficiently monodisperse. Thus, if a given system is composed of rod-like particles of relatively monodisperse cross-sectional dimension, the plot ln $I(q)q$ vs. q^2 should show a straight line. Equation (7.4) is known as the Guinier approximation for rod-like particles [36,38].

7.3.2. Form factor of length polydisperse cylinders

Equations (7.3) and (7.4) are approximations of more rigorous expressions. For rod-like particles of length L and circular cross-section radius r_0, the cylinder form factor Equation (7.5) can be used [40,41].

$$P_{cyl}(q, r_0, L) = \int_0^{\pi/2} \left[\frac{2J_1(qr_0 \sin\alpha)}{qr_0 \sin\alpha}\right]^2 \left[\frac{\sin\left(\frac{1}{2}qL\cos\alpha\right)}{\frac{1}{2}qL\cos\alpha}\right]^2 \sin\alpha \, \mathrm{d}\alpha \qquad (7.5)$$

where $J_1(x)$ is the first order Bessel function, and α is the angle between the long axis of the cylinder and the primary beam. In most systems the polydispersity must also be taken into account. In the case of polydisperse cylinders of z-average form factor $P_z(q,r_0,L)$, the volume distribution $w(L)$ is included as in equation (6) [42-45]:

$$P_z(q,r_0,L)=\frac{\int_0^\infty L\cdot w(L)\cdot P_{cyl}(q,r_0,L)\,dL}{\int_0^\infty L\cdot w(L)\,dL} \quad \Rightarrow \quad I(q)=I(0)\cdot P_z(q,r_0,L) \qquad (7.6)$$

Due to its convenient parameterization, the Zimm-Schulz-Flory distribution Equation (7.7) is used in the present work. This distribution has often been employed to analyse scattering data from ladder-like or worm-like polymers [43-45].

$$w(L)=\frac{L^z}{\Gamma(z+1)}\left(\frac{z+1}{L_w}\right)^{z+1}\exp\left(-\frac{z+1}{L_w}\cdot L\right) \qquad (7.7)$$

Here L_w is the weight-averaged length of the cylinders, L_n is the number-averaged length and $z^{-1} = L_w/L_n - 1$. The ln $I(q)q$ vs. q^2 plots were made based on Equations (7.3) and (7.4), to evaluate the shape of the particles, and determine values for R_C from appropriate linear regression fits. Then, based on these representations the more advanced polydisperse cylinder models were employed. Equations (7.5) – (7.7) were used to fit all experimental data using the well-known Levenberg – Marquardt algorithm [46,47]. Sets of parameters $I(0)$, r_0, L_w and z were calculated for all individual scattering curves, providing more detailed information about the dimensions and polydispersity of the particles.

7.4. Results and Discussion

7.4.1. Time-resolved SAXS experiments

Figure 7.1A shows plots of ln $I(q)q$ as a function of q^2 of the zirconia precursor sol. Figure 7.1B and 7.1C show similar data of PZT precursor sols with hydrolysis ratios $[H_2O]/[Zr,Ti]$ = 9.26 and 27.6, respectively. The insets on the right-hand side of Figures 7.1A – C show linear fits to the first and last scattering curve from each series in the range $20 < q^2 < 40$, where Equation (7.4) is valid. The linear ranges in this Guinier representation for rod-like particles ln $I(q)q$ versus q^2 in Figure 7.1 indicate that all three sols consisted of anisotropic, elongated scatterers, and that the scatterers in all three sols had identical cross-sectional dimensions. The cross-sectional radius of gyration R_C was calculated using Equation (7.4). Under the assumption that the scatterers have a circular cross-section, the factor $2^{1/2}R_C$ is plotted as a function of time in Figure 7.2. The scattering particles in the zirconia precursor sol had a constant value of $2^{1/2}R_C$ of *ca.* 0.27 nm throughout the experiment. The PZT precursor sol with $[H_2O]/[Zr,Ti]$ = 9.26 had a similar value of 0.24 – 0.27 nm, and the PZT sol with $[H_2O]/[Zr,Ti]$ = 27.6 had a lower value of ~ 0.13 nm for $2^{1/2}R_C$. The similar values and trends in R_C for the zirconia sol and the PZT precursor sol with $[H_2O]/[Zr,Ti]$ = 9.26 may indicate that these two sols contain very similar species in

terms of dimensions and shape. Differences between the respective values are discussed below. The smaller values of R_C of the PZT sol with $[H_2O]/[Zr,Ti]$ = 27.6 suggests that another kind of species was formed in the precursor solution at higher hydrolysis ratio.

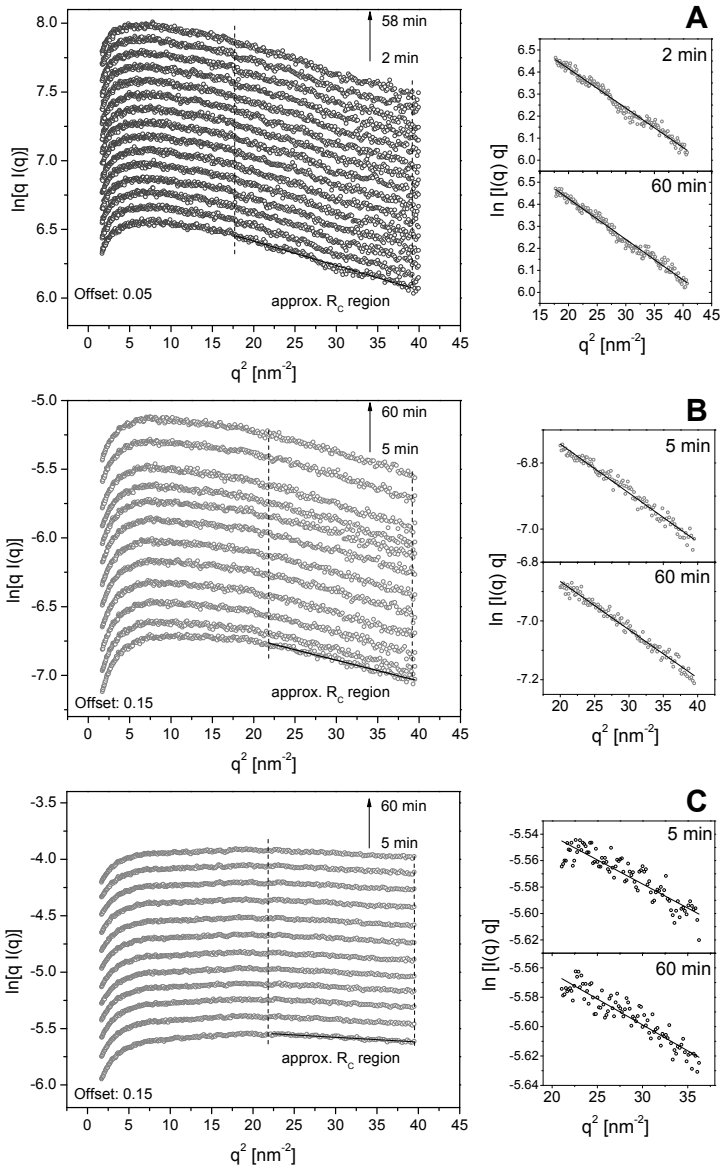

Figure 7.1. ln $I(q)q$ vs. q^2 plots and exemplary linear plots from which cross-section radius of gyration, R_c, was calculated for: a) zirconia precursor sol of initial concentration of 0.67 mol/dm^3 and hydrolyzed with $[H_2O]/[Zr]$ = 5; b) PZT precursor sol of initial concentration of 0.30 mol/dm^3 and hydrolyzed with $[H_2O]/[Zr,Ti]$ = 9.26; c) PZT precursor sol of initial concentration of 0.30 mol/dm^3 and hydrolyzed with $[H_2O]/[Zr,Ti]$ = 27.6.

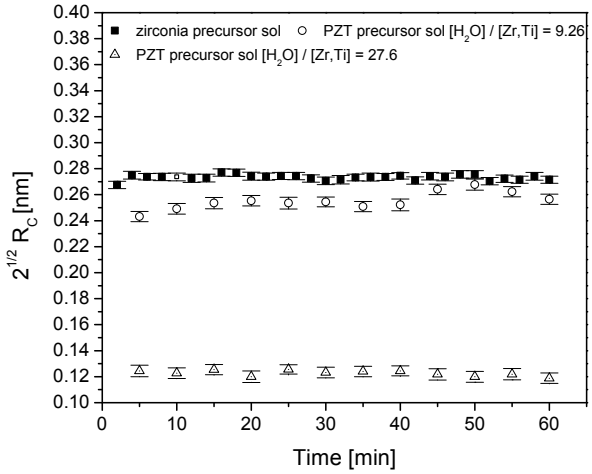

Figure 7.2. Evolution of R_c as a function of time for zirconia precursor sol of initial concentration of 0.67 mol/dm^3 and hydrolyzed with [H_2O]/[Zr] = 5; PZT precursor sol of initial concentration of 0.30 mol/dm^3 and hydrolyzed with [H_2O]/[Zr,Ti] = 9.26; PZT precursor sol of initial concentration of 0.30 mol/dm^3 and hydrolyzed with [H_2O]/[Zr,Ti] = 27.6. The parameter values were derived from data in presented Figure 7.1.

A more detailed analysis was carried out by fitting the experimental data with a length-polydisperse cylinder model using Equations (7.5) to (7.7). Different form factors were attempted in the fitting routines, such as cylinders with elliptical cross-section, elongated ellipsoids, and core-shell variations of these form factors. These analyses confirm that a cylinder form factor described the investigated structures best. The data sets of all three sols are shown on the left side in Figure 7.3. Experimental data of two selected scattering curves and their best fits are presented on the right hand side in Figure 7.3.

For each scattering curve a set of four fit parameters was determined, namely r_0 (radius of cylinder), L_w (mass averaged cylinder length), z (a measure of the polydispersity in the length of a set of cylinders), and $I(0)$, the scattering intensity in the limit towards zero scattering angle. It is noted that all scattering curves were fitted independently from each other.

Figures 7.4 – 7.6 show fitted values of r_0, L_w and z, respectively. The latter two parameters are directly related to the polydispersity index (*PDI*), defined here as $PDI = L_w/L_n = z^{-1} + 1$. The inset in Figure 7.7 shows the evolution of $I(0)$ as a function of time of the same sols. Due to the fact that all three samples were measured in capillaries with slightly varying dimensions, and the SAXS patterns of the PZT and zirconia sols were measured using different calibrations of the experimental setup, the intensity is shown in arbitrary units. The values of $I(0)$ can therefore only be compared within a single measurement series, and only trends can be interpreted. However, since $I(0) = NV^2(\Delta\rho)^2$ and $V \sim r_0^2 L_w$, the mass-averaged product of particle

number density and squared electron density difference $\langle N(\Delta\rho)^2\rangle_w$ can be expressed as:

$$\left\langle \left(\Delta\rho\right)^2 N \right\rangle_w = \left\langle I(0)V^{-2} \right\rangle_w \sim \left\langle I(0)L_w^{-2}r_0^{-4} \right\rangle_w \qquad (7.8)$$

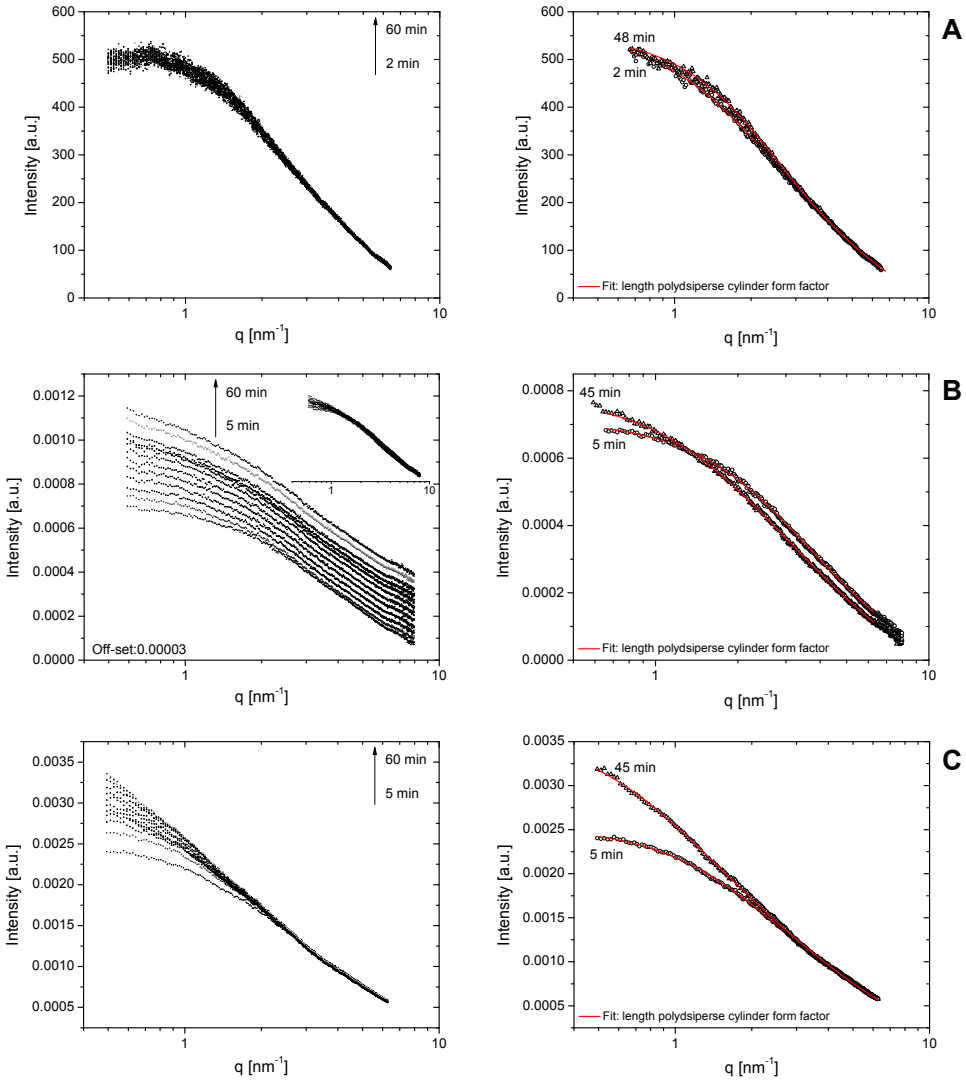

Figure 7.3. Time-resolved *in situ* SAXS data of the investigated exemplary fits with the model from Equations (7.5) to (7.7); a) Zirconia precursor sol of initial concentration of 0.67 mol/dm^3 and hydrolyzed with [H_2O]/[Zr] = 5; b) PZT precursor sol of initial concentration of 0.30 mol/dm^3 and hydrolyzed with [H_2O]/[Zr,Ti] = 9.26; c) PZT precursor sol of initial concentration of 0.30 mol/dm^3 and hydrolyzed with [H_2O]/[Zr,Ti] = 27.6.

The graph in Figure 7.7 presents the factor $\langle I(0)L_w^{-2}r_0^{-4}\rangle$ of all three sols as a function of time. Since it contains only N and $\Delta\rho$ as variables, $\langle I(0)L_w^{-2}r_0^{-4}\rangle$ is a measure of the number density of particles when $\Delta\rho$ can be assumed to remain constant.

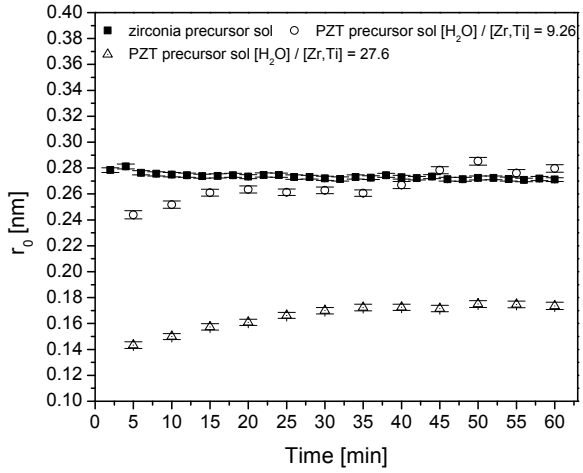

Figure 7.4. Evolution of r_0 as a function of time for zirconia precursor sol of initial concentration of 0.67 mol/dm^3 and hydrolyzed with [H_2O]/[Zr] = 5; PZT precursor sol of initial concentration of 0.30 mol/dm^3 and hydrolyzed with [H_2O]/[Zr,Ti] = 9.26; PZT precursor sol of initial concentration of 0.30 mol/dm^3 and hydrolyzed with [H_2O]/[Zr,Ti] = 27.6. The parameter values were derived from the model based on Equations (7.5) to (7.7).

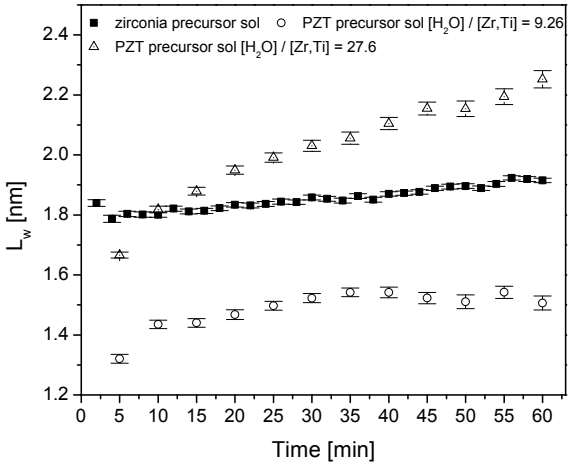

Figure 7.5. Evolution of L_w as a function of time for zirconia precursor sol of initial concentration of 0.67 mol/dm^3 and hydrolyzed with [H_2O]/[Zr] = 5; PZT precursor sol of initial concentration of 0.30 mol/dm^3 and hydrolyzed with [H_2O]/[Zr,Ti] = 9.26; PZT precursor sol of initial concentration of 0.30 mol/dm^3 and hydrolyzed with [H_2O]/[Zr,Ti] = 27.6. The parameter values were derived from the model based on equations (7.5) to (7.7).

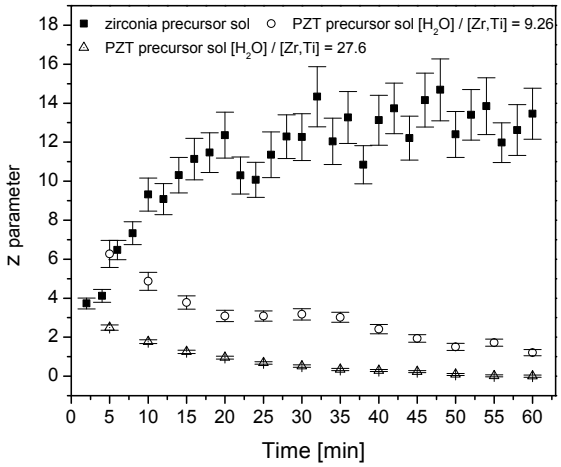

Figure 7.6. Evolution of z-parameter as a function of time for zirconia precursor sol of initial concentration of 0.67 mol/dm^3 and hydrolyzed with $[H_2O]/[Zr]$ = 5; PZT precursor sol of initial concentration of 0.30 mol/dm^3 and hydrolyzed with $[H_2O]/[Zr,Ti]$ = 9.26; PZT precursor sol of initial concentration of 0.30 mol/dm^3 and hydrolyzed with $[H_2O]/[Zr,Ti]$ = 27.6. The parameter values were derived from the model based on Equations (7.5) to (7.7).

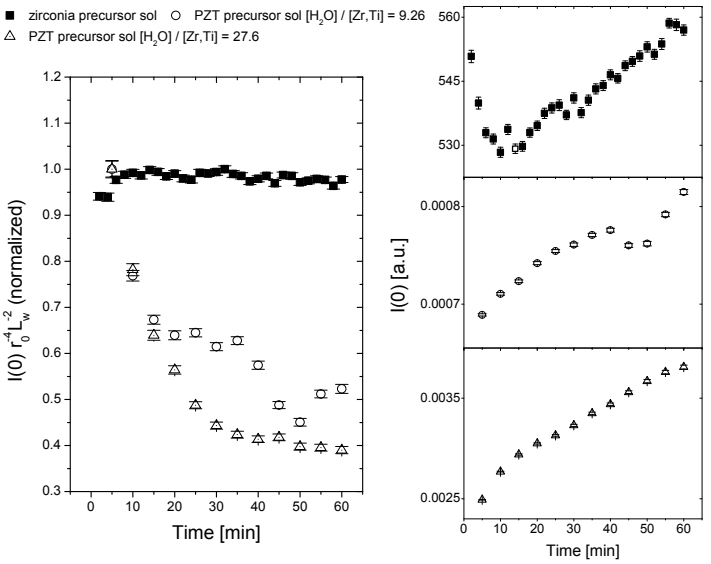

Figure 7.7. Evolution of $I(0)$ divided by a mass-averaged volume of a particle and normalized in the function of time for zirconia precursor sol of initial concentration of 0.67 mol/dm^3 and hydrolyzed with $[H_2O]/[Zr]$ = 5; PZT precursor sol of initial concentration of 0.30 mol/dm^3 and hydrolyzed with $[H_2O]/[Zr,Ti]$ = 9.26; PZT precursor sol of initial concentration of 0.30 mol/dm^3 and hydrolyzed with $[H_2O]/[Zr,Ti]$ = 27.6. The parameter values were derived from the model based on Equations (7.5) to (7.7). Inset on the right-hand side presents $I(0)$ as a function of time for three investigated sols.

7.4.2. Interpretation of data

The SAXS patterns of the zirconia sols shared some typical characteristics with the patterns of the PZT precursor sols at $q > 2$ nm^{-1}, where part of $I(q)$ scaled with q^{-1}. We may therefore assume that the zirconium alkoxide and PZT sols also share similar structural species.

In general, no directly detectable contributions from Pb or Ti were present in the PZT SAXS patterns. The absence of a Pb signature is indicative of the very limited reactivity of lead ions under these conditions. Pb^{2+} ions are very soluble at low pH and do not condense or precipitate easily from solution until the pH increases considerably. Homogeneously dissolved Pb^{2+} ions in solution are not detectable by SAXS.

The scattering power of Ti is comparatively smaller than that of Zr due to its smaller electron density. Contributions from Ti-rich scatters might therefore be shielded by the stronger signals arising from Zr-rich scatterers. While the formation of mixed Zr/Ti alkoxoacetate structures has been reported [48], it is known that pure Ti alkoxides in an excess of acetic acid form oligomeric compounds with stoichiometry $TiO(CH_3COO)_2$ [49]. Such oligomers would yield SAXS patterns with characteristics of fractal-like agglomerate morphologies, constructed from spherical primary scatterers [50-52]. Such patterns are quite distinct from the patterns observed in the present study.

Several small zirconium complexes have been reported. Jutson *et al.* conjectured from SAXS experiments the cylindrical shape of ziconia clusters and the constancy of their radius [53]. Toth *et al.* investigated the properties of hydrous zirconium(IV) tetramers [54]. They observed discrete $[Zr_4(OH)_8(H_2O)_{16}]^{8+}$ units derived from $Zr(NO_3)_4$ at high pH. Zirconia tetramers as building blocks of oligomeric structures were already proposed several decades earlier by Clearfield [55-57]. The authors reported an R_g of 0.46 nm and suggested that these structures have a cylindrical shape as found by SAXS. However, the accuracy of the fits was limited compared to today's standards. Another SAXS study on a system of zirconyl chloride revealed the co-existence of tetrameric $[Zr_4(OH)_8(H_2O)_{16}Cl_6]^{2+}$ and octameric $Zr_8(OH)_{20}(H_2O)_{24}Cl_{12}$ species at a given pH-dependent equilibrium [58], with radii of gyration of 0.37 and 0.50 nm, respectively. Growth and aggregation of zirconium hydrous polymers were extensively studied under various experimental conditions with SAXS by Singhal et al. [59] and by Riello et al. [60]. Both groups found that cylinder shaped particles of constant cross-sectional radius formed in early stages of sol development. An analogous polydisperse cylinder model was used to analyze data [60], yielding comparable results as I obtained here. The measured radius of the cylinder cross-section equaled 0.46 nm.

The structure of a hydroxylated zirconium tetramer was also determined by crystallographic methods and modelled by Carr-Parinello Molecular Dynamics [54,55,61]. The average Zr-Zr distance in a tetramer is equal to *ca.* 0.38 nm. It is the distance between the apexes of a square. Finally, in a SAXS study of hydrolyzed zirconium acetate xerogels it was proposed that the primary units were cylindrical, containing either three or four cyclic tetramer units in a single plane, stacked on top of each other in the direction perpendicular to the plane [62]. Such structural motifs may be stacked into several layers forming larger cylindrical objects. Thus, the choice of length polydispersed cylindrical form factor Eq. (7.5) seems to be reasonable, as this geometrical shape is a recurring structural feature of zirconia based structures at several length scales as outlined above. If one assumes that (1) a tetrameric unit constitutes a primary building block, and (2) larger structures are composed of stacked tetramers, then a cylinder with a tetramer inscribed in its base would have a radius of *ca*. 0.27 nm ($r_0 = 2^{1/2} \cdot 0.38 / 2$ nm, see Figure 7.8A), which is in close agreement with the values of $2^{1/2}R_C$ in Figure 7.1A, and the r_0 parameters of the investigated zirconia sols in Figure 7.4.

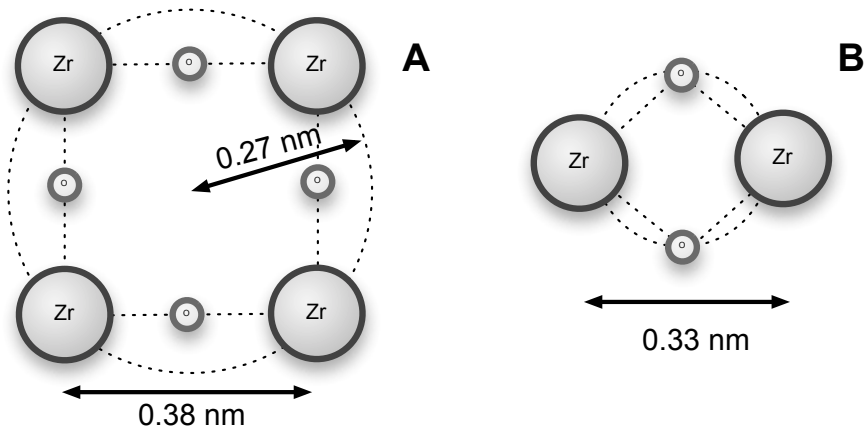

Figure 7.8. Schematic representation of a) zirconium oxo tetramer; b) zirconium oxo dimer.

Zirconium is a relatively heavy element, and therefore the scattering contrast between the organic solvent medium and the scattering entities is large. The scattering contrast between the solvent medium and the external organic ligands coordinated to zirconium is probably negligible, as they are very similar to the solvent medium. The electron density of these ligands will therefore not contribute significantly to the scattering intensity of the complex. Thus, only the central Zr–based framework contributes to scattering contrast. This may explain why the cross-sectional radius observed by me is lower than in studies where zirconia chloride, nitrate, and sulphate salts were synthesized [59,60].

Figure 7.5 shows the evolution of the mass-averaged length of cylinders in time. In the zirconia sol L_w increased only slightly from 1.79 to 1.85 nm. Simultaneously, the z-parameter increased from ~ 3 to a plateau at ~ 13 in Figure 7.6. This implies that the polydispersity decreased, finally reaching *PDI* = 1.08. The evolution of $\langle I(0) r_0^{-4} L_w^{-2} \rangle_w$ in Figure 7.7 shows that the mass-averaged product $\langle N(\Delta\rho)^2 \rangle_w$ slightly increased and then reached a plateau. Since the electron density of the scattering Zr-based complexes remains virtually constant ($\Delta\rho$ is constant), the trend suggests that the number of particles N in the zirconia sol increased initially and became constant after 15 min of reaction. The high final value of z shows that polydispersity was low, and indicates that only one length of cylindrical particles remained in the system by that time.

The hydrolyzed 0.3 mol/dm^3 PZT sols showed different trends. For the sol with $[H_2O]/[Ti+Zr]$ = 9.26 the circular cross-section radius $2^{1/2}R_C$ and r_0, determined from the Guinier approximation in Figure 7.2 and the cylinder model in Figure 7.4, were 0.24 – 0.27 nm and 0.24 – 0.28 nm, respectively. L_w increased from 1.3 to 1.5 nm before levelling off (Figure 7.5). On the other hand, the z parameter decreased from 6.3 to 1.2, yielding *PDI* = 1.83, i.e. a substantially higher polydispersity than found in the zirconia sol. The evolution of these parameters suggests that the initial structure resembled the structure of the zirconia sol. However, due to hydrolysis and the presence of Pb and Ti-containing species, not only their length, but also their cross-sectional dimensions increased during growth. The normalized plot of $\langle I(0) r_0^{-4} L_w^{-2} \rangle_w$ in Figure 7.7 shows a gradual decrease. Reduction of this parameter indicates reduction of the overall extent of scattering. Since its value is proportional to $N(\Delta\rho)^2$ and $\Delta\rho$ is probably constant, it follows that N probably decreased in the course of reaction, possibly due to agglomeration and growth of particles.

The PZT sol with $[H_2O]/[Ti+Zr]$ = 27.6 has a smaller radius of cross-section, $2^{1/2}R_C$ = 0.13 nm, as found from Eqn. (7.4). The scattering intensity was low due to the small dimensions of the scatterers. The particle shape and an approximate value of R_C could be extracted from the experimental data, but the absolute values should be interpreted with some care. The r_0 values obtained from the length-polydisperse cylinder model are more accurate. r_0 varied from 0.145 to 0.175 nm in the first 30 min of reaction. These values are smaller than found in the zirconia and other PZT sol. This indicates that the nature of the scatterers may be different at high hydrolysis ratio, although their shape was also cylindrical. Rao *et al.* reported dimeric $[Zr_2(OH)_2(H_2O)_{12}]^{6+}$ and trimeric $[Zr_3(OH)_3O(H_2O)_{18}]^{7+}$ in a computational study [63]. A cylindrical structure consisting of dimers stacked in the direction perpendicular to the cyclic $Zr_2(OH)_2$ plane would have a radius r_0 = 0.18 nm, and stacking of dimers in their respective planes would yield a smaller r_0 (essentially a chain of Zr-O-Zr surrounded by ligands). Similar stacks of tetramers along their respective planes would yield a structure analogous to the structure of stacked

zirconia dimers. However, in such a case one would expect more a ribbon (or stiff lamella) rather than pseudo-cylinder in rotation. It is not possible to distinguish between these two situations at such small dimensions or R_C. For the corresponding trimer-based cylinder, r_0 = 0.20 nm. The simulations indicated that trimetric units are less stable than dimers or tetramers. The actual Zr-Zr distance is strongly dependent on the surrounding ligands in the dimer structure, as shown by EXAFS [64]. The Zr-Zr distance in Zr(IV) *iso*-propoxide and *n*-butoxide modified with acetylacetone (acac) was 0.353 nm, independent of [Zr]/[acac] ratio. When these alkoxides were modified with acetic acid, the distances decreased to 0.335 – 0.339 nm at [Zr]/[CH_3COOH] = 0.5 [64]. These dimensions are similar to the experimental values of r_0 = 0.145 – 0.175 nm obtained in this study (Figure 7.8B). The L_w parameter ranged from 1.7 to 2.3 nm, without reaching an obvious upper limiting value. The z parameter decreased from 2.5 to 0, yielding $PDI >> 10$, which is typical for systems with a high degree of polydispersity. Thus, a clear structural reconfiguration towards a polydisperse system of cylindrical scattering entities occurred upon hydrolysis. The plot of $\langle I(0) r_0^{-4} L_w^{-2} \rangle_w$ in Figure 7.7 shows that the mass-averaged number of particles decreases. All data suggest that condensation and/or agglomeration processes take place in the solution, yielding a broad mass distribution. So while not being detectable directly, the presence of Ti and Pb affects the growth of the Zr-based phase, as reflected in the decrease of $\langle I(0) r_0^{-4} L_w^{-2} \rangle_w$, and the decrease of z in both PZT sols.

In Chapter 6 on the microstructure of as-dried PZT precursor thin films, I found that the films contained nanocrystalline Zr–rich spherical domains of 2 – 10 nm diameter embedded in an amorphous matrix of Zr, Ti and Pb. Electron energy loss spectroscopy (EELS) showed that these nanocrystals contained no or a very low concentration of Ti. Probably, the cylindrical Zr-based structures that were observed in the present study are the starting nuclei for these zirconia domains. The dimensions of the scattering entities that were extracted from the data in the present study, *i.e.*, $2^{1/2} R_C < 0.5$ nm and $L_w < 2.5$ nm for all samples, suggests that substantial agglomeration of Zr-rich entities takes place during or after the stage in which the sol is dried as a thin film. This suggests that the Zr-rich domains in as-dried films were formed in a process that was relatively isolated from the condensation of the amorphous solid phase that contained Pb, Ti and Zr.

7.5. Conclusions

Cylinder-shaped particles constitute one of the primary building blocks of zirconia and lead zirconate titanate precursor sols. SAXS curves from these systems were modelled with a length polydispersed cylinder form factor. In the zirconia sol the particles had a radius of *ca.* 0.27 nm and a length L_w of *ca.* 1.8 nm. Such a structure can be explained in terms of a stack of cyclic zirconia tetramers. Similar structural

motifs were also present in the PZT sol with $[H_2O]/[Ti,Zr]$ = 9.3 – 27.6. These sols contained anisotropic particles with L_w values of 1.4 – 2.3 nm and $2^{½}R_c$ < 0.3 nm. The number of particles in the PZT sols decreased in the course of time, while the zirconia sol seemed to converge to a stable and monodisperse state after some time. This suggests that condensation and/or agglomeration processes take place in the PZT solutions, yielding broad mass distributions of cylindrical particles based on zirconia-related structures. No direct evidence for the presence of Pb- or/and Ti-related structures was found the investigated PZT sols.

7.6. References

[1] Scott, J. F.; Paz De Araujo, C. A. *Science*, 246, 1400-1405, **1989**.

[2] Scott, J. F. *Science*, 315, 954-959, **2007**.

[3] Muralt, P. *J. Micromech. Microeng.*, 10, 136-146, **2000**.

[4] Kondo, M.; Sato, K.; Ishii, M.; Wakiya, N.; Shinozaki, K.; Kurihara, K. *Jpn. J. Appl. Phys.*, 45, 7516-7519, **2006**.

[5] Kim, H. R.; Jeong, S.; Jeon, C. B.; Kwon, O. S.; Hwang, C. S. *J. Mater. Res.*, 16, 3583-3591, **2001**.

[6] Otani, Y.; Okamura, S.; Shiosaki, T. *J. Electroceram.*, 13, 15-22, **2004**.

[7] Lin, Y. C.; Chuang, H. A.; Shen, J. H. *Vacuum,* 83, 921-926, **2009**.

[8] Bouregba, R.; Poullain, G.; Vilquin, B.; Murray, H. *Mater. Res. Bull.,* 35, 1381-1390, **2000**.

[9] Zhu, T. J.; Lu, L.; Lai, M. O. *Appl. Phys. A,* 81, 701-714, **2005**.

[10] Dekkers, M.; Nguyen, M. D.; Steenwelle, R.; te Riele, P. M.; Blank, D. H. A.; Rijnders, G. *Appl. Phys. Lett.,* 95, 0129021-0129023, **2009**.

[11] Schwartz, R. W. *Chem. Mater.,* 9, 2325-2340, **1997**.

[12] Schwartz, R. W.; Boyle, T. J.; Lockwood, S. J.; Sinclair, M. B.; Dimos, D.; Buchheit, C. *Integr. Ferroelectrics, 7*, 259-277, **1995**.

[13] Yi, G.; Sayer, M. *Ceram. Bull.*, 70, 1173-1179, **1991**.

[14] Klee, M.; Eusemann, R.; Waser, R.; Brand, W.; van Hal, H. *J. Appl. Phys.*, 72, 1566-1576, **1992**.

[15] Cui, T.; Markus, D.; Zurn, S.; Polla, D. L. *Microsyst. Technol.,* 10, 137-141, **2004**.

[16] Schwartz, R. W.; Voigt, J. A.; Tuttle, B. A.; Payne, D. A.; Reichert, T. L.; DaSalla, R. S. *J. Mater. Res.*, 12, 444-456, **1997**.

[17] Assink, R. A.; Schwartz, R. W. *Chem. Mater.*, 5, 511-517, **1993**.

[18] Chae, H. K.; Payne, D. A.; Xu, Z.; Ma, L. *Chem. Mater.*, 6, 875-877, **1994**.

[19] Brethon, A.; Hubert-Pfalzgraf, L. G. *J. Sol-Gel Sci. Technol.*, 39, 159-167, **2006**.

[20] Brethon, A.; Hubert-Pfalzgraf, L. G., Daran, J. -C. *Dalton Trans.*, 1, 250-257, **2006**.

[21] Hubert-Pfalzgraf, L. G.; Daniele, S.; Papiernik, R.; Massiani, M. C.; Septe, B.; Vaissermann, J.; Daran, J. -C. *J. Mater. Chem., 7*, 753-762, **1997**.
[22] Daniele, S.; Papiernik, R.; Hubert-Pflazgraf, L. G.; Jagner, S.; Hikansson, M. *Inorg. Chem., 34*, 628-632, **1995**.
[23] Schwartz, R. W.; Schneller, T. S.; Waser, R. *C. R. Chimie*, *7*, 433-461, **2004**.
[24] Schwartz, R. W.; Narayanan, M. Chemical Solution Deposition - Basic Principles, In *Solution Processing of Inorganic Materials*, ed. Mitzi, D. B., John Wiley & Sons, Inc., New Jersey, 33-76, **2009**.
[25] Malic, B.; Kosec, M.; Arcon, I.; Kodre, A. *J. Europ. Ceram. Soc.,* 25, 2241-2246, **2005**.
[26] Schneller, T.; Waser, R. *J. Sol-Gel Sci. Technol., 42*, 337-352, **2007**.
[27] Zhang, Q.; Huang, Z.; Vickers, M. E.; Whatmore, R. W. *J. Eur. Ceram. Soc.,* 19, 1417-1421, **1999**.
[28] Zhang, Q.; Vickers, M. E.; Patel, A.; Whatmore, R. W. *J. Sol-Gel Sci. Technol.*, 11, 141-152, **1998**.
[29] Zhang, Q.; Whatmore, R. W.; Vickers, M. E. *J. Sol-Gel Sci. Technol.*, 15, 13-22, **1999**.
[30] Khan, S. U.; Göbel, O. F.; Blank, D. H. A. ten Elshof, J. E. *Appl. Mater. Interfaces*, 10, 2250-2255, **2009**.
[31] Stawski, T. M.; Veldhuis, S. A.; Castricum, H. L.; Keim, E.G.; Eeckhaut, G.; Bras, W.; Blank, D. H. A.; ten Elshof, J. E. *Langmuir,* 27, 11081-11089, **2011**.
[32] Zhang, M.; Salvado, I. M. M.; Vilarinho, P. M.; Silvestre, A. J. D.; Silva, A. M. S. *J. Am. Ceram. Soc.,* 90, 358-363, **2007**.
[33] Caruso, R.; de Sanctis, O.; Frattini, A.; Gil, C. S. R., *Surface and Coating Techn.*, 122, 44-50, **1999**.
[34] Boyle, T. J.; Dimos, D.; Schwartz, R. W.; Alam, T. M.; Sinclair, M. B.; Buchheit, C. D. *J. Mater. Res.,* 12, 1022-1030, **1997**.
[35] Bras, W.; Dolbnya, I. P.; Detollenaere, D.; van Tol, R.; Malfois, M.; Greaves, G. N.; Ryan, A. J.; Heeley, E. *J. Appl. Crystallogr., 36*, 791-794, **2003**.
[36] Guinier, A.; Fournet, G. Small Angle Scattering of X-rays, John Wiley & Sons Inc, New York, **1955**.
[37] Kratky, O. A Survey In *Small Angle X-ray Scattering*, ed. Glatter, O.; Kratky, O. Academic Press, London, 3-13, **1982**.
[38] Porod, G. General theory In *Small Angle X-ray Scattering*, ed. Glatter, O.; Kratky, O. Academic Press, London, 17-52, **1982**.
[39] Craievich, A. F. *Mater. Res.,* 5, 1-11, **2002**.
[40] Fournet, G. *Bull. Soc. Fr. Minéral. Cristt., 74*, 39–113, **1951**.
[41] Pedersen, J. S. *Adv. Colloid Interface Sci., 70*, 171-210, **1997**.
[42] Svergun, D. I.; Konarev, P. V.; Volkov, V. V.; Koch, M.H.J., Sager, W.F.C., Smeers, J.; Blokhuis, E. M. *J. Chem. Phys.* 113, 1651-1665, **2000**.

[43] Pötschke, D.; Hickl, P.; Ballauff, M.; Åstrand, P-O; Pedersen, J. S. *Macromol. Theory Simul.*, 9, 345-353, **2000**.
[44] Hickl, P.; Ballauff, M.; Scherf, U.; Müllen, K.; Lindner, P. *Macromolecules,* 30, 273-279, **1997**.
[45] Sauer, T.; Wegner, G. *Macromolecules,* 24, 2240-2252, **1991**.
[46] Levenberg, K. *Q. Appl. Math.,* 2, 164–168, **1944**.
[47] Marquardt, D. *SIAM J. Appl. Math.,* 11, 431–444, **1963**.
[48] Laaziz, I.; Larbot, A.; Julbe, A.; Guizard, C.; Cot, L. *J. Solid State Chem.,* 98, 393-403, **1992**.
[49] Doeuff, S.; Henry, M.; Sanchez, C. *Mat. Res. Bull.,* 25, 1519-1529, **1990**.
[50] Torma, V.; Peterlik, H.; Bauer, U, Rupp, W.; Hüsing, N.; Bernstorff, S.; Steinhart, M.; Goerigk, G.; Schubert ,U. *Chem. Mater.,* 17, 3146-3153, **2005**.
[51] Kamiyama, T.; Mikami, M.; Suzuki, K. *J. Non-Cryst. Solids,* 150, 157-162, **1992**.
[52] Stawski, T. M.; Veldhuis, S. A.; Besselink, R.; Castricum, H. L.; Portale, G.; Blank, D. H. A.; ten Elshof, J. E. *J. Phys. Chem. C*, 115, 20449-20459, **2011**.
[53] Jutson, J. A.; Richardson, R. M.; Jones, S. L.; Norman C. In *Better Ceramics through Chemistry IV*, Mater. Res. Soc. Symp. Proc. 180, 123, ed. Zelinski B. J.; Brinker C. J.; Clark, D. E.; Ulrich, D. R., Mater. Res. Soc., Pittsburgh, **1990**.
[54] Toth, L. M.; Lin, J. S.; Felker, L. K. *J. Phys. Chem.,* 95, 3106-3108, **1991**.
[55] Clearfield, A., *Inorg. Chem.*, 3, 146-148, **1964**.
[56] Clearfield, A.; Vaughan, P. A. *Acta. Cryst.,* 9, 555–558, **1956**.
[57] Clearfield, A.; Serrette, G. P. D.; Khazi-Syed, A. H. *Catal. Today,* 20, 295-312, **1994**.
[58] Singhal, A.; Toth, L. M.; Lin, J. S.; Affholter, K. *J. Am. Chem. Soc.,* 118, 11529-11534, **1996**.
[59] Singhal A.; Toth, L. M.; Beaucage, G.; Lin, J. S.; Peterson, J. *J. Colloid Interface. Sci.* 194, 470-481, **1997**.
[60] Riello, P. ; Minesso, A.; Craievich, A.; Benedetti, A. *J. Phys. Chem. B* 107, 3390-3399, **2003**.
[61] Rao, N.; Holerca, M. N.; Klein, M. L.; Pophristic, V. *J. Phys. Chem. A,* 111, 11395-11399, **2007**.
[62] Corina-Geiculescu, A.; Rack, H. J. *J. Non-Cryst. Solids,* 306, 30-41, **2002**.
[63] Rao, N.; Holerca, M. L.; Pophristic, V. *J. Chem. Theory Comput.*, 4, 145-155, **2008**.
[64] Peter, D.; Erstel, T . S.; Bertagnolli, H. *J. Sol-Gel Sci. Technol.*, 5, 5-14, **1995**.

7.7. Appendix: Partially analytical expression for length-polydisperse cylinder form factor

The z-averaged length-polydisperse cylinder form factor as defined by Eqs. (7.5) and (7.6) can be partially solved analytically with respect to dL when it is combined with the Zimm-Schulz-Flory distribution, $w(L)$, of Eq. (7.7). Riello *et al.* reported an analytical solution for the number distribution in ref. [60]. They modeled the scattering intensity by averaging the scattering contribution over the square of volume, which simplifies to integrating over L^2 for L-polydisperse cylinders. Below, a solution for the volume distribution is presented, where averaging is performed by integrating over volume to the first power, hence over L. It is noted that both approaches yield identical results. All relevant equations and relationships between volume and number distributions can be found in ref. [42].

The cylinder form factor Eq. (7.5) can be rewritten as:

$$P_{\mathrm{cyl}}(q,r_0,L) = \int_0^{\pi/2} \left[\frac{2\mathrm{J}_1(qr_0\sin\alpha)}{qr_0\sin\alpha}\right]^2 \cdot \left[\frac{\sin\left(\frac{qL}{2}\cos\alpha\right)}{\frac{qL}{2}\cos\alpha}\right] \cdot \sin\alpha \,\mathrm{d}\alpha$$

$$= \int_0^{\pi/2} F_{\mathrm{C}}^2(q,r_0,\alpha) \cdot F_{\mathrm{L}}^2(q,L,\alpha) \cdot \sin\alpha \,\mathrm{d}\alpha \tag{7.9}$$

where $F_{\mathrm{C}}(q,r_0,\alpha)$ is the cross-section-related component of the scattering amplitude and $F_{\mathrm{L}}(q,L,\alpha)$ is the length-related component. Therefore, the L-polydisperse cylinder form factor from Eq. (7.6) takes the form of Eq. (7.10) when it is expressed in terms of Eq. (7.9):

$$P_{\mathrm{z}}(q,r_0,L) = \int_0^{\infty} L \cdot w(L) \cdot P_{\mathrm{cyl}}(q,r_0,L)\,\mathrm{d}L =$$
$$= \int_0^{\pi/2} F_{\mathrm{C}}^2(q,r_0,\alpha) \int_0^{\infty} L\, w(L) \cdot F_{\mathrm{L}}^2(q,L,\alpha)\,\mathrm{d}L \cdot \sin\alpha \,\mathrm{d}\alpha \tag{7.10}$$

For $w(L)$ defined by the Zimm-Schultz-Flory distribution Eq. (7.7), the integral Eq. (7.11) can be solved analytically.

$$F_{\mathrm{z,\,L}}^2(q,z,L_{\mathrm{w}},\alpha) = \int_0^{\infty} L\, w(L) \cdot F_{\mathrm{L}}^2(q,L,\alpha)\,\mathrm{d}L \tag{7.11}$$

The relevant solution is given by Eq. (7.12):

$$F^2_{z,\,L}(q,z,L_w,\alpha) = \left(\frac{2}{z\cdot L_w / q^2\cos^2\alpha}\right)\cdot\left\{\frac{z+1}{L_w} - \left(\frac{z+1}{L_w}\right)^{z+1}\cdot\frac{\cos\left[z\cdot\operatorname{atan}\left(\frac{q\cdot L_w\cdot\cos\alpha}{(z+1)}\right)\right]}{\left[\left(\frac{z+1}{L_w}\right)^2 + q^2\cos^2\alpha\right]^{z/2}}\right\} \quad (7.12)$$

When z goes to zero, *i.e.* $\lim_{z\to 0} z^{-1} = \infty$, Eq. (7.12) reduces to

$$\lim_{z\to 0} F^2_{z,\,L}(q,z,L_w,\alpha) = \frac{\ln\left[L_w^2 q^2\cos^2\alpha + 1\right]}{L_w^2 q^2\cos^2\alpha} \quad (7.13)$$

Hence, the z-averaged length-polydisperse cylinder form factor can be written as:

$$\begin{aligned} P_z(q,r_0,z,L_w) &= \int_0^{\pi/2} F^2_C(q,r_0,\alpha) F^2_{z,\,L}(q,z,L_w,\alpha)\cdot\sin\alpha\ \mathrm{d}\alpha \\ &= \int_0^{\pi/2}\left[\frac{2J_1(qr_0\sin\alpha)}{qr_0\sin\alpha}\right]^2 F^2_{z,\,L}(q,z,L_w,\alpha)\cdot\sin\alpha\ \mathrm{d}\alpha \end{aligned} \quad (7.14)$$

Eq. (7.14) requires only a single numerical integration procedure.

8

Influence of High Temperature Processing of Sol-Gel Derived Barium Titanate Thin Films on Platinum and Strontium Ruthenate Coated Silicon Wafers*

Abstract

Thin films of barium titanate (BTO) of 200 nm thickness, derived from an alkoxide-carboxylate sol-gel process, were deposited on Pt/Ti and $SrRuO_3/ZrO_2$-8%Y_2O_3 coated Si wafers. Films with a dense columnar microstructure were obtained by repeated deposition of thin amorphous layers from low-concentrated sols, and crystallization at 800 °C. This method added 10 nm thickness to the crystalline BTO film in each deposition step. The harsh processing conditions had a negative impact on the platinized silicon wafers, where Pt-Si silicides were formed. This led to diffusion of Si into BTO and interfacial silicate formation. The interfacial silicate layer was the cause of deteriorated dielectric and ferroelectric properties of the BTO layer. Use of $SrRuO_3/ZrO_2$-8%Y_2O_3/Si substrates solved the problem. No diffusion of Si was observed, and BTO films with good dielectric and ferroelectric properties were obtained.

8.1. Introduction

Barium titanate ($BaTiO_3$; BTO) is a widely used high-*k* ceramic dielectric material. I t is utilized in a wide range of applications, many of which are based on the use of BTO thin films. BTO is an important dielectric material, for instance in commercial multi-layer ceramic capacitors. The minimum $BaTiO_3$ layer thickness that can be achieved with state of the art tape casting methods is about 1 µm. Barium titanate is used in crystalline form, which implies the use of starting powders

with a particle size of *ca.* 200 nm [1]. Further reduction of the barium titanate layer thickness requires finer powders obtained by new synthesis and deposition techniques. One of the feasible alternatives is the deposition of amorphous precursors of barium titanate and their further reaction and crystallization to a perovskite phase

* In preparation:
Stawski, T. M.; Vijselaar, W. J. C.; Göbel, O. F.; Veldhuis, S. A.; Smith, B. F.; Blank, D. H. A.; ten Elshof, J. E.

[2]. Good control and understanding of the process in all stages is required to obtain a film with desired electrical and morphological properties. This can be achieved by wet-chemical processing methods. Moreover, as the wet-chemical methods are based on liquid precursors, direct deposition of precursor thin films onto substrates by means of spin-casting, deep-casting or misted source deposition, followed by pyrolysis and crystallization is possible [2-5]. These off-contact deposition techniques enable direct fabrication of thin films of $BaTiO_3$ on bare silicon and electrode-coated silicon wafers. It opens up the possibility to integrate inexpensive chemically derived barium titanate with silicon (primarily CMOS) technology, *e.g.* as dielectric material for dynamic random access memories (DRAMs) [6] and non-volatile ferroelectric memories (FeRAMs) [7]. It has been demonstrated that chemically fabricated thin films of $BaTiO_3$ yield very good dielectric properties, with relative permittivities >600 at a layer thickness <200 nm [8,9]. Use of oxides with high dielectric constant for DRAM applications would enable fabrication of high-capacity memory chips using simple planar capacitor geometries, instead of the currently used complicated trench of stacked capacitors with SiO_2 ultra-thin (< 4 nm) films. This would simplify the production process significantly, and reduce costs [6].

Among the synthesis methods the sol-gel process, in particular the alkoxide-carboxylate synthesis, the double alkoxide synthesis, the micro-emulsion synthesis, and the precipitation methods (alkoxide-hydroxide sol precipitation) received much attention [2]. The alkoxide-carboxylate was employed widely for $BaTiO_3$ synthesis since the first reports [10].

In order to obtain a barium titanate thin film of desired electrical properties a number of factors have to be taken into account, among which thermal processing plays probably the most important role [3,4,11]. The heat treatment can be divided into several stages [12]: (1) removal of residual solvents, T < 200 °C; (2) pyrolysis of organic moieties, T = 250 – 500 °C, (3) onset of perovskite phase crystallization, thermal decomposition of residual carbonates, T = 600 – 800 °C; (4) sintering, T > 800 °C. According to Mosset *et al.*, barium carbonate and titanium dioxide are formed after pyrolysis and form $BaTiO_3$ above 650 °C [13]. A number of intermediate phases have been suggested in literature, such as $Ba_2Ti_2O_5CO_3$ [2,12]. The crucial point in the syntheses is that temperatures > 650 °C are essential for this phase to decompose and for barium titanate to crystallize.

The heating protocol can be a one- or a two-step procedure. In the latter case, the as-deposited film is initially processed at a pyrolysis temperature < 500 °C, and then heated to 850 °C at a rate of 1 °C/min, yielding relatively dense barium titanate [3,8,9]. In the one-step process a dried xero-gel film is placed in an oven preheated at *ca*. 850 °C. At this temperature the rate of pyrolysis is orders of magnitude higher than below 500 °C [3,14]. The thin film density is improved by delaying the onset of crystallization to higher temperatures, thereby reducing the number of nucleation

events and yielding larger grains [3,8]. It was demonstrated that one-step processing yielded films with better dielectric properties than two-step processing [8,9]. One-step processed films were denser and had larger grains than films obtained from a two-step process.

The highest reported permittivity values for sol-gel derived barium titanate films with a thickness < 200 nm on Pt electrodes were measured for BTO with a columnar microstructure [8,9]. Barium titanate is known to nucleate homogenously, yielding films of grainy microstructure [3,4,11]. In order to nucleate the perovskite phase heterogeneously, it must be deposited in a sequence of very thin layers, with a heat-treatment at T = 700 – 800 °C after each deposition step. This is done by spincasting sol-gel precursors of very low concentration, typically < 0.2 mol/dm^3 for barium titanate or barium strontium titanate from alkoxide-carboxylate precursors [9]. Each cycle adds typically 10 – 20 nm to the total thickness of the film. The films have a high relative density, close to 100%, and high relative permittivities, typically above 600, when annealed at 800 °C.

The method of production exposes the film to extreme conditions, such as fast cooling and heating, and high temperature, which may be a problem when silicon-based substrates are used. TiO_2 is unstable in contact with silicon > 700 °C, whereas $SrTiO_3$ was demonstrated to react with Si at temperatures as low as 200 – 600 °C [15].

It was the purpose of this work to investigate the formation of barium titanate thin films on Pt/Ti/SiO_2/Si and $SrRuO_3$/ZrO_2-8%Y_2O_3/Si substrates. I investigated the formation of interfacial phases from one-step processed sol-gel derived columnar barium titanate thin films. Field-emission scanning electron microscopy (FE-SEM), x-ray powder diffraction (XRD), and depth-resolved x-ray photoelectron spectroscopy (XPS) were used for structural analysis.

8.2. Experimental

8.2.1. Synthesis of barium titanate (BTO) precursor sols

Barium acetate (> 99%, Riedel-deHaën) and titanium(IV) *iso*-propoxide (99.999 %, Sigma-Aldrich) were used as precursor materials. Glacial acetic acid (99.8%, Acros) and 2-methoxyethanol (> 99.3%, Sigma-Aldrich) were used as solvents, stabilizers, and chelating agents. Two stock solutions were made. A Ba-acetate solution was prepared by dissolving barium acetate in acetic acid and subsequent refluxing at 105 °C for 8 h to remove all remaining water. The final concentration was adjusted to 1.0 mol/dm^3. The second stock solution was based on titanium *iso*-propoxide with 2-methoxyethanol as solvent, yielding a precursor concentration of 1.0 mol/dm^3. It was stirred in a glove box under nitrogen atmosphere. Both stock solutions were stirred at room temperature for 24 h. They were then stored at room temperature.

Prior to the experiments, the stock solutions were mixed in 1 : 1 molar ratios and stirred for 5 minutes, yielding a concentration of 0.50 mol/dm^3 in the final BTO precursor solution. In the next step they were diluted with 2-methoxyethanol to reach a concentration of 0.1 mol/dm^3 in the final BTO precursor solution.

8.2.2. Thin film fabrication

BTO precursor sols of 0.1 mol/dm^3 were spin-cast (Laurell WS-400B-6NPP-Lite spincoater) onto 1 x 1 cm^2 substrates at 3000 rpm for 40 s. The as-prepared films were dried on a hot-stage at 100 °C for 15 min. In subsequent steps, substrates with BTO films were placed in a pre-heated oven (Milestone PyroPrep) at 800 °C for 5 min, then quenched to room temperature and used as substrate for the next layer of BTO sol. The process was repeated several times, typically 20. Two kinds of substrates were investigated:

(1) Si(001) with native SiO_2, a Ti adhesion layer of 40 nm thickness, and a 200 nm thick Pt(111) electrode. This substrate is further referred to as Si/Ti/Pt;

(2) Si(001) with native SiO_2, a 70 nm thick buffer layer of yttrium stabilized zirconia (YSZO), and a 200 nm thick $SrRuO_3$ electrode. This substrate is further referred to as Si/YSZO/SRO.

The Si/Ti/Pt substrates were made by sputtering (Sputterke, DC sputter system, p_{Ar} = 0.0066 mbar, T = 25 °C), and the Si/YSZO/SRO substrates were manufactured by pulsed laser deposition using a KrF excimer laser, as described elsewhere [16,18]. Typically, several monolayers of YSZO buffer were grown under argon instead of oxygen atmosphere (p_{Ar} = 0.02 mbar, T = 850 °C). This step enabled scavenging of native silicon oxide by reduced Zr and Y, and provided a basis for coherent and epitaxial growth of YSZO in an oxygen atmosphere (p_{O2} = 0.02 mbar, T = 850 °C) without HF processing of Si [17,18]. SRO was deposited at p_{O2} = 0.13 mbar, T = 650 °C. By this means, oriented metallic conductive substrates SRO(110)/YSZO(001)/Si(001) were obtained [18].

8.2.3. Thin film characterization

Selected samples were broken with pliers and the cross-section was analysed by Field Emission-Scanning Electron Microscopy (FE-SEM, 0.5 – 2.0 keV, Zeiss 1550) to determine layer thickness and film microstructure. X-ray powder diffraction (XRD) patterns of films were measured on a diffractometer with Cu anode and Ni filter using Cu $K_{\beta 1}$ radiation (Philips PW1830). Patterns were measured in a continuous mode with 0.02° step size and counting time 5 s.

XPS spectra were recorded to determine elemental surface composition (Physical Electronics Quantera SXM, Al K_α 1486.6 eV). Depth profiles were recorded with an Ar^+ beam of 3 kV, rastering an area of 9 mm^2 using Zalar rotation to avoid shadowing

effects of the sputter beam. Due to the unknown sputtering rate of Ar^+, one cannot directly correlate elemental composition to a specific depth under the surface of the film. The surface of the samples was sputtered away by removing in each step approximately 5 – 20 nm thickness of the film, and the XPS spectra were being collected afterwards, yielding information about surface elemental composition as a function of total sputter time. Total counting time per element was 5 min. Data reduction was performed by means of Multipak 8.0 software. Fitting of spectra was done by shifting the measured spectra with respect to known reference binding energies (BE): aliphatic carbon C 1*s* at 284.8 eV or gold Au $4f_{7/2}$ at 83.96 eV, silver Ag $3d_{5/2}$ at 368.21 eV and copper Cu $2p_{3/2}$ at 932.62 eV. Specific elements and their characteristic chemical shifts were identified by comparing measured spectra with information contained in the NIST Database for the Simulation of Electron Spectra for Surface Analysis ver. 1.1 [19] and other references available in literature.

Gold-palladium electrodes were sputtered on the top surface of selected films (95% Au – 5% Pd, Polaron SC7640, p_{Ar} = 0.01 mbar, T = 30 °C) through a silicon micro-machined shadow mask, with a good contact between the film and the mask. The area of the electrode was 1.0 mm^2 ± 0.04% and the thickness was 100 nm. Films with deposited top electrodes were post-annealed at 350 °C for 1 h to improve adhesion of the electrodes to the surface. The *C-V* measurement of as-prepared capacitors was carried out in a top-to-bottom configuration at 500 kHz at room temperature, with a bias of - 5 V to + 5 V and AC voltage of 1 V (Karl Suss PM8 low-leakage Manual Probe Station). The dielectric constant was extracted using the plate capacitor equation, with a dielectric layer averaged-thickness obtained from FE-SEM characterization.

Local piezoresponse force microscopy (PFM) loops were obtained using a Bruker Dimension Icon atomic force microscope with a conducting Cr/Pt coated silicon probe with a resonance frequency of 75 kHz and a force constant of 3 N/m. The DC voltage was ramped from +10 V to -10 V and back to +10 V with a ramp frequency of 0.05 Hz. The AC probe voltage used to measure the piezoresonse during the DC ramp was 5 V at a frequency of 350 kHz.

8.2.4. Reaction of BTO with amorphous SiO_2

High temperature XRD (Philips X'Pert MPD, Anton-Paar HTK16 high-temperature chamber, Cu anode and Ni filter for Cu $K_{\beta 1}$ radiation) was used to study phases that formed in the reaction between barium titanate and silicon. Patterns were measured in a continuous mode with 0.04° step size and 15 s counting time. The as-synthesized powder of nano-crystalline barium titanate (particle diameter < 10 nm) prepared following the recipe in ref. [20] was thoroughly mixed in a mortar with 10 wt% fine amorphous SiO_2 powder (Sigma-Aldrich), and placed on a Pt heater in the high-temperature chamber. XRD patterns were collected at selected temperatures ranging

from 200 °C to 850 °C, with a typical dwell time of 20 h at a given temperature. This ensured that samples were always in thermal equilibrium.

8.3. Results and Discussion

8.3.1. FE-SEM and XRD analysis

Figures 8.1A and B present the FE-SEM pictures of cross-sections of BTO thin films on Si/Ti/Pt and Si/YSZO/SRO. The corresponding BTO layer thicknesses were 208 nm ± 2% and 201 nm ± 2%, respectively. The same number of deposition steps was used to fabricate the two films. A dense columnar structure is visible, indicating that one-step thermal treatment combined with multi-step deposition yielded the desired microstructure. The inset in Figure 8.1A illustrates the linear dependence between the number of deposited layers and the final thickness of the thermally processed film. In the film fabricated on a Si/YSZO/SRO substrate, all the expected phases can be distinguished by FE-SEM: Si substrate, *ca.* 70 nm of dense YSZO and *ca.* 200 nm of dense SRO electrode, underneath the barium titanate film (Figure 8.1A). No interfacial phases can be observed, as confirmed by XRD in Figure 8.2A, where $BaTiO_3$, $SrRuO_3$, and YSZO are present. The preferential (100) orientation of YSZO can be concluded from the presence of only (200) and (400) peaks in the XRD pattern. The coherence was further extended to the SRO film, which exhibited only (110) and (220) peaks in XRD. Making a clear distinction between tetragonal and cubic barium titanate was not possible due to peak broadening caused by the small grain size. Furthermore, the BTO film was (110) oriented, as suggested by the strongly increased relative intensitity of the peak in the proximity of $2\theta \sim 31°$ in respect to other BTO diffraction peaks and clear indication from the rocking curve (FWHM = 1.8°) at BTO (110) peak (figure not shown here).

In the BTO film deposited on Si/Ti/Pt, no individually distinguishable Ti or Pt layer was present. Instead, a single dense layer of 200 nm thickness had formed. Barium titanate was also present in the film, see Figure 8.2B. Moreover, a number of strong unidentified peaks, and a peak of Si (100) at $2\theta = 69.2°$ (004) were recognized. Some of the peaks coincided with BTO peaks, like the one at $2\theta \sim 56°$. An interfacial phase of 20 nm thickness formed between the barium titanate thin layer and the Pt electrode (Figure 8.1B).

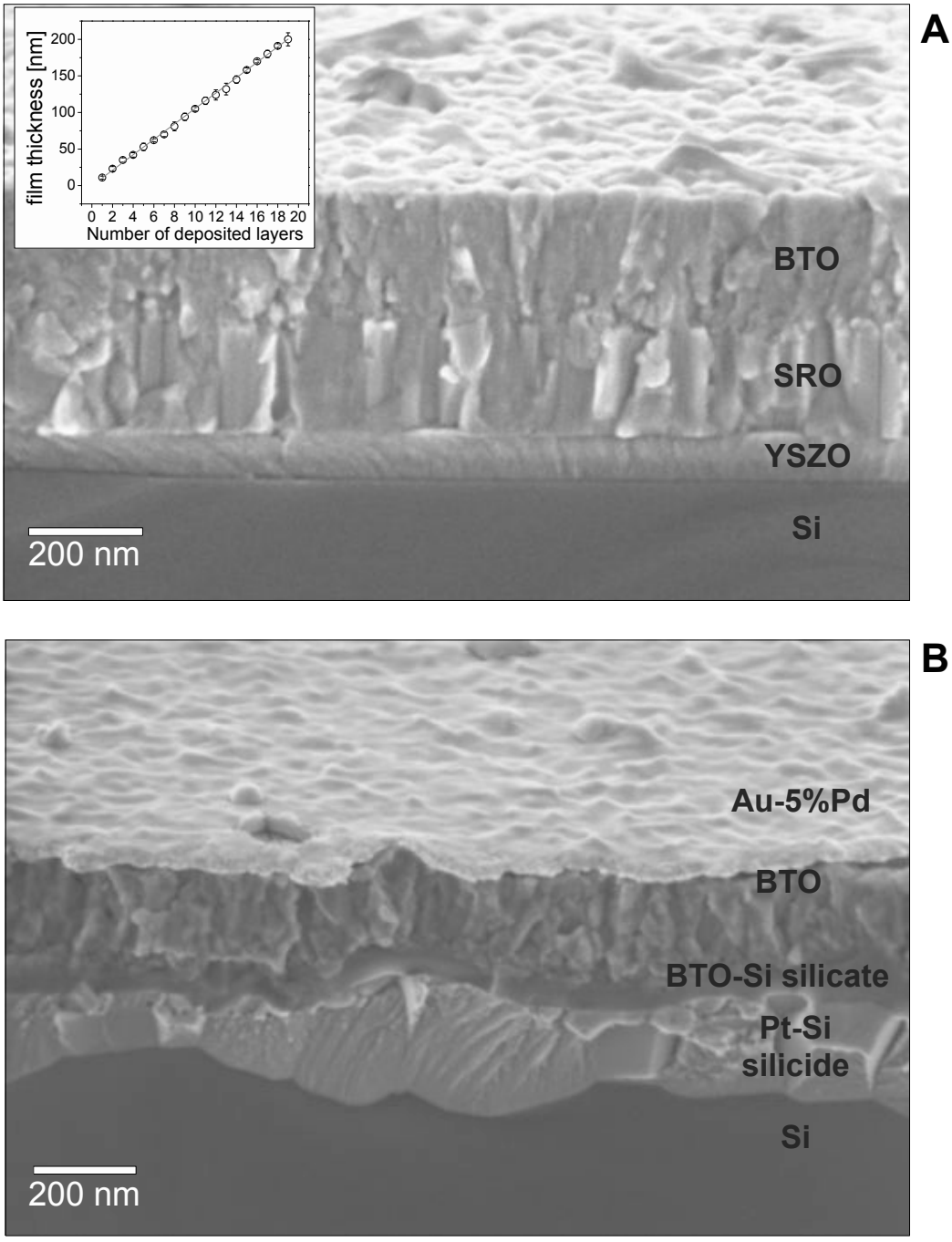

Figure 8.1. FE-SEM images of cross-sections of films of barium titanate fabricated by multi-layer deposition and processed by one-step annealing at 800 °C. a) BTO/SRO/YSZO/Si film; b) BTO/Pt/Ti/Si film. Inset shows the dependence between number of deposition steps and BTO layer thickness.

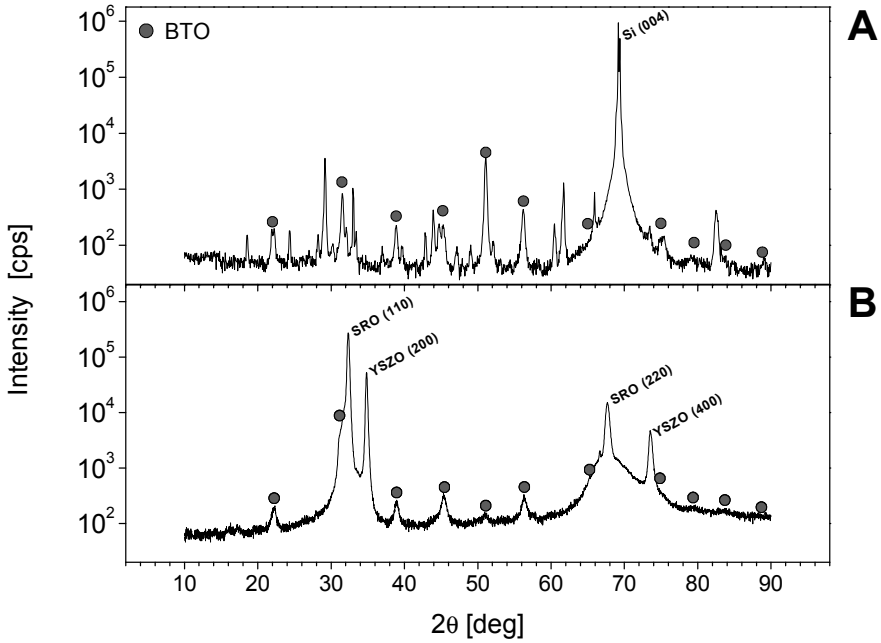

Figure 8.2. XRD patterns of films of barium titanate fabricated by multi-layer deposition and processed by one-step annealing at 800 °C. a) BTO/SRO/YSZO/Si; b) BTO/Pt/Ti/Si. A number of unmarked diffraction peaks from silicate and silicide phases are present. BTO peaks are marked by a symbol.

8.3.2. Depth-resolved XPS analysis

Elemental composition as a function depth into both types of thin films was determined by depth-resolved XPS analysis. In the case of BTO on Pt/Ti/Si, survey scans from 1345 eV to 5 eV with dE = 0.8 eV in three cycles demonstrated clearly that only Ti, Ba and O were present at the sample surface. Scans with depth profiling were performed in the selected binding energy (BE) ranges of all present elements, i.e. Pt *4f*; Si 2*p*; Ti 2*p*; O 1*s*; Ba $3d_{5/2}$. Atomic concentrations as a function of sputter time are shown in Figure 8.3A. The concentrations are based on the peak areas and the relative sensitivity factors.

While Ar^+ sputtering does not provide direct information on the sputtering depth, Figure 8.3A shows clearly that stoichiometric $BaTiO_3$ was present in the film during 25 min of sputtering. This means that the barium titanate layer was sputtered at a rate of 8 nm/min. The high concentration of Si at the top surface is an artifact from the measurement, caused by shake-up peak of Ba *4d*. A real Si signal was present after t = 25 – 40 min, indicating an increasing silicon concentration with depth. At t = 40 min a Pt *4f* signal appeared, which reached 50 at% by the end of the sputtering process. The Si concentration was *ca.* 40 at% at the same depth. Peak analysis of the Si 2*p* spectrum showed that Si was present in two oxidation states, namely Si^{4+} with a BE of 108 eV [22] at t = 25 – 40 min, and Si^0 with a BE of 100 eV [22] at t > 40 min, see Figure 8.3B. The chemical shift of Pt *4f* over the whole

investigated depth range is typical for PtSi or Pt_2Si, see Figure 8.3C [23]. At t < 40 min, the Ba concentration was approximately two times higher than the Ti concentration, and at t ~ 40 min, the concentrations of Ba and Ti were close to 0 and 5 at%, respectively. The chemical shift of Ti suggested that it was present in oxidized form [24] (Figure 8.3D). Analysis of O 1*s* depth-resolved spectra showed that the oxygen concentration remained constant until t = 25 min, after which it decreased substantially until t = 40 min (Figures 8.3A&E). Until t = 25 min the chemical shift of O 1*s* corresponded to the one found for barium titanate, *i.e.* BE = 527.5 eV [25]. At t > 25 min, the chemical shifts were attributed to two Si/O stoichiometries: SiO at t = 25-40 min with BE = 529.0 eV [26], followed by SiO_2 at t > 40 min with BE = 531.7 eV [22].

The following film morphology can be deduced from these data. Stoichiometric barium titanate forms a layer of >200 nm thickness. Beneath that, a 20 nm thick interfacial silicate layer composed of Ba, Ti, Si, and O was formed. The detected silicate phase may correspond to fresnoite, $Ba_2Ti(Si_2O_7)O$, at t ~ 38 min. Considering the varying concentrations of Si and O, a diffusion mechanism is proposed to explain silicate interface formation. Thus, other stoichiometries than fresnoite were probably also present. Beyond the interfacial layer, at the position of the Pt/Ti/Si electrode, a silicide phase with gross composition 50 at% Pt – 40 at% Si, and very small concentrations of Ti and O were detected.

The question is if the observed interfacial layer formed as a result of the repeated cooling and annealing cycles, *i.e.* 20 cycles of 5 min at 800 °C and back to room temperature, in the barium titanate film formation process, or if it started directly at the beginning of the process, when the first layer of barium titanate was deposited. To answer this question, a 20 – 25 nm barium titanate film was made via deposition in two layers. The annealing time at 800 °C was reduced to 60 s. Survey scans (not shown here) from 1345 eV to 5 eV with dE = 0.8 eV in three cycles demonstrated clearly that not only Ti, Ba and O were present at the sample surface, but also Si. The depth-resolved elemental composition is shown in Figure 8.4A. The sputter Ar^+ rate was in the barium titanate layer was approximately 4 – 5 nm/min. Ba and Ti remained in a near-stoichiometric ratio until t = 5 min. Then the Ba concentration dropped to 0, and Ti remained at a constant level of 5 at% until t = 12 min. A non-negligible signal of Si was present in the material from the surface, and its concentration reached 40 at% at t = 5 min. Similarly, a Pt 4*f* signal that corresponded to a concentration of ~50 at% was detected from t = 5 min onwards. Pt formed a silicide phase over the whole thickness of the electrode. Si was present in two oxidation states (Figure 8.4B), with Si^{4+} at a depth corresponding to the location of the interface between BTO and Pt electrode. This shows undoubtedly that Si diffusion to the barium titanate precursor film occurs very fast at a temperature of 800 °C, and silicate formation occurs from the very beginning of the process. On the other hand, Pt does not diffuse into the

BTO or interfacial layer. The results can be rationalized by considering the semi-amorphous character of the barium titanate precursor sol, and the low stability of TiO_2 in contact with Si and silicide phases at the processing temperature [15].

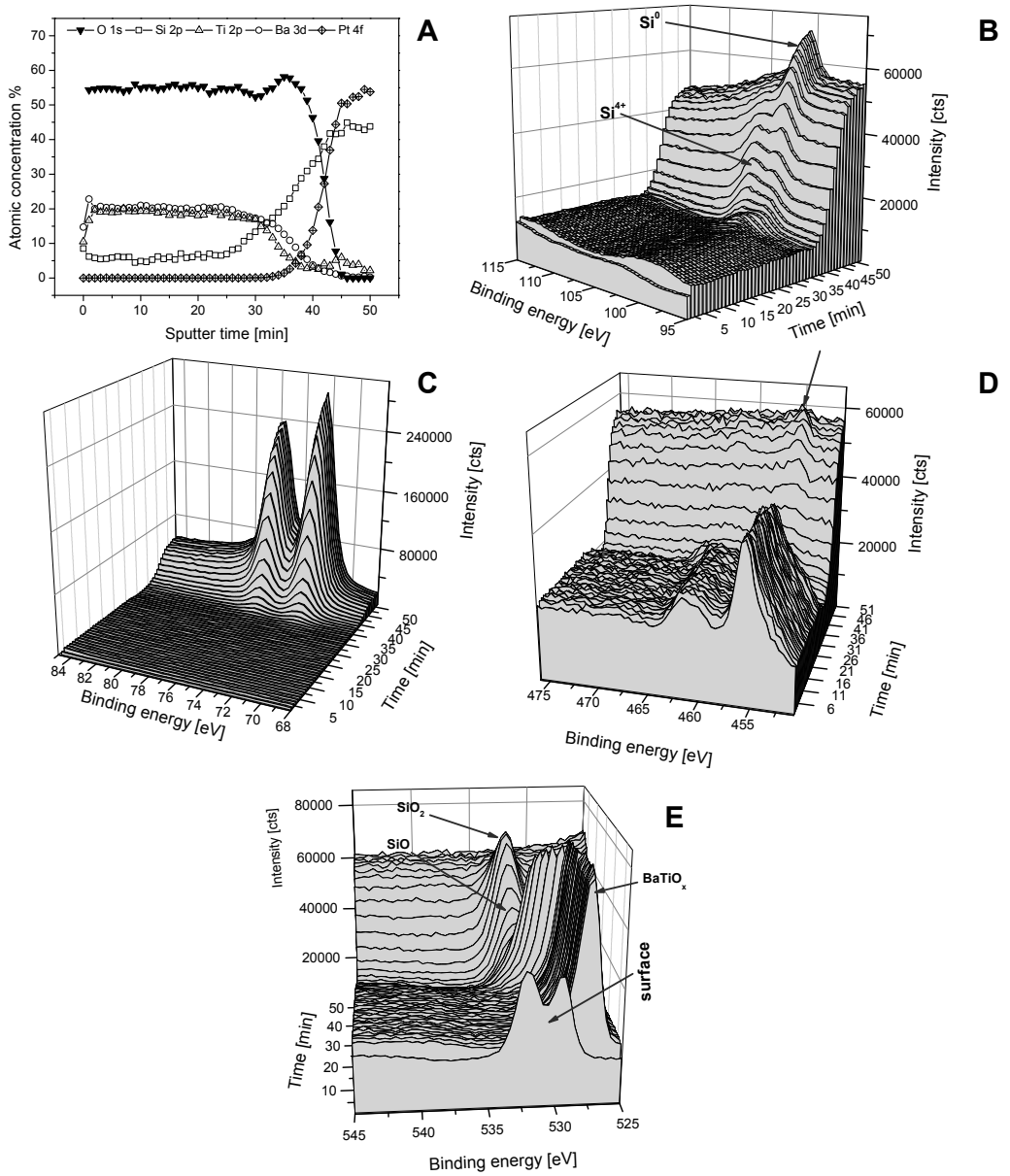

Figure 8.3. XPS depth profile of 200 nm barium titanate film on Pt/Ti/Si. a) Atomic concentrations in film as function of sputter time. XPS spectra shown: b) Si 2*p*; c) Pt 4*f*; d) Ti 2*p*; e) O 1*s*. Sputter rate is approximately 8 nm/min for BTO.

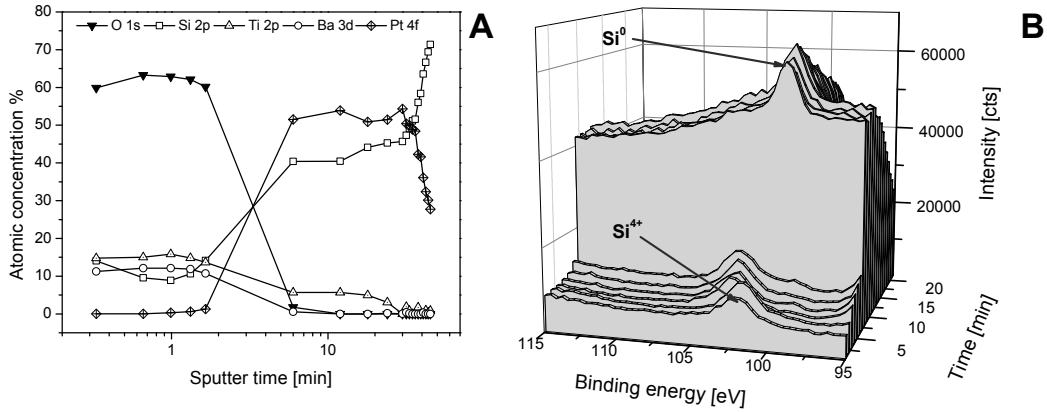

Figure 8.4. XPS depth profile of 25 nm barium titanate film on Pt/Ti/Si. a) Atomic concentrations in film as function of sputter time; b) XPS spectra of Si 2*p* region as a function of sputter time. Sputter rate is approximately 4 nm/min for BTO.

XPS analysis with depth profiling was also performed on a BTO/SRO/YSZO/Si film. Here, Si 2*p*; Y 3*d*; Zr 3*d*; Sr 3*d*; Ru $3p_{3/2}$ and 3*d*; Ti 2*p*; O 1*s*; Ba $3d_{5/2}$ spectra were measured. A 200 nm thick film of barium titanate prepared in 20 deposition and calcination steps was analyzed. The measurement clearly showed that well-defined layers were present in the stack (Figure 8.5A). In the first 20 min of the sputter process only stoichiometric $BaTiO_3$ was present. At t = 22 – 26 min an interface containing Ru, Ti, Ba and Sr was detected. The XPS spectra of Ru $3p_{3/2}$ overlap with a part of the Ti $2p_{3/2}$ peak until t = 24 min (Figures 8.5B).

The stoichiometry of the SRO layer was established on the basis of the Ru $3p_{3/2}$ peak, because Ru 3*d* coincides with Sr $3p_{1/2}$ around 280 eV [27-29]. The positions of the Sr and Ru peaks remained constant at t = 32 – 56 min (Figures 8.5B – D), suggesting a constant composition. The layer contained 20 at% Ru – 30 at% Sr – 50 at% O, *i.e.* a stoichiometry that differed from $SrRuO_3$. The Ru 3*d* and $3p_{3/2}$ peaks were clearly asymmetric, indicating the presence of nonequivalent Ru atoms or multiplet splittings in metallic SRO caused by correlated electron behaviour [26,28] (Figure 8.5B&C). The binding energy of Ru $3d_{5/2}$ at 280.3 eV indicated that this element was present in the form found in RuO_2 or Ru^0 [29-31]. The stoichiometry of the film suggests that a Sr-rich ruthenate phase may have formed upon annealing, when part of Ru^{4+} was oxidised to gaseous RuO_4 or RuO_3 [27]. Indeed, a small maximum at 282.2 eV at t = 26 – 28 min (Figure 8.5C) may possibly be attributed to RuO_3 [30,31]. The O 1*s* spectrum showed an oxygen peak at a single energy BE = 529.4 eV throughout the whole SRO film. This binding energy is typical for RuO_2, SrO and for $SrTiO_3$ surfaces [30,31]. Its symmetric, non-split shape clearly indicated that only one form of oxygen was present in the film. This excluded, for instance, the presence of OH^- [32]. The Sr $3d_{5/2}$ spectrum is shown in Figure 8.5D. Two closely localized peaks at BE = 132.4 eV and BE = 134.0 eV can be distinguished and they remain unchanged at t = 32 – 56 min. These binding energies are in good agreement with the binding

energies of $SrTiO_3$, while they differ from values typically found for pure SrO (132.6 eV and 135.3 eV) [32]. It indicates that Sr has a slightly different chemical environment in SRO than in pure SrO. Hence, the presence of a Sr-rich ruthenate phase seems very likely. Its stoichiometry is difficult to asses, but considering the thermodynamic requirements for the co-existence of phases, $SrRuO_3$, Sr_2RuO_4, and/or $Sr_3Ru_2O_7$ are possible, because $SrRuO_3$ and SrO cannot co-exist [26]. I compared these spectra with those of an unprocessed SRO/YSZO/Si surface. Several nanometers deep into a fresh SRO film the composition 30 at% Sr – 30 at% Ru – 40 at% O was found. Therefore, it is evident that part of the Ru was lost upon addition and heat treatment of the BTO layer.

After t = 55 min the YSZO layer of general composition 35 at% Zr – 6 at% Y – 59 at% O was reached. A sharp interface was detected between the YSZO and SRO layers, showing that no intermixing between these two phases occurred (insets in Figures 8.5C and D). After 90 min of sputtering only metallic Si^0 was present.

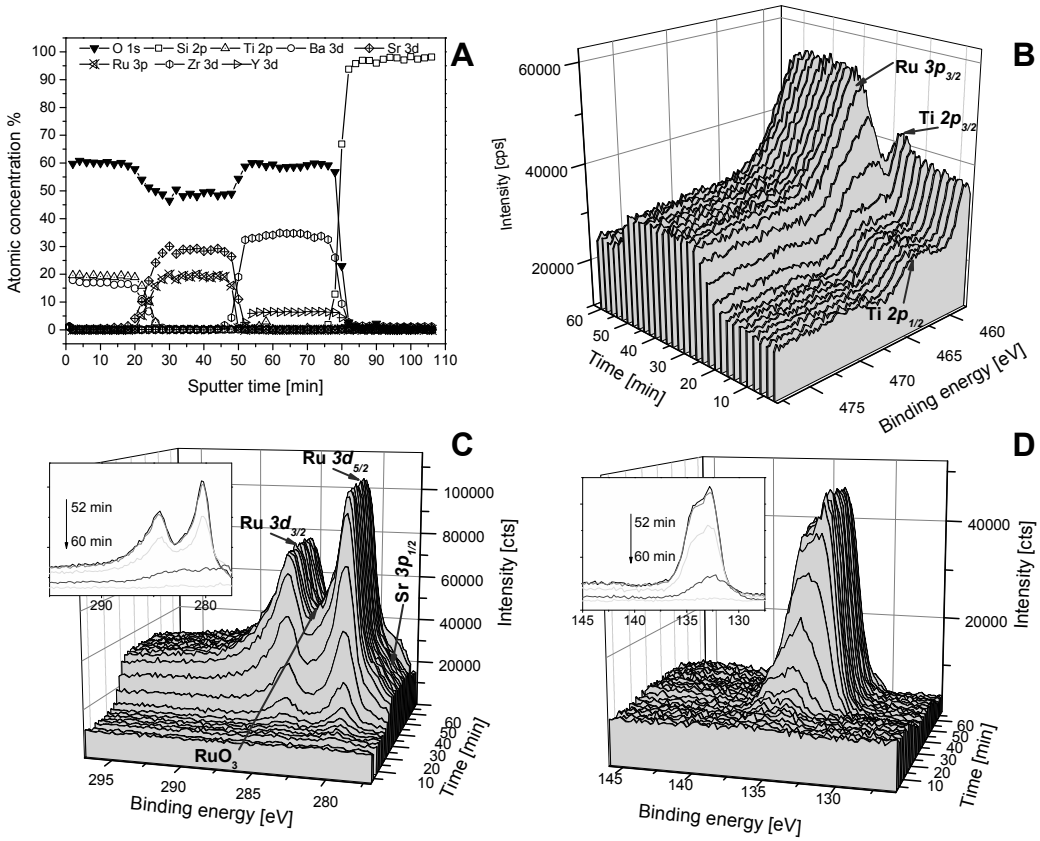

Figure 8.5. XPS depth profile of 200 nm barium titanate film on SRO/YSZO/Si. a) Atomic concentrations in film as function of sputter time. XPS spectra shown: b) Ru $3p_{3/2}$ and Ti $2p$ (partially); c) Ru $3d$ and Sr $3p_{1/2}$ (partially); d) Sr $3d$. Sputter rate is approximately 8 nm/min for BTO.

8.3.3. Formation of Ba-Ti-silicate phase

The formation of silicate was investigated by HT-XRD using a model system of 90 wt% BTO nano-powder mixed and 10 wt% silicon dioxide powder. Figure 8.6 shows x-ray diffractograms measured between 200 and 850 °C, with a hold time of 20 h at each temperature. Up to 650 °C only diffraction peaks originating from barium titanate, barium carbonate impurity and the Pt holder were measured. As the temperature was raised to 750 °C, numerous new peaks were detected. The new compound was undoubtedly recognized as fresnoite, $Ba_2Ti(Si_2O_7)O$ [33]. At 850 °C the fresnoite phase showed higher intensity diffraction peaks of lower FWHM. Hence, no reaction between BTO and SiO_2 took place at temperatures up to 650 °C, even when extremely long dwell times were used. This observation illustrates the high stability of barium titanate in contact with Si at this temperature. It is known from literature that crystalline silicate is formed at 730 °C [34].

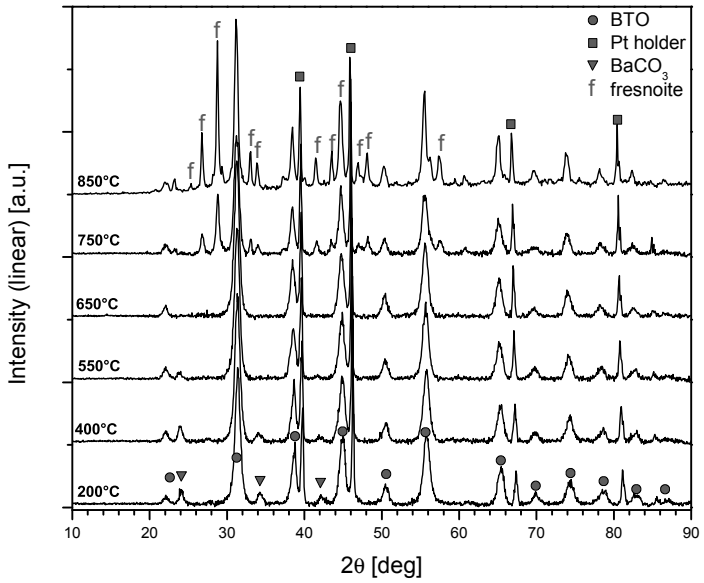

Figure 8.6. HT-XRD patterns of 90 wt% barium titanate nano-powder mixed with 10 wt% amorphous SiO_2 powder between 200 and 850 °C, with a typical dwell time of 20 h at all temperatures. Identified phases are marked by symbols.

8.3.4. Dielectric and ferroelectric properties

C-V measurements were performed on two investigated films, namely BTO/SRO/YSZO/Si and BTO/Pt/Ti/Si. Results are presented in Figures 8.7A. The relative permittivities were ε_r = 672 ± 1% for BTO/SRO/YSZO/Si, and ε_r = 161 ± 1% for BTO/Pt/Ti/Si at the peak maximum. In both cases a non-linear dielectric response was measured, yielding the characteristic "butterfly" shape in the *C-V* curve, with two distinguishable maxima of relative permittivity dependent on electric field direction. The shape indicates that the films were ferroelectric. A horizontal shift of the "butterfly" curve relative to 0 V is visible. This can be explained by the fact that the top and bottom electrodes were made of different materials and processed at different temperatures, which results in asymmetric properties of the upper and lower electrode-dielectric interfaces. The effect is discussed further below. The measured relative permittivity value of 670 – 680 at room temperature on SRO/YSZO/Si is comparable to values found for other sol-gel derived BTO thin films [3,8,9]. The high value of ε at 500 kHz suggests that BTO may be applicable in DRAMs, where good high-frequency performance is required [6]. The YSZO buffer layer is crucial to prevent diffusion of Si to the SRO electrode and the dielectric phase [15,17,18].

The local piezoelectric/ferroelectric properties of films were measured using PFM. Due to the considerable roughness of the film surface, the effect of domain switching could not be visualised by "domain-writing" with the PFM tip. However, local piezoresponse loops could be obtained easily, as shown in Figure 8.7B. The data demonstrate that a domain structure exists and domain switching takes place. The phase difference between applied AC signal and piezoresponse is determined by the orientation of the local ferroelectric polarization in the sample. The obtained signal as a function of DC bias between sample and tip resembles *P-V* hysteresis loops. Values obtained from the phase axis cannot be translated easily to actual polarization values (and hence to remnant polarization), but coercive field values correspond approximately to those found in *P-V* measurements. It can be seen in Figure 8.7B that the BTO/SRO/YSZO/Si film exhibited very good piezoresponse properties, with a coercive field of 48 kV/cm, compared to 120 kV/cm and poor piezoresponse for the BTO/Pt/Ti/Si film. The increase of the coercive field in the latter case can be related directly to the presence of a non-ferroelectric, non-conductive silicate layer at the interface with BTO [35,36].

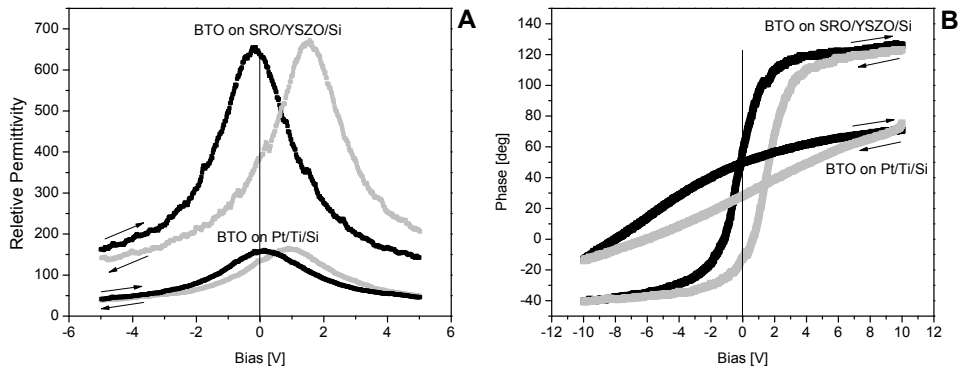

Figure 8.7. a) *C-V* data of BTO films fabricated by multi-layer deposition and processed by one-step annealing at 800 °C. BTO/SRO/YSZO/Si and BTO/Pt/Ti/Si; b) Piezoresponse force microscopy (PFM) loops of the same films.

At the interface between BTO and SRO a transition layer was found by XPS that was not visible by FE-SEM. The influence of an interfacial layer on the dielectric properties of a barium titanate capacitor can be evaluated in terms of the well-established metal-ferroelectric-metal model [37], in which the total capacity is expressed in terms of the capacity of the BTO-based capacitor C_0, and the interface-based capacitors C_{i1} and C_{i2}, in series:

$$\frac{1}{C} = \frac{1}{C_{i1}} + \frac{1}{C_{i2}} + \frac{1}{C_0} \tag{8.1}$$

Here C is the total capacity, C_{i1} is the capacity of the interface at the dielectric-lower electrode-interface, and C_{i2} is the corresponding capacity at the interface with the upper electrode. It is easily shown that for any finite value of C_{i1} or C_{i2}, the overall capacitance $C < C_0$. Hence, the interface acts as a dead layer that deteriorates the dielectric properties of the BTO film. It is known that epitaxial perovskite-perovskite interfaces such as the BTO/SRO interface provide superior dead-layer-originating capacities, close to the theoretical limit [37]. Nonetheless, it has also been demonstrated that mixing between SrO and BaO occurred at the $SrRuO_3$/BTO interface on a $SrTiO_3$(001) substrate. A complex interface is thus formed, even with well-defined surfaces and epitaxial films of two perovskites [38]. The formation of a dead layer at the interface with the bottom Pt or SRO electrode is therefore also expected in relatively imperfect polycrystalline BTO sol-gel films.

The influence of the upper electrode/BTO interface on dielectric properties is also important. Sputtering at low temperature is known to yield defects in the metal electrode microstructure, impeding conductivity. The difference in processing temperatures of bottom and top electrodes, and the different work functions of the

two materials are likely to result in Schottky contact formation. That could also explain the asymmetric position of the *C-V* dependence with respect to 0 V bias (Figure 8.7A).

Bulk strontium ruthenate is thermally stable up to 900 °C at ambient oxygen partial pressure [39]. Stable surfaces of $SrRuO_3$ have been reported up to at least 700 °C in oxygen/ozone atmospheres [26]. The stability at higher temperatures was not reported. On the other hand, $SrRuO_3$ exposed to oxygen/ozone, but post-annealed in vacuum formed Ru^0 and Sr_2RuO_4 [26]. The loss of ruthenium was due to formation of gaseous RuO_4. My data show that the $SrRuO_3$ surface is unstable at 800 °C, and a small amount of what seems to be RuO_3 was detected in the film near the upper interface with BTO. When SRO is processed under vacuum, Sr-rich ruthenates, $Sr_{n+1}Ru_nO_{3n+1}$, containing partially reduced Ru are formed [26,40]. In my experiments the loss of Ru probably did not lead to quantitative amounts of $Sr_{n+1}Ru_nO_{3n+1}$ phases, as XRD only showed the presence of oriented $SrRuO_3$. Loss of Ru therefore seems to be limited to the surface layer.

Processing of sol-gel derived BTO films on Pt/Ti/Si substrate led to a number of undesired effects. Titanium is a popular adhesion layer for platinizing Si/SiO_2 wafers [41]. It is known that annealing at ambient oxygen partial pressure leads to oxygen diffusion through Pt grain boundaries, partial oxidation of Ti to TiO_{2-x}, and migration of titanium dioxide to Pt [41]. Apparently, the reactivity of these phases at 800 °C is high, leading to diffusion of Si to Pt, and to platinum silicide formation. The Pt–Si binary system includes a number of phases, such as PtSi and Pt_6Si_5, that both match the stoichiometry found by XPS [42]. It is known that titanium dioxide can diffuse through platinum to the surface of an electrode at high temperature [41]. The XPS spectra showed that both Pt and Si were present in reduced forms in the Pt-based electrode, whereas Ti was present in oxidized form. The formation of a silicide phase presented no practical problem, since the measured conductivity of the platinum silicide electrode was only 4% lower than that of pure Pt.

Silicate formation was shown to occur in these films within a minute at 800 °C. Due to the presence of silicon on the surface of the electrode, a Ba-Ti-silicate phase nucleated directly at the interface, and grew upon heat treatment. Under the assumption that the interfacial capacitance of the top electrode and the capacitance of the BTO layer were the same in both investigated capacitor architectures, it can be estimated that the 20 nm interfacial silicate layer has a relative permittivity of approximately 20. This value is a good agreement with values reported in literature for bulk fresnoite [34].

Decreasing the crystallization temperature of $BaTiO_3$ to below 650 °C could possibly prevent silicate phase formation, even if PtSi had formed. However, reduced processing temperatures will also affect the morphology of the BTO film. It has been demonstrated that the dielectric properties depend strongly on processing

temperature, and 650 °C was found to be insufficient to obtain high relative permittivities [8,9]. The poor performance of $BaTiO_3$ at low processing temperatures is related to the stability of the oxocarbonate phase $Ba_2Ti_2O_5CO_3$, which shifts the onset of perovskite phase formation to 600 – 650 °C. It has been shown that the crystallization temperature of barium strontium titanate films can be decreased to 500 °C, but these films were obtained from a non-alkoxide-carboxylate process involving the processing of metallic Ba and Sr [43]. Furthermore, stable hydroxyl defects in the structure are known to stabilize the non-ferroelectric cubic phase instead of the high-*k* tetragonal phase at room temperature. The unit cell of the cubic phase is larger than that of the defect-free tetragonal phase, as shown in Chapter 3 and in refs. [2,44,45]. High temperature processing leads to removal of hydroxyl defects, but the high density of wet-chemically-derived $BaTiO_3$ is retained only above 800 °C [45]. This is due to the fact that removal of hydroxyl defects leads to formation of thermodynamically stable internal pores in barium titanate grains. Both hydroxyl defects and internal porosity lead to a loss of dielectric properties, unless it is processed at sufficiently high temperature [44,45].

8.4. Conclusions

The formation of silicates such as fresnoite at the interface between barium titanate and platinum silicide leads to formation of a dead layer of very low relative permittivity (*ca*. 20). The existence of the interface degenerates the dielectric properties of barium titanate based capacitors, leading to a considerable decrease of relative permittivity. The problem is related to high-temperature processing of dense sol-gel-derived films of barium titanate by rapid thermal annealing and multi-layer deposition. As long as a high annealing temperature is necessary to obtain the desired dielectric properties, the problem of Si diffusion and silicate interface formation can be solved by the use of $SrRuO_3$ electrodes with a ZrO_2-8%Y_2O_3 buffer film between the electrode and the silicon substrate.

8.5. References

[1] Yoon, D. *J. Ceram. Proc. Res.*, *7*, 343-354, **2006**.

[2] Pithan, C.; Hennings, D. H.; Waser, R. *Int. J. Appl. Ceram. Technol.*, 2, 1-14, **2005**.

[3] Schwartz, R. W.; Schneller, T. S.; Waser, R. *C. R. Chimie*, *7*, 433-461, **2004**.

[4] Schwartz, R. W.; Narayanan, M. Chemical Solution Deposition - Basic Principles, In *Solution Processing of Inorganic Materials*, ed. Mitzi, D. B., John Wiley & Sons, Inc., New Jersey, 33-76, **2009**.

[5] Huffman, M. *Integr, Ferroelectrics*, 10, 39-53, **1995**.

[6] Schroeder, H.; Kingon, A. High-Permittivity Materials for DRAMs. In *Nanoelectronics and Information Technology: Advanced Electronic Materials and Novel Devices*, ed. Waser, R., Wiley VCH GmbH & Co, Weinheim, 540-563, **2003**.
[7] Scott, J. F.; Paz de Araujo, C. A. *Science*, 246, 1400-1405, **1989**.
[8] Hasenkox, U.; Hoffmann, S.; Waser, R. *J. Sol-Gel Sci. Technol.*, 12, 67-79, **1998**.
[9] Hoffmann, S.; Waser, R. *J. Eur. Ceram. Soc.*, 19, 1339-1343, **1999**.
[10] Phule, P. P.; Risbud, S. H. *Adv. Ceram. Mater.*, 3, 183-185, **1988**.
[11] Schwartz, R. W. *Chem. Mater.*, 9, 2325-2340, **1997**.
[12] Frey, M. H.; Payne, D. A. *Chem. Mater.*, *7*, 123-129, **1995**.
[13] Mosset, A.; Gautier-Luneau, I.; Galy, J.; Strehlow, P.; Schmidt, H. *J. Non-Cryst. Solids,* 100, 339-344, **1998**.
[14] Schwartz, R. W.; Clem, P. G.; Voigt, J. A.; Byhoff, E. R.; van Stry, M.; Headley, T. J.; Missert, N. A. *J. Am. Ceram. Soc.*, 82, 2359-2367, **1999**.
[15] Hubbard, K. J.; Schlom, D. G. *J. Mater. Res.*, 11, 2757-2776, **1996**.
[16] Nguyen, M. D.; Karakaya, K.; te Riele, P. M.; Blank, D. H. A.; Rijnders, A. J. H. M. In *Proceedings of the Third IEEE-NEMS,* Sanya, China, 315, 6-9 January. **2008**.
[17] Wang, S. J.; Ong, C. K.; You, L. P.; Xu, S. Y. *Semicond. Sci. Technol.*, 15, 836-839, **2000**.
[18] Dekkers, M.; Nguyen, M. D.; Steenwelle. R.; te Riele, P. M.; Blank, D. H. A.; Rijnders, G. *Appl. Phys. Lett.*, 95, 012902- 1-3, **2009**.
[19] Werner, W. S. M.; Smekal, W.; Powell, C. J. In *NIST Datanase for the Simulation of Electron Spectra for Surface Analysis*, National Institute of Standards and Technology, Gaithersburg, **2006**.
[20] Chapter 2; Stawski, T. M.; Veldhuis, S. A.; Göbel, O. F.; ten Elshof, J. E.; Blank, D. H. A. *J. Am. Ceram. Soc.*, 93, 3443-3448, **2010**.
[21] Carriere, B.; Deville, J. P.; Brion, D.; Escard, J. *J. Electron. Spectrosc. Relat. Phenom.*, 10, 85-91, **1977**.
[22] Grunthaner, P. J.; Grunthaner, F. J.; Madhukar, A. *J. Vac. Sci. Tech.*, 20, 680-683, **1982**.
[23] Göpel, W.; Anderson, J. A.; Frankel, D.; Jaenig, M.; Phillips, K.; Schäffer, J. A.; Rocker, G. *Surf. Sci.*, 139, 333-346, **1984**.
[24] Hung, C. C.; Riman, R. E.; Caracciolo, R. *Ceram. Trans.,* 12, 17-24, **1990**.
[25] Nguyen, T. P.; Lefrant, S. *J. Phys. Cond. Matter I*, 5197-5204, **1989**.
[26] Shin, J.; Kalinin, S. V.; Lee, H. N.; Christen, H. M.; Moore, R. G.; Plummer, E. W.; Baddorf, A. P. *Surf. Sci.*, 581, 118-132, **2005**.
[27] Rama Rao, M. V.; Sathe, V. G.; Sornadurai, D.; Panigrahi, B.; Shripathi, T. *J. Phys. Chem. Solids,* 61, 1989-1999, **2000**.
[28] Cox, P. A.; Egdell, R. G.; Goodenough, J. B.; Hamnett, A.; Naish, C. C. *J. Phys. C*, 16, 6221-6239, **1983**.

[29] Sarma, D. D.; Rao, C. N. R. *J. Electron Spectrosc Relat. Phenom.*, 20, 25-45, **1980**.
[30] Kim, K. S.; Winograd N. *J. Catal.*, 35, 66-72, **1974**.
[31] Lewrenz, H. J.; Stucki, S.; Kötz, R. *Surf. Sci.*, 126, 463-468, **1983**.
[32] Vasquez, R. P. *J. Electron Spetrosc.*, 56, 217-240, **1991**.
[33] PDF 00-022-0513. International Centre for Diffraction Data, **2005**.
[34] Rangarajan, B.; Shrout, T.; Lanagan, M. *J. Am. Ceram. Soc.*, 92, 2642-2647, **2009**.
[35] Tagantsev, A. K.; Stolichnov, I. A. *Appl. Phys. Lett.*, 83, 3356-3358, **2003**.
[36] Pertsev, N. A.; Rodriguez Contreras, J.; Kukhar, V. G,; Hermanns, B.; Hohlstedt, H.; Waser, R. *Appl. Phys. Lett.*, 74, 1326-1328, **1999**.
[37] Stengel, M.; Spaldin, N.A. *Nature*, 443, 679-682, **2006**.
[38] Shin, J.; Borisevich, A.Y.; Meunier, V.; Zhou, J.; Plummer, E. W.; Kalinin, S. V.; Baddorf, A. P. *ACS Nano*, 4, 4190-4196, **2010**.
[39] Bensch, W.; Schmalle, H. W.; Reller, A. *Solid State Ionics,*43, 171-177, **1990**.
[40] Mallika, C.; Sreedharan, O.M. *J. Alloys and Compounds*, 191, 219-222, **1993**.
[41] Sreenivas, K.; Reaney, I.; Maeder, T.; Setter, N.; Jagadish, C.; Elliman, R. G. *J. Appl. Phys.*, 75, 232-239, **1994**.
[42] Tanner, L.E.; Okamoto, H. *J. Phase Equilib.*, 12, 571-574, **1991**.
[43] Halder, S.; Schneller, T.; Waser, R. *J. Sol-Gel Sci. Technol.*, 33, 299-306, **2005**.
[44] Frey, M. H.; Payne, D. A. *Phys. Rev. B*, 54, 3158-3168, **1996**.
[45] Hennings, D. F. K.; Metzmacher, C.; Schreinemacher, B. S. *J. Am. Ceram. Soc.*, 84, 179-182, **2001**.

9

Final Words and Outlook

9.1. General conclusions

In this thesis a number of research projects was described in which sol-gel processing and characterization of precursors used to obtain either PZT or BTO ceramics constituted the ubiquitous theme. In the scope of the current and future demand for products based on perovskite ceramics the sol-gel-based methods of manufacturing seem to be for the asking. Especially when it comes to thin film preparation under laboratory conditions, sol-gel techniques could not be less onerous. One needs only basic glassware, chemicals and substrates, a coater (*e.g.* dip-coater) and a high-temperature oven. How illusive! The complexity of sol-gel processing does not lie in its "hardware" aspects, but in its subtle chemistry, as this thesis has undoubtedly shown. Only profound understanding, or at least a will to comprehend some of crucial aspects, can lead to mass-production of sol-gel derived ceramics of expected properties and performance.

For instance, an alkoxide-hydroxide process as described in Chapter 2 and partially in Chapter 3, is uncomplicated in its experimental rendering. Hardware-wise, efficient mixing of precursors upon reaction and careful adjustment of the stoichiometry yields phase-pure nano-sized barium titanate. In the scope of further research, it was possible to synthesize by this method $SrTiO_3$, $BaZrO_3$, $Ba(Zr_{1-x}Ti_x)O_3$, and $Ba_{1-x}Sr_xTiO_3$ with $0 \leq x \leq 1$. As flexible as the method is in terms of the final product, it has always been based on benzyl alcohol or related solvents such DL-1-phenyethanol, *i.e.* solvents of high boiling point that react with the precursor Ti(IV) *iso*-propoxide to yield alkoxides of higher stability, yet leading to low-temperature precipitation of crystalline perovskite rather than formation of amorphous xero-gels. Thermal post-processing of the raw product could thus be avoided. On the other hand, the precipitate in benzyl alcohol $BaTiO_3$ is quite unique in its properties, as the study in Chapter 3 clearly demonstrated. Especially when compared with its other wet-chemically-derived equivalents such as hydrothermal barium titanate. Not only exhibited the as-synthesized $BaTiO_3$ a narrow size distribution with an average crystallite < 10 nm, but it retained a tetragonal structure (in XRD and FR-RS) at room temperature after annealing at 850 °C, with only minor grain growth to 60 – 100 nm. This is probably one of the finest tetragonal

barium titanate powders reported in the literature up to date [1]. Although the material required thermal processing after precipitation, it was the sol-gel route with the utilization of Ti(IV) phenylmethoxide that provided $BaTiO_3$ of given properties. Again, the alkoxide-hydroxide route clearly differs from the alkoxide-carboxylate route discussed in Chapters 4, 5 and 8 (BTO), and Chapter 6 and 7 (PZT). The alkoxide-hydroxide sol precipitation proved to be an excellent method to obtain nano-sized powders of several perovskites. But due to the local inhomogeneities of the precursor gels and their overall high viscosity, it did not enable easy deposition of thin films from the sol-gel, at least by means of high-shear techniques such as spin-casting. Hence, an appropriate choice of a given chemical route is essential for a physical form of the ceramics.

The alkoxide-carboxylate route is a widely applied synthetic method to obtain high-quality films of numerous perovskite materials [2]. In general it is possible to obtain precursors of adjustable viscosity and high homogeneity. It was demonstrated in this thesis that the microstructure of the amorphous precursor is dependent on metal alkoxide, metal carboxylate, hydrolysis ratio, and processing conditions (constant composition or physical drying). In Chapters 4 and 5 of this thesis it was shown that the structural evolution of the sol depends primarily on the oligomerization of monomeric titanium oxo-alkoxo-carboxylate clusters. Barium seemed to remain dissolved in the acetic acid solvent phase, but had an indirect stabilizing effect by suppressing precipitation of titania from solution. The structures in solution were titania-related, and could be divided into fractal-like branched oligomers, and agglomerates of similarly sized nanoparticles. Both types of structures consisted of the same type of primary particle. The fractal-like morphologies disappeared during film drying, most likely because they were not stable in the absence of a solvent matrix. Only the agglomerate-like structures remained in the as-dried films. Such an evolution suggests that an ongoing phase evolution could lead to reaction-condition-dependent inhomogeneity and separation effects preserved in xero-gels. I showed that separation between barium and titanium-rich domains occurred during the drying of these thin films, and was dependent on the initial hydrolysis ratios of the sol. Non-hydrolysed sols yielded a homogenous distribution of elements, whereas high hydrolysis ratios promoted separation of Ba- and Ti-rich domains with a correlation length of *ca.* 15 nm. This demonstrates that such as-dried films are not necessarily uniform on the mesoscopic level. Hence, one could speculate that in such a case, $BaTiO_3$ crystallization from the Ti-rich and Ba-rich domains resembles a solid state reaction between two separate materials, but at much shorter length scales. Provided that even non-hydrolyzed films are not fully homogenous in terms of component mixing, homo-nucleation [2] of the perovskite phase in the film, instead of the hetero-nucleation at the interface with the substrate, could be rationalized. This phenomenon is partially explored in Chapter 8 of this thesis. I based my study on a well-known work of Hoffmann *et al.* [3], in which it was shown that only multi-step deposition

and calcination of low-concentrated alkoxide-carboxylate BTO precursor solutions could deliver dense films with columnar morphology. I hypothesized that the low concentration of a sol could play a twofold role: (1) the lower the concentration, the thinner the synthesized film is; hence, the surface/volume ratio increasingly promotes hetero-nucleation [6]; (2) due to the low concentration of the sol, the overall rate of oligomerization and agglomeration of titania-related species decreases, yielding a more homogenous microstructure.

From the technological point of view, it was shown in this thesis that restrictions resulting from sol-gel processing and conditions for a given morphology can affect the performance of the device. This factor should always be considered in view of possible applications, since *e.g.* barium strontium titanate is a promising material for DRAMs [4], but its successful integration with CMOS is only possible when very thin diffusion layers are sufficiently effective to stop Si from diffusing into the dielectric material.

This thesis has also demonstrated that primary differences in the structure of alkoxide-carboxylate precursors of lead zirconate titanate emerged when compared with barium titanate precursor sols and xero-gels (Chapters 6 and 7). The differences were attributed, among others, to the presence of the third component, namely zirconium alkoxide. Its hydrolysis and condensation patterns differ strongly from what was observed in the case of titanium alkoxide. Zr-rich "nanoparticles" of 1 – 10 nm size were present in as-dried PZT films. At even relatively high hydrolysis ratios, these nanoparticles were crystalline, and the surrounding Ti and Zr-rich matrix was amorphous. At very high hydrolysis ratios no crystallization of Zr-rich nanoparticles occurred in the as-dried film. It was shown that this phenomenon was drying-related, since PZT precursor sols at equivalent hydrolysis ratios were stable and did not contain any large crystals. Cylinder-shaped particles constituted one of the primary building blocks of lead zirconate titanate precursor sols. The number of particles in the PZT sols decreased in the course of time. This suggests that condensation and/or agglomeration processes took place in the PZT solutions, yielding a broad mass distributions of cylindrical particles. No direct evidence for the presence of Pb- or/and Ti-related structures was found in the investigated PZT sols.

Thus, in the case of BTO sols and xero-gels the water concentration was reversely related to the degree of homogeneity of the systems, whereas in PZT sols water helped to increase the overall stability of the sols and the homogeneity of the amorphous films. Secondly, in the case of BTO sols and as-dried films, the inhomogeneity development was an ongoing process, whereas in the case of precursor PZT, phase separation took place only in the course of drying. Thirdly, in PZT precursor films and sols, Pb and Ti seemed to be homogenously mixed at all times, whereas in BTO sols component separation did not occur only in non-hydrolyzed sols. Hence, processing of sol-gel precursors has indeed an impact on the

microstructure of the xero-gel. I hypothesize that such a microstructure of PZT xero-gels, with zirconia nano-crystals and amorphous Pb-Ti-Zr-matrix could be related to the phenomenon of hetero-nucleation of the PZT perovskite phase at the interface, and hence growth of oriented columnar PZT films, as easily obtained on *e.g.* Pt as reported in numerous works [2,5]. I present a basis for this claim in the Outlook.

9.2. Outlook

The alkoxide-carboxylate synthesis route for PZT is one of several possible methods. Far more popular is a water-free full-alkoxide route involving [5]: (1) complete dehydration of lead(II) acetate, (2) formation of lead(II) alkoxide in the course of reaction between 2-methoxyethanol and water-free lead(II) acetate under reflux, (3) further mixing and refluxing with zirconium and titanium alkoxides in 2-methoxyethanol. This reaction yields a fine precursor, but the route is demanding, because it is time-consuming and requires a water-free atmosphere. From that point of view the alkoxide-carboxylate route constitutes an irresistible alternative. Recently we showed [6] that the sol of composition as in Chapters 5 and 7 at a hydrolysis ratio of 27.6 yielded highly oriented PZT(110) patterned films of 50 nm thickness on SRO(110)/YSZO(001)/Si(001). The patterns were prepared by the novel Micromoulding with Selective Dewetting technique, and were deposited in a single step and annealed at 700 °C for 30 min (rapid thermal annealing). Figure 9.1A presents a FE-SEM image of the film cross-section. The inset in the image shows a top view demonstrating the large-area quality of the pattern. Ferroelectric switching of the film was confirmed by PFM (Figure 9.1B&C). The XRD pattern of the film is presented in Figure 9.2A with characteristic peaks marked. Figure 9.2B contains rocking curves at selected peaks confirming the (110) orientation of PZT. These preliminary results demonstrate the high potential of the alkoxide-carboxylate route for PZT investigated by me.

The fact that an inhomogeneous microstructure of an amorphous precursor film (as shown in Chapter 6) could yield a high quality oriented film is very important for the understanding of the nucleation and growth phenomena in PZT and BTO. I speculate that the presence of crystalline zirconia and the amorphous matrix containing Pb, Ti and remaining Zr, could favor the formation of crystalline phases upon heat-treatment, which would then not be perovskite related, due to the stoichiometric and thermodynamic constraints. Namely, crystalline zirconia will have a much lower free energy than the remaining amorphous matrix. Hence, it is energetically more favorable that an amorphous matrix first crystallizes into a transition phase of lower free energy, and then reacts with zirconia. Obviously, an amorphous matrix cannot crystallize into a perovskite due to the insufficient content of suitable B-site cations. Transition phases are most likely to be nucleated in the volume of the film, whereas then perovskite phase could be nucleated at the interface

with a favorable substrate, and grow in the course of consumption of other non-perovskite phases, yielding an oriented film, as explained in detail in ref [2]. Such interpretation agrees well with thermodynamic theories introduced by Roy *et al.* [7] and utilized by R. W. Schwartz and his colleagues [2]. On the other hand, in the case of BTO precursor films, a perovskite phase most likely nucleates in the entire volume of the film due to the equal spatial distribution of Ti- and Ba-rich regions. It is decreasing the probability of hetero-nucleation due to the fact that activation energies of crystallization and composition are identical at different sites.

A detailed knowledge of sol-gel morphologies and related reactions seems to be crucial to understand phenomena taking place at much higher processing temperatures that lead to desired ceramic materials. The three routes examined in this thesis were related to only two materials, and constituted only a fraction of available sol-gel methods in literature that have been used to obtain hundreds of ceramic materials. It seems literally impossible to explore all of them within a broad spectrum of reaction conditions. I wish I could draw more general conclusions. Furthermore, in my work I focused on "super-structural" properties of the colloids, ignoring vastly the chemical aspects. Hopefully, in the future I will be able to study in more detail the local structure of the precursor sols, which would provide me a critical view on my current findings.

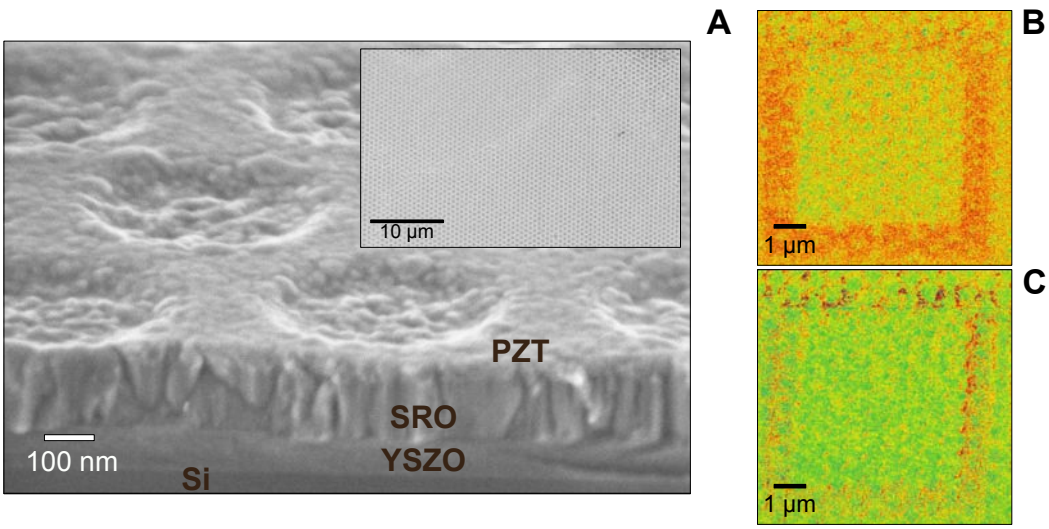

Figure 9.1. a) FE-SEM image of the cross-section of a PZT pattern on SRO/YSZO/Si substrate heat-treated at 700 °C. Inset presents a low-magnification top-view image of the same pattern; b) PFM image of the pattern demonstrating ferroelectric switching, amplitude; c) PFM image of the pattern demonstrating ferroelectric switching, phase.

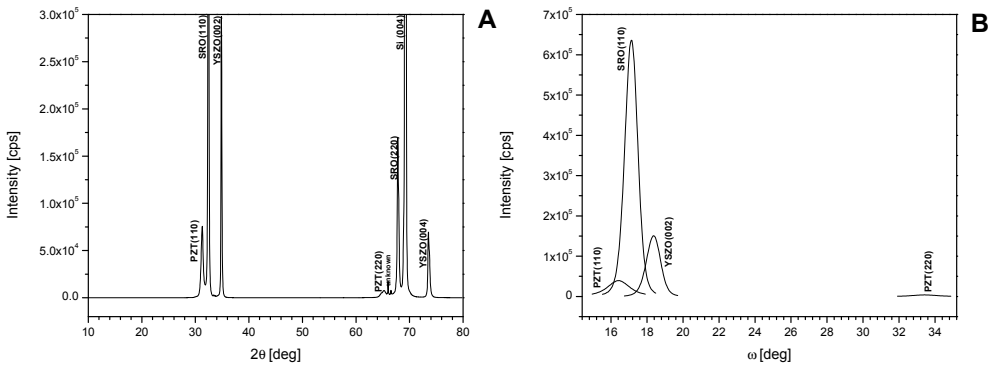

Figure 9.2. a) XRD pattern of a PZT pattern on SRO/YSZO/Si substrate heat-treated at 700 °C; b) rocking-curves of the selected peaks.

9.3. References

[1] Yoon, D. *J. Ceram. Proc., 7*, 343-354, **2006.**

[2] Schwartz, R. W.; Schneller, T. S.; Waser, R. *C. R. Chimie, 7*, 433-461, **2004**.

[3] Hoffmann, S.; Waser, R. *J. Eur. Ceram. Soc.*, 19, 1339-1343, **1999**.

[4] Schroeder, H.; Kingon, A. High-Permittivity Materials for DRAMs. In *Nanoelectronics and Information Technology: Advanced Electronic Materials and Novel Devices*, ed. Waser, R., Wiley VCH GmbH & Co, Weinheim, 540-563, **2003**.

[5] Schneller, T.; Waser, R. *J. Sol-Gel Sci. Techn.*, 42, 337-352, **2007**.

[6] Stawski, T.; George, A.; Smith, B. F.; Blank, D. H. A.; ten Elshof, J. E. in preparation.

[7] Roy, R. *J. Am. Ceram. Soc.*, 344, 52, **1969**.

Summary

This thesis comprises of seven full research chapters on the morphology, properties and processing of sol-gel precursor systems of barium titanate and lead zirconate titanate thin films and powders as explained in Chapter 1. In all the considered problems, the synthesis leading to nano-sized perovskite ceramics constitutes the main research theme.

The low-temperature alkoxide–hydroxide precipitation synthesis of nano-sized crystalline barium titanate in non-aqueous media is presented in Chapter 2. In this report, I show the influence of the reaction medium on the nature of the product by investigating the reaction of titanium (IV) *iso*-propoxide with barium hydroxide hydrates in 2-methoxyethanol and benzyl alcohol, respectively. A perovskite phase precipitated only in benzyl alcohol, but not in 2-methoxyethanol. One molar equivalent of water, present in barium hydroxide monohydrate, was sufficient to hydrolyze the alkoxide and form nanocrystalline $BaTiO_3$. Depending on the water concentration, the process led directly to crystalline powder of particle sizes ranging from 3 to 10 nm, and with a clear correlation between particle size and amount of water.

The evolution of morphology, phase, and defect structure of nano-sized $BaTiO_3$ powders synthesized by an alkoxide-hydroxide process in benzyl alcohol under reflux conditions were investigated in Chapter 3. Powders were heat-processed at temperatures ranging from 250 to 850 °C. X-ray powder diffraction revealed that $BaTiO_3$ remained in a room temperature cubic phase with a crystallite size below 30 nm when heat-processed up to 700 °C. Limited particle growth and sintering effects were observed with transmission electron microscopy, but internal pores of 1 – 2 nm diameter inside the crystallites were well visible. Their presence is attributed to curing of lattice hydroxyl defects, as was confirmed by infrared spectroscopy and thermogravimetric analysis and differential scanning calorimetry. Raman spectroscopy revealed the development of local tetragonal/orthorhombic distortions in nanocrystalline grains after heat treatment at 350 °C or higher, but the volumetric cubic-to-tetragonal transition was observed only after heat treatment at 850 °C. Its occurrence was accompanied by substantial grain growth to ~100 nm size, and that transformation enabled the complete removal of hydroxyl defects and reordering/crystallization due to volume diffusion.

In Chapter 4 the evolution of hydrolyzed alkoxide-carboxylate sol-gel precursor solutions of barium titanate was investigated by time-resolved small angle x-ray scattering and viscosity measurements. Sols were prepared from titanium(IV) iso-propoxide in 2-methoxyethanol and barium acetate in acetic acid. Analysis of the experimental data showed that the evolution of the sol went through three stages. In

stage (i) mainly isolated primary scatterers of *ca.* 0.45 nm radius formed. Stage (ii) showed the growth of branched oligomeric mass fractal-like structures with 3 – 15 nm gyration radius and fractal dimension 1.9 – 1.5, as well as the presence of internally ordered structures with a correlation length of *ca.* 1.8 nm. In stage (iii) higher-level hierarchy developed in the sol, probably due to cluster-cluster aggregation of the fractal-like branched oligomers into a gel. The data suggest that the agglomerates of scatterers are Ti-based, and are constructed of small spherical primary particles of very similar size. The inorganic core of these particles has a radius of *ca,* 0.45 nm, and they have a outer organic ligand shell of *ca,* 0.45 nm thickness. Ba-related species remained dissolved in the acetic acid matrix, and were present as ions. No Ba-related species could be seen with SAXS. Ba seemed to exert an indirect influence on the growth and precipitation or stabilization of the titanium-based structures from solution.

In Chapter 5 the structural evolution in wet alkoxide-carboxylate sol-gel precursor films of barium titanate upon drying was investigated by time-resolved small angle x-ray scattering. The morphology of as-dried amorphous precursor thin films was investigated by transmission electron microscopy and electron energy loss spectroscopy . Sols were prepared from titanium(IV) *iso*-propoxide in 2-methoxyethanol and barium acetate in acetic acid. The structures that were visible with SAXS could be divided into oligomeric structures with fractal-like scattering characteristics, and randomly packed agglomerates of nanoparticles of similar size. The fractal-like morphologies disappeared during film drying, probably because they were not stable in the absence of a solvent matrix. Only the ordered agglomerate-like structures remained in the as-dried films. EELS on as-dried films showed that spatial separation between barium and titanium-rich domains occurred during the drying of the thin films on a length scale of nanometers, depending on hydrolysis ratio. This demonstrates that as-dried films are not necessarily uniform on the mesoscopic level.

The structural evolution of sol-gel derived lead zirconate titanate precursor films during and after physical drying was investigated by transmission electron microscopy, electron energy loss spectroscopy selected area electron diffraction and time-resolved x-ray diffraction in Chapter 6. Films were deposited from initial 0.3 mol/dm^3 precursor sols with varying hydrolysis ratios. Zr-rich grains of 1 – 10 nm size, embedded in a Pb-, Zr-, Ti- containing amorphous matrix were found in as-dried films. The Zr-rich regions were crystalline at hydrolysis ratios $[H_2O]/[Zr,Ti] < 27.6$, and amorphous at ratios > 100. X-ray diffraction analysis of lead zirconate titanate and zirconia sols revealed that the crystalline nanoparticles in both sols were identical, and were probably composed of nanosized zirconium oxoacetate-like clusters. This study demonstrates that time-resolved x-ray diffraction combined with electron energy loss spectroscopy mapping is a powerful tool to monitor the nanoscale structural evolution of sol-gel derived thin films.

In Chapter 7, the evolution of nanostructure in sol-gel derived lead zirconate titanate and zirconia precursor sols at different hydrolysis ratios was investigated by small angle x-ray scattering . The shape of the clusters in the zirconia sol could be described by the length-polydisperse cylindrical form factor. The zirconia-based clusters were characterized by a cross-sectional radius, r_0, of 0.28 nm, and a practically monodisperse length of *ca*. 1.85 nm. These clusters were probably constructed of zirconia-related tetrameric building blocks. Similar cylindrical structural motifs were observed in lead zirconate titanate precursor sols with $[H_2O]/[Zr,Ti]$ = 9.26 and 27.6, but the polydispersity in length was much higher. Clear scattering contributions from Ti and Pb centers were not detected, which was interpreted in terms of a homogeneous distribution of unbound lead ions in solution, and the relatively low scattering intensity from any Ti-based clusters or oligomers that may have been present in the sols.

In Chapter 8, thin films of barium titanate of 200 nm thickness, derived from an alkoxide-carboxylate sol-gel process, were deposited on Pt/Ti and $SrRuO_3/ZrO_2$-8%Y_2O_3 coated Si wafers. Films with a dense columnar microstructure were obtained by repeated deposition of thin amorphous layers from low-concentrated sols, and crystallization at 800 °C. This method added 10 nm thickness to the crystalline barium titanate film in each deposition step. The harsh processing conditions had a negative impact on the platinized silicon wafers, where Pt-Si silicides were formed. This led to diffusion of Si into barium titanate and interfacial silicate formation. The interfacial silicate layer was the cause of deteriorated dielectric and ferroelectric properties of the barium titanate layer. Use of $SrRuO_3/ZrO_2$-8%Y_2O_3/Si substrates solved the problem. No diffusion of Si was observed, and barium titanate films with good dielectric and ferroelectric properties were obtained.

In Chapter 9 general conclusions are drawn. It is stated that the complexity of sol-gel processing does not lie in its "hardware" aspects, but in its subtle chemistry. I postulate that only profound understanding, or at least a will to comprehend some of crucial aspects, can lead to mass-production of sol-gel derived ceramics of expected properties and performance.

Samenvatting

Dit proefschrift bevat *zeven* onderzoek hoofdstukken over de morfologie, de eigenschappen en de verwerking van het sol-gel precursor systeem van barium titanaat (BTO) en lood zirconaat titanaat (PZT) dunne films en poeders, zoals wordt uitgelegd in Hoofdstuk 1. De synthese van nanoschaal grootte keramische perovskieten is het belangrijkste thema van dit proefschrift, en staat centraal bij alle onderzoeksvraagstukken en -problemen.

De alkoxide-hydroxide precipitatie van nano-kristallijn barium titanaat (bij lage temperaturen) is beschreven in Hoofdstuk 2. In dit artikel laat ik de invloed van het reactie medium op het reactieproduct zien, door te kijken naar de reactie van titanium(IV) *iso*-propoxide met barium hydroxide hydraten in respectievelijk 2-methoxyethanol en benzyl alcohol. Een perovskiet fase precipiteert slechts in benzyl alcohol en niet in 2-methoxyethanol. Een equivalent van 1 mol water, aanwezig in barium hydroxide monohydraat, was genoeg om de alkoxide te hydrolyseren en nano-kristallijn barium titanaat te vormen. Afhankelijk van de water concentratie, leidde de reactie direct tot een kristallijn poeder met groottes van 3 tot 10 nm, met een sterke correlatie tussen de deeltjesgrootte en de hoeveelheid water.

De evolutie van de morfologie, de fase, en de defect structuur van nanoschaal grootte $BaTiO_3$ poeders, gesynthetiseerd uit het alkoxide-hydroxide proces in benzyl alcohol, is onderzocht in Hoofdstuk 3. Na de synthese hebben de poeders een hittebehandeling ondergaan in het temperatuurgebied van 250 tot 850 °C. Poeder röntgendiffractie liet zien dat poeder verhit tot 700 °C in de stabiele kubische fase bleef, met kristalliet groottes kleiner dan 30 nm. Gelimiteerde deeltjesgroei en sintereffecten zijn opgemerkt met transmissie elektronenmicroscopie (TEM). Echter, de interne porositeit (1 – 2 nm diameter grootte) van de kristallieten was goed zichtbaar.
De aanwezigheid van deze poriën wordt toegekend aan de verwijdering van hydroxyl defecten in het kristalrooster. Raman spectroscopie onthulde, na een hitte behandeling bij temperaturen > 350 °C, een lokale ontwikkeling van een tetragonaal/orthorhombische deformatie in de nano-kristallijne korrels. Echter, de volumetrische kubisch-naar-tetragonale overgang was alleen zichtbaar na behandeling bij 850 °C. Deze overgang ging gepaard met aanzienlijke korrelgroei tot ~ 100 nm grootte. Door deze volume diffusie werden alle hydroxyl defecten verwijderd en vond herordening/kristallisatie van de korrels plaats.

In Hoofdstuk 4 wordt de evolutie van gehydrolyseerde alkoxide-carboxylaat sol-gel precursor oplossing van barium titanaat onderzocht met Kleine-hoekstrooiing van Röntgenstraling (SAXS) en viscositeitsmetingen. De sols zijn bereid met titanium(IV) *iso*-propoxide in 2-methoxyethanol en barium acetaat in azijnzuur.

Analyse van de experimentele data wees uit, dat de evolutie van de sol via drie verschillende stadia verliep: (i) voornamelijk geïsoleerde primaire verstrooiingsdeeltjes, met een radius van ongeveer 0.45 nm worden gevormd; (ii) laat de groei van vertakte oligomere massa fractalen zien, met een radii van gyratie van 3 – 15 nm en fractalische dimensies van 1.9 – 1.5. Tevens zijn er intern-geordende structuren aangetroffen met een correlatie lengte van ca. 1.8 nm en (iii) complexere hiërarchie in de sol is verder ontwikkeld tot een gel, waarschijnlijk door cluster-cluster aggregatie van de vertakte (fractale) oligomeren. De data suggereert dat voornamelijk titanium-rijke geagglomereerde deeltjes ontstaan, die sferisch en van bijna dezelfde grootte zijn. De anorganische kern van deze deeltjes heeft de radius van ca. 0.45 nm, met een organische (liganden) schil van ook ca. 0.45 nm. Barium gerelateerde deeltjes blijven opgelost in de azijnzuur matrix als ionen. Geen van deze deeltjes waren te zien met SAXS metingen. Barium lijkt indirect de groei en precipitatie of stabilisatie van de titanium-structuren te beïnvloeden.

Hoofdstuk 5 beschrijft de structuur evolutie in dunne films van het alkoxide-carboxylaat sol-gel precursor systeem van barium titanaat door middel van SAXS. De morfologie van gedroogde amorfe films is onderzocht met TEM en elektronen energieverlies spectroscopie (EELS). Sols op basis van titanium(IV) *iso*-propoxide in 2-methoxyethanol en barium acetaat in azijnzuur zijn hiervoor gebruikt. De zichtbare structuren (met SAXS) kunnen onderverdeeld worden in oligomere structuren met fractalische verstrooiingseigenschappen, en willekeurig gepakte nanodeeltjes van gelijke grootte. Tijdens het drogen verdwijnt de fractalische structuur, waarschijnlijk door instabiliteit veroorzaakt door afwezigheid van de oplosmiddel-matrix. Slechts geordende geagglomereerde structuren blijven aanwezig in de gedroogde films. EELS metingen op de gedroogde films lieten, afhankelijk van de hydrolyse ratio, een scheiding van barium- en titaniumrijke domeinen op nanometerschaal zien. Hierdoor werd duidelijk aangetoond dat de gedroogde films niet zozeer uniform hoeven te zijn op mesoscopisch niveau.

De structurele evolutie van sol-gel verkregen lood zirconaat titanaat films is, zowel tijdens als na fysieke droging, beschreven in Hoofdstuk 6. De films zijn geproduceerd vanuit een precursor oplossing van 0.3 mol/dm^3 met verschillende hydrolyse ratio's. Zirconiumrijke deeltjes van 1 – 10 nm grootten zijn aangetroffen in een Pb-, Zr- en Ti-houdende amorfe matrix. De Zr-rijke regio's waren kristallijn bij hydrolyse ratio's $[H_2O]/[Zr,Ti] < 27.6$ en amorf bij ratio's > 100. XRD analyse van lood zirconaat titanaat en zirconia sols wees uit dat de ontstane kristallijne nanodeeltjes in beide systemen identiek waren (en waarschijnlijk bestaan uit zirconium oxoacetaat-achtige clusters). Deze studie toont aan dat tijdsgemeten XRD, gecombineerd met EELS kartering, een krachtige methode is om de structurele evolutie van dunne films op nanoschaal te kunnen volgen.

In Hoofdstuk 7 is de evolutie van sol-gel verkregen lood zirconaat titanaat en zirconia, bij verschillende hydrolyse ratio's, met SAXS onderzocht. De vorm van de clusters in de zirconia sol kunnen beschreven worden als een form factor van een polydisperse cilindrische lengteverdeling. De zirconia-clusters worden gekarakteriseerd door een dwarsdoorsnede radius, r_0, van 0.28 nm en een nagenoeg monodisperse lengte van ca. 1.85 nm. Waarschijnlijk zijn deze clusters opgebouwd uit zirconia-gerelateerde tetramerische bouwblokken. In lood zirconaat titanaat sols zijn gelijkwaardige cilindrische structuren aangetroffen (bij hydrolyse ratio's $[H_2O]/[Zr,Ti]$ = 9.26 en 27.6), echter met een veel grotere lengte dispersie. Sterke verstrooiing van Ti en Pb-centra zijn niet aangetroffen; dit is geïnterpreteerd als een homogene distributie van ongebonden Pb-ionen in oplossing en een relatieve lage verstrooiingsintensiteit van Ti-clusters of -oligomeren.

In Hoofdstuk 8 zijn 200 nm dunne films van barium titanaat (vanuit alkoxide-carboxylaat sol gel precursors) gedeponeerd op Pt/Ti en $SrRuO_3/ZrO_2$-8%Y_2O_3 gecoate Si-substraten. Films met een dichte zuilvormige microstructuur zijn verkregen door het herhaaldelijk deponeren van amorfe lagen uit laag-geconcentreerde sols en kristallisatie bij 800 °C. Iedere depositie stap leverde een kristallijne laag barium titanaat op van 10 nm. De zware verwerkingsmethode had een negatieve impact op de Pt/Ti gecoate Si-substraten, daarbij zijn Pt-Si silicides gevormd. Als gevolg diffundeerde Si in het barium titanaat en vormde silicaat op het grensvlak. Deze gevormde silicaat laag (op het grensvlak) is de reden voor verslechterde ferroelektrische eigenschappen van de barium titanaat film. Het gebruik van $SrRuO_3/ZrO_2$-8%Y_2O_3/Si-substraten heeft dit probleem opgelost. Er vindt geen diffusie van Si plaats en de barium titanaat films met goede dielektrische en ferroelektrische eigenschappen zijn verkregen.

In Hoofdstuk 9 worden algemene conclusies getrokken. Er is beschreven dat de moeilijkheid van sol-gel verwerking niet ligt in de "hardware", maar voornamelijk in de onderliggende subtiele chemie. Mijn veronderstelling is, dat alleen met grondige kennis (of tenminste de wil om de cruciale aspecten te begrijpen) kan leiden tot massaproductie van sol-gel verkregen keramische materialen met de verwachte eigenschappen en prestaties.

Acknowledgements

First of all I would like to thank Andre ten Elshof, Dave Blank and Guus Rijnders for giving me an opportunity to work in the STW project that constituted a basis for my research described in this book. I appreciate the involvement of Andre, who had always practically unlimited time for our endless discussions, and who played a splendid role as a promotor. I knew that I could always count on him.

Secondly, since I value team-work more than research in solitude, I especially enjoyed the collaboration with Sjoerd Veldhuis and Ole Göbel, and later with Rogier Besselink, Antony George and Hessel Castricum, who occurred not only to be colleagues but also good mates with whom I could always have a beer (or an orange juice in some cases) or share time during long countless journeys. They had also lots of patience for me (especailly Sjoerd). I also thank Brian Smith and Giuseppe Portale for their input and time.

Furthermore, I thank several fellows that I had to spend 40 hours a week with, and I must admit - I was usually looking forward to that: again Sjoerd, but also Suresh Kumar, Michiel Maas, Nico Hindelbrand and recently but memoreably Gerard Cadafalch.

My life at the university would have been miserably difficult if it had not been for the help from Jose Rietman, Marion Bollaan and of course Henk Veldhuis. I thank also Mark Smithers and Rico Keim for their professional work. Their efforts are here kindly acknowledged.

Finally, I would like to thank all the members of the IMS group. I hope that you are going to forgive me that I do not mention the names of all people interested. The group was always a stimulating environment for my research and I enjoyed greatly working in it.

Tomek